

**Development of a technology framework for rapid polymer MEMS fabrication process
based on SU-8 photoresist**

by

Chang Ge

MSc, University of Alberta, 2015

A THESIS SUBMITTED IN PARTIAL FULFILLMENT OF
THE REQUIREMENTS FOR THE DEGREE OF

Doctor of Philosophy

in

THE FACULTY OF GRADUATE AND POSTDOCTORAL STUDIES
(Electrical & Computer Engineering)

THE UNIVERSITY OF BRITISH COLUMBIA

(Vancouver)

April 2021

© Chang Ge, 2021

The following individuals certify that they have read, and recommend to the Faculty of Graduate and Postdoctoral Studies for acceptance, the dissertation entitled:

Development of a technology framework for rapid polymer MEMS fabrication process based on SU-8 photoresist

submitted by Chang Ge in partial fulfillment of the requirements for

the degree of Doctor of Philosophy

in Electrical & Computer Engineering

Examining Committee:

Edmond Cretu, Electrical & Computer Engineering, UBC
Supervisor

John Madden, Electrical & Computer Engineering, UBC
Supervisory Committee Member

Anasavarapu Srikantha Phani, Mechanical Engineering, UBC
Supervisory Committee Member

Carlos E Ventura, Civil Engineering, UBC
University Examiner

Guangrui Xia, Material Engineering, UBC
University Examiner

Abstract

This Ph.D. thesis introduces a technology framework to fabricate MEMS devices using SU-8 photoresist. The lithography process of SU-8 photoresist can directly create polymeric microstructures with good chemical and mechanical stability. This characteristic makes the SU-8 photoresist suitable as the structural material for polymeric MEMS devices. However, there are several issues in the current primary fabrication methods for SU-8 MEMS devices. Existing microfabrication methods suffer from processing complexity, uncertainties, and relatively high cost. This thesis focuses on addressing these issues. Novel methodologies are used to improve the fabrication process of SU-8 out-of-plane and in-plane MEMS devices. Sacrificial-layer-free fabrication of SU-8 out-of-plane MEMS devices has been implemented using an advanced lithography principle, pixel-level dose modulation, resulting in a three-step fabrication method. A novel processing strategy is proposed to implement optimum processing for SU-8 in-plane MEMS fabrication, resulting in a four-step fabrication method. Experimental case studies with test structures have been carried out to evaluate the newly-developed methods. The main features (process predictability, reproducibility, robustness, etc.) of the newly-developed microfabrication processes have been validated after calibration. The research work of this thesis presents two new technological paths to fabricate SU-8 MEMS devices. The technology framework proposed in this thesis validates the feasibility of the two new paths' methodologies, building up the basis towards a customizable, low-cost, and rapid platform to fabricate polymeric MEMS devices. Meanwhile, the technology framework itself can be used for the rapid fabrication of SU-8 MEMS prototypes, accelerating the application and validation of novel principles and designs for polymeric MEMS devices.

Lay Summary

Microelectromechanical systems (MEMS) are microsensors and microactuators functioning as front-end interfaces between electronics and the real world. Using a photosensitive polymer called SU-8, technologies developed in this thesis provide a reliable manufacturing platform for low-cost polymeric MEMS devices. Compared with research works on similar topics, the technologies developed in this thesis have increased simplicity. They address many shortcomings of the previously existing polymer-based microfabrication, leading to low-cost, reliable microfabrication process flows. For polymer MEMS devices, the platform developed in this thesis can significantly shorten the path from a novel idea regarding a MEMS device to its fabrication and validation. It also builds up the basis of novel applications like low-cost/disposable MEMS inertial sensors. Such devices have promising potentials in applications such as the Internet-of-Things and wearable electronics.

Preface

The research objectives conducted in this thesis are identified and designed by the author, Chang Ge, and his supervisor, Dr. Edmond Cretu.

Both the theoretical and experimental studies in this thesis have been conducted solely by the author. Dr. Cretu has provided helpful advice in the fields to study, academic milestones, and experimental methodologies.

The research conducted in this Ph.D. thesis has led to 6 publications. The detail is listed below:

The main research work of Chapter 2 has been published as a journal paper:

- Ge C, Cretu E. MEMS transducers low-cost fabrication using SU-8 in a sacrificial layer-free process. *Journal of Micromechanics and Microengineering*. 2017 Apr; 27(4).

Some of the conclusions from Chapter 2 have been used in a review paper about tactile sensors. Co-authors are Dr. Liang Zhou, Dr. Jane Z Wang, Dr. Cretu, and Dr. Xiaoou Li. Chang Ge and Dr. Liang Zhou wrote the manuscript. Dr. Jane Z Wang, Dr. Edmond Cretu, and Dr. Xiaoou Li provided feedbacks on revision. Chang Ge is responsible for the content about electromechanical coupling principles, structural materials, and fabrication technologies for tactile sensors. Dr. Liang Zhou is responsible for the content about signal processing algorithms and applications of tactile sensors:

- Zou L, Ge C, Wang ZJ, Cretu E, Li X. Novel Tactile Sensor Technology and Smart Tactile Sensing Systems: A Review. *Sensors*. 2017;17:2653.

Major results of Chapter 4 have been published as a journal paper:

- Ge C, Cretu E. Design and fabrication of SU-8 CMUT arrays through grayscale lithography. *Sensors and Actuators A: Physical*. 2018 Sep 1;280:368-75.

Major results of Chapter 5 have been published as a journal paper:

- Ge C, Cretu E. A sacrificial-layer-free fabrication technology for MEMS transducer on flexible substrate. *Sensors and Actuators A: Physical*. 2019 Feb 1;286:202-10.

Major results of Chapter 6 have been published as a journal paper:

- Ge C, Cretu E. A Simple and Robust Fabrication Process for SU-8 In-Plane MEMS Structures. *Micromachines*. 2020 Mar;11(3):317.

The controllable polyimide laser micromachining process used in Chapter 6 has helped the research of Thibault Delhayé, a visiting Ph.D. student from Université Catholique de Louvain, Belgium, in manufacturing capacitive pressure sensors made using polyimide. This research work has been published at the 45th International Conference on Micro & Nano Engineering. Co-authors are Thibault Delhayé, Dr. Laurent Francis, Dr. Edmond Cretu, and Dr. Denis Flandre. Chang Ge is responsible for the development of the calibration method for polyimide laser micromachining. Delhayé Thibault used Chang Ge's calibration method for the fabrication of his membrane devices. The characterization was also done by Delhayé. Thibault Delhayé wrote the manuscript. Dr. Laurent Francis, Dr. Edmond Cretu, and Dr. Denis Flandre provided feedbacks as supervisors.

- Delhayé T, Ge C, Francis L, Cretu E, Flandre D. One-Day Fast-Prototyping Process for Functionalized Membrane Array on Flexible Substrate. In 45th International Conference on Micro & Nano Engineering 2019.

Table of Contents

Abstract.....	iii
Lay Summary	iv
Preface.....	v
Table of Contents	vii
List of Tables	xiii
List of Figures.....	xv
Acknowledgments	xxi
Dedication	xxii
Chapter 1: Background information and definition of research objectives.....	1
1.1 General information about MEMS microfabrication technology.....	2
1.1.1 Concept and criteria	2
1.1.2 Example of high-quality MEMS microfabrication: silicon-based micromachinings.	4
1.1.3 New trends in MEMS fabrication: from silicon to polymer	7
1.2 Polymeric MEMS fabrication technologies: general information	8
1.2.1 General characteristics of polymer MEMS fabrication flow	8
1.2.2 Comparison between polymer micromachining and micro-molding	10
1.3 Capacitive MEMS fabrication based on micromachining of SU-8 photoresist.....	10
1.3.1 Photopolymerization mechanism and material properties of SU-8 photoresist.....	11
1.3.2 Characteristics of current SU-8 MEMS fabrication flows.....	13
1.3.3 Issues in the current fabrication methods of SU-8 capacitive MEMS devices.....	17
1.4 Research with promising potential in SU-8 MEMS fabrication.....	18
1.4.1 Advanced lithography methods for SU-8 photoresist.....	18

1.4.2	Advanced micromachining methods.....	21
1.4.3	Enhancement of SU-8 electrical conductivity	21
1.5	Thesis Scope	22
1.5.1	Goals	22
1.5.2	Thesis organization	24
Chapter 2: Grayscale lithography of SU-8 for polymer MEMS fabrication		26
2.1	Substeps of SU-8 lithography process and their influence	27
2.1.1	Overview of SU-8 and its lithography flow.....	27
2.1.2	Influence of soft baking	30
2.1.3	Influence of UV exposure dose.....	32
2.1.4	Influence of post-exposure baking.....	36
2.1.5	Influence of developing	37
2.1.6	Summary of the review.....	39
2.2	Functionalization of SU-8 photoresist to enhance electrical conductivity	41
2.2.1	Theories behind the electrical conductivity through functionalization.....	41
2.2.2	Experimental modulation of the electrical conductivity in polymers.....	44
2.3	Exposure dose modulation in maskless grayscale lithography.....	45
2.4	Evaluation of grayscale lithography and conductive SU-8 in MEMS fabrication	46
2.4.1	Fabrication flows based on grayscale lithography.....	46
2.4.2	Material selection and preparation for experimental evaluation.....	48
2.4.3	Design of the out-of-plane SU-8 MEMS test structures.....	49
2.4.4	The fabrication process of the MEMS test structures.....	54
2.4.5	Characterization method	54

2.5	Characterization result and discussion.....	55
2.5.1	Optical inspections.....	55
2.5.2	Measurement of mechanical resonance under electrostatic actuation	58
2.6	Summary.....	65
Chapter 3: Calibration for grayscale lithography of standard SU-8.....		67
3.1	Collapsing of structures during grayscale lithography	68
3.1.1	During developing phase	68
3.1.2	During hard baking phase	70
3.1.3	Inspirations for the calibration of SU-8 grayscale lithography.....	73
3.2	A simple calibration method for SU-8 grayscale lithography	74
3.2.1	Design of the calibration method.....	74
3.2.2	Experimental set up to validate the new calibration method	76
3.2.3	Qualitative predictions of the experimental case study	78
3.3	Characterization result and discussion.....	79
3.3.1	Optical inspection	79
3.3.2	Thickness measurement	80
3.4	Summary.....	82
Chapter 4: A new way to fabricate SU-8 out-of-plane MEMS structures.....		83
4.1	General characteristics of SU-8 out-of-plane MEMS structures	84
4.1.1	Structure configuration	84
4.1.2	Electromechanical behaviors	85
4.2	A new fabrication method for SU-8 out-of-plane capacitive MEMS.....	89
4.2.1	The traditional method to make SU-8 out-of-plane MEMS structures.....	89

4.2.2	A new Fabrication method using grayscale lithography.....	90
4.3	Experimental case study of the newly-developed microfabrication technology	91
4.3.1	Design of the fabrication process.....	92
4.3.2	Lithography calibration.....	94
4.3.3	Simulation and computations for process quality evaluation	95
4.3.4	Characterization methods.....	97
4.4	Characterization result and discussion.....	98
4.4.1	Yellow light microscopic inspection	98
4.4.2	Measurement of mechanical resonance during the electrical actuation.....	99
4.4.3	Electrical impedance measurement during the electrical actuation	102
4.5	Discussion about the practicability of the new fabrication methodology.....	103
4.5.1	Process-related constrains and practicability	103
4.5.2	Material-related constraints and practicability.....	106
4.5.3	Equipment-related constraints and practicability.....	107
4.6	Summary	108
Chapter 5: Using metal-polymer composites as substrates for SU-8 MEMS.....		110
5.1	Characteristics of metal-polymer composites as low-cost and flexible substrates	111
5.1.1	Surface condition characterization.....	111
5.1.2	Influence on SU-8 grayscale lithography	112
5.2	Setup for the experimental case study	113
5.2.1	Design of structural dimensions and processing parameters	113
5.2.2	Bending test of the flexible substrates	116
5.2.3	Finite element simulations	117

5.2.4	Characterization methods.....	122
5.3	Characterization result	122
5.3.1	Optical inspection and measurement of planar dimensions.....	122
5.3.2	Mechanical resonance during the electrostatic actuation.....	125
5.3.3	Measurement of the electrical impedance magnitude.....	133
5.4	Summary	134
Chapter 6: A new fabrication technology for SU-8 in-plane MEMS structures.....		135
6.1	General characteristics of in-plane SU-8 MEMS structures.....	136
6.1.1	Structural characteristics.....	136
6.1.2	Electromechanical behaviors	137
6.2	A novel fabrication methodology for SU-8 in-plane capacitive MEMS structures....	139
6.2.1	Fabrication flows: from silicon to SU-8 photoresist.....	139
6.2.2	Issues for SU-8 in-plane MEMS fabrication	143
6.2.3	A four-step fabrication flow of in-plane SU-8 MEMS structures	143
6.3	Experimental case study of the newly-developed fabrication flow	148
6.3.1	Calibration for laser micromachining on the copper-polyimide composite	149
6.3.2	SU-8 lithography calibration.....	151
6.3.3	Design and simulation of in-plane MEMS test structures	157
6.3.4	Simulation and prediction for electromechanical behaviors.....	159
6.3.5	Fabrication of the in-plane MEMS test structures	160
6.3.6	Characterization methods.....	161
6.4	Characterization result and discussion.....	162
6.4.1	Optical inspection	162

6.4.2	Measurement of mechanical resonance under electrical actuation.....	164
6.4.3	Electrical impedance measurement.....	166
6.5	Discussion about the practicability of the new strategy and technology	167
6.6	Summary.....	168
Chapter 7: Thesis summary		170
7.1	Summary of accomplished research work	170
7.2	Scope of future work.....	172
7.2.1	Implementation of SU-8 MEMS devices for specific applications	172
7.2.2	Research and development towards massive production.....	173
7.2.3	Conductive SU-8 for controllable MEMS fabrication.....	173
Bibliography		175

List of Tables

Table 1.1 Influential factors of a MEMS fabrication method.....	3
Table 1.2 Comparison between the deposition and etching of polymer and silicon	7
Table 1.3 Summarization of important SU-8 properties related to MEMS applications.....	12
Table 1.4 Summary of current SU-8 MEMS fabrication methods	15
Table 1.5 Advanced lithography methods for SU-8 photoresist.....	19
Table 1.6 Nanofillers for conductive SU-8.....	22
Table 2.1 Dependence of the SU-8 lithography process quality on main substeps	29
Table 2.2 Soft baking temperature and the influence on SU-8 lithography quality	31
Table 2.3 Summary of the photochemistry of the photoinitiators in SU-8 during UV exposure .	33
Table 2.4 The relationship between crosslinking ratio and the condition of post-exposure baking	36
Table 2.5 The elastic property and structural strength of SU-8 under different PEB condition...	37
Table 2.6 Net tensile stress generated by liquid agents to develop SU-8 photoresist	38
Table 2.7 Influence of processing steps on the final quality of SU-8 lithography	41
Table 2.8 Material parameters related to the functionalization of SU-8 for electrical conductivity	42
Table 2.9 Dimensions of out-of-plane polymeric MEMS transducers to be fabricated	49
Table 2.10 Statistic information of each type of SU-8 transducers fabricated	63
Table 2.11 Relative sensitivity of the natural frequency to the material and geometric parameters	64
Table 3.1 Surface tension and contact angle of liquids involved in the SU-8 lithography process	69

Table 3.2 SU-8 material properties used in the finite element analysis.....	72
Table 3.3 Recipe of SU-8 grayscale lithography process to validate the calibration method	76
Table 4.1 Process parameters and structure design for application potential validation on silicon	92
Table 4.2 SU-8 material properties used in FEA simulation	95
Table 5.1 Structural designs for the experimental validation on flexible substrates	113
Table 5.2 Processing recipes for the experimental case study	114
Table 5.3 Mechanical properties of SU-8 used in FEA analysis	117
Table 5.4 Measurement of transducer planar dimensions and comparison with design	124
Table 5.5 Statistical information on mechanical resonance for selected devices to test	126
Table 5.6 Relative error between the measured resonant frequency and the FEA simulations..	127
Table 6.1 Setup of the laser micromachining to determine the proper repeated times.....	149
Table 6.2 Process parameters for SU-8 lithography calibration.....	151
Table 6.3 Dimensions of the mask design for SU-8 lithography calibration.....	154
Table 6.4 Design of the in-plane MEMS test structures.....	157
Table 6.5 SU-8 material properties used for simulation and computation	158
Table 6.6 Statistics of the mechanical resonance for selected in-plane MEMS test structures..	164
Table 7.1 Summary of the fabrication technology developed in this thesis: process controllability	171

List of Figures

Figure 1.1 The relationship between research regarding MEMS fabrication technology and MEMS design/application.	1
Figure 1.2 The generic flow for silicon surface micromachining.....	4
Figure 1.3 The generic flow for silicon bulk micromachining.	5
Figure 1.4 Depiction of generic micro-molding flow for polymeric microstructures.	9
Figure 1.5 Surface micromachining for SU-8 MEMS structures	13
Figure 1.6 Bulk micromachining for SU-8 MEMS structures.....	14
Figure 1.7 The methodology used in existing research works of SU-8 MEMS devices.	16
Figure 1.8 The general methodology to be used in this thesis.....	23
Figure 1.9 Depiction of the objective and organization of the Ph.D. thesis.	24
Figure 2.1 Illustration of the research conducted in Chapter 2.	26
Figure 2.2 Schematic of SU-8 lithography flows and the involved chemical reactions.	28
Figure 2.3 Detailed view of SU-8 lithography process and the role of each substep.....	40
Figure 2.4 Comparison between grayscale modulation predicted by the numerical model and the measurement.	45
Figure 2.5 Two manufacturing flows based on grayscale lithography and conductive SU-8.	46
Figure 2.6 Comparison of SU-8 MEMS fabrication processes.	47
Figure 2.7 Mask designs for doubly-clamped beams made by grayscale lithography of standard SU-8.	50
Figure 2.8 Mask designs for membranes made by grayscale lithography of standard SU-8.	51
Figure 2.9 Mask designs for doubly-clamped beams made by grayscale lithography of SU-8 mixed with silver nanoparticles.	52

Figure 2.10 Mask designs for membranes made by grayscale lithography of SU-8 mixed with silver nanoparticles..	53
Figure 2.11 Microscopic inspection of polymeric out-of-plane transducers fabricated by grayscale lithography of standard SU-8 2015.....	55
Figure 2.12 The transmission and reflection of yellow light within SU-8 microstructures with different final status.	56
Figure 2.13 Representative issues polymeric MEMS structures fabricated by conductive SU-8.	58
Figure 2.14 Mechanical resonance of MEMS transducers made by grayscale lithography of standard SU-8.....	59
Figure 2.15 Mechanical resonance of MEMS transducers made by grayscale lithography of SU-8 mixed with silver nanoparticles.	60
Figure 2.16 The distribution of the measured resonant frequency for doubly-clamped beams ...	62
Figure 2.17 The distribution of the measured resonant frequency for membranes.	62
Figure 3.1 Research work in Chapter 3.	67
Figure 3.2 Crossecional distribution profile of photoacids at exposed regions after grayscale lithography	70
Figure 3.3 SEM images of the crosssection of doubly-clamped beams fabricated by SU-8 grayscale lithography.....	71
Figure 3.4 Simulation of hard baking for SU-8 beams fabricated by grayscale lithography.	72
Figure 3.5 Simulation of hard baking for SU-8 beams with uniform cross-section.	73
Figure 3.6 General flow of the new calibration method for SU-8 grayscale lithography	74
Figure 3.7 An example of mask designs for the newly-developed calibration method of grayscale lithography	75

Figure 3.8 Computed N_{EC} values for the calibration structures during the experimental case study	77
Figure 3.9 Examples of doubly-clamped beams fabricated by SU-8 grayscale lithography for calibration.	79
Figure 3.10 Thickness calibration result for grayscale lithography using SU-8 2015 spin-coated at different speed values.	80
Figure 3.11 Distribution of standard deviation for the thickness measurement	81
Figure 4.1 Illustration of the research work of Chapter 4.	83
Figure 4.2 Schematic of a capacitive SU-8 out-of-plane MEMS structures.	84
Figure 4.3 Surface micromachining for capacitive SU-8 out-of-plane MEMS transducers.	89
Figure 4.4 Illustration of the newly-designed fabrication flow for out-of-plane SU-8 MEMS structures	90
Figure 4.5 Mask designs for the experimental validation.	93
Figure 4.6 Lithography calibration result for the thickness values used for out-of-plane transducer fabrication on silicon wafers.	94
Figure 4.7 FEA simulation results for the circular membranes fabricated.	96
Figure 4.8 Relationship between equivalent mechanical spring constant and electrical voltage.	96
Figure 4.9 Microscopic inspection of the SU-8 circular membrane arrays fabricated on a silicon wafer.	98
Figure 4.10 Electrical-mechanical actuation and the measurement result.	99
Figure 4.11 Representative result for the frequency modal analysis and coherence analysis of the measurement obtained from the LDV.	100

Figure 4.12 Impedance measurement of the SU-8 circular membranes during electrical actuation	102
Figure 4.13 Calibration results for six different layers, normalized view	103
Figure 4.14 Simulation result for a set of structural dimensions achievable by application- specifically optimized SU-8 grayscale lithography.	105
Figure 5.1 Depiction of the research work for Chapter 5	110
Figure 5.2 The surface topological characteristics of the copper-polyimide composites.	111
Figure 5.3 Mask designs for the SU-8 out-of-plane transducers to be fabricated on flexible substrates.....	115
Figure 5.4 Illustration of the temporary bendings.	116
Figure 5.5 Simulation for the fundamental resonant modes of the proof-of-concept out-of-plane SU-8 MEMS structures.....	118
Figure 5.6 Simulation of stress during bending, cantilevers.....	119
Figure 5.7 Simulation of stress during bending, doubly-clamped beams.....	120
Figure 5.8 Simulation of stress during bending, membranes.....	121
Figure 5.9 Yellow light microscopic inspection for the fabricated SU-8 transducers.....	123
Figure 5.10 Proof-of-concept out-of-plane MEMS structures after metallization.	125
Figure 5.11 The distribution of natural frequency measurement for cantilevers.....	128
Figure 5.12 The distribution of natural frequency measurement for double-clamped beams. ...	129
Figure 5.13 The distribution of natural frequency for circular membranes.....	130
Figure 5.14 Visualization of electrostatically actuated mechanical vibrations of the fabricated structures, before and after the temporary bending.	131

Figure 5.15 Comparison of resonant frequency shift before and after the temporary bending at the individual transducer level	132
Figure 5.16 Electrical impedance measurement of the SU-8 circular membranes before and after the temporary bending.	133
Figure 6.1 Depiction of the detailed research work carried out in Chapter 6.....	135
Figure 6.2 The generic characteristics of in-plane MEMS structures.	136
Figure 6.3 SOIMUMPs, the fabrication technology for silicon-based in-plane MEMS structures.	139
Figure 6.4 Polymeric micro-molding for in-plane MEMS devices	141
Figure 6.5 SU-8 surface micromachining for in-plane MEMS devices.	142
Figure 6.6 Step 1, copper-polyimide processing based on a new strategy	144
Figure 6.7 Step 2: SU-8 lithography on the copper surface.....	146
Figure 6.8 Step 3: multi-purpose copper etching.....	147
Figure 6.9 The metallization process of the in-plane structures	148
Figure 6.10 Experimental calibration result for laser cutting on polyimide layers.	150
Figure 6.11 Experimental study for the influence of the surface thread-like pattern on the lithography qualities.....	152
Figure 6.12 Mask design to calibrate SU-8 lithography for optimum exposure duration and structure design.	153
Figure 6.13 Calibration result for interdigitated fingers in Table 6.3.	155
Figure 6.14 Calibration result for the elastic beams in Table 6.3.	156
Figure 6.15 Mask files used to fabricate the proof-of-concept SU-8 in-plane MEMS comb drives.	158

Figure 6.16 Finite element analysis simulation result for the resonant mode of the in-plane MEMS test structures.....	159
Figure 6.17 Optical inspections of the in-plane MEMS test structures at different phases of the new fabrication flow.	163
Figure 6.18 Visualization of the mechanical resonance measurement of the fabricated in-plane MEMS test structures.....	165
Figure 6.19 Measurement of the electrical impedance of the in-plane MEMS test structures...	166
Figure 6.20 Illustration of the implementation of the ‘Border-bulk’ strategy based on polyimide RIE	168

Acknowledgments

I offer my enduring gratitude to Dr. Edmond Cretu, as my supervisor, Dr. Anasavarapu Srikantha Phani, and Dr. John Madden, as my committee members. They have provided invaluable guidance and instructions for my research work.

I also want to thank the laboratory staff of SBQMI Advanced Nanofabrication Facility, Advanced Material and Process Engineering Laboratory (AMPEL), the University of British Columbia, Canada. They have helped me to use many apparatuses that are vital to my research.

I also want to thank my wife, Yingxue (Leona), Li. She has provided irreplaceable support during these years.

Dedication

To everyone who has helped me to complete this thesis.

Chapter 1: Background information and definition of research objectives

Microelectromechanical systems (MEMS) are sensors and actuators coupling energy flows between the electrical and mechanical domains at the microscale. They are essential front-end components in modern microsystems [1]. The research related to MEMS has two subcategories: MEMS design and MEMS fabrication, both of great significance. The relationship between the two research categories is illustrated in Figure 1.1.

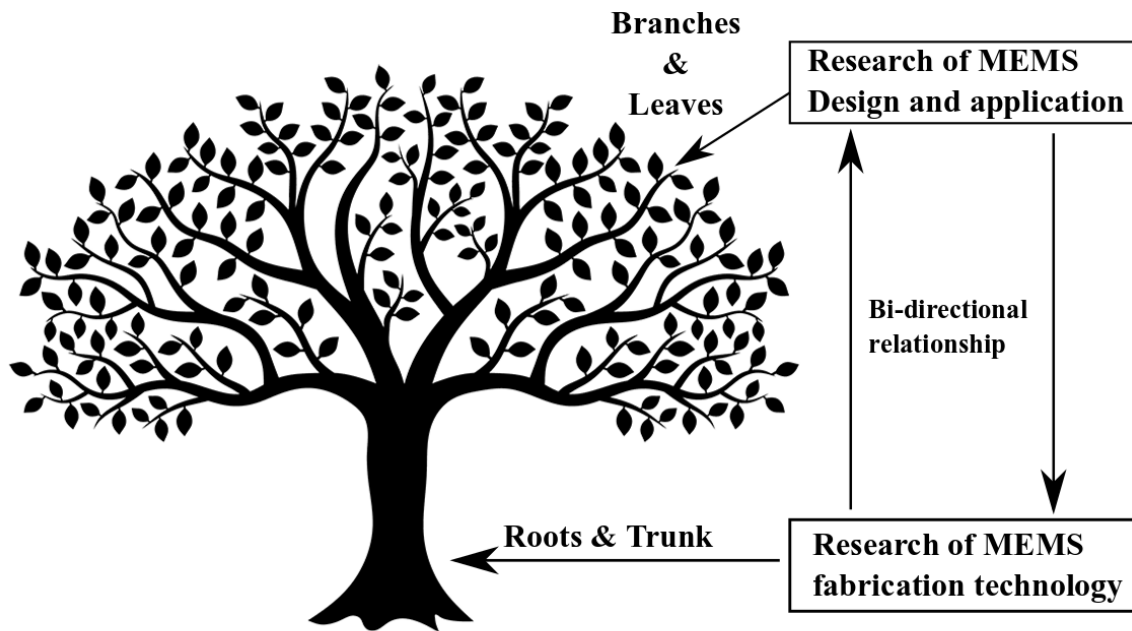


Figure 1.1 The relationship between research regarding MEMS fabrication technology and MEMS design/application.

As shown in Figure 1.1, the whole field of MEMS is like a tree, with the fabrication level being the roots and trunk, while the application level being the branches and leaves. Fabrication technologies bring concepts and designs into physical existence, supporting the research at the application level, similar to how the roots and trunk support the canopy of a tree.

This Ph.D. thesis is dedicated to research over capacitive polymeric MEMS fabrication using SU-8 photoresist as structural materials. Originally, capacitive MEMS devices were manufactured using silicon microfabrication technologies. Recently, increasing attention has been paid to polymeric-based MEMS fabrications. Using photoresists as structural materials has been one major branch of exploratory work for polymeric MEMS devices [2-5].

As the introduction of the whole thesis, this chapter reviews the relevant fields, pointing out the issues to address, and defines the research objectives. Section 1.1 introduces general information about MEMS fabrication. The discussion focuses on the essential criteria for a usable MEMS fabrication technology and the generic methodology of most microfabrication technologies to manufacture microstructures. The latter has been reflected well in the silicon surface and bulk micromachining processes. Here, these two micromachining processes are discussed as the most classic microfabrication technologies. In the last part of Section 1.1, polymeric MEMS fabrication methods are compared with silicon MEMS fabrication processes to explain why they have attracted intense research attention in recent years. Section 1.2 presents the general characteristics of polymer MEMS fabrication processings. The characteristics and issues of current SU-8 MEMS fabrication attempts are presented in Section 1.3. Section 1.4 summarizes the research progress in the associated fields. The research objectives and specifications for this Ph.D. thesis are provided in Section 1.5.

1.1 General information about MEMS microfabrication technology

1.1.1 Concept and criteria

Microfabrication flows of MEMS devices involve a series of physical and chemical material processing steps, with the typical resolution ranging from submicrometer to thousands of micrometers, to turn a design into physically-existing microdevices [1]. A MEMS microfabrication

flow has to fulfill some fundamental performance criteria to obtain broad applicability for the fabrication of microdevices. Most-commonly used criteria to evaluate MEMS fabrication methods are summarized in Table 1.1 [6, 7].

Group	Criterion	Definition
Process controllability	Being calibratable (calibratability)	Possibility to map process recipe to process results, particularly structural dimensions
	Being predictable (predictability)	Possibility to predict the electromechanical behavior of manufactured MEMS devices, using calibration result in the design and simulation phase
	Being consistent (reproducibility)	Possibility to get devices with identical performance within a single batch and from one batch to another
	Being robust	Technology is less sensitive to small fluctuations of process parameters
Process resolution and accuracy		The smallest achievable dimensions for manufactured structures

Table 1.1 Influential factors of a MEMS fabrication method

In Table 1.1, the process controllability is the *'must-have.'* All the detailed criteria for process controllability must be fulfilled for a well-designed MEMS fabrication flow. Missing any of the criteria will directly compromise the application potential.

Process resolution and accuracy are mainly used to evaluate the performance of microfabrication technology. Compared with process controllability, process resolution and accuracy are less critical for many applications. For a MEMS fabrication method, on the premise

that it has good controllability, a lower process resolution and accuracy is not catastrophic. It can be compensated by using novel principles during the design phase or in peripheral electronics [8].

1.1.2 Example of high-quality MEMS microfabrication: silicon-based micromachinings

Silicon surface and bulk micromachining processes are the most widely-used MEMS microfabrication methods. The classic approach to fabricate microstructures has been well-reflected in these two methods. Their general flows are shown in Figures 1.2 and 1.3 [1, 6, 7, 9, 10].

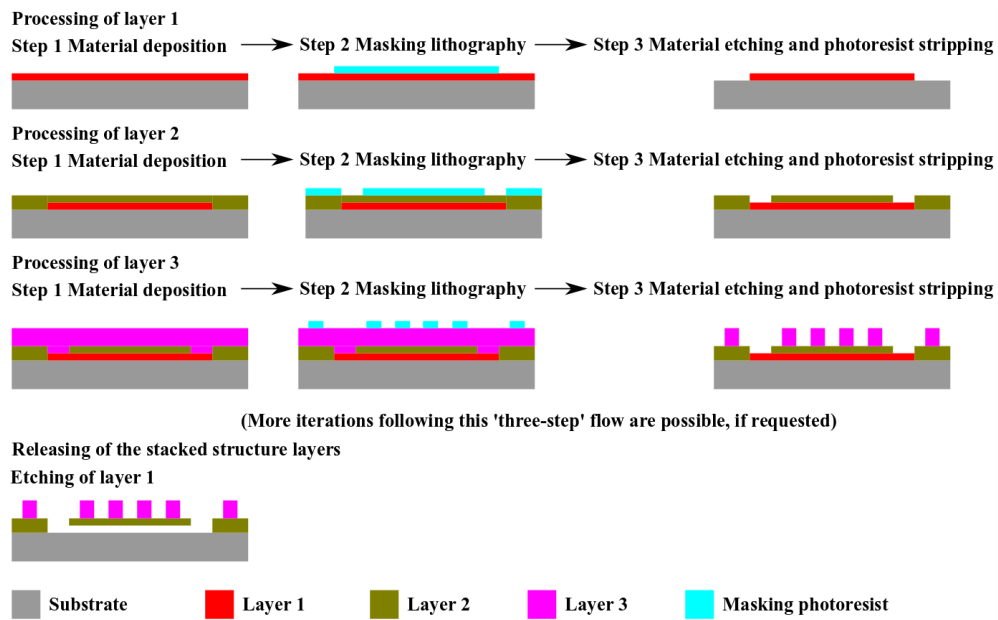


Figure 1.2 The generic flow for silicon surface micromachining.

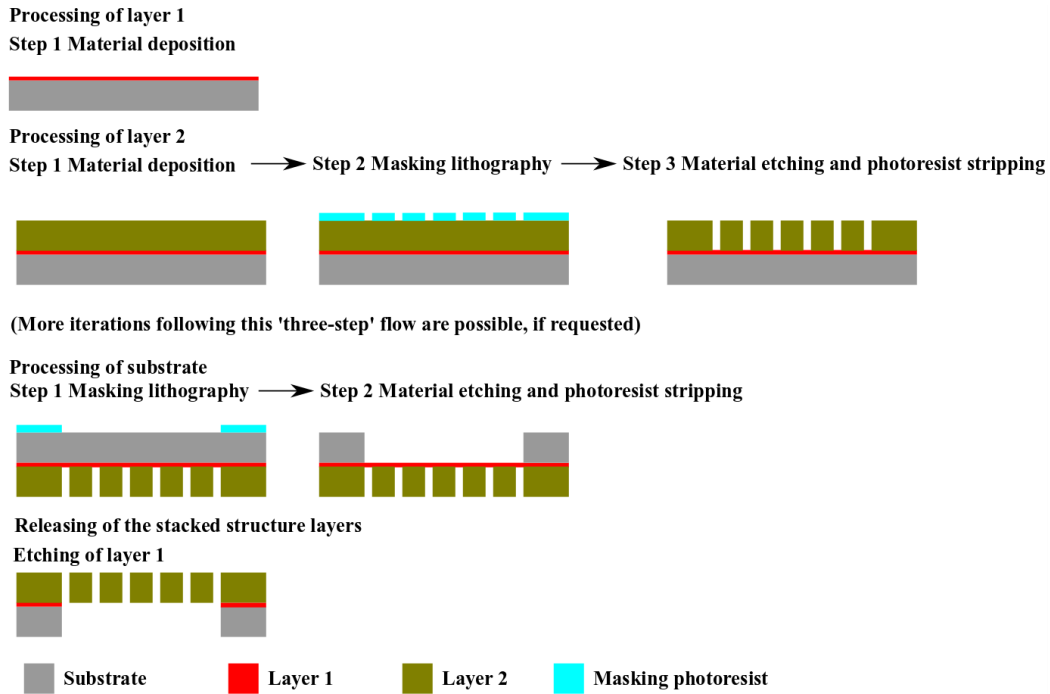


Figure 1.3 The generic flow for silicon bulk micromachining.

As shown in Figures 1.2 and 1.3, the classic way to get microstructures is to use the layer-by-layer patterning technique. The material processing of each layer uses the deposition-masking-etching cycles for material processing. New cycles can be inserted into existing ones to achieve specific processing purposes.

Generally, MEMS structures consist of both movable and fixed parts. In order to form movable parts, a sacrificial layer is used, such as Layer 1 in both Figures 1.2 and 1.3. It is removed in the subsequent steps to release the movable microstructures. Silicon surface and bulk micromachining processes have two significant differences. Firstly, surface micromachining and bulk micromachining use different ways to make microstructures movable. During surface micromachining in Figure 1.2, the microstructures are released by etching the sacrificial layer. After the releasing process, a small gap exists between the movable structures and the substrate. During silicon bulk micromachining in Figure 1.3, multiple layers, including the substrate, are

etched to release the MEMS structures. As a result, the final MEMS structures are suspended within open windows created on the substrate layers. Secondly, surface micromachining has a thinner structural layer than bulk micromachining.

Silicon surface and bulk micromachining technologies have been used to fabricate various MEMS structures, making many life-changing innovations possible. Silicon surface micromachining has higher compatibility with integrated circuits than bulk micromachining [10], and it has been used to fabricate both in-plane and out-of-plane MEMS structures. Silicic bulk micromachining is more frequently used for the fabrication of in-plane MEMS structures. Out-of-plane MEMS structures move in the direction vertical to the substrate to realize their functions. Representative examples of out-of-plane MEMS structures include RF switches, microphones, pressure sensors. In-plane MEMS structures move in the direction parallel to the substrates for their functions. Representative examples are MEMS inertial sensors.

The silicon-based microfabrication's main issues are the lack of process flexibility and the long fabrication duration cycles [1, 6, 7, 9, 10].

Silicon-based microfabrication technologies have a very high total cost related to apparatuses and infrastructures. They rely on the scale effect of the massive production to reduce the average cost for every single microdevice. The fabrication processes are generally standardized for such massive productions. Though process customization for small-scale production is possible, it generates an impractically high cost that many researchers cannot afford. The high cost related to infrastructures has also influenced the interaction between the design and fabrication phases. Currently, the fabrication capability is mainly concentrated in the hands of a few foundries. They offer annual time windows to the MEMS designers. The designers must submit their designs in time to join the waiting queues and wait for months before their devices are sent back for tests.

The role of designers is very passive. If adjustments are made in the design of MEMS devices, they cannot be updated to the foundries in a fast and economical way. They have to start to wait again in the queue for fabrication. These issues have significantly increased the time consumption for research about MEMS devices.

As a solution, more and more researchers are trying to accelerate their research progress through MEMS fabrication based on polymeric materials.

1.1.3 New trends in MEMS fabrication: from silicon to polymer

With the rapid progress in material science and engineering, many polymers have shown potentials as MEMS structural materials [2-5]. The primary motivations to use polymers for MEMS fabrication include simpler deposition methods, faster and safer etching methods, and, correspondingly, the lower cost of the micromachining flows. Table 1.2 provides detailed information regarding these advantages of polymers for MEMS fabrication.

Material	Silicic [1, 6, 7, 9, 10]	Polymeric [11-14]
Deposition method and the typical rate	CVD, 10s ~ 100s nm/min	Spin-coating, 0.1s ~ 100s $\mu\text{m}/\text{min}$
Wet etchant and the typical etching rate	KOH, TMAH, EDP, HF, 10s ~ 1000s nm/min	Acetone, PGMEA, NMP, and other organic solvents 1s ~ 10s $\mu\text{m}/\text{min}$
Dry etchant and the typical etching rate	CF ₄ , SF ₆ , NF ₃ , XeF ₂ 10s ~ 100s nm/min	O ₂ +SF ₆ , O ₂ +CHF ₃ , O ₂ +CF ₄ 1s $\mu\text{m}/\text{min}$

Table 1.2 Comparison between the deposition and etching of polymer and silicon

In Table 1.2, polymer layers with good qualities can be achieved by methods as simple as spin-coating. A wide range of polymer layer thickness can be achieved by properly tuning the viscosity of the solution. In contrast, high-quality silicic films with more-reduced thickness can only be achieved from vapor deposition. This fact means that the deposition of polymeric material is simpler, faster, and more flexible. The etchants of polymers are less corrosive, and the etching rate is significantly higher. Consequently, the overall processing safety has been increased, and the cost of waste processing and personnel protection has been reduced [2-5].

Based on these advantages, polymer MEMS fabrication becomes very promising in enhancing the coupling between design and fabrication. The simpler infrastructures and, correspondingly, the lower cost makes it possible to have MEMS design and fabrication in the same facility/laboratory. In this way, adjustments in design can be dynamically implemented by fabrication flows. The research activities to validate new concepts or principles for MEMS devices are significantly accelerated. Meanwhile, the lower cost in infrastructures and shorter fabrication duration cycles make it possible to customize the polymeric microfabrication process based on the demand of designers at a significantly lower price, providing more flexible services. This enlightens the path towards a novel business model in the industry of microfabrication.

1.2 Polymeric MEMS fabrication technologies: general information

1.2.1 General characteristics of polymer MEMS fabrication flow

Generally, polymer-based MEMS fabrication can be split into two phases[2-5]: the formation of polymeric microstructures and the metallization process for the electromechanical interface. During the first phase, polymer layers are shaped into microstructures of MEMS devices. Since most of the polymers used in MEMS fabrication are electrical insulators, it becomes vital to

create electromechanical interfaces through the deposition and patterning of an electrically-conductive layer, known as ‘metallization.’

The formation of polymeric microstructures can be done either using the surface micromachining process or micro-molding, a process unique to polymers. The general flow of polymeric micro-molding is illustrated in Figure 1.4.

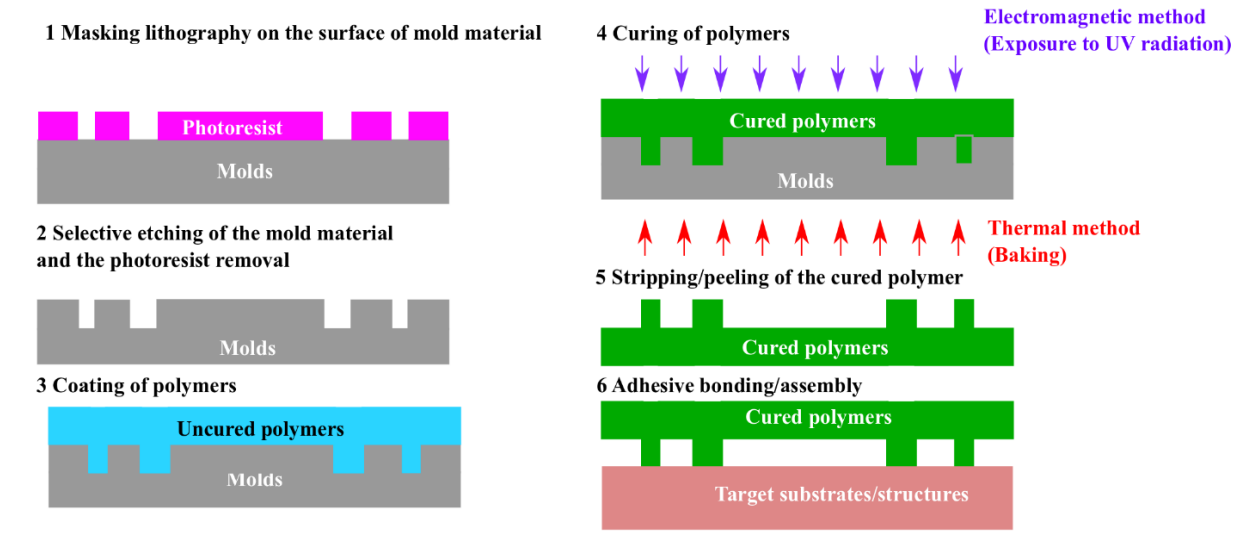


Figure 1.4 Depiction of generic micro-molding flow for polymeric microstructures.

A complete micro-molding process has three phases: the creation of molds, polymer coating and curing, delamination of polymer structures, and assembly. In Figure 1.4, steps 1 and 2 describe the creation of molds. These molds are fabricated in metals or silicon [3, 15-17], using the micromachining flows in Figure 1.4. Steps 3 and 4 show the formation of polymeric structures through molding. Polymers suitable for micro-molding flows have to be curable, either thermally or electromagnetically (UV radiation) [2, 3, 15]. Representative choices include PDMS, PMMA, and Polyimide. Based on the methods used for polymer coating or curing, micro-molding processes can be subcategorized into hot embossing [18], jet molding [19], injection [20], micro-transfer molding [21], and molding in capillaries [22]. In order to assemble separate structures into

the final devices, after micro-molding, a wafer bonding process is always used, shown as steps 5 and 6 in Figure 1.4 [23, 24].

1.2.2 Comparison between polymer micromachining and micro-molding

Polymer micromachining and micro-molding have some distinct differences regarding their process simplicity and flexibility.

During the micromachining process of a polymeric material for MEMS structures, some fabrication steps for silicic material are *replaced* with the ones for polymers. The replacement makes the whole fabrication flow benefit from the merits of polymeric materials discussed in Section 1.1.3. During a polymer micro-molding, polymeric microstructures are obtained by embossing and debossing after molds are created by the classic surface micromachining process. The process flexibility is lower than polymer micromachining because of the fabrication process for molds. If the structural design needs frequent adjustment, the cost may be higher.

However, micro-molding has been demonstrated as a powerful method for fabricating sophisticated multi-layer microfluidic devices [25, 26]. The intricate 3D microstructures in multi-layer microfluidic devices are more challenging to fabricate if only micromachining methods are used [3].

This Ph.D. thesis is more focused on addressing the fabrication technology for capacitive polymeric MEMS structures. The research effort has been mainly invested in the polymer micromachining process. In the polymer micromachining for capacitive MEMS devices, it has been a common practice to use photosensitive polymers [2, 11, 12].

1.3 Capacitive MEMS fabrication based on micromachining of SU-8 photoresist

Photosensitive polymers (photoresists) are processed through photolithography for microstructures. Before directly used as permanent MEMS structural material, photoresists have

already played an essential role in the silicon MEMS microfabrication flows. They are widely used as the primary material for temporary etching masks.

When photoresists are used as the MEMS structural materials, the 3-step cycle to get the microstructures turns into a single lithography process. By far, SU-8 negative photoresist has become the most popular photosensitive polymers for MEMS structures [11, 12].

1.3.1 Photopolymerization mechanism and material properties of SU-8 photoresist

SU-8 photoresist is a negative photoresist with di-glycidyl ether bisphenol-A (DGEBA) epoxy as its monomer and triaryl-sulfonium hexafluoro-antimonate salt as photoinitiator [27]. After exposed to 365nm UV radiation, the exposed parts would form permanent structures on the substrates. The photopolymerization mechanism of SU-8 is cationic auto-catalyzed crosslinking, which has given SU-8 outstanding mechanical and chemical stabilities over other photosensitive polymers and promoted its applications as a structural material for MEMS devices.

Generally, there are three physico-chemical paths for photosensitive polymers to be formed into microstructures: radical polymerization, cationic catalyzed crosslinking, and photon-induced scission [28]. Photosensitive polymers for permanent microstructures of MEMS transducers are generally based on the first two mechanisms, with cationic catalyzed crosslinking being superior to radical polymerizations. Photoresists based on radical polymerizations are influenced by radical scavengers, such as oxygen. The scavengers can effectively inhibit radical polymerization, resulting in a deteriorated polymer matrix and corresponding mechanical properties [28]. The photoresist based on cationic catalyzed crosslinking is not influenced by these inhibitors, making the polymerized monomers more chemically and mechanically robust. The corresponding advantages include good contact and adhesion with various types of surface, good elasticity, and minor shrinkage after hardening [28].

Since its emergence, various research works have characterized SU-8's material properties related to applications in polymeric MEMS, demonstrating its suitability as structural material for polymeric MEMS devices. Table 1.3 summarizes these properties of SU-8 photoresist.

Mechanical properties				
Property	Young's Modulus (E)	Thermal expansion coefficient (CTE)	Poisson ratio(ν)	Degradation temperature (T_d)
Typical value	4.95 (± 0.42) GPa [29, 30]	102 (± 5.01) ppm/K [31]	0.33[31]	380 °C [32]
Electrical and optical properties				
Property	Breakdown voltage	Relative dielectric constant (ϵ_r)	Refractive index (n)	
Typical value	$4.43(\pm 0.16) \times 10^8$ V/m [33]	4 [34]	1.7 [35]	

Table 1.3 Summarization of important SU-8 properties related to MEMS applications

The Young's modulus of SU-8 of 4.95 GPa is much higher than the modulus for the other two common polymer MEMS materials: PDMS (kPa level) [36] and PMMA [2] (GPa level, <3 GPa) and makes SU-8 more suitable as the structural material for polymeric electromechanical transducers. The high breakdown voltage of SU-8 makes it suitable for capacitive-based electromechanical coupling. The thermal expansion coefficient is sufficient for electrothermal-based actuation. The suitability of application in thermal actuators is also supported by the high degradation temperature, a necessary material property for electro-thermally induced large displacement.

1.3.2 Characteristics of current SU-8 MEMS fabrication flows

The fabrication flows used to fabricate SU-8 MEMS devices in existing research works are summarized in Figures 1.5, Figure 1.6, and Table 1.4 [3, 37-59].

Step 1 Deposition of sacrificial layers



Step 2 Patterning of structure layers

2.1 Photolithography for masking 2.2 Sacrificial layer selective etching 2.3 Photoresist stripping

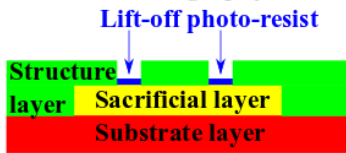


Step 3 Photolithography of structure layers

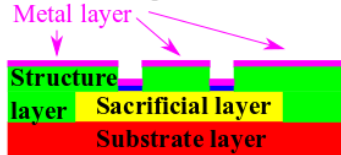


Step 4 Selective metalization

4.1 Lift-off lithography



4.2 Metal deposition



4.3 Lift-off photoresist stripping



Step 5 Releasing the structure layer by etching sacrificial layers

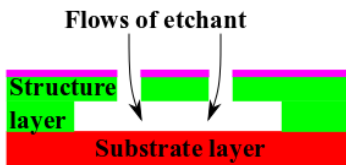


Figure 1.5 Surface micromachining for SU-8 MEMS structures

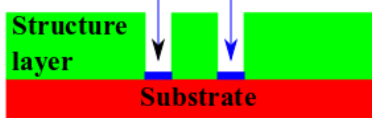
Step 1 Photolithography of structure layers



Step 2 Selective metalization

2.1 Lift-off lithography

Lift-off photo-resist



2.2 Metal deposition

Metal layer

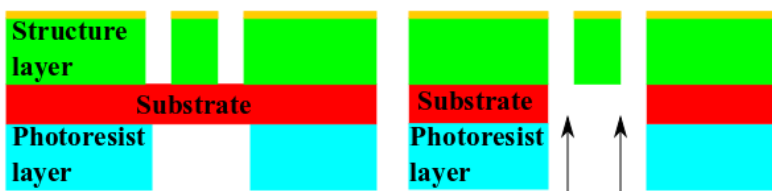


2.3 Lift-off photoresist stripping



Step 3 Releasing by bulk micromachining of substrate

3.1 Photolithography for masking 3.2 Etching of substrate



3.3 Photoresist stripping

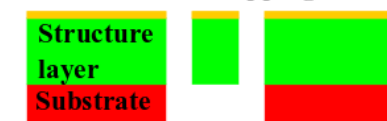


Figure 1.6 Bulk micromachining for SU-8 MEMS structures

Process for sacrificial layers			
Sacrificial layer types	Photoresist[48, 50, 60, 61]	Metal[38, 46, 47, 52, 53, 62-65]	Silicic[3, 37-43, 66]
Process flows	1. Sacrificial layer lithography	<ol style="list-style-type: none"> 1. Masking layer lithography 2. Metal E-beam evaporation 3. Sacrificial layer lift-off 4. Sacrificial layer electroplating (optional)[59] 5. Polishing (optional) [59] 	<ol style="list-style-type: none"> 1. Silicic material CVD/E-beam evaporation 2. Masking lithography 3. Metal mask E-beam evaporation/Sputtering (optional) 4. Metal mask lift-off (optional) 5. Sacrificial layer wet etching/dry etching 6. Masking material stripping
The shaping of MEMS structure			
SU-8 lithography			
Metalization process			
Processing flows		<ol style="list-style-type: none"> 1. Lift-off lithography 2. Metal E-beam evaporation/Sputtering Electrode lift-off 	
Structure releasing			
Sacrificial layer wet etching or Silicon DRIE (deep reactive ion etching, for bulk micromachining) [41, 43]			

Table 1.4 Summary of current SU-8 MEMS fabrication methods

As shown in Figures 1.5 and 1.6, current SU-8 MEMS fabrication flows are similar to silicon micromachining processes. The surface micromachining flow in Figure 1.5 has been widely

used to manufacture in-plane and out-of-plane SU-8 capacitive MEMS structures [46-54, 58, 59]. For SU-8 thermal actuators, besides the SU-8 surface micromachining, many of them have been manufactured by bulk micromachining in Figure 1.6 [3, 37-43]. The silicon substrate underneath the SU-8 electrothermal grippers is etched by deep reactive ion etching (DRIE) to make it easier for the grippers to approach and capture samples.

The fabrication flows in Figures 1.5 and 1.6 rely heavily on sacrificial layers. However, the sacrificial layer selection has been diverse, as presented in Table 1.4. The existing fabrication flows of SU-8 capacitive micromachined ultrasound transducers (CMUT) are representative examples with this respect [46-48, 50, 52, 63]. All three types of sacrificial layers in Table 1.4 have been used for the fabrication processes of SU-8 CMUT devices, but little explanation for the selections has been given. This thesis has attributed such a phenomenon to the methodology behind the current research works of SU-8 MEMS devices. This methodology is depicted in Figure 1.7.

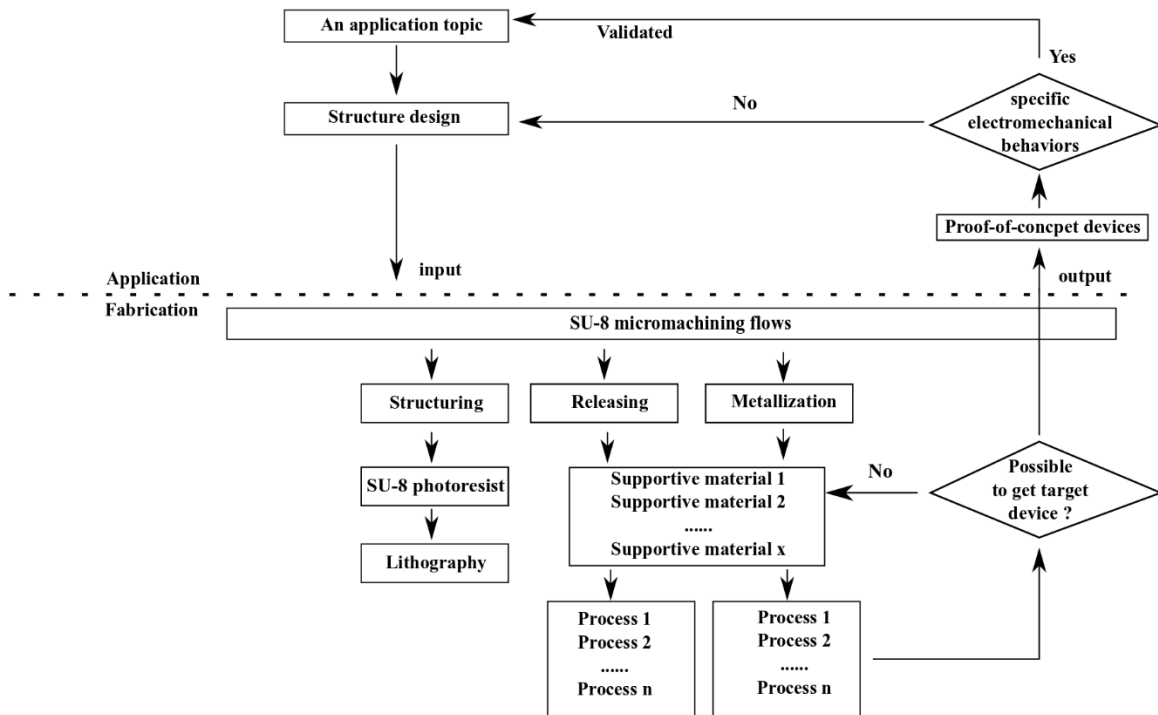


Figure 1.7 The methodology used in existing research works of SU-8 MEMS devices.

As shown in Figure 1.7, most current research works focus on the possibility of making specific types of MEMS devices with SU-8 photoresist as the structural material [3, 37-59]. The primary goal is a proof-of-concept. As long as the selection of materials and processes can produce the expected MEMS structures, the corresponding microfabrication flows can be considered as acceptable. This application-specific methodology has extensively demonstrated the potential of SU-8 photoresist from the perspective of possible applications, but microfabrication technologies developed for this methodology have several issues to address.

1.3.3 Issues in the current fabrication methods of SU-8 capacitive MEMS devices

First of all, the usage of sacrificial layers has resulted in extra process complexity and uncertainty. Sacrificial layers are also processed by the deposition-masking-patterning cycles and their variants. In many cases, such processing uses equipment and etchants similar to the one for silicon micromachinings, diminishing the advantages regarding the faster, safer, and cheaper microfabrication with polymeric materials.

Secondly, the information regarding the process controllability in the existing SU-8 micromachining process with a diversified selection of sacrificial layers is minimal [3, 37-59]. In most cases, neither the SU-8 lithography nor the processing of the sacrificial layer has been calibrated. As for predictability, only a few of them have compared the manufactured proof-of-concept devices' electromechanical behavior with simulations. Meanwhile, most of the reported researches have not repetitively manufactured their SU-8 MEMS devices to evaluate the process reproducibility. As discussed in Section 1.1.1, a controllable fabrication technology is the root of supporting any MEMS designs and their application. The application potentials of SU-8 MEMS devices will be compromised if their manufacturing process's controllability remains unknown.

The fabrication of SU-8 in-plane MEMS devices additionally suffers from a process constraint related to surface micromachining. Such a microfabrication flow does not remove the substrate underneath the movable components of the microdevices. In contrast, the fabrication flow for silicon in-plane MEMS devices, SOIMUMPs, removes the substrate underneath, reducing the risk of failure [9]. Though a classic silicon bulk micromachining process can be used to address this issue, it offsets all the advantages of making in-plane MEMS devices with polymers. These processing limits could provide a reasonable explanation for the much rarer effort invested into the fabrication of SU-8 in-plane MEMS devices. As far as to the author's knowledge, there are only two existing works reporting the fabrication of SU-8 in-plane MEMS devices [58, 59]. Both of them are using surface micromachining processes. Their fabrication flows suffered from issues related to the process complexity and uncertainty.

Polymer-based MEMS microfabrication technologies, including the ones based on SU-8 photoresist, rely on the advantages related to higher simplicity and shorter turnaround time to counterbalance the issues related to inferior material properties when compared with silicon-based microfabrication technologies. If polymeric microfabrication flows are not optimized in these aspects, the value of using them for MEMS microfabrication will be totally lost.

There are multiple research progress and directions that may improve the fabrication of SU-8 MEMS devices and address these issues.

1.4 Research with promising potential in SU-8 MEMS fabrication

1.4.1 Advanced lithography methods for SU-8 photoresist

The advanced lithography methods of SU-8 photoresist can directly make suspended, 3D polymer microstructures through a single lithography process. These suspended polymeric microstructures can serve as movable components to implement electromechanical coupling. In

this context, advanced SU-8 lithography methods are promising in eliminating the usage of sacrificial layers and related issues. Table 1.5 summarizes the advanced lithography methods that have been studied by far.

Methods	Fabrication speed	Process complexity	Error risk	Other aspects
Two-point laser direct writing [67-69]	Lowest point-by-point writing	Low One step 3D fabrication	Low	Very high 3D resolution
Stereolithography[70]	Low Layer-by-layer writing	Low One step 3D fabrication	Medium	Liquid-bath based process
Hard mask alternation [71]	High Area exposure but inevitable hard mask alternation	Medium Hard mask alternation in between	medium (hard mask misalignment)	Require pre-fabrication of mask sets
DMD grayscale maskless lithography[72, 73]	medium Simultaneous exposure with a varied dose within a single area	Low One step 3D fabrication	Low	Semi-parallel process

Table 1.5 Advanced lithography methods for SU-8 photoresist

The four methods in Table 1.5 represent two primary principles used in the one-step formation of SU-8 3D microstructures: focal plane adjustment and pixel-level dose modulation.

Two-point laser direct writing [67-69] and stereolithography [70] vary the focal height to concentrate the UV energy at the points-of-interest for one-step 3D fabrications. In two-point laser direct writing, only the point where the focal point of two beams converges has sufficient energy for photolysis. 3D fabrication is done point-by-point [67-69]. In micro-stereolithography, the entire 3D structure is sliced into multiple layers. Within a single lithography process, exposure is

done layer by layer. Between each exposure, either the focal plane (radiance source) or the substrate is moved in a vertical direction to implement the focal height adjustment[70].

Two-point laser direct writing and stereolithography are both serial processes. They tend to have high equipment-level precision and resolution(nanometer level). However, the advantages come at the cost of fabrication speed and scalability. From the perspective of applications, SU-8 two-point laser direct writing is mainly used to fabricate encapsulated micro-channels and polymeric photonic devices [69]. Fixed SU-8 micro gears and scaffolds have been fabricated by stereolithography [70].

Both hard mask alternation and maskless grayscale lithography rely on the localized exposure dose modulation at the pixel level to directly create 3D SU-8 structures. As suggested by the name, hard mask alternations use multiple lithography masks. Some patterns are only exposed in a few of the masks, while others are exposed all the time. Consequently, different regions of the same coated SU-8 layer result in different thicknesses [71]. Maskless grayscale lithography varies the exposure dose by modulating a digital mirror device (DMD) arrays [72, 73]. Every single micromirror unit corresponds to a pixel on the software mask design. It periodically switches between ‘reflecting’ and ‘deflecting’ mode based on the gray shade color on the mask design, tuning the exposure dose.

Hard mask alternation is a purely parallel process, but UV exposure is divided into segments or partial time steps. The hard masks are changed between the partial exposure steps in order to obtain the localized exposure dose modulation. Maskless grayscale lithography needs only a single software mask design to complete the whole lithography. However, it is a semi-parallel process limited by the effective exposure area of the DMD array. Based on the used area of the DMD array, the mask design is divided into an array of ‘patches’ and projected onto the substrate.

As for the resolution, neither hard mask alternation nor maskless grayscale lithography can compete with two-photon direct writings [71-73], but it is still possible for them to maintain a resolution at the sub-micron level.

Meanwhile, both processes are significantly faster than two-photo direct writing and micro-stereolithography, making them suitable for SU-8 MEMS fabrication. Currently, maskless grayscale lithography has been used to fabricate encapsulated channels and cantilevers [73], and hard mask alternation has proven effective by fabricating double clamped beams [71].

1.4.2 Other alternative micromachining methods

In some cases of SU-8 MEMS fabrication, the processing of sacrificial layers or substrates is inevitable. Direct micromachining technologies may provide safer and faster processing than traditional wet or dry etching. Among all direct processing methods, laser micromachining is more recent and promising [74]. It is a non-contact, thermal process over almost the whole range of materials [74], at room temperature [75], and ultrafast speed [76]. However, laser ablation is a serial process. Specific strategies need to be developed to improve the time efficiency if laser ablation is used to develop the SU-8 MEMS fabrication technology with low complexity and cost.

1.4.3 Enhancement of SU-8 electrical conductivity

At the material level, conductive SU-8 provides the possibility of eliminating the metallization process. Electrically conductive SU-8 can be achieved by mixing nanoscale additives into the SU-8 photoresist. The electrical conductivity is enabled by a mechanism called carrier percolation [77, 78]. Common conductive nanofillers for SU-8 are summarized in Table 1.6.

Nanofiller name	Category
Carbon black nanoparticles [66]	Carbon
Graphene/Reduced graphene oxide (RGO) [79, 80]	
Multi-walled carbon nanotube (MWNT) [81, 82]	
Nickel nanoparticles [83]	Metal
Silver nanoparticles [84, 85]	
Polyaniline [86]	Organic polymer

Table 1.6 Nanofillers for conductive SU-8

The majority of the fillers in Table 1.6 cannot join the crosslinking-based polymerization process of SU-8 monomers [66, 81-87]. Existing works have focused on achieving fixed electrical components (resistors, inductors, and capacitors), not movable MEMS structures [81, 84, 85]. Research work is necessary to evaluate the controllability of fabrication flows using conductive SU-8.

1.5 Thesis Scope

1.5.1 Goals

This thesis aims to provide a new solution to the existing issues in the fabrication methods of SU-8 out-of-plane and in-plane MEMS devices. A framework consisting of two fabrication technologies will be developed. Novel methodologies will be used to improve the fabrication process of SU-8 out-of-plane and in-plane MEMS devices.

The idea of avoiding any use of sacrificial layers will be tested for the fabrication of SU-8 out-of-plane MEMS devices. The dose-modulation lithography method will be used for this purpose.

The idea of removing supportive layers underneath the movable component will be used for the fabrication of SU-8 in-plane MEMS devices. A new micromachining strategy will be developed for this purpose. This strategy will remove the substrate underneath the movable

components to release the microdevices in a way with extra simplicity and lower cost than silicon bulk micromachining.

The general methodology to be used in this thesis is depicted in Figure 1.8.

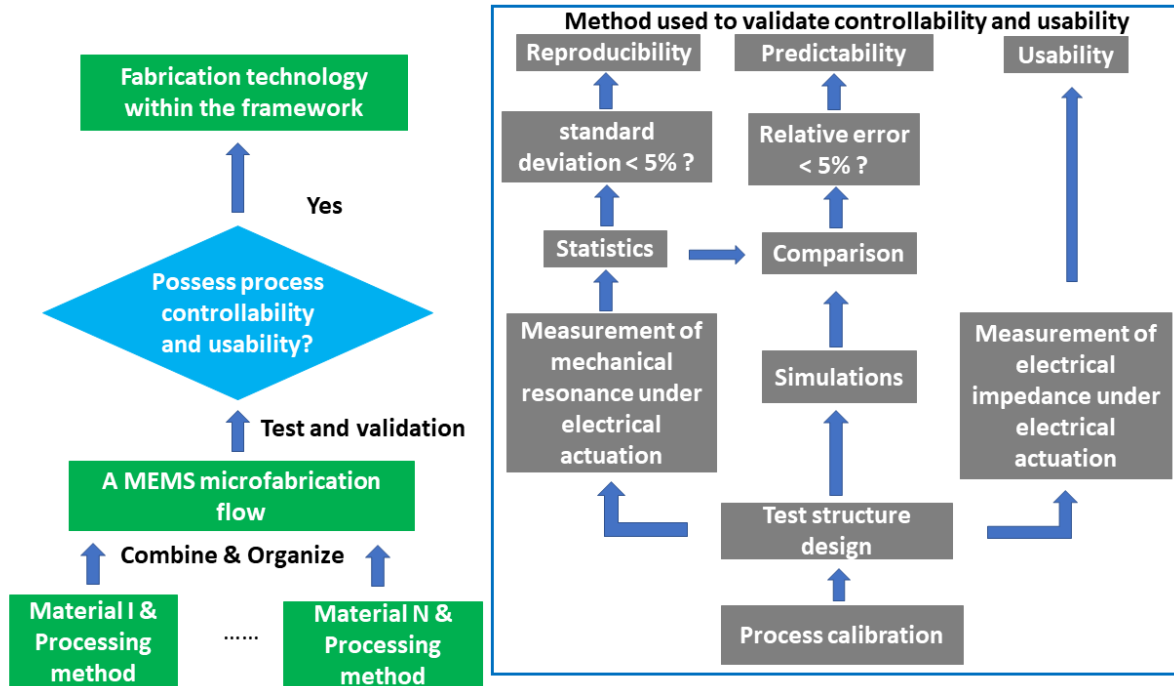


Figure 1.8 The general methodology to be used in this thesis

As shown in Figure 1.8, this Ph.D. thesis uses a bottom-to-top methodology for research activities. Though this methodology is different from the application-specific methodology used in other existing research works, it allows new processing methods and strategies to be incorporated into SU-8 MEMS fabrication flows and tested robustly.

The experimental characterization methods for the fabrication technologies to be developed in this thesis are also shown in Figure 1.8. Key factors for process controllability will be evaluated by the statistics of the mechanical resonance measurement result under electrical actuation. The maximum standard deviation and relative error are set to 5% for acceptable reproducibility and predictability. Though the research activities in this thesis do not aim at the

optimization for a specific application, electrical impedance measurement will be used to evaluate whether the newly-developed fabrication technologies are capable of creating bi-directional coupling interfaces between electrical and mechanical energy domains. Such interfaces are the basis of MEMS devices for specific applications.

The evaluation result validates the suitability of the new methodologies and the corresponding fabrication flows in manufacturing SU-8 MEMS devices, demonstrating their application potentials and building up the incipient step towards a customizable, rapid, and low-cost manufacturing platform for SU-8 MEMS devices.

1.5.2 Thesis organization

Figure 1.9 depicts the organization for the rest of the thesis.

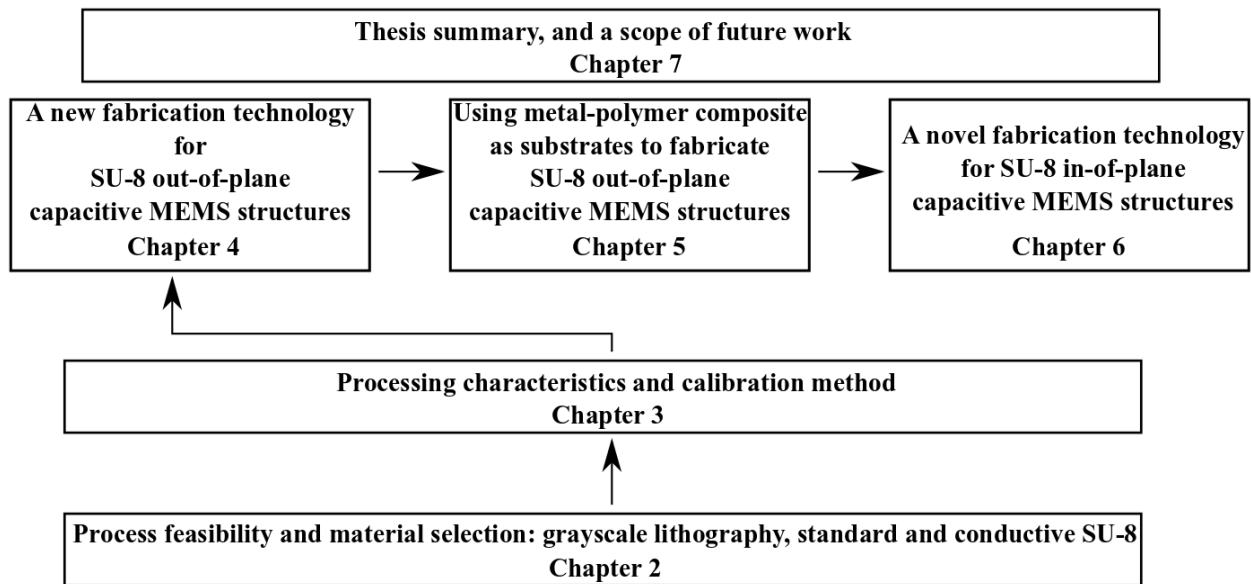


Figure 1.9 Depiction of the objective and organization of the Ph.D. thesis.

Chapter 2 is dedicated to the suitability of using maskless grayscale lithography to improve SU-8 MEMS fabrication. Maskless grayscale lithography is selected to implement the dose-modulation lithography in this thesis. Though it is a semi-parallel process slower than hard mask alternation, it is more flexible for incipient, explorative research like this thesis. An experimental

case study will be carried out. Grayscale lithography is conducted on two material platforms: standard and conductive SU-8.

Chapter 3 focuses on developing a calibration process for grayscale lithography to evaluate the controllability of any new fabrication flows using this advanced lithography technique.

Chapter 4 uses the grayscale lithography to develop a sacrificial-layer-free fabrication method for SU-8 out-of-plane MEMS structures. In Chapter 5, this technology is used on metal-polymer composites as low-cost substrate alternatives to silicon wafers. Traditional microfabrication methods for SU-8 out-of-plane MEMS devices have been used on similar composites [47]. Testing the newly-developed, sacrificial-layer-free fabrication method on metal-polymer composite will demonstrate a similar robustness and application potential.

Chapter 6 develops and validates a novel fabrication technology for SU-8 in-plane capacitive MEMS structures. This novel fabrication method will be based on a new micromachining strategy to implement a better releasing process for SU-8 in-plane MEMS devices.

Chapter 7 summarizes the whole thesis. The accomplishment of the thesis is reviewed, and the scope of future work is provided.

Chapter 2: Grayscale lithography of SU-8 for polymer MEMS fabrication

The research of Chapter 2 evaluates the suitability of maskless grayscale lithography for polymer MEMS fabrication. Figure 2.1 depicts the detailed research carried out in this chapter.

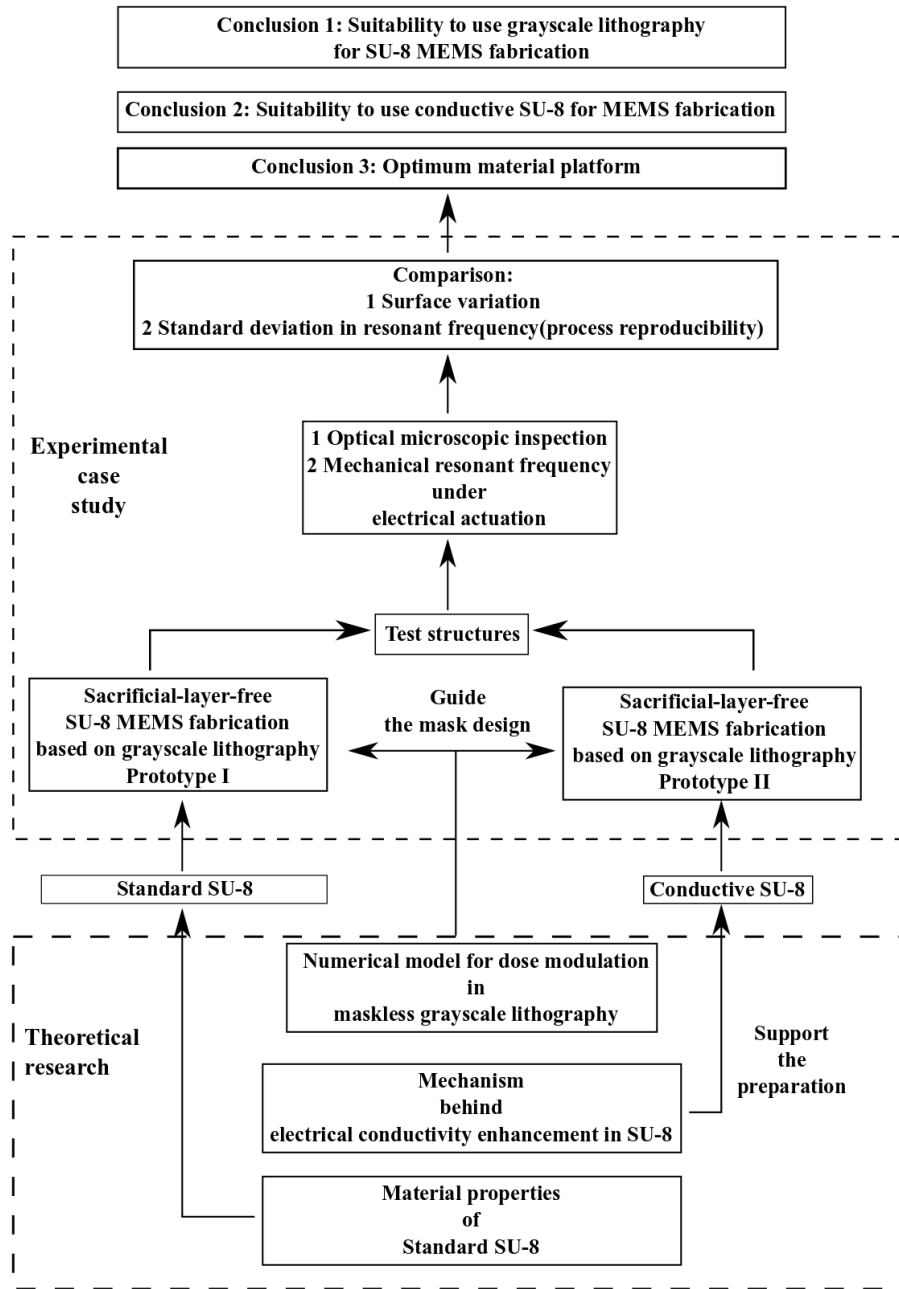


Figure 2.1 Illustration of the research conducted in Chapter 2.

As shown in Figure 2.1, the advanced lithography method will be tested on two material platforms, standard and conductive SU-8. The research in Chapter 2 starts with the reviewing and discussion about the two material platforms. Section 2.1 provides a review of standard SU-8 lithography. The main substeps of the lithography flow are identified first. Then, their impact on the final structures is reviewed in detail. Section 2.2 briefly reviews the essential details behind the functionalization of polymeric materials. The dose modulation mechanism for grayscale lithography is studied in Section 2.3, with a numerical relationship established and validated for the dose modulation coefficient. Section 2.4 introduces the detail of the experimental case studies. The characterization results are presented and discussed in Section 2.5. They provide critical information regarding the suitability of grayscale lithography and conductive SU-8 for polymeric MEMS manufacturing. The accomplishments of Chapter 2 are summarized in Section 2.6.

2.1 Substeps of SU-8 lithography process and their influence

2.1.1 Overview of SU-8 and its lithography flow

SU-8 photoresist is a crosslinking-based, negative photoresist. Its monomer is a type of diglycidyl ethers of bisphenol-A epoxy (DGEBA). Its polymerization mechanism is cationic catalyzed cross-linking[27]. The catalysts of the crosslinking are the photoacids generated by the photolysis of triarylsulfonium hexafluoroantimonate salts (photoinitiators) [27, 88, 89].

Currently, the SU-8 photoresist series are mainly manufactured by Kayaku Advanced Material (previously known as MicroChem). They use the Epon™ SU-8 resin as the monomer. The photoinitiators are purchased from Union Carbide (Product serial number: UVI 6974). Older types of SU-8 photoresist, such as SU-8 series, SU-8 25 series, and SU-8 50 series, use gamma-butyrolactone as the solvent, while the newer types, such as SU-8 2000 series, use cyclopentanone.

Propylene glycol methyl ether acetate (PGMEA) is used as the developer to dissolve uncrosslinked SU-8. Figure 2.2 illustrates the general flow of a SU-8 lithography process.

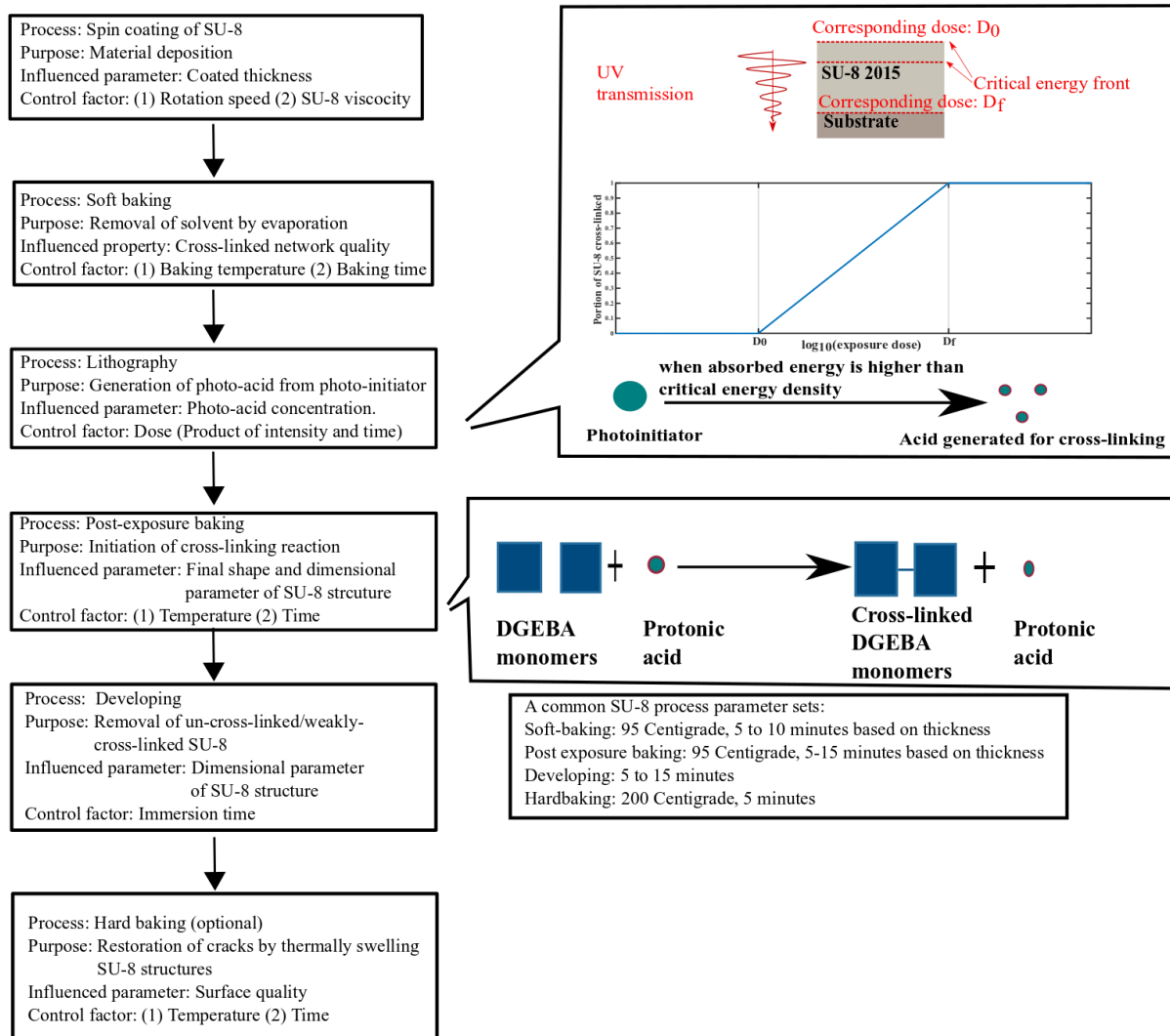


Figure 2.2 Schematic of SU-8 lithography flows and the involved chemical reactions.

As illustrated in Figure 2.2, the SU-8 lithography process always starts from depositing SU-8 photoresist on a substrate. Spin-coating is the most common way to do this task. The thickness of the layer is determined by the rotation speed of the spin-coater and the viscosity of SU-8. Achievable thickness ranges from submicron to hundreds of microns. Soft baking is the step after spin-coating. This baking step evaporates the solvent, turning the coated layer into a solid

material. UV exposure is the step after soft baking. Photolysis of the photoinitiators is triggered during the exposure to generate photoacids. Another baking process is conducted after UV exposure. This baking process is also known as post-exposure baking. Crosslinking of SU-8 monomers is accelerated during this process. SU-8 layer is immersed in PGMEA after the post-exposure baking. Uncrosslinked SU-8 is dissolved, leaving the final structures on the substrate. Occasionally, cracks on SU-8 structures appear after developing. They can be eliminated by hard baking for one or two minutes at a temperature between 150°C to 200°C.

Zhang *et al.* have identified soft baking, exposure, post-exposure baking, and developing as the main substeps for a SU-8 lithography process. They used Taguchi methods to design experimental case studies for the influences of the four main substeps on SU-8 structures. Their research has analyzed the influence from two perspectives [90]: the geometric dimensions and mechanical strength. The structural geometry has been analyzed and optimized by comparing the differences between its design parameters and the measured values. The mechanical properties are represented by the density of cracks and the severity of deformations. Their conclusion is re-summarized in Table 2.1.

	Soft baking	Exposure	Post-exposure baking	Developing
Geometric dimensions	61.10%	9.07%	7.20%	22.63%
Mechanical strength	48.27%	23.07%	11.91%	17.75%

Table 2.1 Dependence of the SU-8 lithography process quality on main substeps

As shown in Table 2.1, soft baking plays the most influential role in both structural dimensions and mechanical strength. Structural geometry is less sensitive to exposure and post-exposure baking but slightly more sensitive to the developing process.

The influence of these four main substeps identified by Zhang *et al.* is reviewed in more detail in this section.

2.1.2 Influence of soft baking

Anhoj *et al.* systematically studied the influence of soft baking [91]. Though both soft baking temperature and duration affect the amount of solvent residuals, temperature variation makes more significant changes [92]. Due to this reason, Anhoj *et al.* kept the baking duration at 5 minutes. They varied the soft baking temperature for different 40- μm SU-8 layers to evaluate the influence of solvent residuals. Their characterization result is summarized in Table 2.2.

Soft baking temperature (°C)		65	75	85	95	105	115
Minimum post exposure temperature (°C)		22.5	22.5	32.5	37.5	37.5	37.5
Mechanical strength	Crack density (%)	0	6	17.5	20	22.5	12.5
	Vickers hardness (kgf/mm²)	23.5	23	22.5	22.5	20.5	22
Structure geometry	Planar variation	+1%	+0.7%	N/A	-0.6%	N/A	-1.8%
	Vertical variation	0	-7.5%	-10%	-10%	-8.75%	-7.5%

Table 2.2 Soft baking temperature and the influence on SU-8 lithography quality

In Table 2.2, the influence of soft baking temperature on mechanical strength has been evaluated from two perspectives: the crack density and the Vicker's hardness. The mechanical strength decreases when the soft baking temperature increases from 65 °C to 105 °C, but it slightly improves at a soft baking temperature of 115 °C. The influence of soft baking on structure geometry was evaluated by the variation of vertical and planar dimensions. The final thickness had decreased when the baking temperature was increased from 65°C to 95°C, while further increasing the temperature slightly alleviated the thickness reduction. Lower soft baking temperatures tend to expand the planar dimensions of SU-8 structures, while high temperatures reduce the planar dimensions. It is also spotted that decreased soft baking temperature has resulted in a lower initiation temperature to trigger crosslinking during the post-exposure baking.

Anhoj *et al.* associated their findings with the influence of solvent residuals on the photochemistry during the exposure step. They claimed that solvent residuals had promoted another chemical reaction to generate an acidic catalyst [91]. This claim is supported by the study of photochemical reactions during UV exposure, which will be discussed next. Lower soft baking temperature leaves more solvents in the coated layer, generating more photoacids. When more catalysts are generated in the SU-8 layer, the crosslinking of monomers become more thorough, increasing the equivalent hardness, reducing the cracks, and boosting up the resistance against the dissolving effect of the SU-8 developer. The concentration of photoacids diffused into unexposed regions also increases. These photoacids in unexposed regions promote unwanted crosslinking, making the final structure larger.

2.1.3 Influence of UV exposure dose

It is necessary to review the photochemistry of the photoinitiators of SU-8 before the impact of UV exposure dose on the final SU-8 structures can be understood. The photochemistry of the triaryl sulfonium salts has been extensively studied by researchers. Dektar *et al.* systematically summarized the photochemical characteristics of the triaryl sulfonium salts [93]. The basic information regarding the photoacid generation is presented in Table 2.3.

Photolysis phase		
Reaction	Type	Product
Heterolysis	Singlet	Phenyl cation and diphenyl sulfide
Homolysis	Triplet	Phenyl radical and diphenylsulfinyl radical cation (pair)
Photoacid generation phase		
Reaction type	Reactant	Product
Cage reaction	Phenyl cation, diphenyl sulfide	Benzene, diphenyl sulfide, photoacids
Cage reaction	Phenyl radical, diphenylsulfinyl radical cation	
Escape reaction	Phenyl cation, solvent residuals	
Escape reaction	diphenylsulfinyl radical cation, solvent residuals	

Table 2.3 Summary of the photochemistry of the photoinitiators in SU-8 during UV exposure

As shown in Table 2.3, the photochemistry of the photoinitiators can be divided into two phases. Radicals or cations are the product of the first phase, while photoacids are generated during the second one.

Radical/cation generation can be done through two different reaction paths: heterolysis (the main reaction) and homolysis [93]. Heterolysis is dominant because it is a singlet reaction, while homolysis is a triplet reaction [93]. The photoacid generation also has two reaction paths. Cage reactions in Table 2.3 are the primary ways to generate photoacids. The equivalent concentration

of the photo acids is limited by the decomposition and recombination of the reactants. Solvent residuals promote the escape reaction of cations and radicals, generating additional photoacids.

UV exposure affects the structural dimensions and mechanical strength of the final structures through the distribution of exposure dose and the generation of photoacids. The UV exposure dose distribution within a SU-8 layer can be expressed by[94]:

$$\begin{cases} I(z) = I_0(1 - R_1) \exp(-\alpha z) \left(\frac{1 + R_2 \exp(2\alpha(z - H))}{1 + R_2 \exp(-2\alpha H)} \right) \\ D(z) = I(z) \times t \end{cases} \quad (2.1)$$

In Eq(2.1), I is the UV intensity at depth z ($0 \leq z \leq H$). R_1 is the intensity reflective index at the air-SU-8 interface. α is the attenuation coefficient of SU-8. R_2 is the intensity reflective index at the SU-8-substrate interface. H is the layer thickness. The first-order derivative of $I(z)$ is always non-positive, so $I(z)$ has a monolithically decreasing relationship with depth z . If the substrate does not significantly reflect UV radiation ($R_2 \approx 0$), $I(z)$ regresses to the classic Beer-Lambert transmission format.

Eq(2.1) indicates that the top surface of a SU-8 layer will always be the first to fulfill photolysis's energy threshold. This threshold is noted as D_0 in Figure 2.2. Doses smaller than D_0 do not generate any photo acids, resulting in zero cross-linked thickness. The boundary between photolyzed and unphotolyzed layers is pushed towards the substrate when the exposure duration elongates. When this boundary reaches the substrate, the corresponding dose is noted as D_f in Figure 2.2. Doses between D_0 and D_f results in an intermediate thickness between zero and the layer thickness. Such doses have been implemented in hard-mask alternation lithography and maskless grayscale lithography to directly create suspended SU-8 structures through a single exposure [71-73]. Doses higher than D_f promote homolysis, oversaturating a SU-8 layer with

photoacids. The excessive amount of photoacids increases the crosslinking density, resulting in higher mechanical strength and larger structural planar dimensions.

This conclusion is supported by the research work of Zhong *et al.*[95]. They conducted binary lithography processes with exposure dose as the only variable. Then, planar dimensions of SU-8 structures resulted from different exposure doses were compared with the initial mask design. When the exposure dose is lower than a threshold (D_f), the final structures' planar dimensions have always been smaller than the layout design. When the exposure dose is significantly higher than this threshold, the corresponding planar dimensions have been larger than expected, diminishing the gaps in between. Only exposure doses around this threshold can result in structural dimensions in good accordance with the mask design. Zhong *et al.* have attributed the reduction of geometric dimensions to the insufficient generation of photoacids related to underexposure. This insufficiency has resulted in low crosslinking density and weak structures with reduced resistance against the developer's dissolution effect. The crosslinked monomers have been partially dissolved, reducing the geometric dimensions. When the exposure is excessive, homolysis is promoted, generating extra photoacids. The exposed region is oversaturated with photoacids, enhancing the mechanical strength of the structures. The photoacid concentration in the unexposed region is also increased due to solid diffusion. As a result, the final structures become larger than the design.

Eq(2.1) demonstrates that the upper layer always has a higher exposure dose than the lower layer, so the spatial probability for homolysis to happen is not uniform in a SU-8 layer. More homolysis happens in the upper layer than the lower one. As a result, canopy-like structures can be expected, particularly for standalone SU-8 structures. Evidence for this conclusion can be found

in the research of Zhang *et al.* [96] and Kim *et al.* [97]. They have spotted mushroom-like cross-sectional shapes in their SU-8 micropillars made by the binary SU-8 lithography.

2.1.4 Influence of post-exposure baking

Post-exposure baking determines both the reaction rate and maximum conversion (cross-linking) ratio of the crosslinking reaction. The crosslinking of the DGEBA monomers is autocatalyzed. However, if no external heat is applied, the corresponding maximum conversion ratio would be relatively low. Abadie *et al.*[27] are among the very first ones finding this characteristic. They found that the post-exposure baking temperature and duration determine the maximum achievable conversion ratio (theoretical cap), as shown in Table 2.4.

Post-exposure baking temperature (°C)	25	35	45	55
Maximum conversion ratio %	20	20	30	50
Ramping time to saturation (minutes)	1	1.5	2	4

Table 2.4 The relationship between crosslinking ratio and the condition of post-exposure baking

In Table 2.4, the maximum conversion ratio describes the level of thoroughness of crosslinking under fixed photoacid concentration. Higher PEB temperature has led to an increment in the maximum conversion ratio. Keller *et al.* [98] experimentally validated that a conversion ratio close to 100% can be achieved if the post-exposure baking temperature is set to 95°C. This experimental result explains why Kayaku Advanced Material recommend a post-exposure baking temperature of 95°C. It can also be found in Table 2.4 that the baking duration determines the actually-achieved conversion ratio. Proper baking duration at the optimum temperature is essential to the mechanical quality of final structures. The research work of Feng *et al.*[99] provides extra evidence to support this claim. Since the conversion ratio determines the final structures' mechanical properties, the relationship between baking duration and the cross-linking ratio can be

checked by the mechanical properties of structures baked with different durations. Feng *et al.* have used Young's modulus and tensile strength as benchmarks of mechanical strength. They characterized the mechanical strength of SU-8 baked for different durations at 95°C. The result is re-summarized in Table 2.5.

PEB time (min)	0	3	5	15	30
Young's modulus (GPa)	0.7	0.7	1.7	2.2	2.4
Tensile strength (MPa)	16.1	16.1	37.2	48.3	52.6

Table 2.5 The elastic property and structural strength of SU-8 under different PEB condition

In Table 2.5, the exposed SU-8 has a relatively low mechanical strength if it is not baked. When the PEB duration is elongated, the mechanical strength increases.

Keller *et al.* have discovered that their test structures have the dimensions increased when the baking temperature increases from 70 °C to 95 °C [98]. This increment in the geometric dimension can be attributed to the fact that baking is a global effect. It simultaneously enhances the crosslinking in both the exposed and unexposed regions.

2.1.5 Influence of developing

The developing step uses three liquid agents: PGMEA, isopropanol (IPA), and DI water. PGMEA is used as the solvent for uncrosslinked SU-8, while the other two are used as rinsing agents. The three liquid agents mainly affect the SU-8 structures through swelling.

Wouter *et al.* have experimentally studied the three liquid agents' swelling effect on crosslinked SU-8 structures. They measured the tensile stress in fabricated SU-8 structures under static and dynamic conditions [92]. A static condition means that SU-8 structures are immersed solely in one of the three liquid agents, while a dynamic condition indicates that SU-8 structures

experience alternations of liquid agents. The tensile stress values measured for static conditions are re-summarized in Table 2.6.

Agent	Net internal tensile stress (MPa)
PGMEA	12(70°C)~13(50°C)
IPA	15.5(70°C)~16(50°C)
DI water	1(50°C) ~5(70°C)
Cleanroom air (humidity: 45%)	10(70°C)~12(50°C)

Table 2.6 Net tensile stress generated by liquid agents to develop SU-8 photoresist

In Table 2.6, the temperature values in the brackets are the soft baking temperature of the tested samples. The study and discussion about soft baking indicate that samples soft baked at 50°C have higher crosslinking density and mechanical strength than those baked at 70°C. Samples with lower crosslinking density and mechanical strength have swelled less in PGMEA and IPA, but they swelled more in DI water.

Wouter *et al.* [92] associated their experimental results with the absorption of water molecules, the formation of hydrogen bonds, and PGMEA and IPA's dehydration effect. Crosslinked SU-8 can absorb water molecules and form hydrogen bonds using their hydroxyl groups. The hydrogen bond density has a positive dependence on the density of crosslinking [91, 100]. After the hydrogen bonds are generated, the water molecules can be considered as being trapped within the matrix of crosslinked SU-8. When crosslinked SU-8 structures are exposed to an ambient that allows the trapped water molecules to escape, such as a miscible liquid or air, the ambient will ‘drag’ the water molecules out by breaking the hydrogen bonds, imposing tensile stress on the crosslinked SU-8 structures, and resulting in swelling.

Samples soft baked at 50°C have a higher crosslinking density. Though the dense network reduces the absorption of water molecules when immersed in DI water (1 MPa swelling tensile stress for 50°C compared with 5 MPa for 70°C), more hydrogen bonds have been generated for absorbed molecules. This higher hydrogen bond density has resulted in larger tensile stress when dehydration happens through any viable path.

One result regarding the stress variation under dynamic conditions is worth mentioning. When they were taken out from PGMEA and immersed into IPA, samples had experienced shrinking. Initially, the internal tensile stress has reduced to zero, but it soon recovered to the values in Table 2.6 [92].

The work of Wouter *et al.* [92] has provided a reasonable way to illustrate how the developing process influences the SU-8 structures through swelling. The swelling can result in cracks. These cracks reduce the final structures' mechanical strength. However, the cracks can be fixed by a hard baking process after the developing step. If the crosslinking density is low, crosslinked monomers may also detach from the structures during the immersion in PGMEA or the quick rinsing with IPA and DI water, reducing the geometric dimensions. This dimension-reducing effect can be observed in many examples discussed by far [90, 91, 98].

2.1.6 Summary of the review

The conclusions achieved from the literature review by far are illustrated in Figure 2.3.

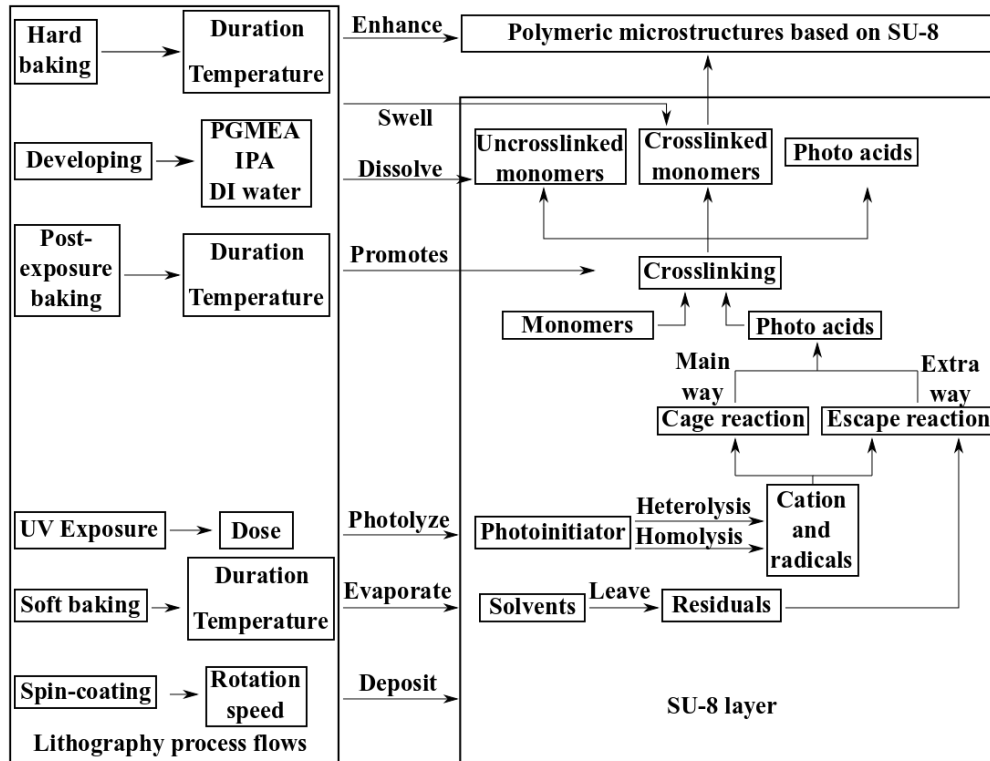


Figure 2.3 Detailed view of SU-8 lithography process and the role of each substep

Figure 2.3 shows that soft baking and UV exposure directly affect the photoacid generation that determines the monomer crosslinking density. Hence, they are the most critical steps for mechanical strength and the geometric dimension of SU-8 structures. The crosslinking density, the corresponding mechanical strength, and the geometric variation are also controlled by post-exposure baking. The PEB temperature sets up the upper cap for the crosslinking ratio and density, and the baking duration determines the actual values of these two parameters. Swelling is the primary interaction with the SU-8 structure during the developing step. It can reduce mechanical strength and geometric dimensions.

The result of tuning soft baking, exposure, post-exposure baking, or developing are summarized in Table 2.7. A green upward arrow means increasing the tunable parameters would

improve the lithography quality, while a red downward arrow means the opposite. A yellow rightward arrow means the parameters do not influence the process quality.

Process	Tunable parameters	SU-8 lithography quality	
		Mechanical strength	Geometric dimensions
Soft baking	Temperature, duration	↓	↓
Exposure	Dose	↑	↑
Post-exposure baking	Temperature, duration	↑	↑
Developing	Immersion duration	→	↓

Table 2.7 Influence of processing steps on the final quality of SU-8 lithography

2.2 Functionalization of SU-8 photoresist to enhance electrical conductivity

2.2.1 Theories behind the electrical conductivity through functionalization

When polymers are functionalized by fillers for electrical conductivity, a minimum quantity threshold of the conductive fillers must be reached before the electrical conductivity experiences a significant increment. This minimum quantity to achieve this jump in electrical conductivity varies with conductive fillers' types and dimensions, as shown in Table 2.8.

Research work	Filler type	Filler size	Conductive threshold
Gunde, M.K <i>et al.</i> [87]	Carbon black	30nm	2~3 wt%
Mionic <i>et al.</i> [81]	Multiwalled carbon nanotube	Diameter:11 nm	0.8~1.6 wt%
		Length: 10 um	
Grimaldi Claudio <i>et al.</i> [82]	Multiwalled carbon nanotube	Diameter:13.3 nm	0.5~1 vt%
		Length: 10 um	
Vinchurkar M <i>et al.</i> [66]	Carbon black	N/A	9 wt%
Jiguet S <i>et al.</i> [84, 85]	Silver nanoparticle	200 nm	6 vt%
Patel C V <i>et al.</i> [86]	Polyaniline	N/A	8.5 wt%

Table 2.8 Material parameters related to the functionalization of SU-8 for electrical conductivity

In Table 2.8, the conductive threshold refers to the minimum volumic percentage (vt%) or the mass percentage (wt%) of the filler relative to SU-8 photoresist. Their correspondence is set by the following equation [82]:

$$vt\% = \frac{\rho_{SU-8}wt\%}{(\rho_{filler} + \rho_{SU-8}wt\%)} \quad (2.2)$$

In Eq(2.2), ρ is the density of a material. When the amount of the conductive fillers added into the SU-8 photoresist reaches the threshold, a jump in the mixture's electrical conductivity shows up. This transformation in electrical conduction behavior can be explained by percolation theories [101].

Percolation theories correlate a system's properties with the connectivity of individual objects within the system [101]. When the number of objects within a system exceeds a threshold level, they become so densely distributed that the contact between neighboring objects becomes

inevitable[102-106]. Consequently, a percolation path is formed, inducing changes in the physical properties. In order to make the polymer electrically conductive, conductive filler density must reach a critical threshold that allows the individual particles to form continuous conductive paths within the SU-8 photoresist. When the amount of conductive filler varies from zero to the conductive threshold, the polymers' electrical conductivity experiences a 3-stage variation.

Stage 1: Tunneling dominance stage. When $vt\%$ is smaller than $vt\%_{critical}$, the distribution of the conductive fillers is sparse. The polymer matrix hinders the formation of the percolation path by inhibiting the contact between fillers. Tunneling becomes the dominant mechanism for electrical conductivity [81]. In such a case:

$$\sigma \approx \sigma_2 (vt\%_{critical} - vt\%)^{-\beta} \quad (2.3)$$

Here, σ_2 is the polymer's electrical conductivity, and β is the critical exponent associated with the polymer's geometric properties, ranging from 0.7 to 1.3.

Stage 2: Intermediate stage. When the difference between $vt\%$ and $vt\%_{critical}$ is close to zero, the polymer's conductivity enters the transition region. In such a case:

$$\sigma \propto \sigma_2^\gamma \sigma_1^{1-\gamma} \quad (2.4)$$

In Eq(2.4), γ can be expressed as:

$$\gamma = \frac{\alpha}{\alpha + \beta} \quad (2.5)$$

Here σ_1 is the electrical conductivity of the fillers, and α is the critical exponent. Determined by the fillers' geometric properties, the value of α ranges from 1.1 to 2.0 [107].

Stage 3: Percolation dominance stage. When $vt\%$ exceeds the conductive threshold $vt\%_{critical}$, within the polymer material, the distribution of conductive fillers becomes sufficient to

form a continuous percolation path for the electrons, resulting in order of magnitude increment in electrical conductivity, with the conductivity expressed as:

$$\sigma \approx \sigma_1 (vt\% - vt\%_{critical})^a \quad (2.6)$$

2.2.2 Experimental modulation of the electrical conductivity in polymers

It is common to experimentally determine the critical threshold $vt\%_{critical}$ [66, 81-87] because the techniques used to mix the fillers with the polymers are also influential for electrical conductivity enhancement [101, 108, 109].

The majority of the current conductive additives are insoluble in polymers' solvents, and they cannot crosslink with SU-8 monomers. These characteristics make the aggregation of fillers inevitable. Appropriate mixing methods and dispersing agents can limit the aggregation and promote more uniform dispersion of the conductive fillers. As a result, the conductive additives participate more efficiently in forming the percolation path rather than aggregating into clusters, reducing the average electrical conductive threshold [101, 108, 109].

In order to get a good dispersion, reduce aggregation, and minimize the average conductive threshold, it is common to use the following 4-step method to make SU-8 electrically conductive[66, 81-87, 110].

Step 1: An initial mechanical stir is used to mix the SU-8 with the nanofillers.

Step 2: An ultrasonic bath is carried out to remove the air bubbles induced during the mechanical stir.

Step 3: The mixture is put under constant magnetic stir until being used to avoid sedimentation.

Step 4: Before deposition, a second ultrasonic bath is conducted to remove any air bubbles generated during the magnetic stir.

2.3 Exposure dose modulation in maskless grayscale lithography

The dose modulation in maskless grayscale lithography is implemented through a digital mirror device (DMD) array. Each digital micromirror cell has its switching frequency and duty cycle linearly adjusted by the corresponding pixel's gray shade level [72, 111]. Hence, the most straightforward numerical model for the grayscale modulated exposure dose is:

$$\begin{cases} D = I \times T \times p \\ p = \left(\frac{gs}{255} \right)^2 \end{cases} \quad (2.7)$$

In Eq(2.7), I is the intensity of the UV light source, T is the exposure duration, and p is the modulation coefficient associated with the corresponding grayscale value. The dose modulation coefficient computed by Eq(2.7) has been compared with the measurement made by Rammohan *et al.* [73]. The measured dose values, together with the values predicted by Eq(2.7), are shown in Figure 2.4, where the modulation dose was normalized to its white pattern ($gs=255$) value.

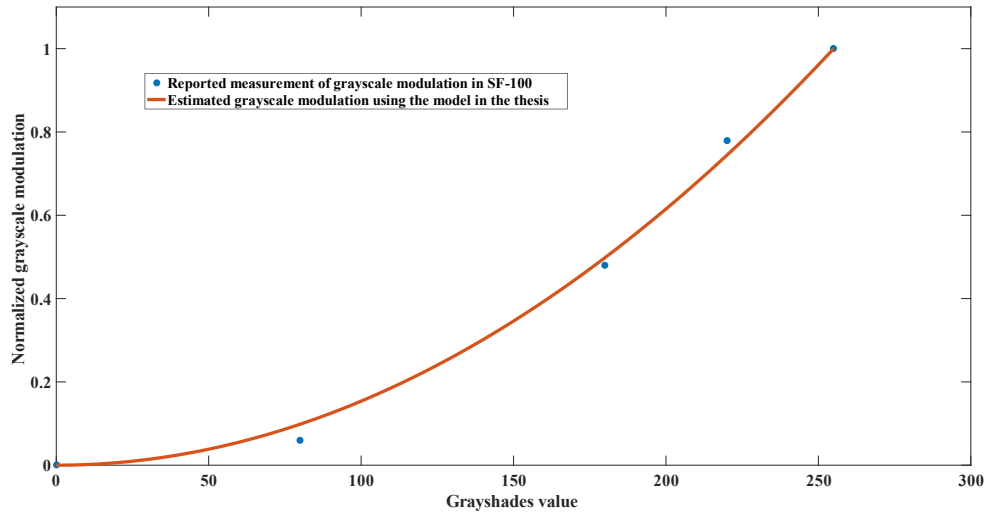


Figure 2.4 Comparison between grayscale modulation predicted by the numerical model and the measurement.

Figure 2.4 indicates a good fit between the theoretical model given by Eq(2.7) and the measurement provided in the literature [73], supporting the accuracy of Eq(2.7).

2.4 Evaluation of grayscale lithography and conductive SU-8 in MEMS fabrication

2.4.1 Fabrication flows based on grayscale lithography

In order to evaluate the suitability of using grayscale lithography and conductive SU-8 for polymeric MEMS fabrication, two manufacturing flows have been developed, as shown in Figure 2.5.

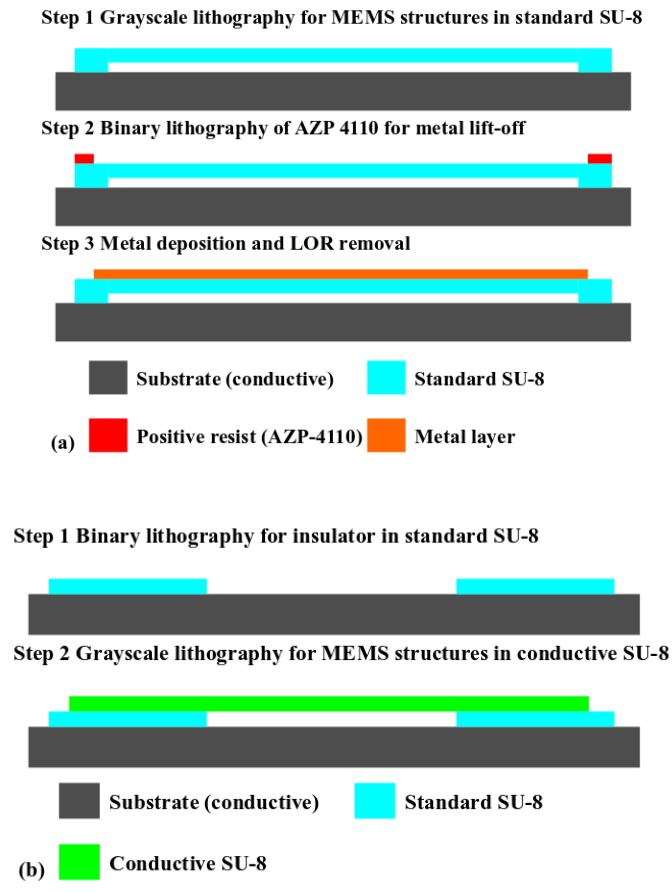


Figure 2.5 Two manufacturing flows based on grayscale lithography and conductive SU-8. (a) Flow I, based on grayscale lithography of standard SU-8 (b) Flow II, based on grayscale lithography of conductive SU-8.

The principle for the one-step fabrication of suspended structures has been provided in Section 2.1.3: Influence of UV exposure dose. In Figure 2.5a, microstructures are manufactured and released directly by the grayscale lithography of standard SU-8, without using any sacrificial

layers. The metallization process has been based on the classic lift-off method for metal films. This metallization process is eliminated in Figure 2.5b because this flow uses the grayscale lithography of conductive SU-8 to shape MEMS structures. Binary lithography of standard SU-8 is used to isolate the substrate electrode and the conductive SU-8 structures. The two fabrication flows have been compared with the traditional fabrication method of SU-8 MEMS devices, as shown in Figure 2.6.

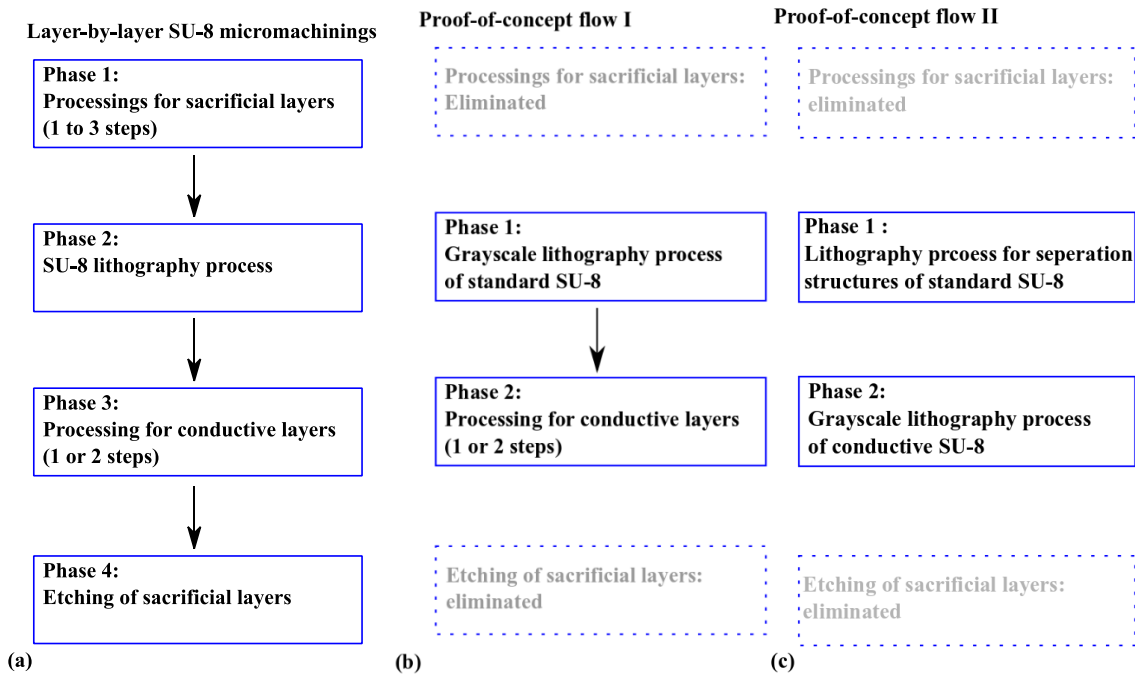


Figure 2.6 Comparison of SU-8 MEMS fabrication processes. (a): Layer-by-layer SU-8 micromachinings in current attempts; (b) Proof-of-concept fabrication flow I developed in this chapter; (c) Proof-of-concept fabrication flow II developed in this chapter.

Figure 2.6 subdivides SU-8 MEMS fabrication flows into different phases. The traditional layer-by-layer SU-8 surface micromachining has four phases, and each phase requires one to three steps for implementation. When the maskless grayscale lithography of standard SU-8 is used for the fabrication of SU-8 MEMS structures, it takes two phases to complete the whole fabrication flow, simplifying the process by two to four steps. The need for the metal layer is eliminated when

the grayscale lithography technique is combined with electrically conductive SU-8. The corresponding fabrication flow in Figure 2.6c removes two process phases from the traditional SU-8 capacitive MEMS fabrication flow.

2.4.2 Material selection and preparation for experimental evaluation

The experimental evaluation of fabrication flow I in Figure 2.5a has used standard SU-8 2015 and Cr thin film. Standard SU-8 2010 was selected to prepare conductive SU-8 to evaluate fabrication flow II in Figure 2.5b. The experimentally-obtained conductive threshold from existing attempts has been used [81, 84, 85]. SU-8 2010 was mixed with 6 wt% of silver nanospheres (diameter: 200nm). The four-step mixing method introduced in Section 2.2.2 was used for optimum dispersion. The mixing of the material has been first done by mechanical stir for 15 minutes, followed by an ultrasonic bath of 60 minutes. The functionalized SU-8 has been put under constant magnetic stirring to minimize sediment and aggregation of the conductive fillers. Before the functionalized SU-8 was spin-coated onto silicon wafers, it was put into an ultrasonic bath for 30 minutes to eliminate as many air bubbles as possible. The author's colleague in the same research group has used this four-step method to mix 6 wt% silver nanoparticles into SU-8, achieving a sheet resistance of $11 \Omega/\square$ [112]. This experimental result indicates that 6 wt% is higher than the percolation threshold, suitable for increasing the electrical conductivity of SU-8. Here, the focus is on the reproducibility of the SU-8 MEMS fabrication flow using this conductive material.

Both SU-8 2015 and SU-8 2010 have been purchased from Kayaku Advanced Material, USA. The conductive fillers were purchased from Nanostructured & Amorphous Materials, Inc, USA. Single-side polished <100> silicon wafers have been selected as the substrate for the fabrication of SU-8 MEMS test structures.

2.4.3 Design of the out-of-plane SU-8 MEMS test structures

Multiple types of out-of-plane SU-8 MEMS test structures have been designed for experimental evaluation. The designs of the out-of-plane MEMS transducer structures are summarized in Table 2.9. The lithography mask designs are shown in Figure 2.7 to Figure 2.10.

	Double-clamped cantilever		Four-points clamped membrane			
Material Type	Width (μm)	Length (μm)	Suspension beam		Membrane	
			Width(μm)	Length(μm)	Radius (μm)	
SU-8 2015	50	200	15	60	60	60
SU-8 2010 with silver nanoparticles	50	100	20	50	Width(μm)	Length(μm)
					50	50

Table 2.9 Dimensions of out-of-plane polymeric MEMS transducers to be fabricated

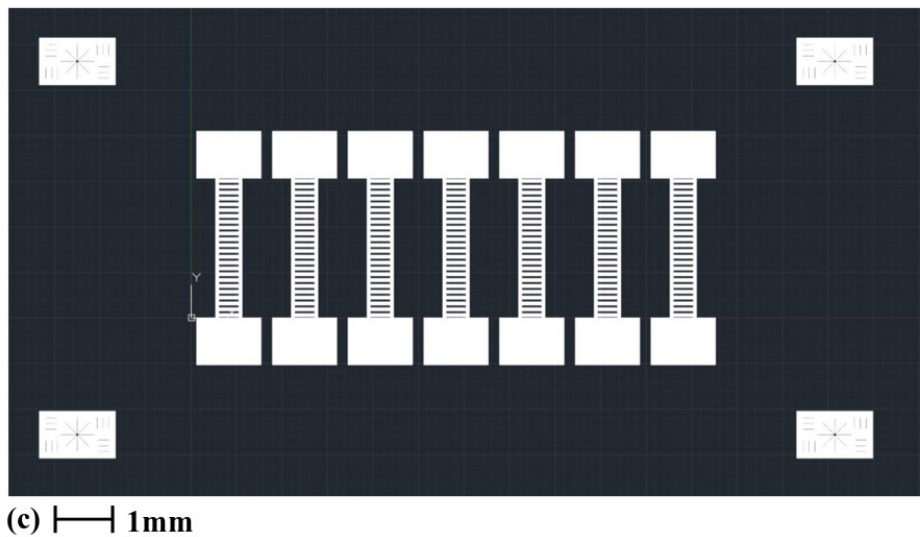
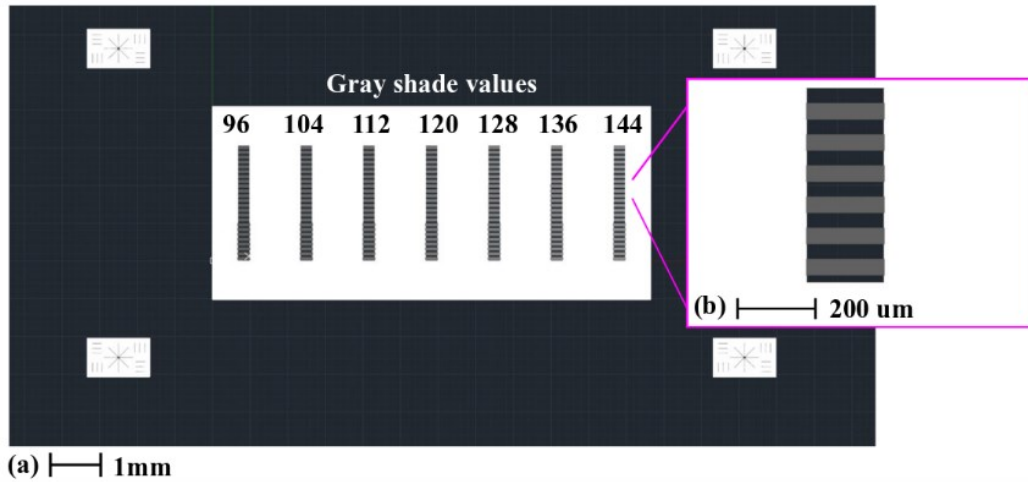


Figure 2.7 Mask designs for doubly-clamped beams made by grayscale lithography of standard SU-8. (a) The overview of the grayscale mask for MEMS structures. (b) The zoom-in view of the grayscale mask. (c) The mask for lift-off of metal layers.

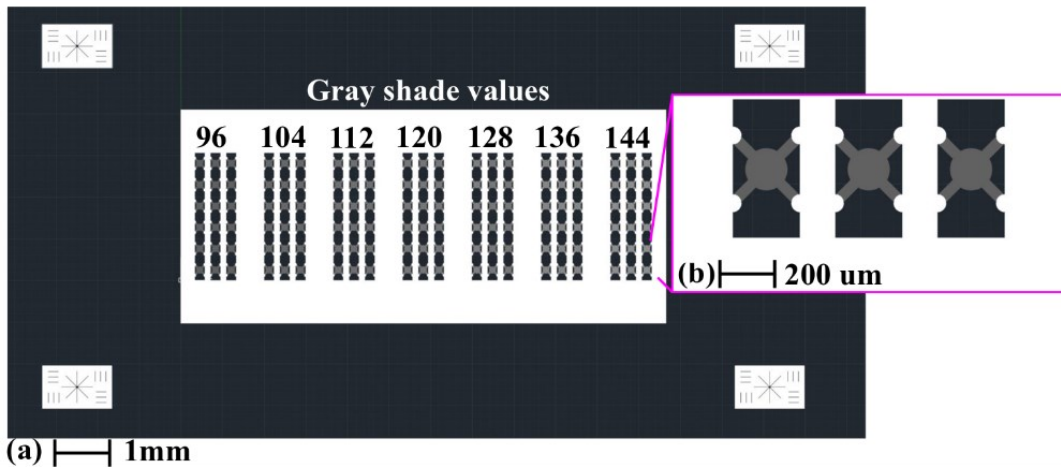
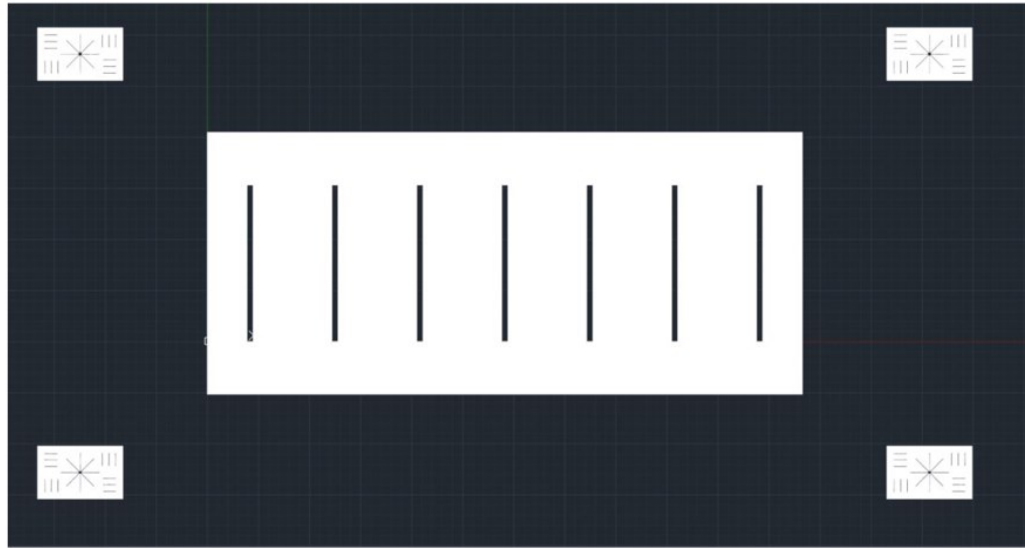
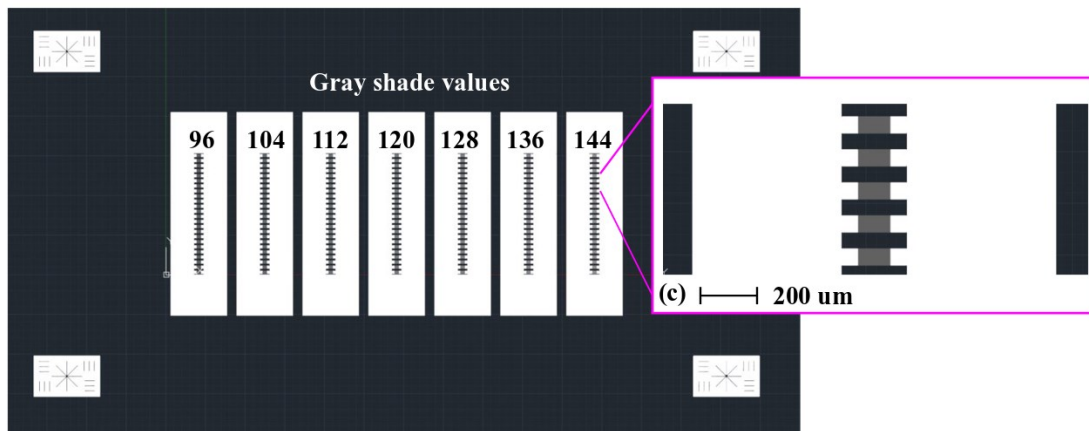


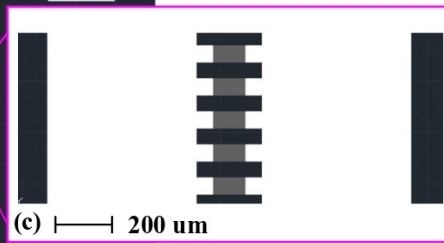
Figure 2.8 Mask designs for membranes made by grayscale lithography of standard SU-8. (a) The overview of the grayscale mask for MEMS structures. (b) The zoom-in view of the grayscale mask. (c) The mask for lift-off of metal layers.



(a) |——| 1mm

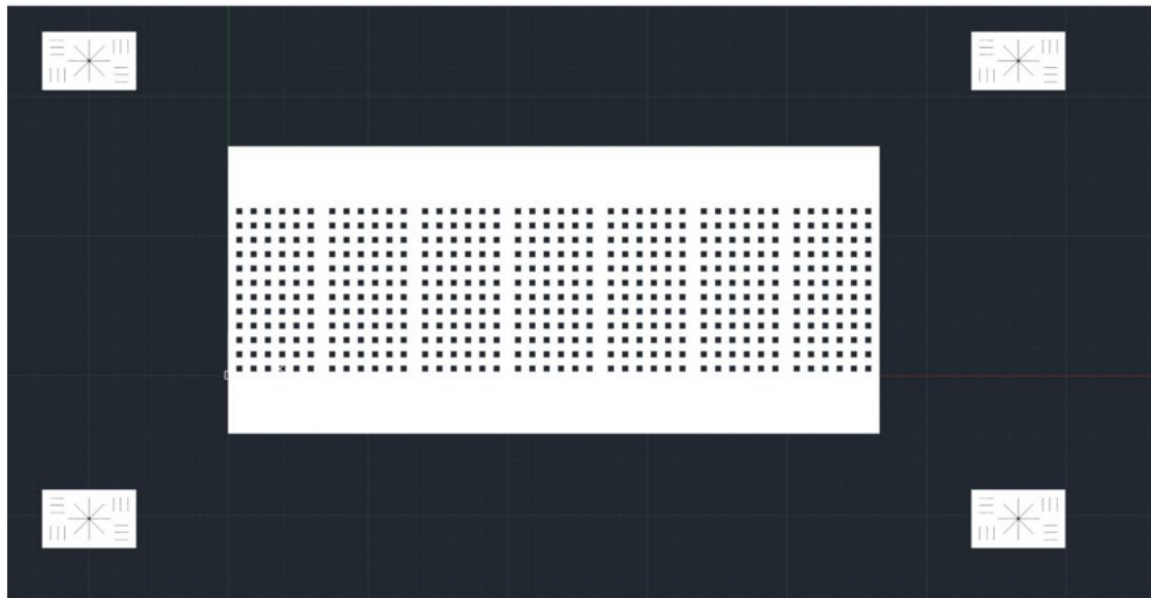


(b) |——| 1mm

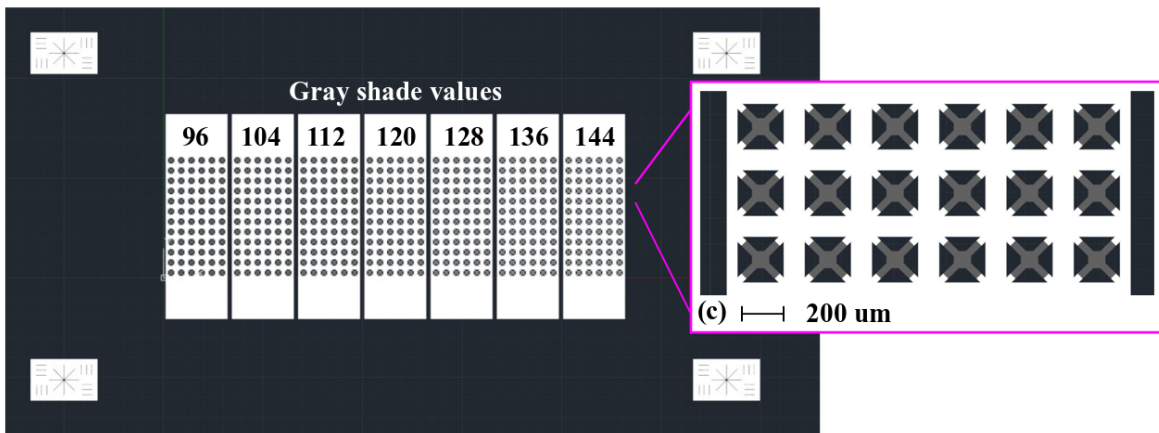


(c) |——| 200 um

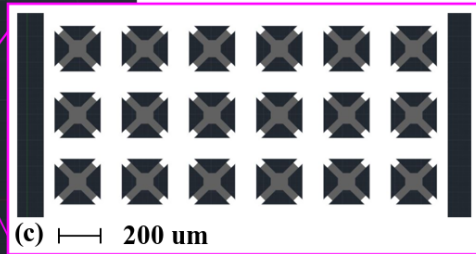
Figure 2.9 Mask designs for doubly-clamped beams made by grayscale lithography of SU-8 mixed with silver nanoparticles. (a) The mask for the insulation layer, (b) The overview of the grayscale mask for MEMS structures. (c) The zoom-in view of the mask for MEMS structures.



(a) |—| 1mm



(b) |—| 1mm



(c) |—| 200 um

Figure 2.10 Mask designs for membranes made by grayscale lithography of SU-8 mixed with silver nanoparticles. (a) The mask for the insulation layer, (b) The overview of the grayscale mask for MEMS structures. (c) The zoom-in view of the grayscale mask for MEMS structures.

All out-of-plane MEMS test structures are fabricated in a layout of 6 arrays. White pixels are fully exposed, and the black ones are not. The parts colored in gray shades correspond to movable components of the test structures. The gray shade levels gradually increase from 96 (14% of initial exposure dose) to 144 (31% of initial exposure dose) from left to right, with an interval

of 8. Since both flows have two SU-8 lithography steps, markers are designed at the masks' corners to allow accurate alignment.

2.4.4 The fabrication process of the MEMS test structures

An SF-100 maskless lithography system from Advanced Micropatterning, USA, has been used (UV wavelength: 365nm, labeled intensity: 10 mW/cm²). The exposure durations for standard SU-8 2015, and the SU-8 2010 mixed with silver nanoparticles, have been set up to 15s and 240s. The drastic increment of exposure duration for SU-8 2010 with silver nanoparticles is due to the more significant UV absorption by metal particles [84, 85]. All other steps related to the grayscale lithography (soft baking, post-exposure baking, and developing) have adopted the recipe recommended in the user manual of SU-8 photoresist.

The metallization process for SU-8 MEMS structures fabricated by standard SU-8 2015 has used the E-beam evaporation and lift-off process.

2.4.5 Characterization method

Test structures have been optically inspected under a microscope after the grayscale lithography. A Polytec MSA-500 laser Doppler vibrometer was used for the electrical actuation and the mechanical resonant frequency measurement. The voltage signal for actuation consists of both AC and DC components. The AC components are periodic chirp signals, sweeping over a band of frequencies to drive the SU-8 MEMS test structures' mechanical vibration. The DC signal used is 5V, and the peak to peak amplitude of the AC signal is 2V. Both signals are amplified by 20 times before being interfaced to the fabricated transducers. The frequency value corresponding to the peak on the Bode plot will be identified as the natural frequency.

2.5 Characterization result and discussion

2.5.1 Optical inspections

Representative results for microstructures fabricated by grayscale lithography of standard SU-8 are shown in Figure 2.11.

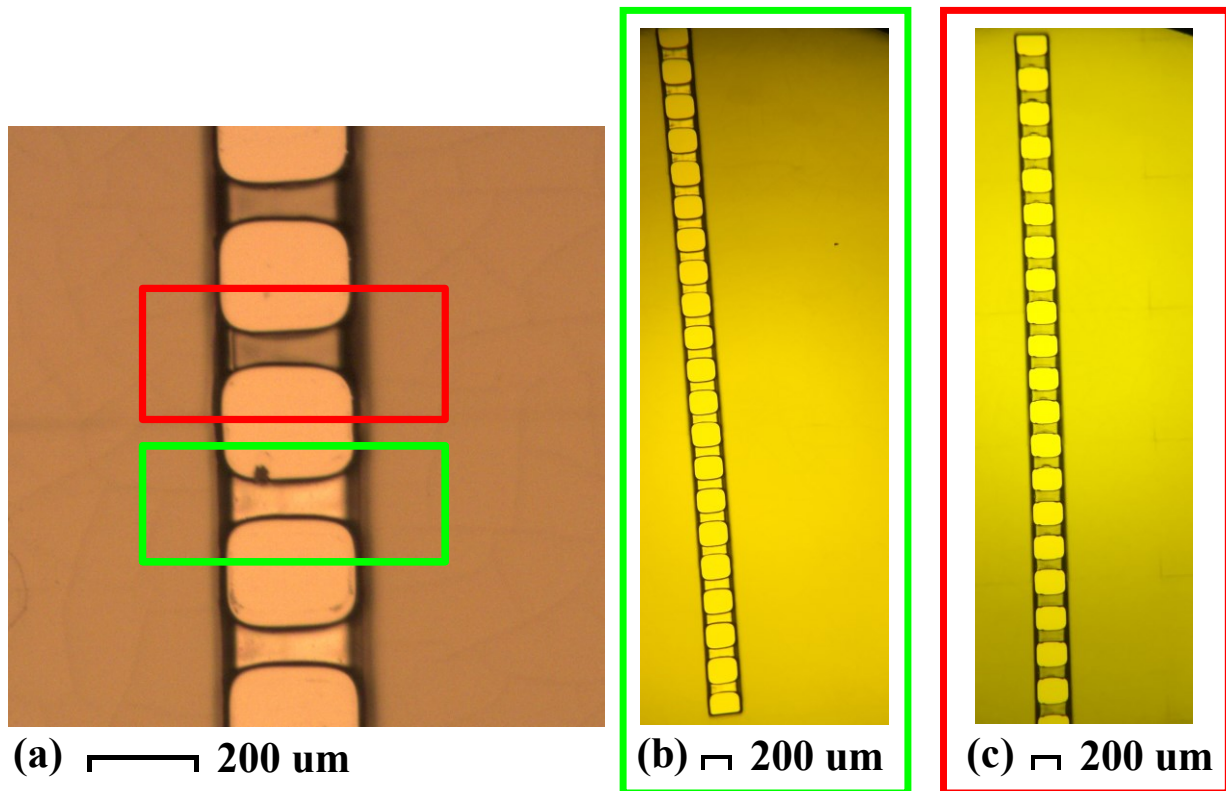


Figure 2.11 Microscopic inspection of polymeric out-of-plane transducers fabricated by grayscale lithography of standard SU-8 2015. (a) Example of both collapsed and suspended structures, corresponding gray shade value: 104; (b) A full array of suspended structures, corresponding gray shade value: 96. (c) A full array of collapsed structures, corresponding gray shade value: 112 and higher.

Figure 2.11 shows that two different optical brightness levels can be observed in the fabricated structures. In Figure 2.11a, some of the beams are significantly brighter than the fixed structures, while others have the same brightness level as the fixed ones. The brightness of the structures made by grayscale masks lithography is an indirect indication of their final status.

Brighter structures are suspended, while darker structures have collapsed. All structures fabricated using the gray shade level of 96 in Figure 2.11b have been found suspended when they are evaluated by this optical criterion. When gray shade values are higher than 112, all structures have collapsed to the substrate after the grayscale lithography, as shown in Figure 2.11c. It has also been found that the final status in Figure 2.11c can also be implemented by hard baking at 200 °C.

The optical brightness difference can be explained by the transmission of yellow light, as illustrated in Figure 2.12.

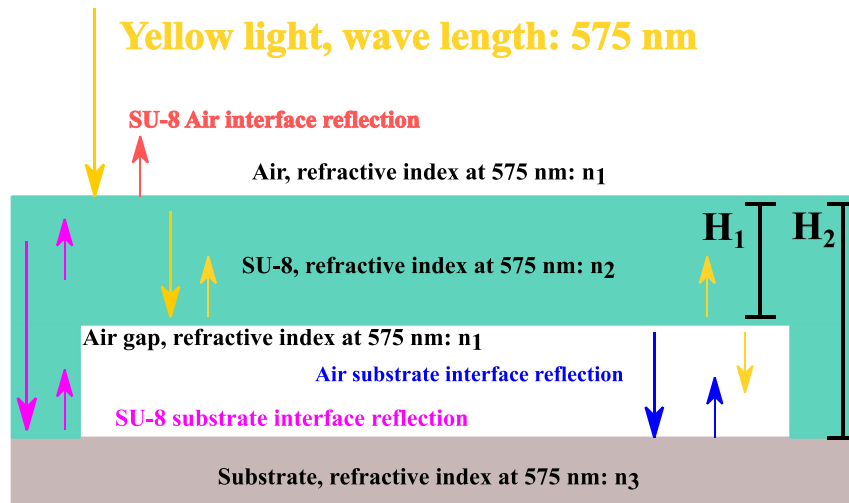


Figure 2.12 The transmission and reflection of yellow light within SU-8 microstructures with different final statuses.

The observed intensity of yellow light is determined by two factors: the reflection/transmission at media boundaries and the attenuation during propagation. The transmission measurement data from Kayaku Advanced Material indicates that SU-8 is highly transparent for yellow light (wavelength: 575nm). Here, the attenuation of yellow light in the air gap is also neglected. In this context, the observed optical brightness becomes only related to the reflection at media boundaries. The yellow light reflection in collapsed SU-8 structures happens only at the interface between the SU-8 layers and the substrate. At the same time, there are three

reflections to consider for suspended SU-8 structures. The primary reflection happens at the interface between air and the substrate. Two minor reflections/transmissions happen at the interface between the bottom surface of the suspended SU-8 structures and the air. The reflected intensity can be computed with the following equation:

$$I_{reflected} = I_{incident} \left(\frac{n_1 - n_2}{n_1 + n_2} \right)^2 \quad (2.8)$$

In Eq(2.8), n_1 and n_2 are the refractive index values of the two mediums at an interface. For yellow light wavelength at 575nm, the value of n is set to 1 for air, 1.55 for SU-8 [113], and 4 for <100> silicon wafer [114]. About 95% of incident yellow light is transmitted into the SU-8 layers at the interface between air and the top surface of SU-8 structures. 20% of the incident intensity is reflected at the interface between SU-8 and <100> silicon wafer. 36% of the incident intensity is reflected at the interface between air and <100> silicon wafer. The observed optical intensity for suspended structures is about 32% of the incident intensity, while it falls to about 18% for collapsed structures. This computation result matches well with the observed phenomenon in optical inspection, validating the optical-based criterion's effectiveness to distinguish SU-8 suspended structures from the collapsed ones.

Some issues have been spotted during the optical observation of MEMS structures made by conductive SU-8, as shown in Figure 2.13.

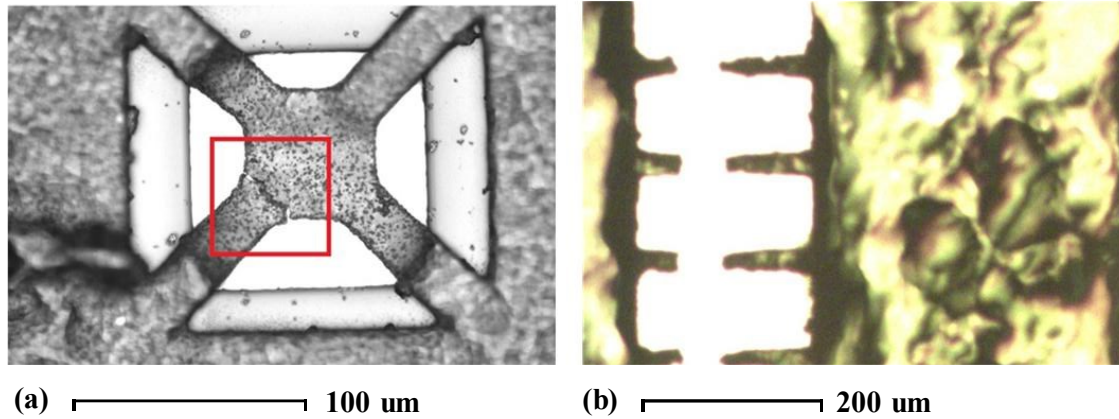


Figure 2.13 Representative issues polymeric MEMS structures fabricated by conductive SU-8. (a) Membranes. (b) Doubly-clamped beams (destroyed)

Figure 2.13 shows that the aggregation of conductive fillers has resulted in visible surface variation and structural damage under microscopic inspection. Figure 2.13a shows a crack on a membrane, while Figure 2.13b illustrates the massive scale destruction of doubly-clamped beams after the grayscale lithography. These issues reflect the inevitable weakening effect of non-cross-linkable, conductive fillers on the strength of the monomer crosslinking network in SU-8, as well as the hard-to-address aggregation issue of solid, insoluble fillers, even after sufficient ultrasound bath and constant stirring. Since structures made by conductive SU-8 are opaque, their final status can only be indirectly confirmed through the measurement of mechanical resonance under the electrical actuation. Suspended structures have measurable mechanical resonance, while the collapsed ones do not.

2.5.2 Measurement of mechanical resonance under electrostatic actuation

The final status of test structures made by grayscale lithography of standard SU-8 can be determined optically, so a selection of test structures has been made before measuring mechanical resonance and natural frequency. A grayscale level of 96 has made most of the test structures suspended. Therefore, only they were measured for mechanical resonance under electrical

actuation. Samples made by conductive SU-8 cannot have their final status determined optically, so all of them were measured. Conductive SU-8 samples fabricated using gray shade levels of 96, 104, 112, and 120 have been found to have measurable mechanical resonant frequencies. Representative measurement results are presented in Figure 2.14 and Figure 2.15.

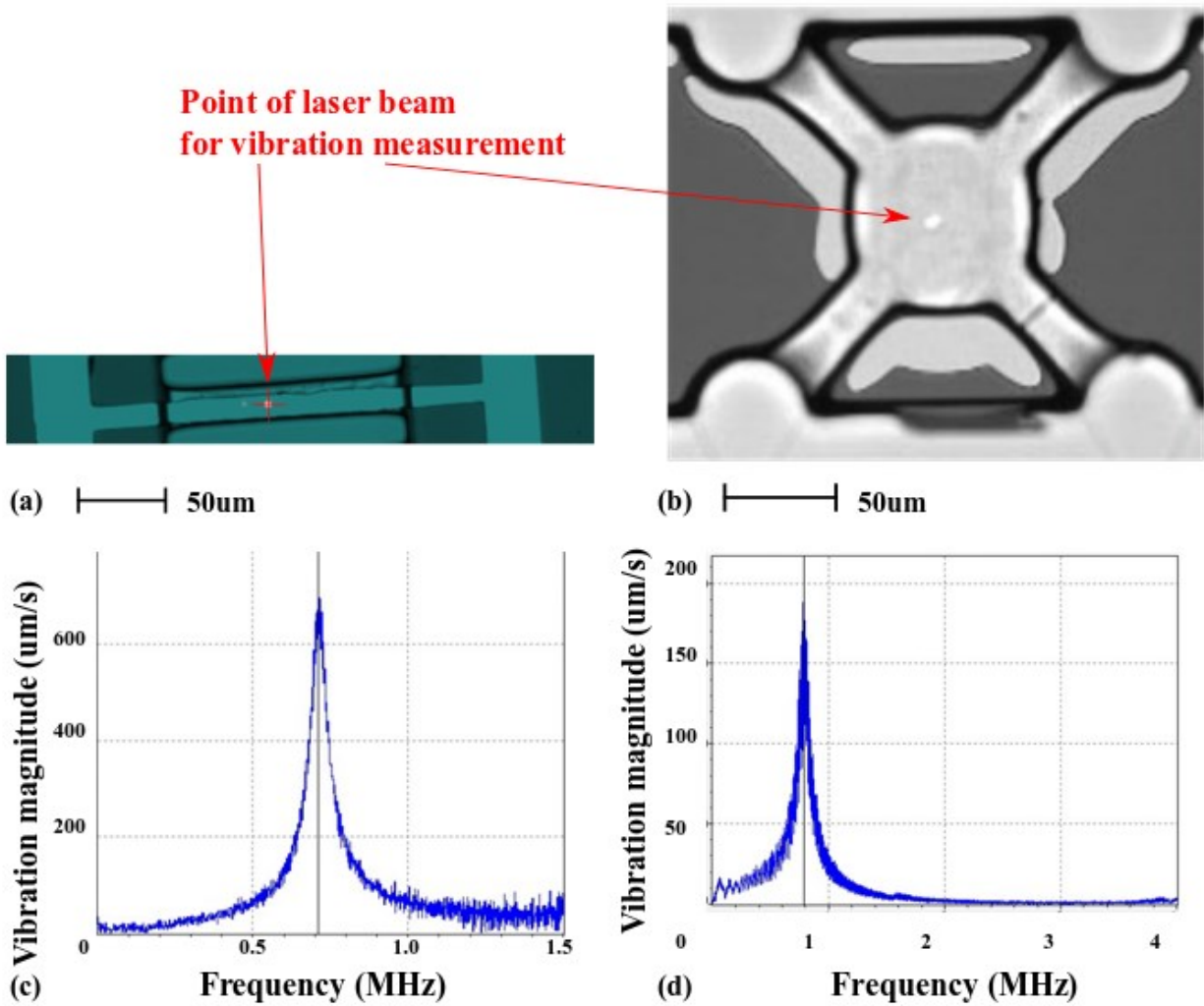


Figure 2.14 Mechanical resonance of MEMS transducers made by grayscale lithography of standard SU-8. (a) Doubly-clamped beams under measurement, (b) Membranes under measurement, (c) The representative measurement result for doubly-clamped beams, (d) The representative measurement result for membranes.

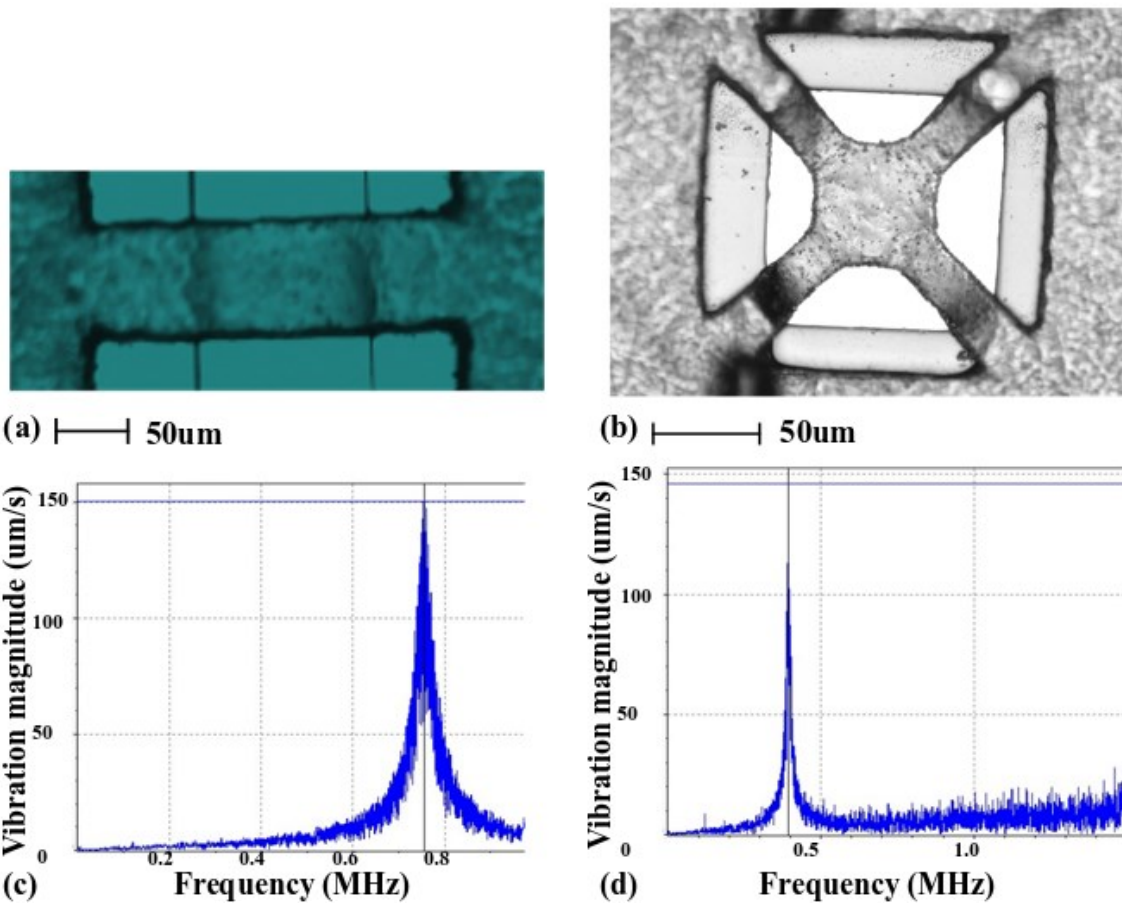


Figure 2.15 Mechanical resonance of MEMS transducers made by grayscale lithography of SU-8 mixed with silver nanoparticles. (a) Doubly-clamped beams under measurement, (b) Membranes under measurement, (c) The representative measurement result for doubly-clamped beams, (d) The representative measurement result for membranes.

In Figure 2.14, the mechanical resonances have peaks clearly distinguishable from the noise floor, which is a sign of good conductivity for the Chromium electrodes. Similar profiles can be observed in the mechanical resonance measurement for test structures made by SU-8 mixed with silver nanoparticles in Figure 2.15. Because the conductive SU-8 has been made using the same method as the one used by the colleague of the author [112], the measurement in Figure 2.15 provides additional evidence for the good electrical conductivity in the SU-8 mixed with 6 wt%

silver nanoparticles. The appearance of these peaks on the Bode plots demonstrates that grayscale lithography can be used to manufacture SU-8 MEMS transducers.

Fundamental resonant modes have been most significant in the measurement result of Figures 2.14 and 2.15. The domination of the fundamental mode is related to the electrode configurations. The metal films have covered the entire movable parts of the movable microstructures made in standard SU-8 photoresist. Conductive SU-8 has volumic electrical conductivity. The entire bottom surface of the movable microstructures made in conductive SU-8 serves as the electrodes.

It is easier for the fabrication flow based on standard SU-8 to implement electrical actuation for higher-order mechanical resonant modes. These modes need the electrodes to be deposited in more selective ways, only partially covering the surface of the movable microstructures. This more selective metal deposition can be implemented by correspondingly changing the positive lithography mask design during the fabrication flow in Figure 2.5a. If higher-order mechanical resonant modes need to be implemented in the MEMS transducers made by conductive SU-8, the process is more complex. Parts of the movable microstructures have to be made by standard SU-8. It is almost impossible to implement such a structure using grayscale lithography in a one-step fabrication flow.

The natural frequency measurement distribution and the corresponding statistics are provided in Figure 2.16, Figure 2.17, and Table 2.10.

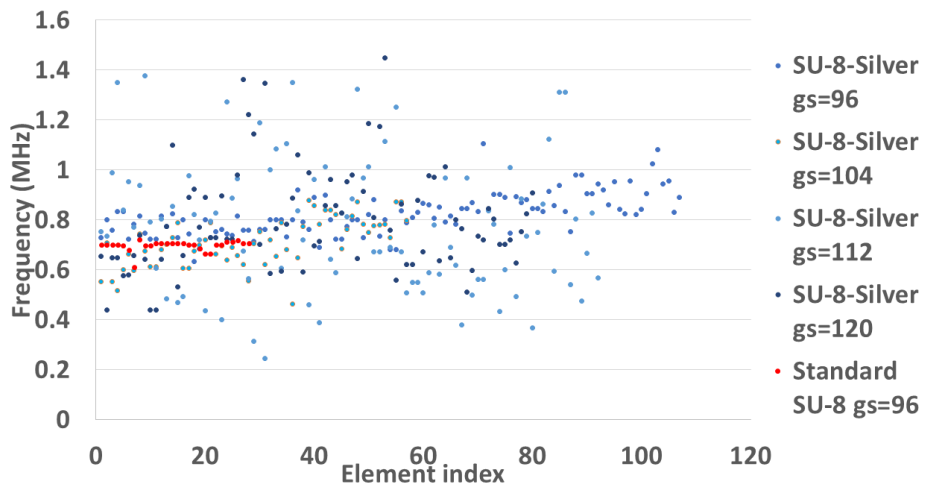


Figure 2.16 The distribution of the measured resonant frequency for doubly-clamped beams

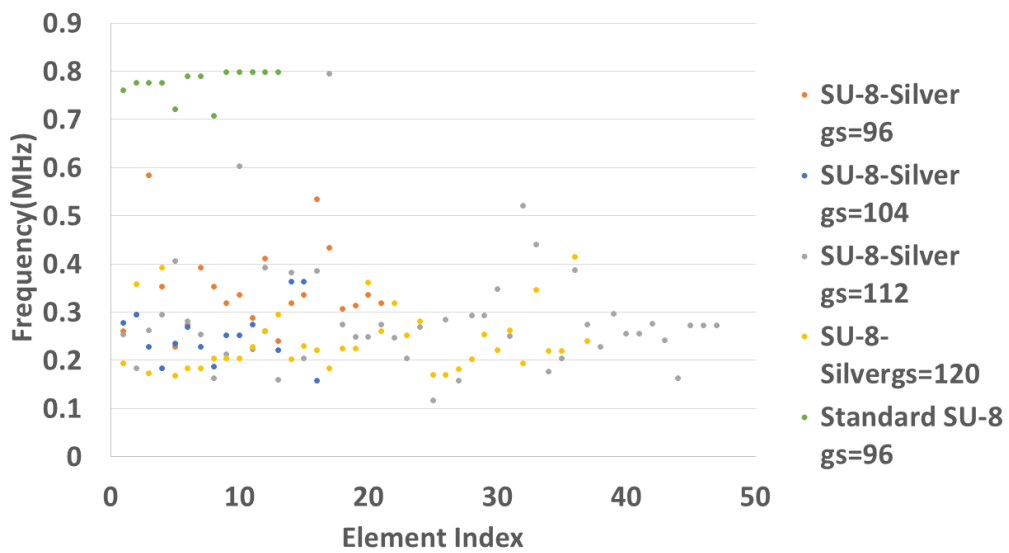


Figure 2.17 The distribution of the measured resonant frequency for membranes.

Test structures made by standard SU-8 2015 (gray shade value: 96)								
Structure type	Average frequency(MHz)				Standard deviation			
Doubly-clamped beam	0.701				1.7%			
Membranes	0.776				3.7%			
Test structures made by SU-8 2010 mixed with silver nanoparticles								
	Average frequency(MHz)				Standard deviation			
Gray shade values	96	104	112	120	96	104	112	120
Doubly-clamped beam	0.709	0.774	0.796	0.823	13.7%	34%	26%	10.2%
Membranes	0.241	0.253	0.287	0.344	27.0%	22.4%	41.4%	25.5%

Table 2.10 Statistic information of each type of SU-8 transducers fabricated

In Figures 2.16 and 2.17, the test structures made by grayscale lithography have shown a more consistent distribution of the natural frequency. In Table 2.10, the standard deviation of frequency measurement for MEMS structures fabricated using standard SU-8 is lower than 4%. The standard deviation for MEMS structures fabricated using conductive SU-8 is between 10% to 41%. The consistent distribution and low standard deviation of the measured resonant frequency indicate that grayscale lithography of standard SU-8 has a higher reproducibility for geometric dimensions, particularly structural thickness.

This conclusion can be understood with the basics of natural frequencies of microstructures. With a doubly-clamped beam as the example, its fundamental natural frequency has the following relationship with the material properties and geometric dimensions [115]:

$$\begin{cases} I = \frac{wh^3}{12} \\ m = \rho whL \\ f_n \propto \sqrt{\frac{EI}{m}} = \sqrt{\frac{E}{12\rho}} \frac{h}{\sqrt{L}} \end{cases} \quad (2.9)$$

In Eq(2.9), f is the natural frequency; E is Young's modulus of the structural material; I is the inertia moment; m is the mass; ρ is the density; w, h , and L are the width, thickness, and height of the microstructures. The relative sensitivity of the natural frequency to the material properties and geometric dimensions are summarized in Table 2.11.

Parameters	E	ρ	h	L
Relative sensitivity	0.5	-0.5	1	-0.5

Table 2.11 Relative sensitivity of the natural frequency to the material and geometric parameters

As shown in Table 2.11, a variation in structural thickness contributes twice as much as equivalent relative variations in planar dimensions and material properties to natural frequencies variation.

For test structures made by grayscale lithography of conductive SU-8, the more dispersed distribution and larger standard deviation of their measured natural frequency are related to the insoluble fillers. As already seen in Figure 2.13, the aggregation of silver nanoparticles has resulted in surface variations and structural damage even visible under optical microscopic inspection. They have caused significant uncertainty in the geometric dimensions, fixing conditions, and

material properties. These factors have significantly increased the uncertainty in the measurement of natural frequency for structures made by the same designs.

The distribution of measurements and their statistics confirm that standard SU-8 is more suitable as the structural material for polymeric MEMS devices than conductive SU-8 made by insoluble conductive additives.

2.6 Summary

The research in Chapter 2 has been conducted with a bottom-to-top methodology flow, starting from the studies about SU-8 photoresist characteristics and its lithography process. Methods to enhance the electrical conductivity of the polymers are summarized. A model has been established and validated to estimate the exposure dose modulation by grayscale levels.

The theoretical studies have supported the subsequent experimental case studies. Two different SU-8 MEMS fabrication flows have been designed with grayscale lithography, one for standard SU-8 and the other for conductive SU-8. These two new fabrication processes are sacrificial-layer-free, being significantly simpler than the traditional layer-by-layer SU-8 micromachining methods. The new fabrication processes have been experimentally evaluated through the design, fabrication, and characterization of test structures. Several conclusions have been reached regarding the suitability of using grayscale lithography for MEMS fabrication.

In this chapter, the dose-modulating lithography process, represented by maskless grayscale lithography, is demonstrated as suitable for the fabrication of SU-8 capacitive MEMS structures. Both standard and conductive SU-8 can be used for this purpose. This conclusion has been reflected by the measurable mechanical resonance of test structures under electrical actuation.

The fabrication flow using standard SU-8 has exhibited higher process reproducibility. It is also simpler for the fabrication flow based on standard SU-8 to implement MEMS transducers

resonating at higher-order mechanical resonant modes. These experimental conclusions indicate that standard SU-8 is the preferred material for coming research work.

Two interesting phenomena have been spotted for the grayscale lithography of standard SU-8. Some of the structures have collapsed after the developing step, while the others fabricated in the same grayscale lithography process were suspended. The hard baking process is considered an optional process good for mechanical strength, but it has also resulted in the collapse of suspended structures.

These phenomena need further study if a controllable polymer MEMS fabrication technology using grayscale lithography of standard SU-8 is to be developed. A calibration method for this lithography process also needs to be developed and validated. This calibration method will build up the foundation to systematically evaluate process predictability. Chapter 3 will be dedicated to research with this respect.

Chapter 3: Calibration for grayscale lithography of standard SU-8

The research of Chapter 3 focuses on the calibration process of grayscale lithography of standard SU-8. After validating grayscale lithography's suitability in SU-8 MEMS fabrication, such a calibration process is essential to evaluating process predictability for any fabrication technologies using the advanced lithography method. Figure 3.1 illustrates the organization of research in this chapter.

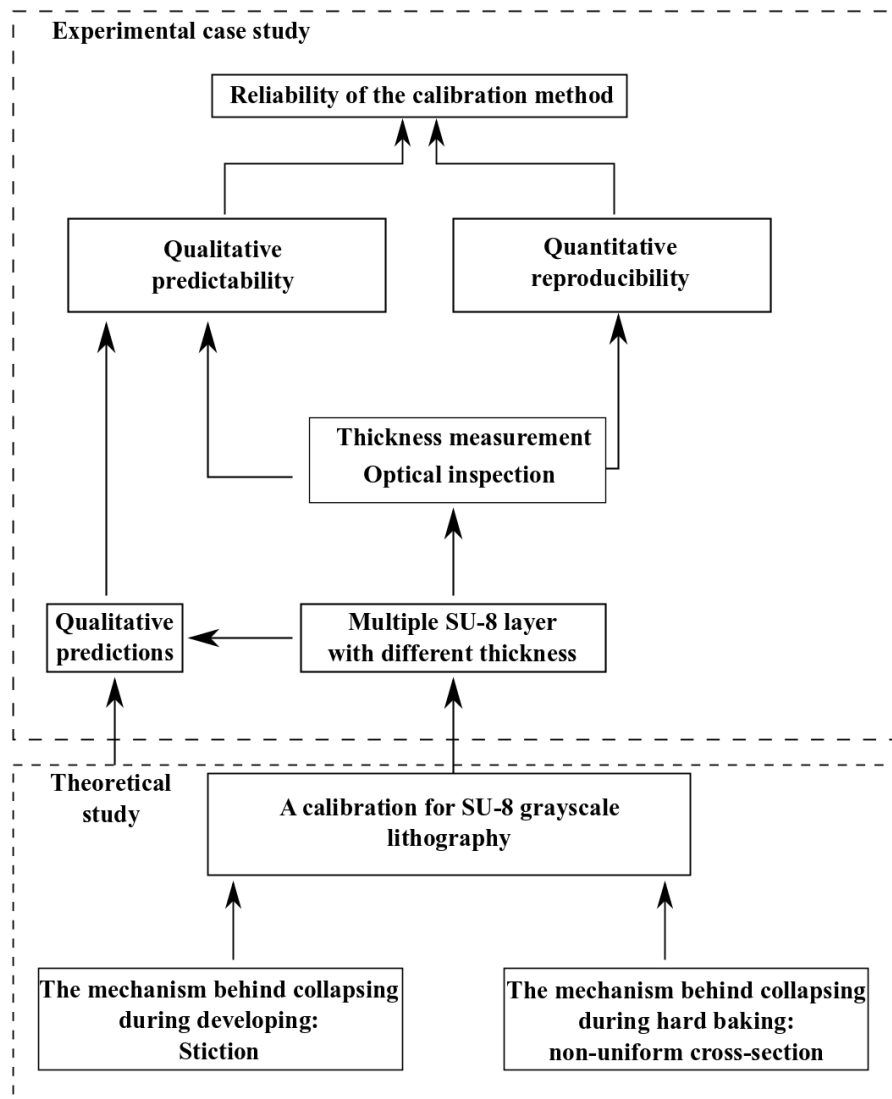


Figure 3.1 Research work in Chapter 3.

As shown in Figure 3.1, the collapse principles during the grayscale lithography process are studied first. Section 3.1 introduces the detail about corresponding research activities. Section 3.2 uses the conclusions from Section 3.1 into the grayscale lithography of SU-8 to develop a new calibration method. The preparation to experimentally validate the new method is also introduced in this section. Section 3.3 presents and discusses the characterization result of the experimental case study. Section 3.4 summarizes the whole chapter.

3.1 Collapsing of structures during grayscale lithography

3.1.1 During developing phase

The developing step of grayscale lithography has one extra purpose than the one of traditional lithography. It releases the structures made by grayscale masks by dissolving the uncrosslinked SU-8 underneath. Because this purpose is related to microstructure releasing, grayscale lithography's developing step becomes subject to the stiction effect that results in the collapse.

When microstructures experience an alternation of surrounding fluidic conditions, a capillary force is generated between the substrate and the microstructures' bottom surface, dragging the structures down to the substrate. If the work done by the capillary force is larger than a critical threshold value, irreversible deformation will happen. This deformation is defined as the stiction effect. If the capillary work can be balanced by elastic energy, the structures will remain suspended.

The stiction effect is related not only to the liquids used during microfabrication but also to structural dimensions. Estimating whether stiction will happen is important for developing microfabrication flows and the design of MEMS devices. Mastrangelo *et al.* have proposed and

validated a dimensionless value called elastocapillary number (N_{EC}) to predict the stiction effect under certain conditions [116, 117].

When N_{EC} is larger than 1, a microstructure will be stiction-free, while it would irreversibly deform if N_{EC} is smaller than 1. As for N_{EC} values close to 1, the structure is at a critical state sensitive to external disturbance. The N_{EC} for doubly-clamped beams is defined as:

$$N_{EC} = \frac{128Eg^2t^3}{15\gamma \cos\theta l^4 \left(1 + \frac{t}{w}\right)} \left(1 + \frac{2\sigma_R l^2}{7Et^2} + \frac{108g^2}{245t^2}\right) \quad (3.1)$$

In Eq(3.1), E is Young's modulus of the material, g is the gap between the beam and the substrate; t is the thickness of the beam; γ is the solid-fluidic tension between the microstructure and environment; θ is the contact angle of the fluid; l is the length of the beam, w is the width of the beam; σ_R is the residual stress within the structure. In Chapter 2, some grayscale-modulated exposure doses have resulted in both suspended and collapsing structures after the developing step. These exposure doses may have led to an N_{EC} value close to 1, increasing the randomness in the doubly-clamped beams' final status.

There are three alternations of surrounding fluidic conditions during the developing step, from PGMEA to IPA, from IPA to DI water, and from water to air. The information about the surface tension and the contact angle of the three liquid agents on a SU-8 surface is provided in Table 3.1.

Liquid agent	PGMEA	IPA	DI water
Contact angle (°)	2.6[91]	5.4[91]	90[118]
Surface tension (N/m)	0.0269	0.023	0.0728

Table 3.1 Surface tension and contact angle of liquids involved in the SU-8 lithography process

As shown in Table 3.1, SU-8 is hydrophobic, but its surface has quite a high wettability to PGMEA and IPA. The contact angle and surface tension of PGMEA and IPA are also quite similar. If the stiction effect happens during the developing phase, it is probably during the rinsing with DI water to remove IPA.

3.1.2 During the hard baking phase

Hard baking is beneficial for a binary SU-8 lithography process. It can restore the cracks resulted from developing. The academic field provides two possible mechanisms to explain the restoration of cracks [98, 119]: thermal-expansion-induced swelling and the thermal-induced promotion of thorough crosslinking. However, hard baking has resulted in the collapse of suspended structures fabricated by grayscale lithography. This Ph.D. thesis proposes and validates one explanation of this phenomenon.

The author attributes the collapse to the solid diffusion of photoacids during SU-8 lithography. The solid diffusion effect leads to a nonuniform cross-sectional distribution of photoacids within the region exposed after post-exposure baking, as illustrated by Figure 3.2.

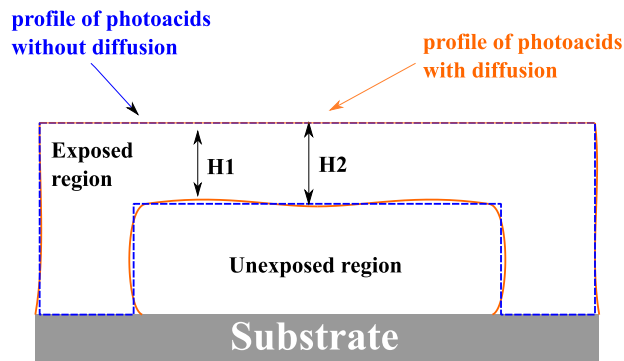


Figure 3.2 Cross-sectional distribution profile of photoacids at exposed regions after grayscale lithography

In Figure 3.2, the profile after diffusion is loosely based on a Gaussian solution rectified by the complementary error function. The two ends near fixed structures have shallower photoacid

distribution than the parts close to the geometric center. These regions will be thinner after the developing step.

Cross-sectional SEM characterization for an array of SU-8 doubly-clamped beams fabricated in Chapter 2 has been conducted to validate the newly proposed explanation. Three representative results are shown in Figure 3.3.

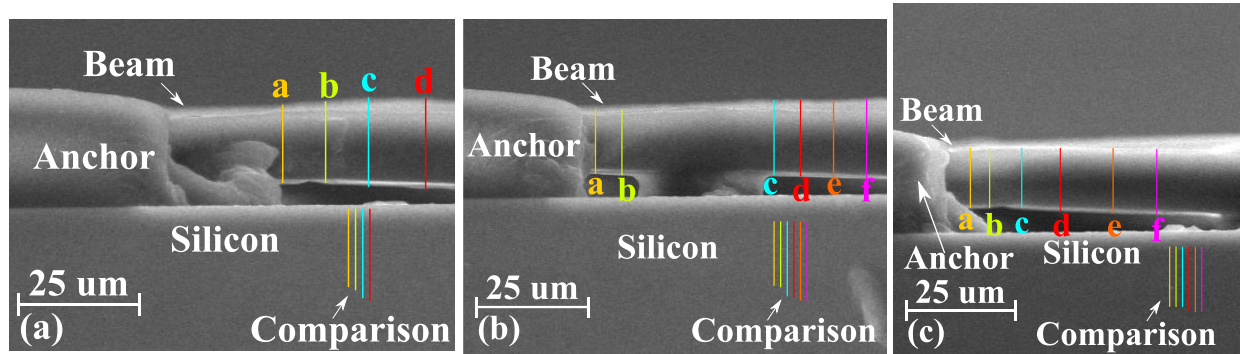


Figure 3.3 SEM images of the crosssection of doubly-clamped beams fabricated by SU-8 grayscale lithography. (a) to (c): Representative result with cross-sectional variation characterized and compared.

In Figure 3.3, the cross-sectional thickness for different parts of the beams has been labeled and compared. The parts closer to the anchors were found thinner than the central parts. This characterization result matches with the prediction in Figure 3.2. When suspended structures with such cross-sectional status are heated, they behave like MEMS thermal actuators. The thinner parts near the fixed end are hot arms [120] and mechanical weak points. They are more sensitive to heat, generating more strain related to thermal expansion and pushing the middle parts downward to the substrate.

Finite element analysis was carried out in COMSOL Multiphysics 5.3 to validate the explanation above. A SU-8 beam with a uniform crosssection has also been simulated for the thermal expansion as the control sample. SU-8 material properties used in the simulation are summarized in Table 3.2. The simulation results are shown in Figures 3.4 and 3.5.

Property	Heat capacity (J/kg·K)	Thermal conductivity (W/mK)	Density (kg/m ³)	Young's modulus (GPa)	Poisson's ratio	Thermal expansion coefficient (ppm/K)
Value	1200 [121]	0.2[32, 122]	1200	4.95[29, 30]	0.32[31]	102 [31]

Table 3.2 SU-8 material properties used in the finite element analysis

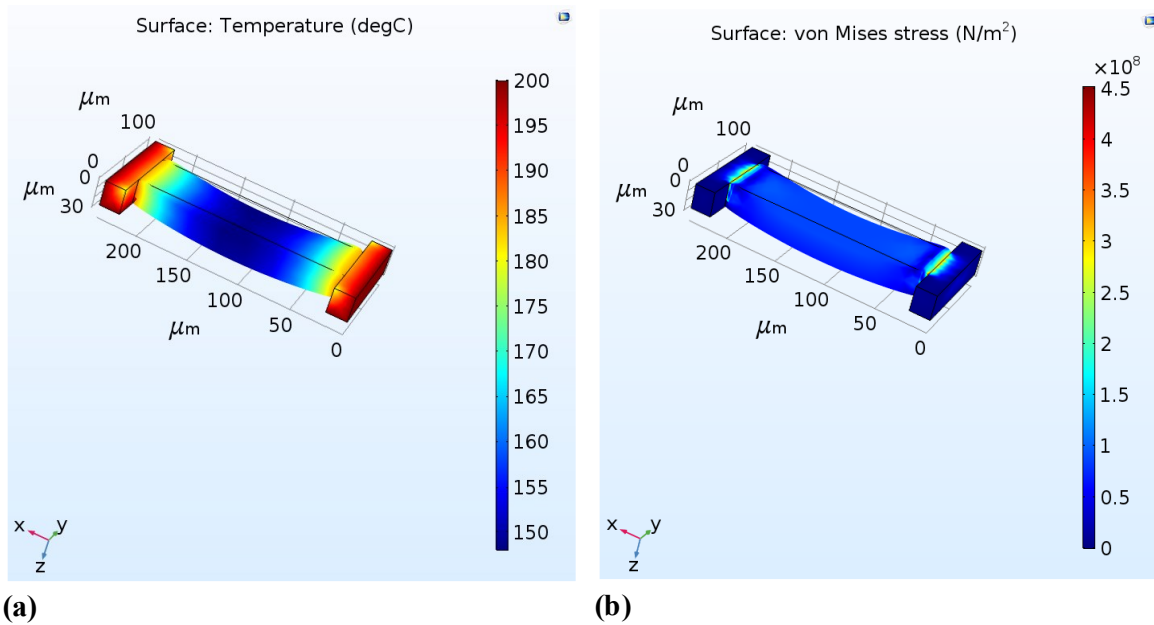


Figure 3.4 Simulation of hard baking for SU-8 beams fabricated by grayscale lithography. (a) Temperature distribution. (b) Stress distribution

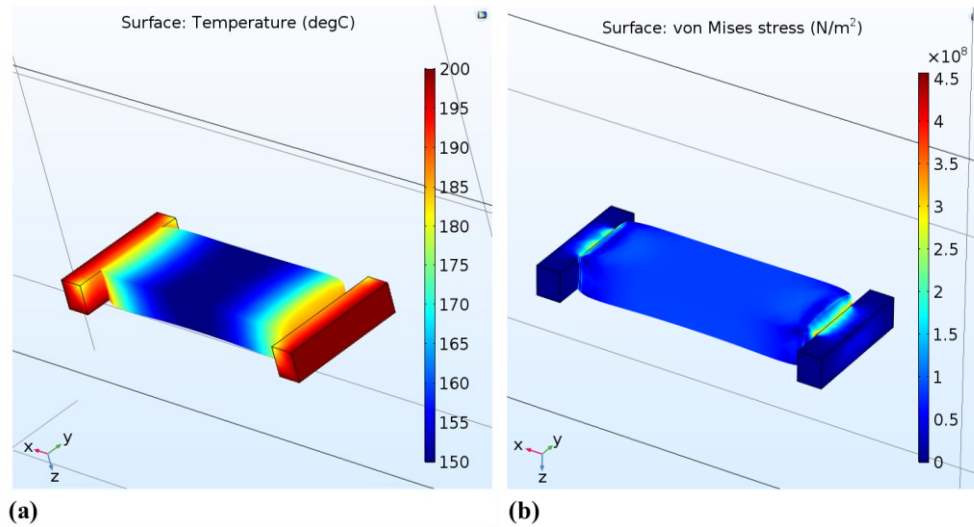


Figure 3.5 Simulation of hard baking for SU-8 beams with uniform cross-section. (a) Temperature distribution. (b) Stress distribution

In both Figure 3.4 and Figure 3.5, heat is applied to the structures from the bottom surface of the fixed anchors. The temperature of these bottom surfaces is set to 200 centigrade. Air is assumed as the ambient.

A downward deformation can be observed during the simulation for beams with varying crosssections after grayscale lithography in Figure 3.4. This simulation result matches well with the observation during the experimental case study in Chapter 2. If the beam has a uniform crosssection, the baking tends to induce expansive isotropic deformation, as shown in Figure 3.5. The thermally-induced stress for both types of beams is concentrated around the clamping point. Such stress distribution could explain the relatively flat surface after the irreversible collapse observed in Chapter 2.

3.1.3 Inspirations for the calibration of SU-8 grayscale lithography

Grayscale lithography of standard SU-8 can produce suspended SU-8 microstructures. In such a case, it is difficult to use simple methods like a contact profilometer or white-light

interferometer to measure the intermediate thickness directly. SEM can do the task well, but the process is intricate. Suppose final structures can be intentionally collapsed to the substrate through proper mask design and hard baking. In that case, it becomes possible to use contact-based methods or white light interferometry to establish the relationship between crosslinked thickness and exposure dose, significantly reducing the difficulty of the calibration process for grayscale lithography.

3.2 A simple calibration method for SU-8 grayscale lithography

3.2.1 Design of the calibration method

A new calibration method for SU-8 grayscale lithography has been developed here. Its generic flow is illustrated in Figure 3.6.

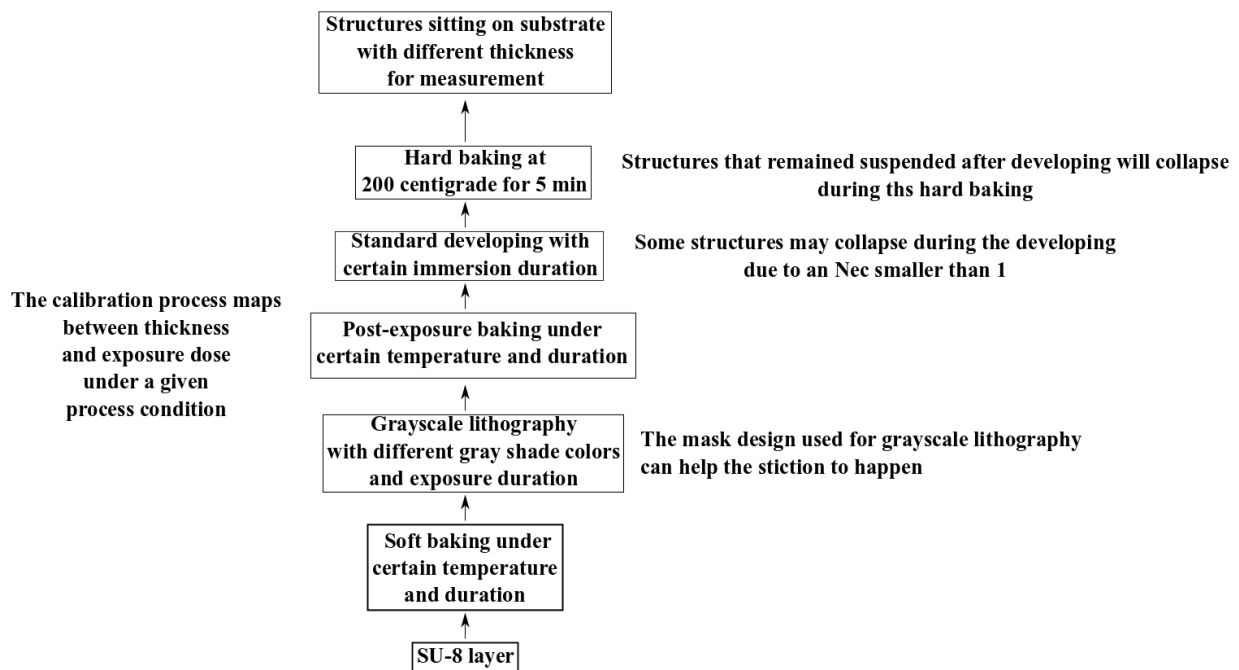


Figure 3.6 General flow of the new calibration method for SU-8 grayscale lithography

The core idea of the new calibration method is to make structures collapse onto the substrate. The two mechanisms studied in Section 3.1 are used to ensure the collapse. Masks are

designed in a specific way to promote stiction during the developing phase. If structures remain suspended after the developing process, hard baking will make them collapse to the substrate. Then simple measurement can be done at the central part of the collapsed structures for the thickness. One type of mask for this new calibration method is shown in Figure 3.7.

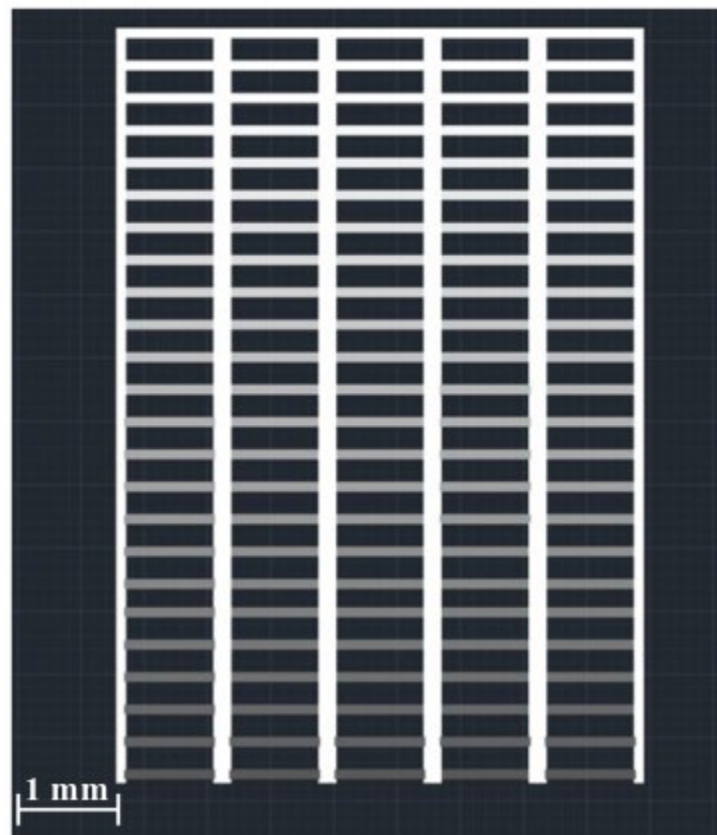


Figure 3.7 An example of mask designs for the newly-developed calibration method of grayscale lithography

The mask design in Figure 3.7 consists of doubly-clamped beams that are 20- μm wide and 1000- μm long. The length is limited by the maximum useable area of the DMD. Longer beams would have part of them exposed twice, impacting the accuracy of the calibration. The gray shade levels range from 88 to 255, with an interval of 8. Five calibration structures will be manufactured for each grayscale level. The average of their thickness measurement is mapped to the grayscale-

modulated exposure dose. The mathematical relationship established and validated in Chapter 2 can be used to compute the exposure dose.

3.2.2 Experimental set up to validate the new calibration method

The recipe used to validate the designed calibration method is shown in Table 3.3.

Substrate	<100> Silicon wafer	
Spin-coating speed	Spin-coating Speed (RPM)	Increment:
	1000 to 2600 rpm (SU-8 2015)	300 rpm
Soft baking	Temperature (°C)	Duration (min)
	95	3
Unmodulated intensity(mW/cm²)	10	
Exposure time	Exposure time (s)	Increment (s)
	3.5 s to 8.5	0.5
Post-exposure baking	Temperature (°C)	Duration
	95	5
Developing	Immersion duration in PGMEA (min)	
	6	
Hard baking	Temperature (°C)	Duration (min)
	250	5

Table 3.3 Recipe of SU-8 grayscale lithography process to validate the calibration method

Achievable SU-8 layers thickness using the spin-coating process in Table 3.3 ranges from 12 μ m to 27 μ m. The samples are first inspected optically under a microscope. Then, their thickness

is measured using a Bruker® Dektak stylus profiler. The measurement is done around the beams' center point to minimize the random errors resulting from the customized lithography process.

N_{EC} values of the test structures made by experimental conditions in Table 3.3 have been estimated. The result is plotted in Figure 3.8.

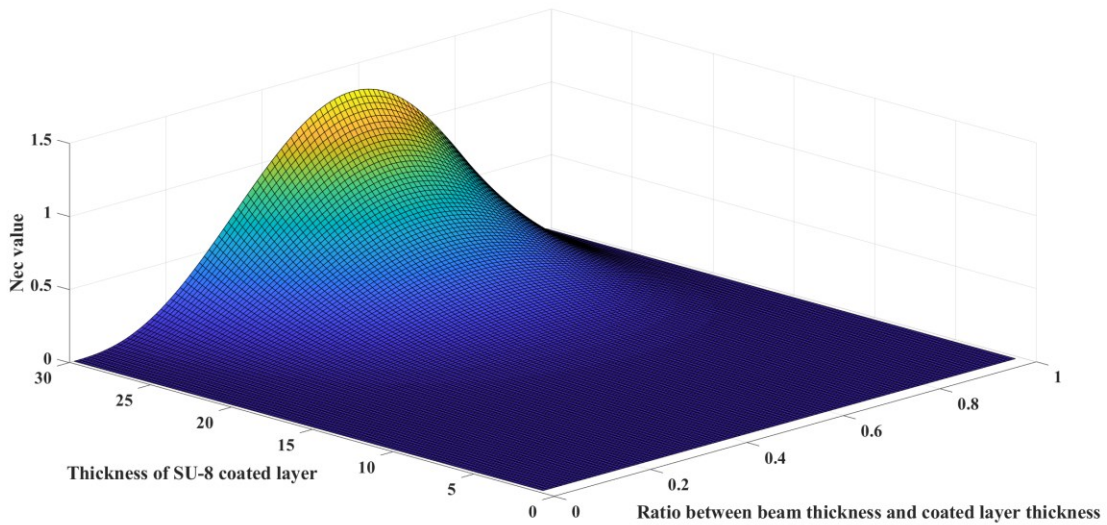


Figure 3.8 Computed N_{EC} values for the calibration structures during the experimental case study

The computation conducted in Figure 3.8 assumes that the coated thickness ranges from $0\mu\text{m}$ to $30\mu\text{m}$, with a $1\mu\text{m}$ step increment. This setup can keep the layer thickness values used in the experimental case study well-included in the computation. The crosslinked thickness is assumed to range from 0% to 100% of the coated thickness, with a 1% step increment. Such a setup is also reasonable. At this moment, the crosslinked thickness resulted from grayscale-modulated exposure dose is unknown. The computation needs to be comprehensive enough so that the thickness resulted from the experimental case study can be included.

In Figure 3.8, the N_{EC} value reaches its peak when the doubly-clamped beam's thickness is around 45% of the total coated thickness, and this maximum value increases with the layer

thickness. When the spin-coated SU-8 layer is thicker than 25 μm , the maximum N_{EC} value will be larger than 1. The 1000- μm long, 20- μm wide beams fabricated with these layers will remain suspended after the developing process. The computation result in Figure 3.8 indicates that the mask design in Figure 3.7 and the process recipe in Table 3.3 are suitable to evaluate the effectiveness of the new calibration method, particularly the effectiveness of the method to collapse test structures for simpler thickness measurement.

3.2.3 Qualitative predictions of the experimental case study

Three predictions for the experimental setup in Table 3.3 have been made to evaluate the newly-developed calibration method's effectiveness. All of them are related to the calibration curves' profile for intermediate doses between D_0 and D_f .

First, if all structures collapse to the substrate as expected, the thickness measurement should be a monotonically increasing function of the doses. Otherwise, the thickness measurements for some intermediate exposure dose values will be close to the coated layer thickness, forming an abnormal 'plateau' on the measurement curve.

Secondly, a reduction in curve slope should be observable when the exposure doses approach D_f . In such a case, homolysis in the upper layer starts to happen more and more frequently. Extra energy from UV radiation will be needed to push the boundary of photolysis towards the substrate. Even after the photolysis boundary reaches the substrate, the swelling effect during the developing step can still reduce the thickness of final structures by washing away weakly-crosslinked monomers. These two factors will reduce the slope of the calibration curve.

Thirdly, for all coated layers, the D_0 and D_f values are expected to be close. In Table 3.10, different layers have used the same soft baking conditions. The 3-minute baking is sufficient for the thinner layers according to the datasheet from Kayaku Advanced Material, but it will result in

additional solvent residuals for the thicker ones. The residuals help generate more photoacids, which can be viewed as an increment in photoresist sensitivity to the exposure dose [91]. This increased sensitivity for thicker layers will exhibit in the format of a reduced D_0 on the calibration result, making it close to the value for thinner layers.

3.3 Characterization result and discussion

3.3.1 Optical inspection

Figure 3.9 presents the calibration structures under the microscopic inspection.

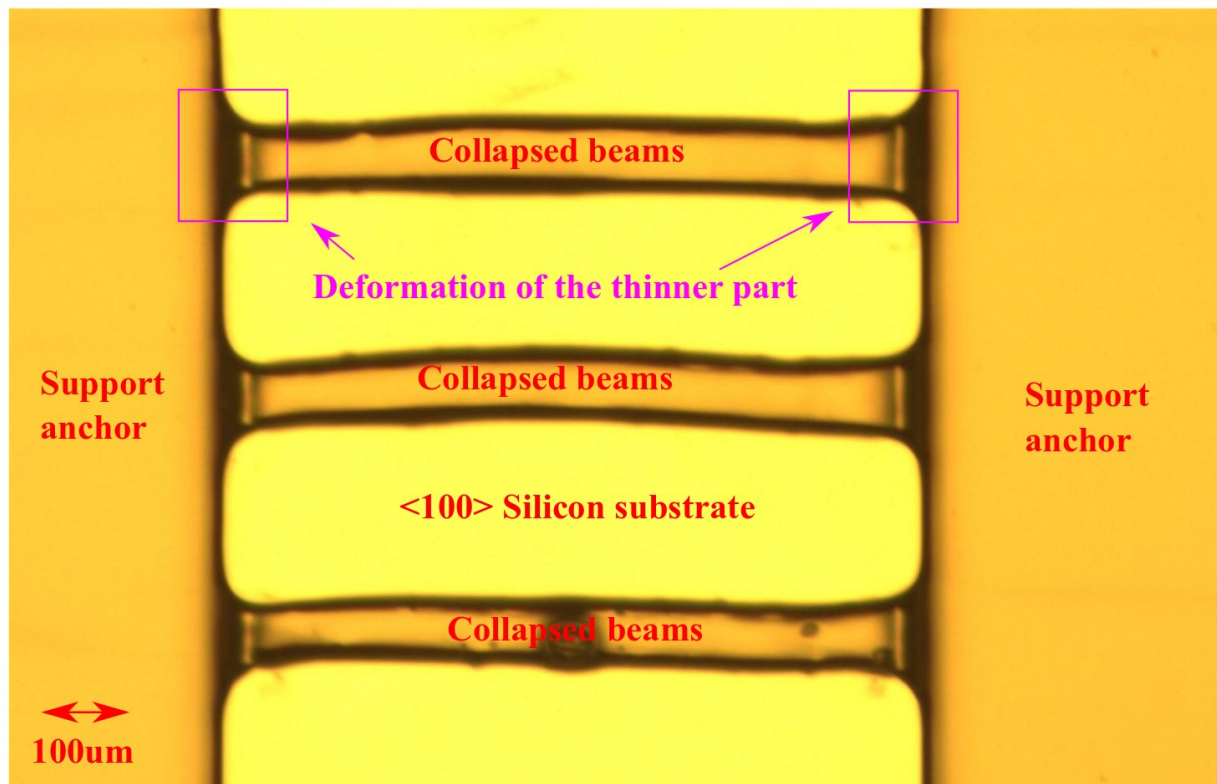


Figure 3.9 Examples of doubly-clamped beams fabricated by SU-8 grayscale lithography for calibration.

In Figure 3.9, the doubly-clamped beams' optical brightness is at the same level as the anchors, indicating that the beams have collapsed to the substrate. Significant deformations can only be observed at the beams' parts close to the anchors within the pink frames, similar to the previous simulation results.

3.3.2 Thickness measurement

The thickness measurement results for all six SU-8 2015 layers are shown in Figure 3.10.

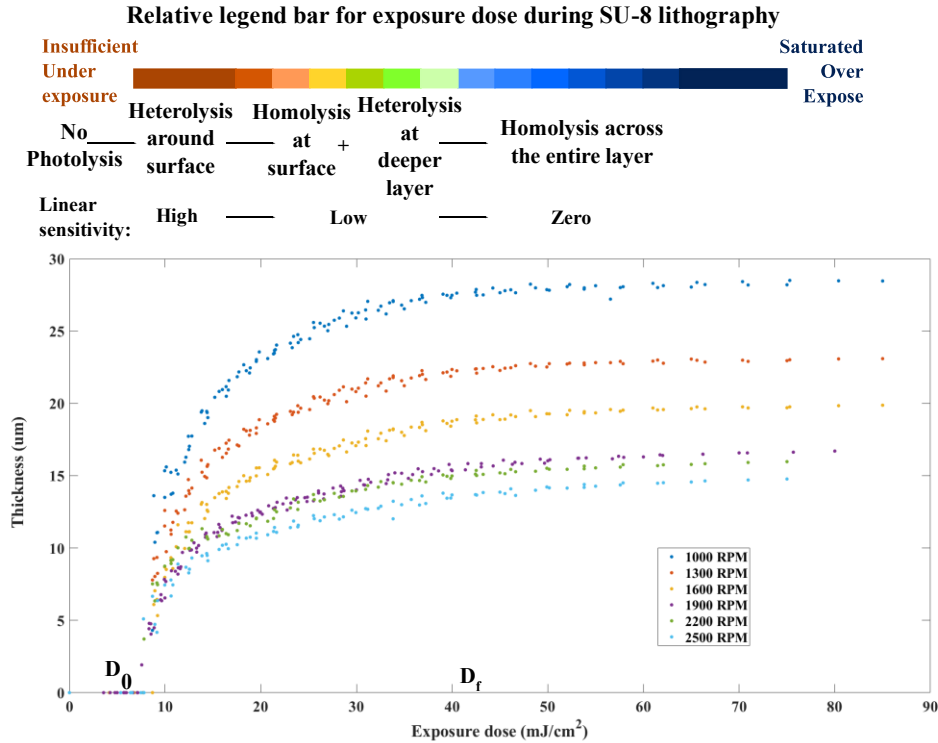


Figure 3.10 Thickness calibration result for grayscale lithography using SU-8 2015 spin-coated at different speed values.

In Figure 3.10, the dose thresholds (D_0 and D_f) are still observable in the calibration result. No crosslinking is happening when the exposure dose is smaller than D_0 . Exposure doses higher than D_f will also not induce further variation in crosslinked thickness. This constant thickness after D_f can be explained by the triplet homolysis. It results in the oversaturation of photoacids around the upper layer. The crosslinking strength during the post-exposure baking is enhanced, making the structures more robust against the geometric dimension reduction during the developing step.

All six calibration curves are monotonically increasing with doses between D_0 and D_f , validating that the combination of structural design and hard baking can effectively make the calibration structures collapse to substrates.

A significant reduction in slopes after a specific value can also be observed on all six curves. The six calibration curves have very similar D_0 and turning points of the slope. Since the experimental conditions in Table 3.3 leave more solvent in thicker layers, it is normal for these two phenomena to happen. They vividly reflect the significant impact of soft baking on the final result of the SU-8 lithography process.

All characteristics predicted in Section 3.2.3 have exhibited in Figure 3.10, supporting the effectiveness of the newly-developed calibration method. There are 792 measured thickness values. Their standard deviation distribution is plotted in Figure 3.11 to evaluate the process reproducibility.

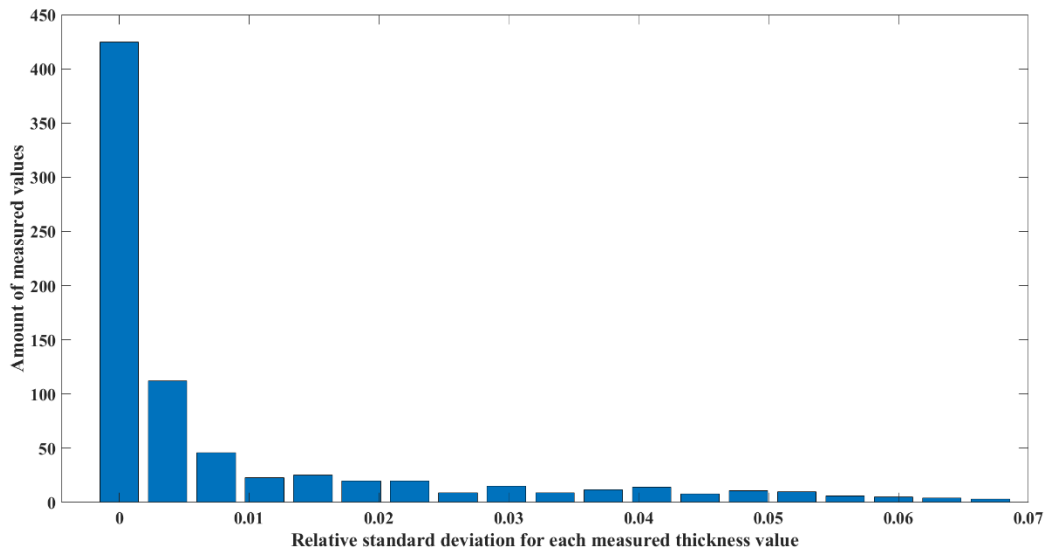


Figure 3.11 Distribution of standard deviation for the thickness measurement

In Figure 3.11, over 73% of the measured thickness values have a standard deviation of less than 1%. Over 99% of all the measured values have a standard deviation of less than 4%, demonstrating the new calibration method's reliability with respect to process reproducibility. The experimental result in Figure 3.11 also supports the conclusion that grayscale lithography of

standard SU-8 has consistent performance. In Chapter 2, a similar conclusion has been reached based on the standard deviation of measured natural frequency.

3.4 Summary

The research carried out in this chapter has taken a more detailed look into SU-8 grayscale lithography characteristics. Two phenomena observed in Chapter 2 have been explained. The collapse after the developing step has been explained by the stiction effect. The collapse during hard baking has been explained by the solid diffusion of photoacids, which resulted in the nonuniform crosssection of the final structures.

The mechanisms behind these two phenomena have been used in the grayscale lithography process to develop a simple calibration method. The effectiveness and robustness of this new method have been experimentally validated. This newly-developed calibration method makes it possible to develop and systematically evaluate new fabrication technologies based on grayscale lithography. The next two chapters will focus on the research work in this aspect.

Chapter 4: A new way to fabricate SU-8 out-of-plane MEMS structures

Chapter 4 presents a new fabrication technology for SU-8 out-of-plane MEMS structures. Achievements of previous chapters have been used in the development and validation of this new technology. Figure 4.1 illustrates the research work framework.

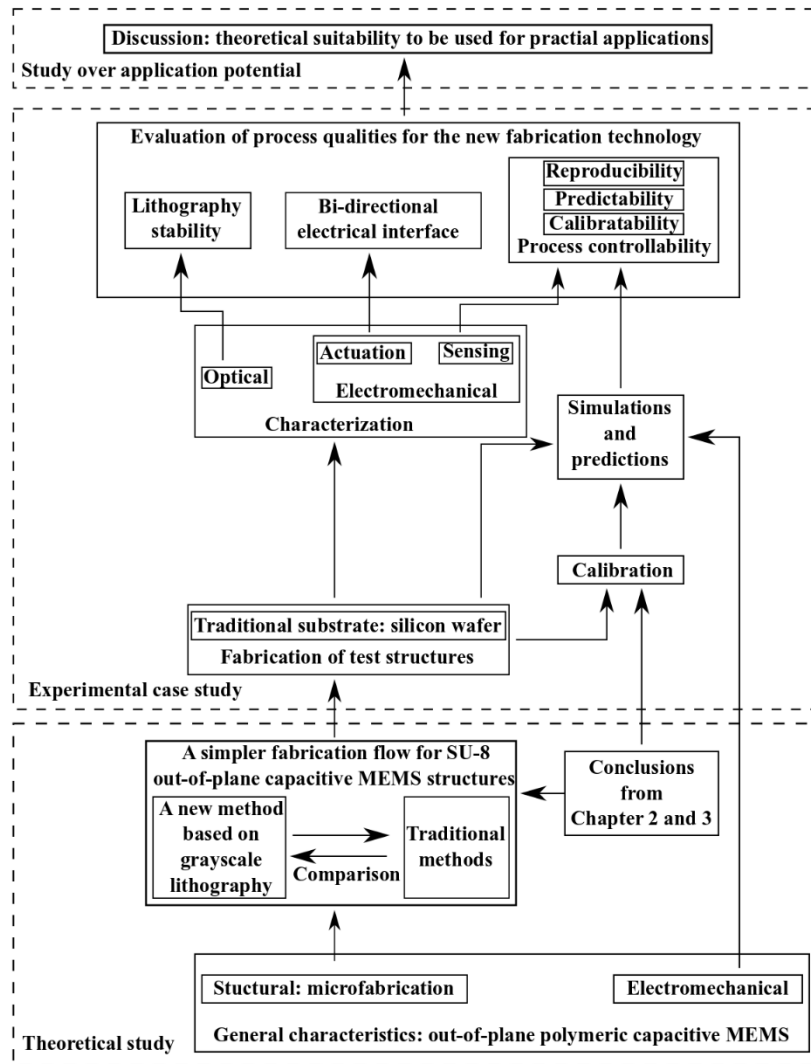


Figure 4.1 Illustration of the research work of Chapter 4.

As shown in Figure 4.1, Section 4.1 introduces the general characteristics of out-of-plane MEMS devices. Their structural configuration and electromechanical coupling are studied in

detail. Section 4.2 presents a new fabrication technology of SU-8 out-of-plane MEMS. This new fabrication technology uses grayscale lithography to create movable microstructures through a single lithography process directly. The fabrication technology developed in this chapter reflects a new ideology for SU-8 out-of-plane MEMS fabrication: replacing sacrificial layers with dose modulation. The experimental case study to validate this newly-developed fabrication technology is presented in Section 4.3. Characterization results are discussed in Section 4.4. Section 4.5 discusses the practicability of the new fabrication technology. Section 4.6 summarizes the accomplishment of this chapter.

4.1 General characteristics of SU-8 out-of-plane MEMS structures

4.1.1 Structure configuration

Out-of-plane MEMS structures move in the direction vertical to the substrates. They are primarily used for applications such as acoustic devices [46, 47, 50, 54, 62, 123], and pressure/tactile sensors [124-126]. SU-8 out-of-plane MEMS devices made by the classic surface micromachining method share some common characteristics, as shown in Figure 4.2.

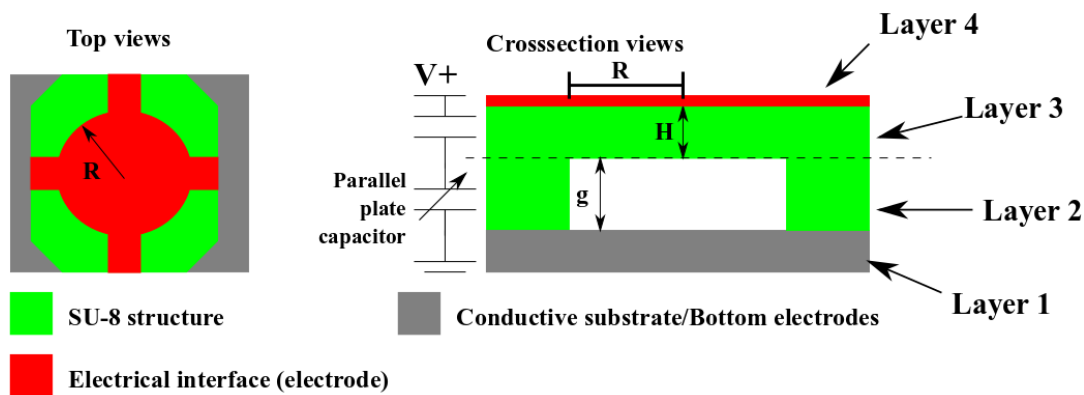


Figure 4.2 Schematic of a capacitive SU-8 out-of-plane MEMS structures.

These structures have at least four layers. The substrate has to be conductive, or there should be a conductive layer on the top surface as the bottom electrode, which is labeled as Layer

1 in Figure 4.2. A fixed layer is created on Layer 1 as the anchor, separating the movable components from the bottom electrode. This fixed layer is labeled as Layer 2 in Figure 4.2. A mechanically deformable/movable elastic layer, shown as Layer 3, is formed on the anchor layer. Since standard SU-8 is not conductive, a conductive layer is deposited and patterned as the top electrode on the top of Layer 3. It is Layer 4 in Figure 4.2. The electromechanical coupling capacitor of SU-8 out-of-plane MEMS structures is formed between the top and bottom electrodes. It consists of two capacitors in series. One of the capacitors uses the deformable SU-8 layer as the dielectric layer. It is a fixed capacitor. The other capacitor is a gap-varying capacitor with air as the dielectric media. Generally, the movable structures' aspect ratio is kept low to promote the motions vertical to the substrate and suppress the horizontal ones.

4.1.2 Electromechanical behaviors

The electromechanical behaviors of a capacitive MEMS device can be described by lumped reduced-order macro models, obeying the energy and electrical charge conservation laws [127, 128]:

$$\left\{ \begin{array}{l} \frac{d}{dt}(E_{capacitor}) = u(t)i(t) + f_{total}(t) \frac{dx(t)}{dt} \\ i(t) = C(t) \frac{du(t)}{dt} + \frac{dC(x)}{dx} u(t) \frac{dx(t)}{dt} \\ f_{electrical}(t) = -\frac{1}{2} \frac{dC(x)}{dx} u(t)^2 \\ m_{effective} \frac{d^2x}{dt^2} + b \frac{dx}{dt} + k_M x = f(t) \end{array} \right. \quad (4.1)$$

In Eq(4.1), the first equation describes energy conservation during the electromechanical coupling. $E_{capacitor}$ is the energy stored in the MEMS capacitor. $u(t)$ is the electrical potential between the capacitor. $i(t)$ is the electrical current. $f_{total}(t)$ is the mechanical force, and $x(t)$ is the mechanical displacement. The second equation is for electrical charge conservation. The third equation is

derived by replacing $i(t)$ in the first equation with the second equation. It describes the electrostatic force generated during the coupling. $C(x)$ is the variable capacitance. The last equation describes the mechanical behavior of the capacitive MEMS structures with reduced macro modeling. In this equation, $m_{effective}$ is the effective mass of the MEMS structure; b is the viscous damping coefficient, k_M is the mechanical spring constant.

Generally, the gap-varying capacitor of an out-of-plane capacitive MEMS structure is expressed as:

$$\begin{cases} C = C_0 \left(1 + \frac{x}{g_0}\right)^{-1} \\ C_0 = \frac{\varepsilon A}{g_0} \\ \frac{dC}{dx} = -\frac{C_0}{g_0} \left(1 + \frac{x}{g_0}\right)^{-2} \end{cases} \quad (4.2)$$

In Eq(4.2), ε is the dielectric constant; A is the overlapping area; g_0 is the gap between the parallel plates; x is the displacement responsible for the gap variation. Eq(4.2) assumes that the whole parallel plate is movable. This mathematical model is accurate for some devices, such as in-plane MEMS devices with a rigid mass. The detail about them will be introduced in Chapter 6. If the devices are out-of-plane, gap-varying capacitive MEMS, only the movable plates' central part will have significant deflection. The area of the variable capacitor is also changing. Eq(4.2) can only be used as a practical approximation.

Nevertheless, this Ph.D. thesis is focused on the fabrication technology and its performance, not the modeling of a specific type of MEMS device. Eq(4.2) is still usable. The expression for the electrostatic force generated on the MEMS structure can be obtained by putting Eq(4.2) into the third equation of Eq(4.1):

$$F = -\frac{1}{2} \frac{C_0}{g_0} \left(1 + \frac{x}{g_0}\right)^{-2} u^2(t) \quad (4.3)$$

In Eq(4.3), the electrostatic force, F , has a non-linear relationship with the displacement x , complicating the equilibrium between mechanical elastic force and the electromechanical force.

The electrostatic force generated on the coupling capacitor can only be balanced by the mechanical elastic force within a limit. When the voltage exceeds a threshold, the equilibrium is no more maintainable. The movable plate of the electromechanical coupling capacitor will run into the fixed plate. When the voltage is below this threshold, the movable plate undergoes displacement, reaching an equilibrium point. The equivalent mechanical spring coefficient of the out-of-plane MEMS structure is reduced after reaching the equilibrium point. The magnitude of the reduction has a positive dependence on the voltage level. The equivalent spring constant reduces to zero when the voltage reaches the aforementioned threshold.

The limited equilibrium and the decreased equivalent mechanical spring are defined as the ‘pull-in’ effect and the electrostatic softening effect for gap-varying capacitive MEMS devices [127, 129]. The voltage threshold is defined as the pull-in voltage. The mechanical displacement induced by pull-in voltage is defined as pull-in displacement. The pull-in voltage and displacement can be computed by:

$$\begin{cases} u_{pull-in} = \sqrt{\frac{8g_0k^2}{27C_0}} \\ x_{max} = \frac{1}{3} g_0 \end{cases} \quad (4.4)$$

When the voltage applied is below the pull-in voltage, the softened equivalent mechanical spring can be computed through linearization at the equilibrium point [130, 131]:

$$k_{eq} = k_M - \frac{1}{2}(u^2) \left. \frac{d^2C}{dx^2} \right|_{x=x_0} \quad (4.5)$$

In Eq (4.5), x_0 is the displacement of the movable plate to reach equilibrium.

Eq(4.4) is suitable for out-of-plane MEMS devices made by conductive materials. The expressions of pull-in voltage and displacement for SU-8 out-of-plane MEMS devices have to consider the difference in their coupling capacitor expression. The coupling capacitor for SU-8 out-of-plane MEMS devices is expressed as:

$$\begin{cases} C(x) = \frac{C_{air} C_{SU-8}}{C_{SU-8} + C_{air}} \\ C_{SU-8} = \frac{\epsilon_{SU-8} A_0}{t_0} \\ C_{Air} = C_0 \left(1 + \frac{x}{g_0}\right)^{-1} \\ C_0 = \frac{\epsilon_{Air} A_0}{g_0} \\ \frac{dC}{dx} = -\frac{C_0}{g_0} \left(\frac{x}{g_0} + 1 + \frac{C_0}{C_{SU-8}}\right)^{-2} \end{cases} \quad (4.6)$$

In Eq(4.6), ϵ is the dielectric constant; A_0 is the overlapped area; g_0 is the original distance between the two parallel plates; t_0 is the thickness of the SU-8 layer; x is the displacement (positive direction: vertically up); C_{SU-8} is the fixed capacitor; C_{Air} is the variable capacitor; C_0 is the initial value of the variable capacitor. Correspondingly, the analytical expression for pull-in voltage and displacement of SU-8 capacitive out-of-plane MEMS structures are:

$$\begin{cases} x = \frac{g_0}{3} \left(1 + \frac{C_0}{C_{SU-8}}\right) \\ u_{pull-in} = \sqrt{\frac{8kg_0^2}{27C_0} \left(1 + \frac{C_0}{C_{SU-8}}\right)^3} \end{cases} \quad (4.7)$$

The pull-in voltage and displacement of SU-8 out-of-plane MEMS devices are controlled by the air gap g_0 and the ratio between the two coupling capacitors connected in series.

4.2 A new fabrication method for SU-8 out-of-plane capacitive MEMS

4.2.1 The traditional method to make SU-8 out-of-plane MEMS structures

Currently, surface micromachining is the most common method to fabricate SU-8 out-of-plane MEMS devices [46, 47, 50, 54, 62, 123-126, 132, 133]. The schematic for this traditional processing flow is illustrated in Figure 4.3.

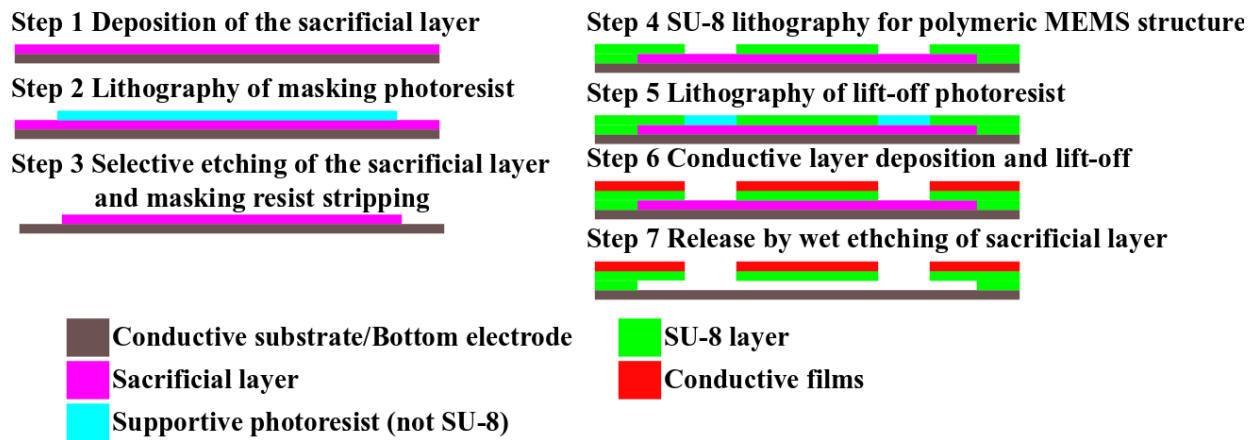


Figure 4.3 Surface micromachining for capacitive SU-8 out-of-plane MEMS transducers.

Figure 4.3 shows that the layer-by-layer SU-8 surface micromachining repeats the ‘deposition-lithography (masking)-etching’ cycles to define a sacrificial layer. SU-8 lithography is carried out afterward. The sacrificial layer is etched after the metallization process to release the final structure. The representative application of this surface micromachining flow in Figure 4.3a includes the fabrication of polymeric CMUTs, on both silicon wafers (rigid substrates) and polyimide films (flexible substrates) [46, 47, 50, 51, 54].

The layer-by-layer SU-8 surface micromachining relies on sacrificial layers to achieve the movable microstructures. As discussed in Chapter 1, the usage of sacrificial layers has inevitably resulted in process complexity and uncertainty in process controllability.

If SU-8 out-of-plane capacitive MEMS structures can be fabricated in a controllable manner without using any sacrificial layers, it would, for sure, significantly alleviate the problems mentioned above. Grayscale lithography of standard SU-8 is very promising in this perspective.

4.2.2 A new Fabrication method using grayscale lithography

The author has developed a sacrificial-layer-free fabrication technology for out-of-plane SU-8 MEMS structures, using the research conclusions from Chapter 2 and Chapter 3. The generic flow of this new method is shown in Figure 4.4.

Step 1 Grayscale lithography to form polymeric microstructures



Step 2 Laser micromachining of polyimide thin film for shadow masks



Step 3 Hard mask based selective deposition of conductive layers



Final out-of-plane MEMS structures:



- | | |
|--|---|
|  Conductive substrate/Bottom electrode |  Polyimide thin film |
|  SU-8 polymeric MEMS structures |  Conductive materials |

Figure 4.4 Illustration of the newly-designed fabrication flow for out-of-plane SU-8 MEMS structures

In Figure 4.4, the new fabrication flow takes only three steps to fabricate SU-8 out-of-plane MEMS structures, removing three steps related to the processing of sacrificial layers in the classic SU-8 micromachining flows.

The metallization in Figure 4.4 has adopted a method based on physical shadow masks. The method minimizes the risk of stiction-related failures. SU-8 structures manufactured by the new method are already suspended after the grayscale lithography process. The study in Chapter 3 has revealed that these suspended structures may suffer from the stiction effect when exposed to complex fluidic conditions, such as the spin-coating process of the photoresist solution for metallization based on lift-off. The stiction effect reduces the yield of the fabrication technology. In contrast, metallization using shadow masks is a purely dry process with no other liquid involved.

MEMS fabrication industry has validated the reliability of shadow-mask-assisted metallization. Traditionally, shadow-mask-assisted metallization is mainly used in the industrialized fabrication technology for silicon MEMS devices, like SOIMUMPs [9].

Here, the shadow masks for metallization are manufactured by the one-step laser micromachining of polyimide thin films. Making shadow masks in polyimide avoids using the silicon bulk micromachining process, reducing the cost. Using a laser beam to cut the polyimide avoids using the corrosive wet etchant and high temperature, increasing the process safety. Existing attempts doing laser cutting of polyimide have found the process efficiency to be acceptable [134, 135]. Polyimide has a low degradation temperature. The laser dot can quickly penetrate the material, creating open windows on a polyimide sheet. The alignment of the shadow mask is also simple. It can be implemented by a contact mask aligner or by hand if alignment accuracy is not critical.

4.3 Experimental case study of the newly-developed microfabrication technology

The newly-developed fabrication technology has been experimentally evaluated and validated through the fabrication and characterization of arrays of SU-8 circular membranes. The

fabrication was conducted on the polished surface on <100> silicon wafers. They are the optimum substrate for the SU-8 lithography process.

4.3.1 Design of the fabrication process

The process parameters and the designs of test structures are summarized in Table 4.1.

Lithography process parameters					
UV intensity from the light source	Soft baking temperature	Soft baking duration	Exposure duration	Post-exposure baking temperature	Post-exposure baking duration
10 mW/cm ²	95°C	3 min	7.5 s	95°C	5 min
SU-8 test structures: Circular membrane					
SU-8 type	Coated thickness	Radius		Amount	
SU-8 2010	~10.5µm	50µm		1500	
Shadow masks					
Polyimide thickness	Laser relative output		Repeated times	Laser moving speed	
12 µm	100%		20	1 mm/s	
Metallization					
Metal type			Thickness		
Aluminum			200 nm		

Table 4.1 Process parameters and structure design for application potential validation on silicon

In Table 4.1, the soft baking duration is shorter than the one recommended on the datasheet to enhance the mechanical strength after grayscale lithography.

An SF-100 maskless lithography system was used for the SU-8 grayscale lithography process.

An Oxford[®] laser micromachining system was used to create the polyimide thin-film shadow masks.

The alignment of the shadow mask with the membrane arrays was done using a contact mask aligner. 200 nm Aluminum was deposited onto the surface of the SU-8 MEMS structures using an E-beam evaporation. The software masks are shown in Figure 4.5.

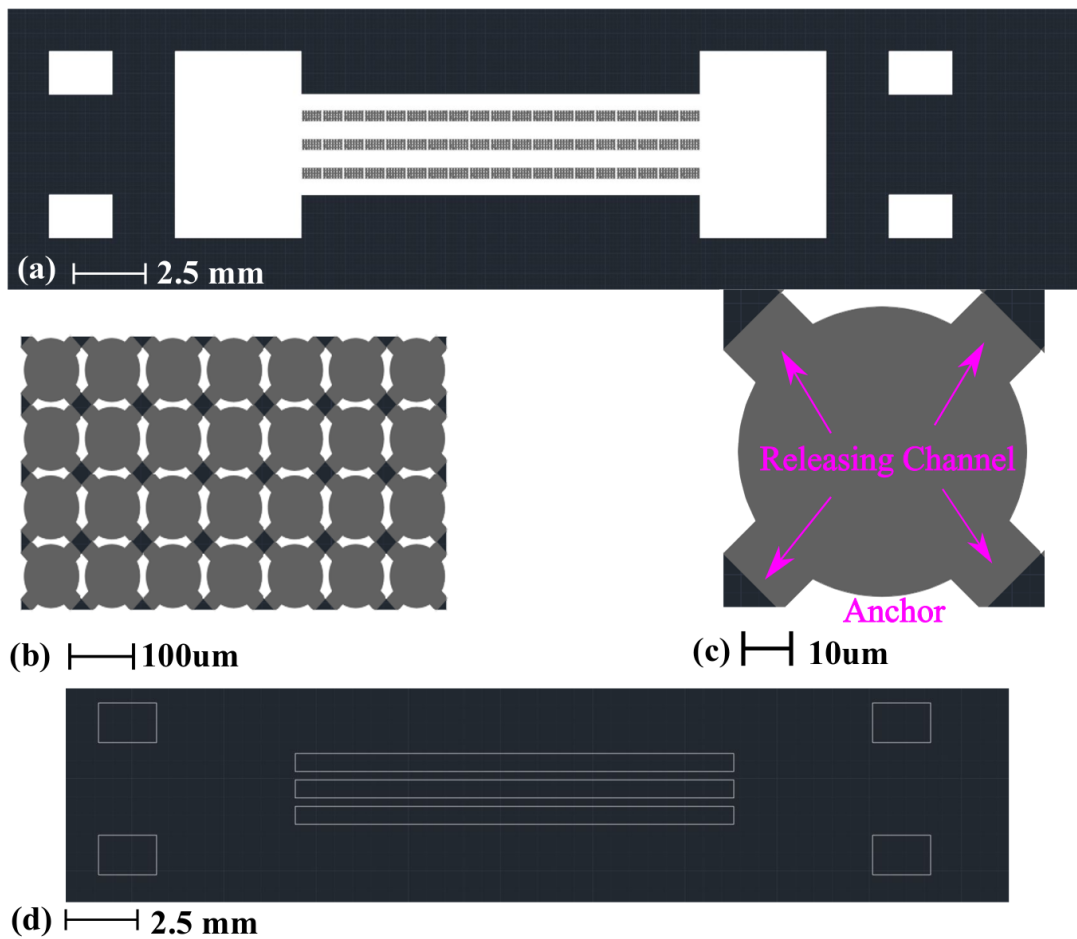


Figure 4.5 Mask designs for the experimental validation. (a) Overview of the mask for 1500 circular membranes. (b) Representative demonstration of the arrangement of the membrane arrays. (c) Design of a single cell. (d) The mask for the laser ablation of polyimide.

In Figure 4.5a, four rectangles are placed at the four corners of the mask files to align the shadow masks. The grayscale level for the circular membranes has been set to 96. The modulation effect of the gray shade design is estimated to be 14%, using the model established in Chapter 2. Four rows of circular membranes are grouped into one element. Rectangular patterns are designed at the four corners of the membranes. They allow the PGMEA to contact and dissolve the uncross-linked SU-8 underneath the crosslinked layers. During the laser ablation, the laser dot is moved along the profiles of the designs to create the open windows for Al deposition.

4.3.2 Lithography calibration

The grayscale lithography recipe in Table 4.1 has been calibrated, with the result shown in Figure 4.6.

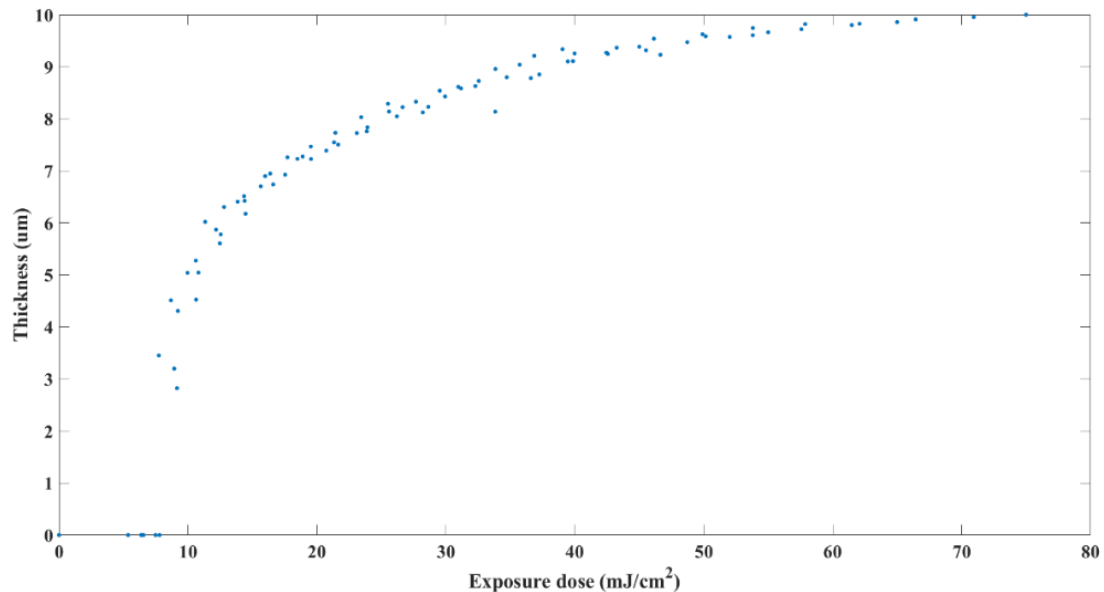


Figure 4.6 Lithography calibration result for the thickness values used for out-of-plane transducer fabrication on silicon wafers.

The calibration curve in Figure 4.6 is very similar to the calibration result shown in Chapter 3. The crosslinked thickness of the circular membranes is predicted to be about 4.25 um.

4.3.3 Simulation and computations for process quality evaluation

Computations and simulations are carried out using the calibration result and designed radius. Their results are used to evaluate the process predictability of the new fabrication method. The values of SU-8 material properties used are summarized in Table 4.2.

Property	Density	Young's modulus	Poisson's ratio	Relative dielectric constant
Value	1200 kg/m ³	4.95 GPa [29, 30]	0.32[31]	4 [34]

Table 4.2 SU-8 material properties used in FEA simulation

The final status (suspended or collapsed) for the circular membranes is predicted based on the N_{EC} number, the constant introduced in Chapter 3. The N_{EC} number for circular plates is [117, 136]:

$$N_{EC} = \frac{10}{9} \left(\frac{5}{2} \right)^{\frac{2}{3}} \frac{Eh^2t^3}{\gamma_1 \cos \theta r^4 (1-\nu^2)} \left[1 + \frac{3(1-\nu^2)}{4} \frac{\sigma_R r^2}{Et^2} + \frac{2187}{2560} \left(\frac{2}{5} \right)^{\frac{2}{3}} \frac{h^2}{t^2} \right] \quad (4.8)$$

In Eq(4.8), E is Young's modulus of crosslinked SU-8; γ_l is the surface tension of IPA; θ is the contact angle of IPA; h is the suspended gap of the membrane; t is the thickness of the membrane; ν is Poisson's ratio of SU-8; σ_R is the residual stress remaining in the structures. The N_{EC} value for the circular membranes to be manufactured has been computed as 370.10. Because the circular membranes have an N_{EC} number significantly larger than 1, they are estimated to be suspended after the SU-8 grayscale lithography.

The fundamental mechanical resonant frequency and the equivalent mechanical spring constant (intrinsic) of the circular MEMS test structures were simulated by finite element analysis (FEA) method, using COMSOL Multiphysics™ 5.3. The FEA simulation result is shown in Figure 4.7.

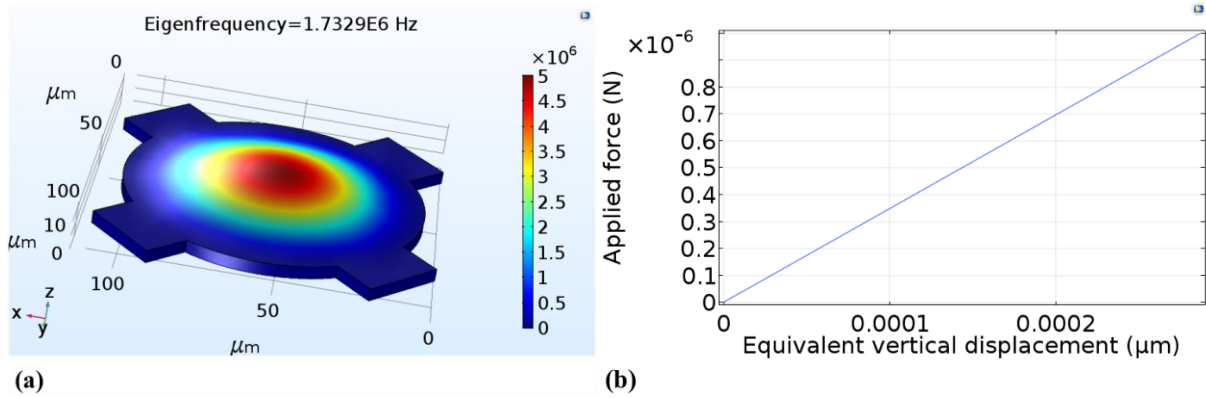


Figure 4.7 FEA simulation results for the circular membranes fabricated. (a) The simulated fundamental resonant frequency: 1.73 MHz. (b) The parametric sweep between applied force and the deflection at the center of the membranes derived equivalent spring constant: 3487 N/m.

The pull-in effect and the electrostatic softening effect on equivalent mechanical springs are also estimated. The relationship between the equivalent mechanical spring of a single circular membrane and the electrical voltage level has been computed by MATLAB 2017 and plotted in Figure 4.8.

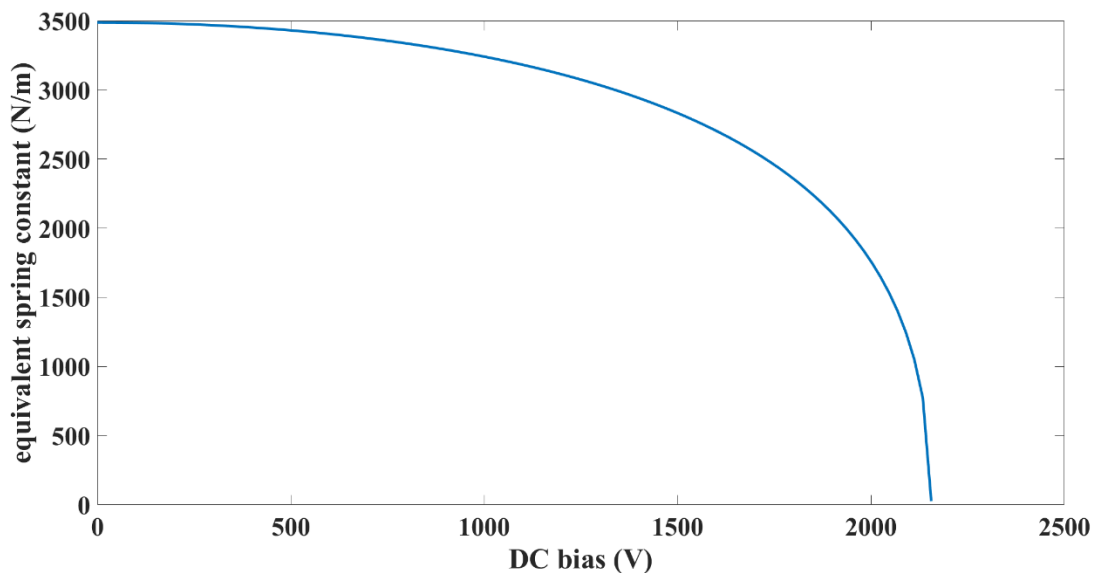


Figure 4.8 Relationship between equivalent mechanical spring constant and electrical voltage

The computation used the whole membrane area for the coupling capacitor. This method has been used somewhere else to simplify the computation while maintaining certain accuracy simultaneously [137, 138]. As shown in Figure 4.8, the pull-in voltage is around 2.1 kV for the circular membranes. Electrical voltage below 500 V barely results in any softening effect, and the mechanical displacement of the membranes to reach equilibrium can be approximated to zero. When the actuation signal's DC bias is smaller than 500V, the measured resonant frequency under electrical actuation should be close to the natural frequency in Figure 4.7a, with minor decrement as the voltage increases. Such measurement can be used to evaluate process predictability.

4.3.4 Characterization methods

Optical characterizations have been conducted after the grayscale lithography and after the metallization process. Samples were inspected under a yellow-light microscope to confirm the final status of the fabricated structures. The optical inspection results provide information about lithography *stability*.

Two methods were used to characterize the electromechanical coupling behavior of the fabricated structures. The mechanical resonance under electrical actuation was measured to evaluate process controllability, while the electrical impedance under electrical actuation was measured to check the existence of a bi-directional electromechanical coupling interface.

The mechanical resonance measurement has used the Laser Doppler Vibrometer module of a Polytec[®] MSA-500 system. 56 out of the 1500 fabricated circular test structures were selected to measure the mechanical resonant frequency. The electrical actuation signals have been tuned in two ways during the measurement. First, the DC component of the electrical actuation signals was tuned from 40V to 240V. The peak-to-peak amplitude of the AC component (periodic chirp signal) was kept at 2V. This set of measurements check the actual electrostatic softening effect on the test

structures. Then, the DC component was kept at 40V to measure the mechanical resonant frequency of the selected circular membranes, aiming to evaluate the *newly-developed fabrication process's predictability and reproducibility*.

The measurement of electrical impedance magnitude has used an Agilent A4294A impedance analyzer. The total impedance of 1500 membranes was measured. The impedance measurement examines the existence of the mechanical-to-electrical interface, supporting the *usability* of the newly-developed fabrication technology.

4.4 Characterization result and discussion

4.4.1 Yellow light microscopic inspection

The representative result of yellow light microscopic inspections for the fabricated SU-8 membranes is shown in Figure 4.9.

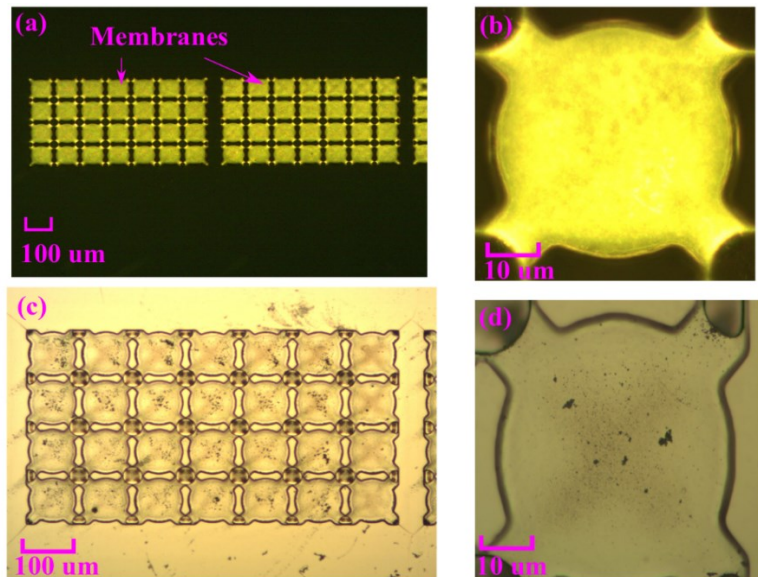


Figure 4.9 Microscopic inspection of the SU-8 circular membrane arrays fabricated on a silicon wafer. (a) Part of the array after grayscale lithography. (b) A single cell after grayscale lithography. (c) Part of the array after the metallization process. (d) A single cell after the metallization process.

In Figure 4.9a and 4.9b, darkfield microscopy has been used to amplify the difference in optical brightness difference. The membranes are significantly brighter than the fixed structures, and this brightness difference can be replicated stably among the test structures. Being optically brighter than the fixed structures indicates that the membranes have been suspended after the SU-8 grayscale lithography stably.

In Figure 4.9b, no cracks can be observed on the surface of the individual diaphragm, indicating sufficient crosslinking density and strength. In Figure 4.9c and 4.9d, the metal film's relatively smooth surface indicates that acceptable deposition quality.

4.4.2 Measurement of mechanical resonance during the electrical actuation

The measurement result of mechanical resonance under electrical actuation is shown in Figure 4.10.

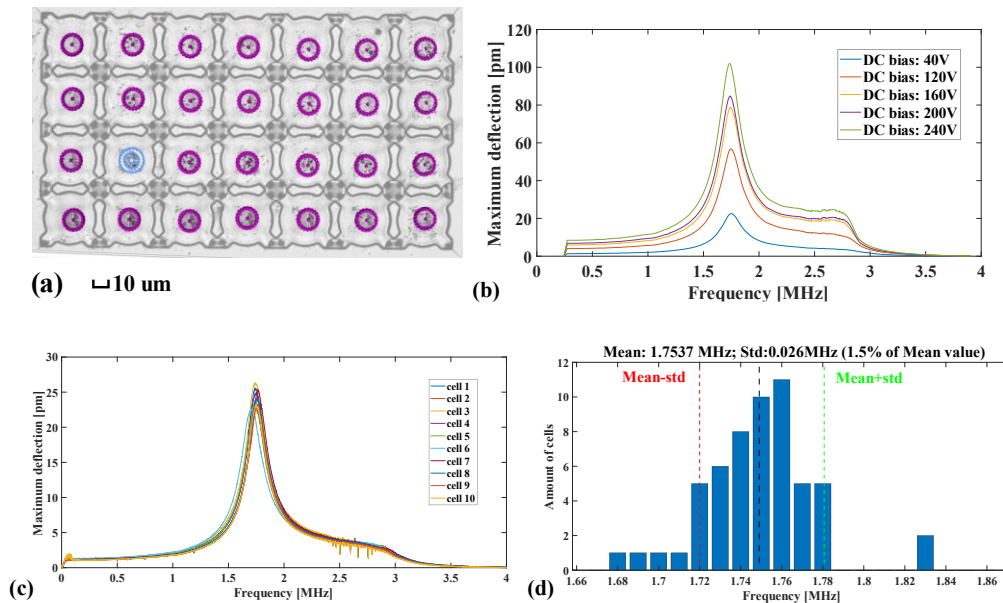


Figure 4.10 Electrical-mechanical actuation and the measurement result. (a) Setup of the multi-point measurement for 28 membranes. (b) The DC sweep result for the 56 measured membranes. (c) Comparison of measurement results for ten individual cells. (d) The statistical information of the measured resonant frequency for the 56 circular membranes.

The data in Figure 4.10 is the frequency-domain measurement result directly extracted from the LDV. Before any conclusion can be drawn regarding process predictability and reproducibility, it is necessary first to evaluate the cogency of the frequency-domain measurement obtained from the LDV. The possibility that the peaks on the frequency-domain measurement result from noise must be excluded. Time-domain excitation signals and output signals have been extracted for frequency modal analysis and coherence analysis in MATLAB 2017, with the representative result shown in Figure 4.11.

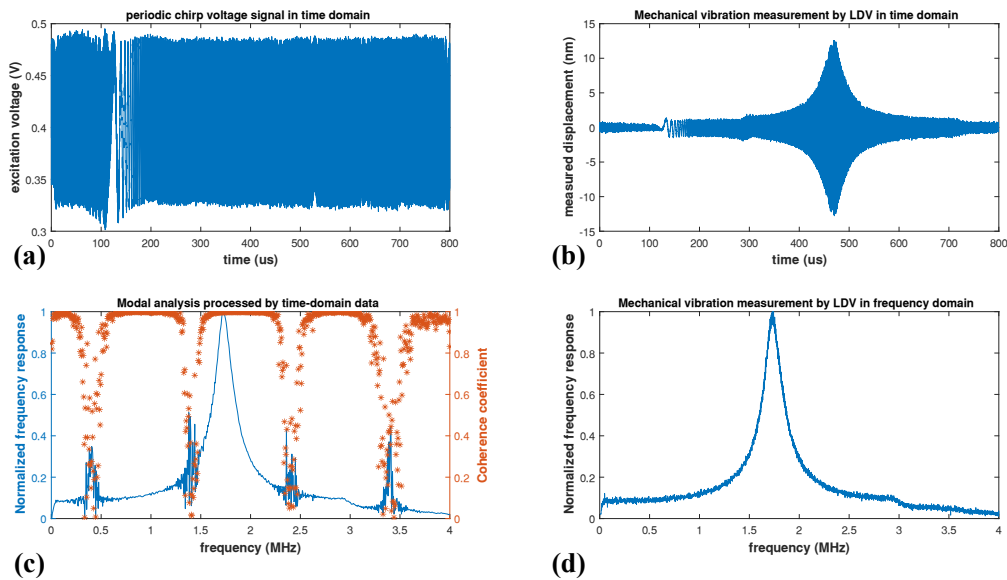


Figure 4.11 Representative result for the frequency modal analysis and coherence analysis of the measurement obtained from the LDV. (a) The excitation signal in time-domain; (b) The mechanical resonance response in time-domain; (c) Frequency modal analysis and coherence analysis of the time-domain data; (d) Frequency-domain measurement directly extracted from the LDV.

As shown in Figure 4.11, there do exist peaks corresponding to noises and other distortions in the frequency modal analysis of the time-domain data. This conclusion is supported by the fact that these peaks' coherence coefficient drops to a value close to zero. In contrast, the peak in Figure 4.11c for the natural frequency has its coherence coefficient being almost one. As shown in Figure

11d, the peaks corresponding to noises have been eliminated in the frequency-domain measurement extracted from the LDV. This difference from the modal frequency analysis in Figure 4.11c demonstrates that the Polytec[®] MSA-500 laser Doppler vibrometer has some built-in functionalities to exclude noise disturbance on the frequency-domain measurement result. The peak on the extracted measurement result can be considered natural frequencies related to the material properties and geometric dimensions. In this context, the measurement results shown in Figure 4.10 can be used to evaluate process qualities.

Figure 4.10a shows the setup to measure the mechanical resonant frequency. The measurement is fully automated point-to-point scanning. After the scanning is done, the points on a single membrane are selected to extract that membrane cell's corresponding vibration-frequency spectrum. The blue ones in Figure 4.10a are the selected points.

When DC bias increases, it can be observed in Figure 4.10b that the reduction in the average resonant frequency is minor. The measured resonant frequency values have been 1.754 MHz (40V), 1.747 MHz (80V), 1.743 MHz (120V), 1.742 MHz (160V), 1.740 MHz (200V), and 1.736 MHz (240V). The actually-negligible variation means that the actual electrostatic softening effect is minor, matching well with the prediction in Figure 4.8.

Figure 4.10c presents the comparison of measured profiles for ten randomly selected membranes. The DC bias has been kept at 40V for the measurement. The similarity among the profiles measured from the same actuation condition demonstrates the *reproducibility* of the fabrication process. This conclusion is further supported by the statistical information related to the measured resonant frequency in Figure 4.10d. The average frequency of 56 circular membranes is about 1.75MHz, with a 1.5% standard deviation.

The relative error between the simulated frequency and the average value of the measurement is 1.2%. This minor difference demonstrates good process *predictability* of the newly-developed fabrication technology.

4.4.3 Electrical impedance measurement during the electrical actuation

The frequency-domain measurement result for the electrical impedance magnitude is shown in Figure 4.12. The ‘R-X’ mode of the impedance analyzer has been used to make the result more visibly significant. In ‘R-X’ mode, the Real part of the complex impedance is measured.

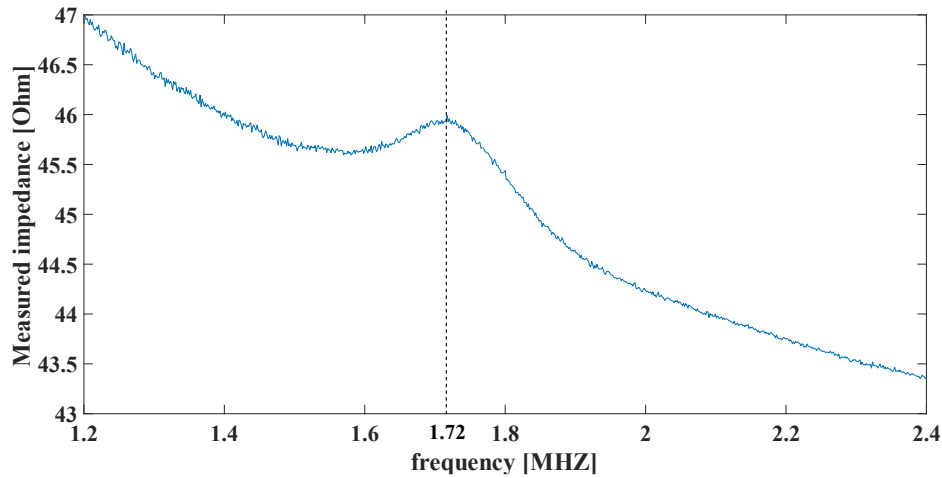


Figure 4.12 Impedance measurement of the SU-8 circular membranes during electrical actuation

As shown in Figure 4.12, a bump is superimposed onto the capacitive impedance characteristic when the frequency is around the mechanical resonant frequency. Under the law of energy conservation, this bump represents that extra energy is drained from the electrical domain to support the gradually-increasing mechanical kinetic and elastic energy. The appearance of this bump on the electrical impedance measurement is a common phenomenon for capacitive MEMS structures with a bi-directional coupling interface. In Figure 4.12, the bump shows up around 1.72 MHz, 0.7% deviated from the simulated mechanical resonant frequency. Since all 1500 fabricated membranes have been connected in parallel for the impedance measurement, this minor deviation

provides additional evidence that the new fabrication process has reproducibility and predictability.

4.5 Discussion about the practicability of the new fabrication methodology

4.5.1 Process-related constraints and practicability

The experimental case study, by far, has validated the controllability and usability of the newly-developed fabrication technology. However, the recipe used has not been optimized for any specific applications. One reflection in this aspect is the huge pull-in voltage of the test structures. Such a high pull-in voltage makes the manufactured SU-8 circular membranes not suitable for applications such as bio-medical ultrasound imaging or tactile sensings. It is necessary to demonstrate the possibility, at least theoretically, that the newly-developed fabrication technology can fabricate out-of-plane SU-8 MEMS structures on thinner layers. Such devices have lower pull-in voltage, making them potentially useful for real applications.

The discussion here uses the experimental calibration results in Chapter 3 as the basis. They are normalized to their coated thickness and replotted, as shown in Figure 4.13.

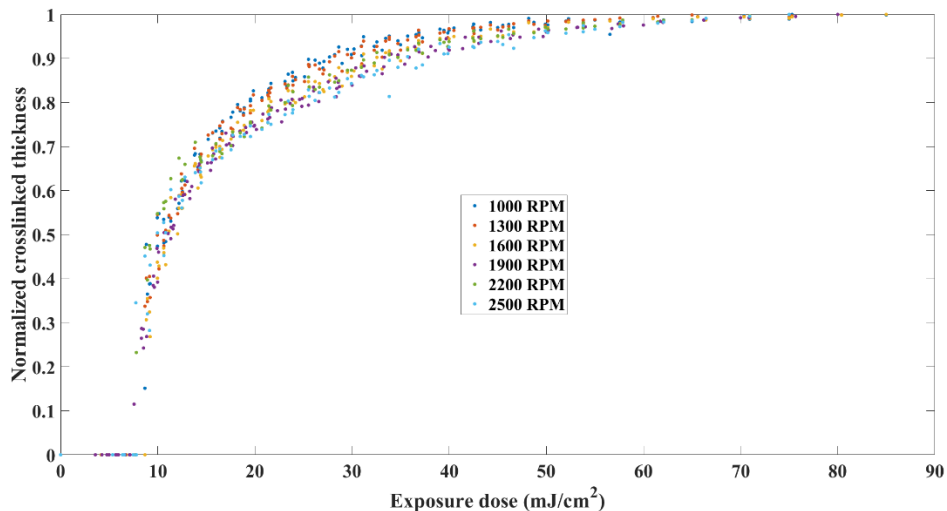


Figure 4.13 Calibration results for six different layers, normalized view

Figure 4.13 demonstrates an important conclusion. The grayscale lithography can achieve any intermediate thickness between zero and the coated thickness. This capability is independent of the lithography conditions. All six coated layers can achieve arbitrary intermediate thickness, even though the lithography conditions, such as photoresist layer thickness and solvent residuals, have been quite different.

Therefore, no foreseeable obstacles are hindering the newly-developed fabrication technology from making SU-8 out-of-plane capacitive MEMS structures on much thinner layers, for example, 1- μm thick membranes on a 2- μm thick SU-8 layer. One only needs to calibrate the grayscale lithography to achieve the exposure dose for 1- μm thick layers and design the corresponding grayscale masks. The resonant frequency, spring-constant, and electrostatic softening effects for such membranes are shown in Figure 4.14.

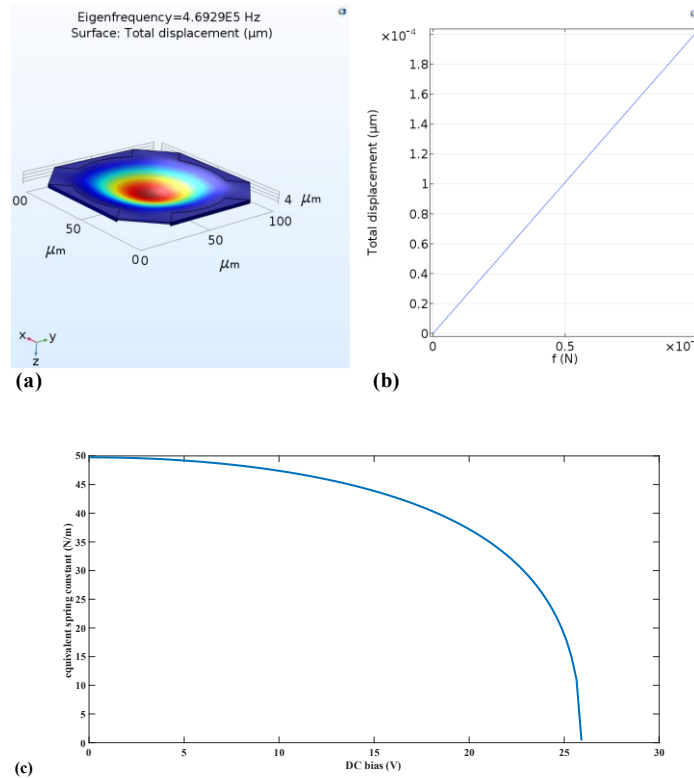


Figure 4.14 Simulation result for a set of structural dimensions achievable by application-specifically optimized SU-8 grayscale lithography. (a) Mechanical resonant frequency. (b) Parametric sweep for mechanical elasticity. (c) Electrostatic softening effect on the mechanical spring constant.

As shown in Figure 4.14, the 1 μm -thick circular membranes have their resonant frequency reduced to 470 kHz. Their spring-constant is reduced to 50 N/m, and the pull-in voltage drops to 26V. They become much more suitable for applications such as pressure sensors and acoustic devices.

The N_{EC} of the 1 μm -thick membranes has also been computed by Eq(4.8). It is around 0.1. If the standard developing process of SU-8 photoresist is used, stiction is inevitable. However, this issue can be simply solved by using the critical point drying technique.

CO₂ critical point dryers are the most effective tools to eliminate stiction issues in thin-film MEMS devices. A critical point dryer dehydrates microstructures while keeping the whole process

free from capillary force. This technique eliminates limitations on structure designs imposed by N_{EC} constant. IPA happens to be the most commonly used liquid agent to immerse samples for critical point drying.

The developing process for the 1- μm membranes can be customized for critical point drying. After the devices are immersed in PGMEA to dissolve uncrosslinked SU-8, they should be immersed in IPA. Then, the container of IPA and the SU-8 sample is placed into a critical point dryer to complete dehydration. This customized developing step allows the membranes to remain suspended, even though their N_{EC} is significantly smaller than 1.

4.5.2 Material-related constraints and practicability

The diffusion of photoacids is inevitable during the lithography process of SU-8. It is difficult to control this physical process. In Chapter 3, photoacid diffusion is confirmed to result in non-uniform thickness for microstructures made by grayscale lithography. The central part of these suspended microstructures will be thicker than their ends. Such 3D geometry of the microdevices increases the difference between their simulated and measured performance, potentially reducing the process predictability. It is necessary to, at least theoretically, evaluate the impact of this uncontrollable diffusion on the controllability of the new fabrication technology.

This thesis considers the variation in process predictability due to the solid diffusion of photoacids will be limited when the dose-modulation methodology is used for more practical application scenarios.

The cross-sectional thickness of microstructures made by grayscale lithography of 25 μm SU-8 has been characterized by SEM in Chapter 3 (Figure 3.3). There, the thickness difference between the ends and the central part has been around 1 to 2 μm . The author found that SU-8 out-of-plane MEMS devices generally have a total thickness lower than 10 μm [46-54, 62, 63, 123,

139-142]. In such cases, solvent residuals left in the SU-8 layers will be less. The total amount of photoacids generated within the layers exposed by grayscale lithography will also be smaller. These two factors will significantly limit the degree of photoacid solid diffusion. If the sacrificial-layer-free fabrication technology developed in this chapter is used on the much thinner layers, it is reasonable to expect the thickness difference to reduce further. The difference due to the photoacid diffusion between simulate and actual performance will be minor.

4.5.3 Equipment-related constraints and practicability

Maskless grayscale lithography, as already discussed in Chapter 1, is a semi-parallel process. A lithography mask design will be divided into an array of exposure windows based on the DMD devices' used area. Patterns within a window are simultaneously exposed. Neighboring exposure windows are exposed one by one, from left to right and from top to bottom. Such a characteristic raises worries about processing speed and scalability for sacrificial-layer-free fabrication technologies of SU-8 out-of-plane MEMS devices.

This thesis considers that such worries are unnecessary, based on the working principle behind maskless grayscale lithography.

Maskless grayscale lithography is based on pixel-level dose modulation. As introduced in Chapter 1, there is another lithography method, hard-mask alternation, using similar principles to get suspended structures by a single lithography process. Hard-mask alternation is purely parallel. It has a higher fabrication speed and process scalability for the massive manufacturing process than maskless grayscale lithography.

Maskless grayscale lithography and hard-mask alternation can be integrated as one toolbox to promote the application of the sacrificial-layer-free fabrication of SU-8 out-of-plane MEMS devices. Maskless grayscale lithography can be used during the initial R&D phase, where design

adjustments are common. This phase can benefit from maskless grayscale lithography for rapid and flexible prototyping. After entering the phase of massive production with fixed designs, mask sets can be made for the hardmask alternation, maximizing the fabrication speed of the sacrificial-layer-free technology.

4.6 Summary

This chapter uses SU-8 grayscale lithography and polyimide laser micromachining to develop a 3-step fabrication technology for out-of-plane SU-8 MEMS structures. The technology developed in this chapter aims at a new technology path to fabricate SU-8 out-of-plane MEMS devices, a way that uses pixel-level dose modulation instead of sacrificial layers to get movable microstructures.

The sacrificial-layer-free fabrication technology has been tested on silicon wafers, with circular membranes as the test structures. The characterization result of test structures validates the good process controllability of the newly-developed fabrication technology. Its ability to fabricate MEMS structures with the bi-directional interface for electromechanical coupling has also been demonstrated.

Discussions have also been carried out regarding the practicability of this new fabrication technology using grayscale lithography. Potential issues exist, but they are all addressable, at least theoretically. There is no major obstacle on the technology path to replace sacrificial layers with dose-modulation for the fabrication of SU-8 out-of-plane MEMS devices.

These research activities demonstrate that the newly-developed fabrication technology and the ideology behind it have great potential in SU-8 out-of-plane MEMS fabrication.

As the next step, the newly-developed fabrication technology will be tested on copper-polyimide composites. The difference between the metal surface of these composites and the

surface of silicon wafers is huge, significantly varying the lithography condition. Using the newly-developed fabrication technology on these composites can test the robustness with this respect. Meanwhile, traditional SU-8 surface micromachining has been used to fabricate SU-8 out-of-plane MEMS devices on these composites for flexible electronics [47]. If the new fabrication technology is usable on such composites, their application potential will be further enhanced. The corresponding research activities will be presented in Chapter 5.

Chapter 5: Using metal-polymer composites as substrates for SU-8 MEMS

Chapter 5 applies the fabrication technology developed in the last chapter on metal-polymer composites. Traditionally, metal-polymer composites are used as flexible substrates for electronic systems, such as the connectors between the motherboard and monitor in laptops[47, 143, 144]. If the fabrication technology developed in the last chapter can be used on these composites in a controllable manner, its robustness is further demonstrated. Since metal-polymer composites are low-cost, flexible alternatives to silicon wafers, applying the newly-developed fabrication technology on these composites also demonstrates its application potential in low-cost, flexible electronics. Figure 5.1 shows the research work carried out in Chapter 5.

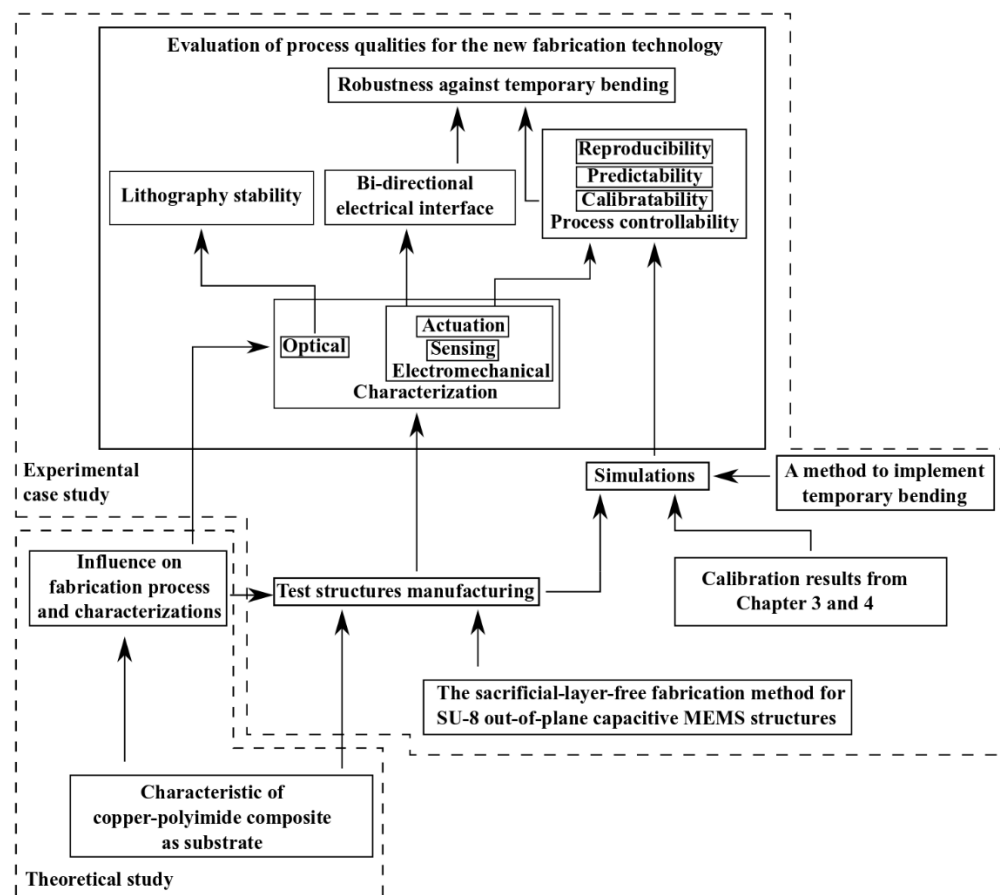


Figure 5.1 Depiction of the research work for Chapter 5

As shown in Figure 5.1, Pyrulax™ copper-polyimide composites from Dupont are used as the substrate in this chapter. The condition of their copper surface is characterized in section 5.1. The influence of the copper surface on SU-8 grayscale lithography is also studied in the same section. Section 5.2 introduces the preparation of experimental case studies. The characterization results of the test structures are presented in section 5.3. Section 5.4 summarizes the accomplishments of the chapter.

5.1 Characteristics of metal-polymer composites as low-cost and flexible substrates

5.1.1 Surface condition characterization

The Pyrulax™ copper-polyimide composites used in this chapter have a 45- μm polyimide layer and a 35- μm copper layer. The copper layer's surface condition is characterized and compared with the surface of a silicon wafer, using a Dektak™ stylus contact profilometer. The area scanning mode has been used to obtain the surface topological information. The characterization result is shown in Figure 5.2.

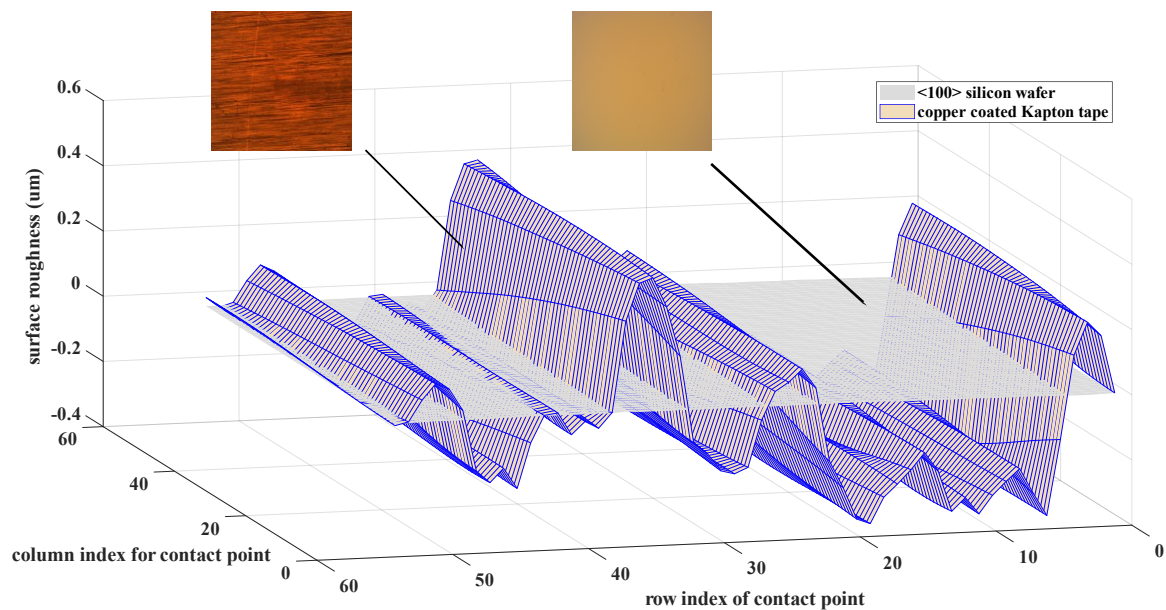


Figure 5.2 The surface topological characteristics of the copper-polyimide composites.

As shown in Figure 5.2, the copper surface of the Pyrulax™ composite samples has a more significant surface variation than the surface of a silicon wafer. The surface variation detected in surface profilometry is also optically observable, as the thread-like patterns in the microscopic image.

The copper surface variation may increase the randomness in the SU-8 lithography result. The degree of this randomness must be checked. Three types of out-of-plane capacitive MEMS structures: cantilevers, doubly-clamped beams, and circular membranes are designed, fabricated, and characterized in this chapter. Their planar dimensions would be measured to evaluate the lithography accuracy.

5.1.2 Influence on SU-8 grayscale lithography

The manufacturer of SU-8 photoresist, Kayaku Advanced Material, recommends increasing the exposure dose by 50% (1.5x) to 100% (2x) on a copper surface (compared with the dose on a silicon wafer). The dose increment has not been limited to a single value. A single exposure dose on a copper surface will be mapped to a segment of exposure doses on a silicon surface, with multiple achievable thickness values. Here, the magnitude of increment in exposure dose on the copper surface of Pyrulax™ composites will be experimentally determined by comparing the simulated and measured mechanical resonant frequency of the test structures, with the help of calibration curves of SU-8 grayscale lithography on silicon wafers.

The optical brightness of collapsed and suspended structures on a copper surface is also different from the brightness on a silicon surface. Copper has a refractive index of 0.77 for yellow light (wavelength: 575nm) [145]. Suspended SU-8 structures on copper reflect 2% of the incident yellow light intensity, while collapsed ones reflect 10%. When SU-8 out-of-plane MEMS

structures are inspected under yellow light after the grayscale lithography, dimmer structures are suspended while brighter ones are collapsed.

5.2 Setup for the experimental case study

The detail of the 3-step, sacrificial-layer-free fabrication technology of out-of-plane SU-8 MEMS structures has been presented in Chapter 4.

5.2.1 Design of structural dimensions and processing parameters

The Pyrulax™ composite used in this chapter is 20 mm in width and 35 mm in length. The planar dimensions of test structures are summarized in Table 5.1. Processing recipes are presented in Table 5.2.

SU-8 selection and structural design					
SU-8 type	Coated thickness	Structure design			Amount
SU-8 2010	~10 μ m	Circular membranes	Radius	45 μ m	1500
SU-8 2015	~15 μ m	Doubly-clamped beams	Width	50 μ m	60
			Length	150 μ m	
		Cantilevers	Width	50 μ m	60
			Length	100 μ m	

Table 5.1 Structural designs for the experimental validation on flexible substrates

SU-8 grayscale lithography process parameters				
Soft baking temperature	Soft baking duration	Exposure duration	Post-exposure baking temperature	Post-exposure baking duration
95°C	3 min	15s	95°C	5 min
Shadow mask laser micromachinings				
Relative intensity		Laser moving speed		Repeating time
100%		1 mm/s		20
Metallization				
Metal	Chromium	Thickness	200 nm	

Table 5.2 Processing recipes for the experimental case study

In Table 5.1, the circular membranes use the same coated thickness as the one used in the experimental validation of Chapter 4, while the cantilevers and beams have used a 15- μm thick layer.

In Table 5.2, processing conditions except exposure dose are also the same as those used in Chapters 3 and 4. In this way, the existing calibration curves for these SU-8 layers from previous chapters can be used. In Table 5.2, the exposure duration of 15s on the copper surface is equivalent to a duration of 7.5~10s on silicon wafers. The mask design for each type of out-of-plane transducers is shown in Figure 5.3.

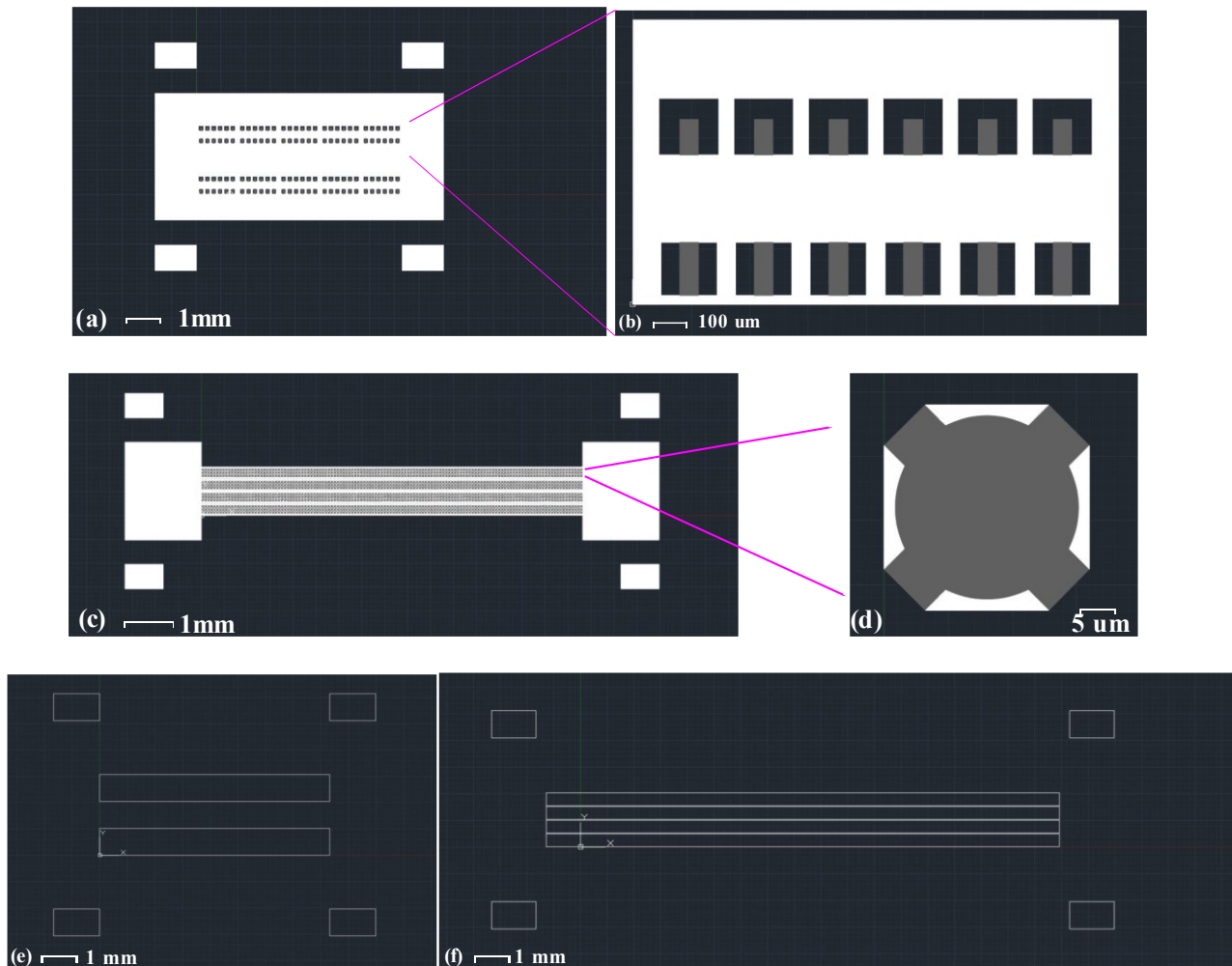


Figure 5.3 Mask designs for the SU-8 out-of-plane transducers to be fabricated on flexible substrates. (a) The design for cantilevers and doubly-clamped beams. (b) The zoom-in view of the design for cantilevers and beams. (c) The array of circular membranes. (d) The zoom-in view of a single membrane. (e) Shadow mask design for cantilevers and beams. (f) Shadow mask designs for the circular membranes.

In Figure 5.3, the gray shade value for all designs has been set to 96, with an estimated dose modulation coefficient of around 14%. The thickness resulted from the grayscale lithography of the 10- μm SU-8 2010 layer on copper should be between 4.25 μm to 6.40 μm , using the calibration curve in Chapter 4. The resulted thickness of the 15- μm SU-8 2015 layer should be between 8.25 μm to 10.75 μm , according to the calibration curve in Chapter 3. Each cantilever or

doubly-clamped beam in Figure 5.3b occupies a 200 μm -by-200 μm area, while each circular membrane in Figure 5.3d occupies a 100 μm -by-100 μm area. Figure 5.3 shows that rectangles have been designed at the four corners of masks to align the shadow masks with the structures.

5.2.2 Bending test of the flexible substrates

It is common for metal-polymer composites to experience temporary bendings in real applications. When the new fabrication technology is applied to Pyrulax™ composites, the test structures' performance before and after the temporary bending should be compared. This test provides another aspect of process robustness, in addition to the process controllability.

The setup to implement temporary bendings is illustrated in Figure 5.4.

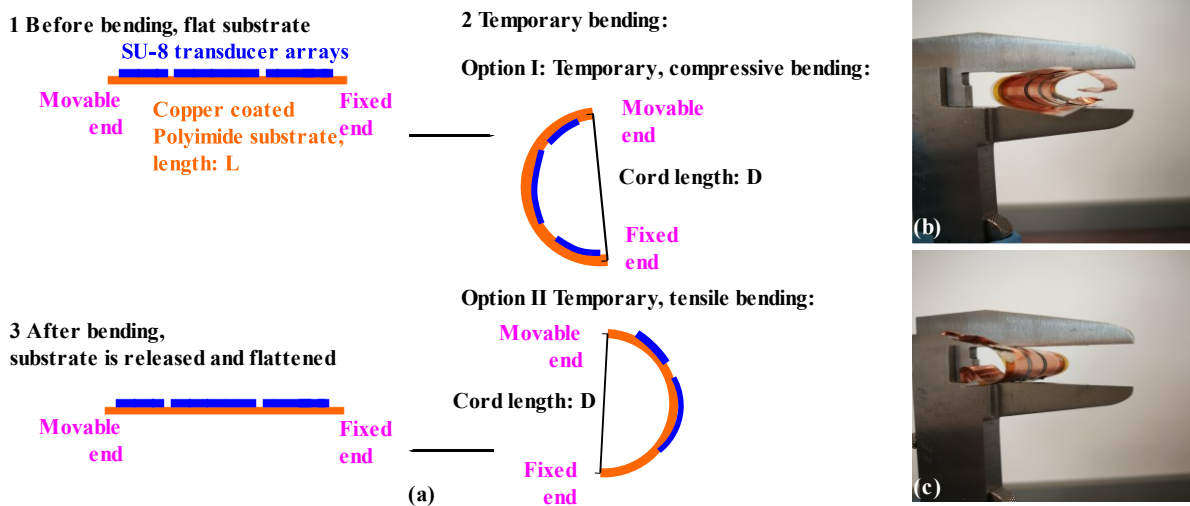


Figure 5.4 Illustration of the temporary bendings. (a) The schematic of both the compressive bending and the tensile bending. (b) Implementation of the compressive bending. (c) Implementation of the tensile bending.

Figure 5.4 depicts the way to implement temporary compressive and tensile bendings. In both cases, the author bends the substrate from flat into a semicircle. The same bending strategy has been practiced before for electronics fabricated onto polyimide substrates using SU-8 silver

mixtures [112]. D in Figure 5.4a is the diameter, which could be computed using the length of the substrate:

$$D = \frac{2L}{\pi} \quad (5.1)$$

The curvature radius of the composite substrates used in this chapter is estimated to be 11.14mm. The bending into semicircle is implemented by fixing one end of the substrate onto a caliber and moving the other end.

5.2.3 Finite element simulations

The mechanical resonant frequency and the stress distribution during the temporary bending are simulated using COMSOL® Multiphysics 5.3. The designs in Table 5.1 have been used as planar dimensions, while the vertical dimensions have used the lower/upper limits estimated by the experimental calibration. The thickness lower limit for membranes is 4.25 μm , and the upper limit is 6.40 μm . The thickness lower limit for cantilevers and beams is 8.25 μm , and the upper limit is 10.75 μm . Table 5.2 presents the material properties used in the FEA simulation. The simulation results are shown in Figure 5.5.

Property	Density	Young's modulus	Poisson's ratio
Value	1200 kg/m ³	4.95 GPa [29, 30]	0.32[31]

Table 5.3 Mechanical properties of SU-8 used in FEA analysis

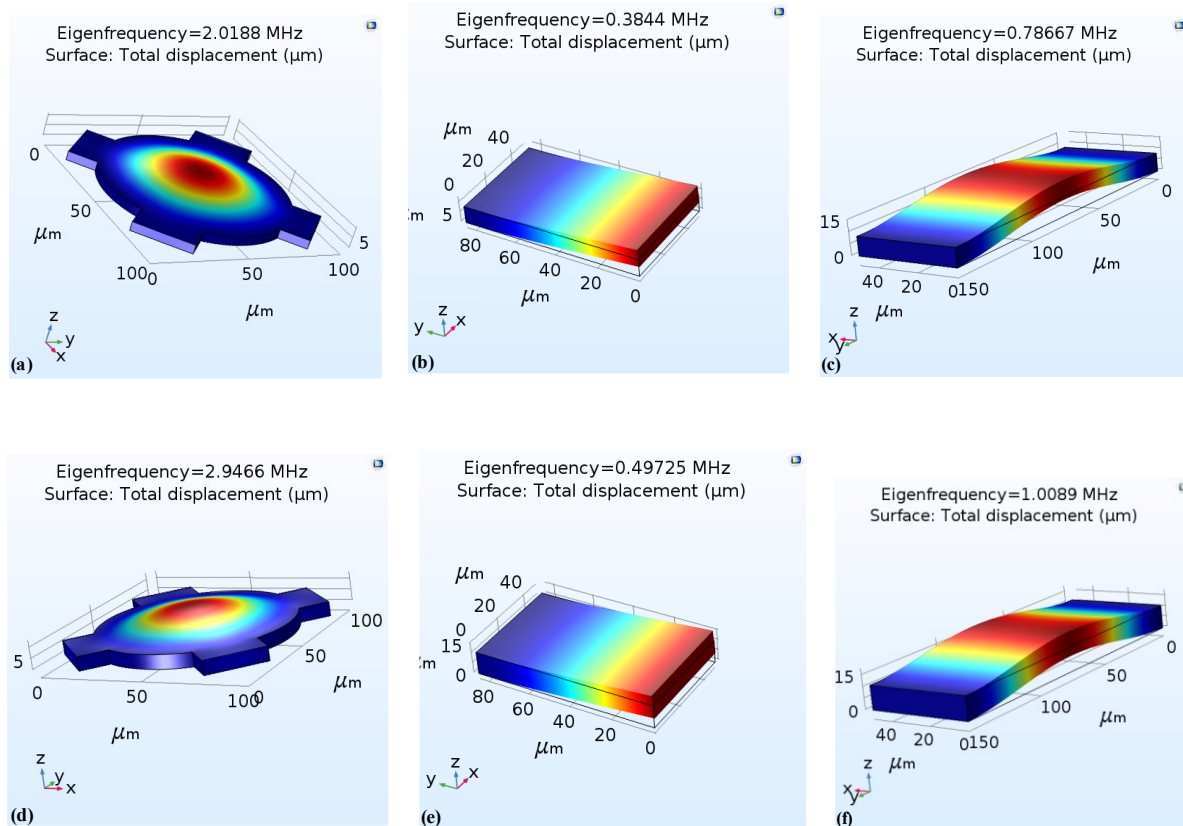


Figure 5.5 Simulation for the fundamental resonant modes of the proof-of-concept out-of-plane SU-8 MEMS structures. (a): Circular membrane, thickness: 4.25 μm (2x exposure dose increment). (b): Centilevers, thickness: 8.25 μm (2x exposure dose increment). (c): Doubly-clamped beams, thickness: 8.25 μm (2x exposure dose increment); (d): Circular membrane, thickness: 6.40 μm (1.5x exposure dose increment). (e): Centilevers, thickness: 10.75 μm (1.5x exposure dose increment). (f): Doubly-clamped beams, thickness: 10.75 μm (1.5x exposure dose increment).

The temporary bending generates temporary stress. If the stress is concentrated on movable components of the test structures, there may be performance variation. This is why the temporary bending needs FEA simulation. Here, the bending is mimicked as an angular displacement applied to one end of every structure, with the other end fixed. The value of the displacement can be computed by:

$$\theta = \frac{d}{L} \pi \quad (5.2)$$

In Eq(5.2), L is the length of the substrate, which is 35 mm; d is the length of a single square occupied by a single device of each type, which is 100 μm for circular membranes, and 200 μm for beams or cantilevers. The simulation results are shown in Figure 5.6 to Figure 5.8.

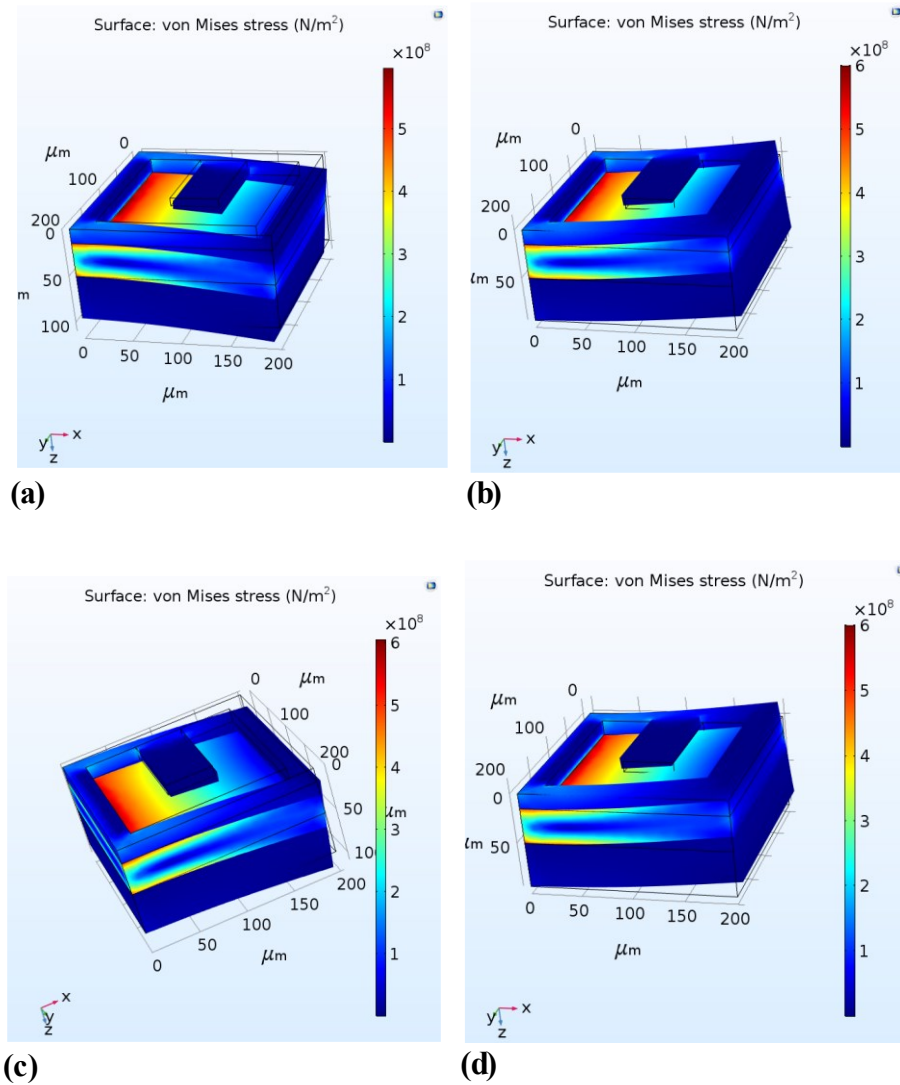
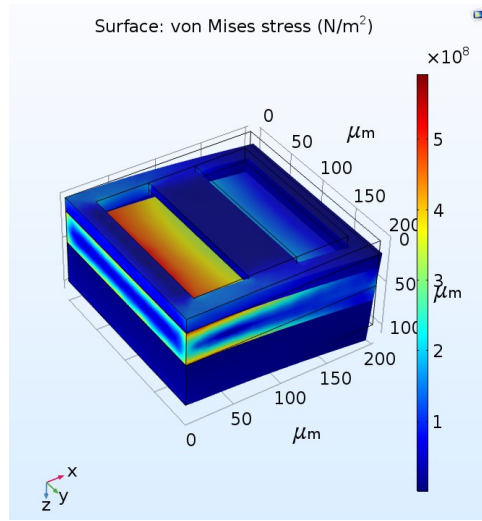
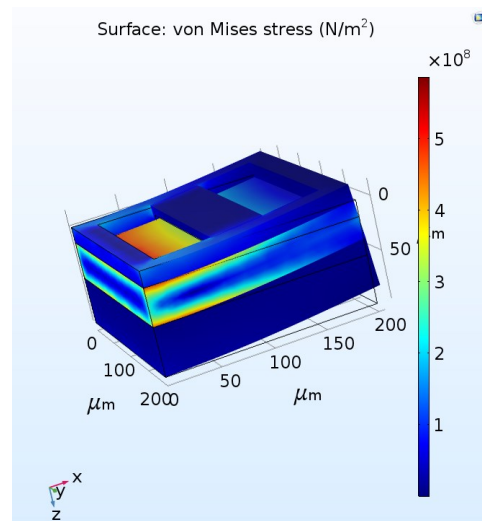


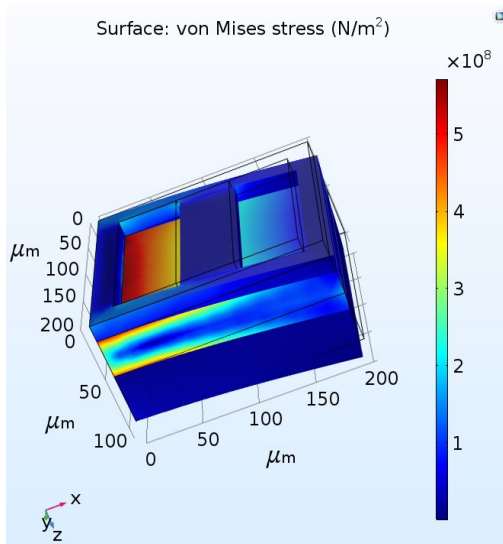
Figure 5.6 Simulation of stress during the bending of cantilevers. (a) Tensile, 2x exposure dose; (b) Compressive, 2x exposure dose; (c) Tensile, 1.5x exposure dose; (d) Compressive, 1.5x exposure dose.



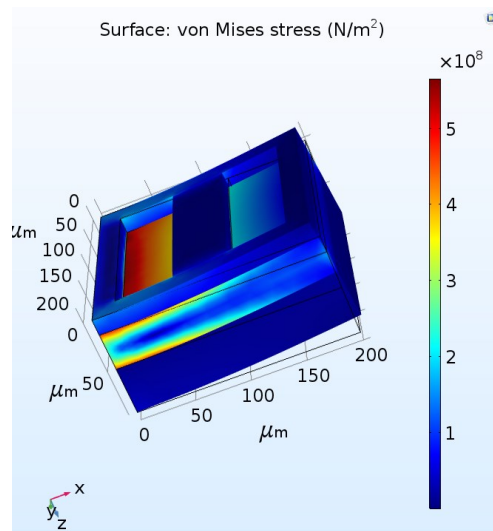
(a)



(b)



(c)



(d)

Figure 5.7 Simulation of stress during the bending of doubly-clamped beams. (a) Tensile, 2x exposure dose; (b) Compressive, 2x exposure dose; (c) Tensile, 1.5x exposure dose; (d) Compressive, 1.5x exposure dose.

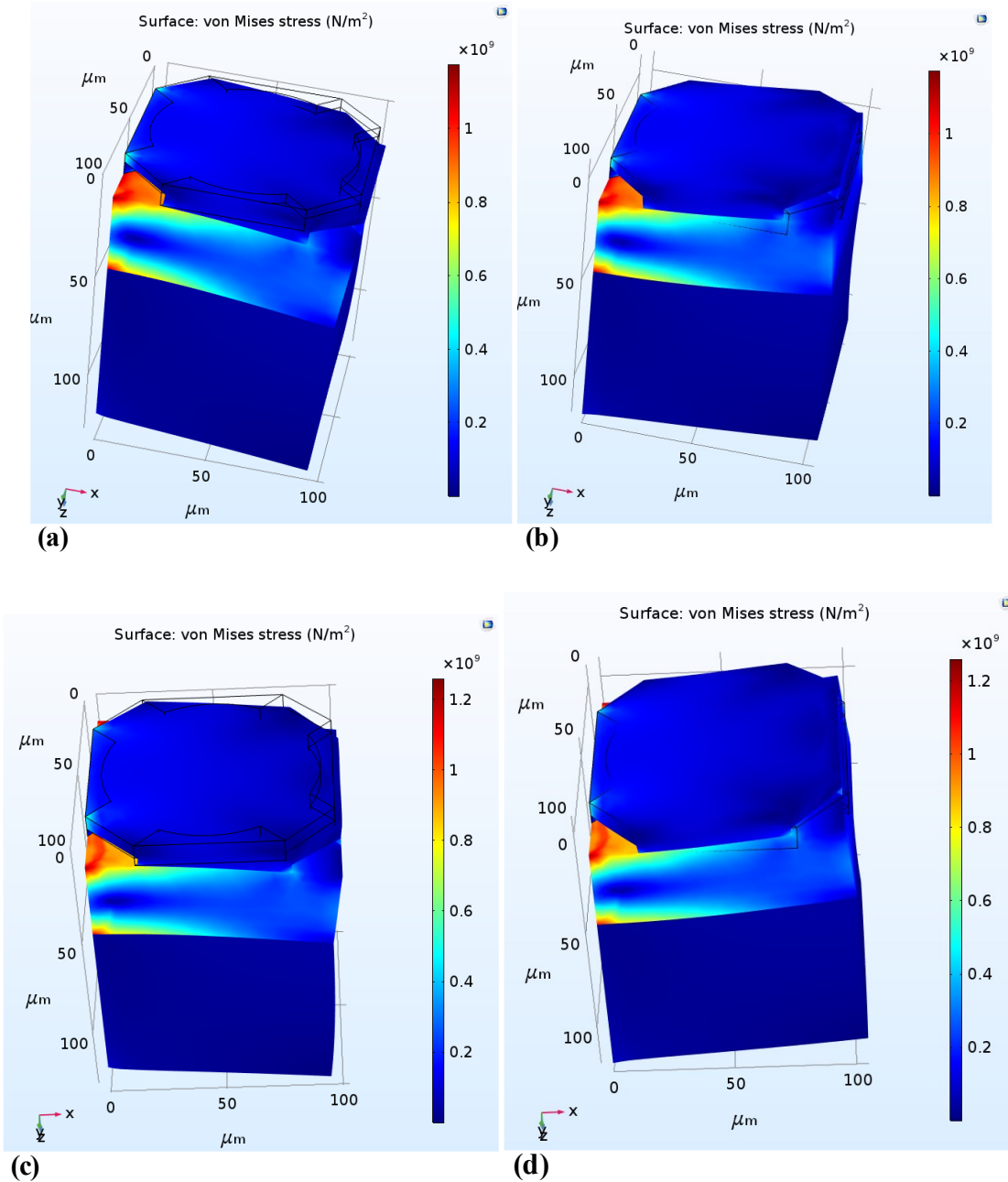


Figure 5.8 Simulation of stress during the bending of membranes. (a) Tensile, 2x exposure dose; (b) Compressive, 2x exposure dose; (c) Tensile, 1.5x exposure dose; (d) Compressive, 1.5x exposure dose.

As shown in Figure 5.6 to Figure 5.8, the stress corresponding to the bending is not concentrated on the movable structures. Most of the stress has been generated in the copper layer.

Since the stress imposed on the SU-8 microstructures is limited, the difference in MEMS structures' performance before and after the temporary bending should be minor.

5.2.4 Characterization methods

Optical microscopic inspections were carried out for the fabricated samples after the grayscale lithography to check the out-of-plane SU-8 MEMS structures' final status. Their planar dimensions were also measured to evaluate the lithography *accuracy*.

The electromechanical characterizations for the test structures are similar to those in Chapter 4, subdivided into the measurement of mechanical resonance and electrical impedance under the capacitive actuation. The mechanical resonance of the fabricated structures was measured by a Polytec MSA-500 system. The electrical actuation signal consists of a 40V DC bias and a periodic 1V (peak-to-peak amplitude) chirp signal. The electrical impedance magnitude of the circular membranes was measured by an Agilent A4294A impedance analyzer. The actuation signal has a 40V DC bias and 2V peak-to-peak periodic chirp. 'R-X' mode was used to make the reflect-back of the mechanical resonance more visible.

The electromechanical characterizations were conducted twice. In between, the samples were disconnected from characterization apparatuses, bent and released 100 times, and reconnected to the apparatuses. The two sets of measurement results have been compared to evaluate the process robustness against the temporary bending.

5.3 Characterization result

5.3.1 Optical inspection and measurement of planar dimensions

For each type of structure, after the grayscale lithography, the representative result of the microscopic inspection of under yellow light is shown in Figure 5.9.

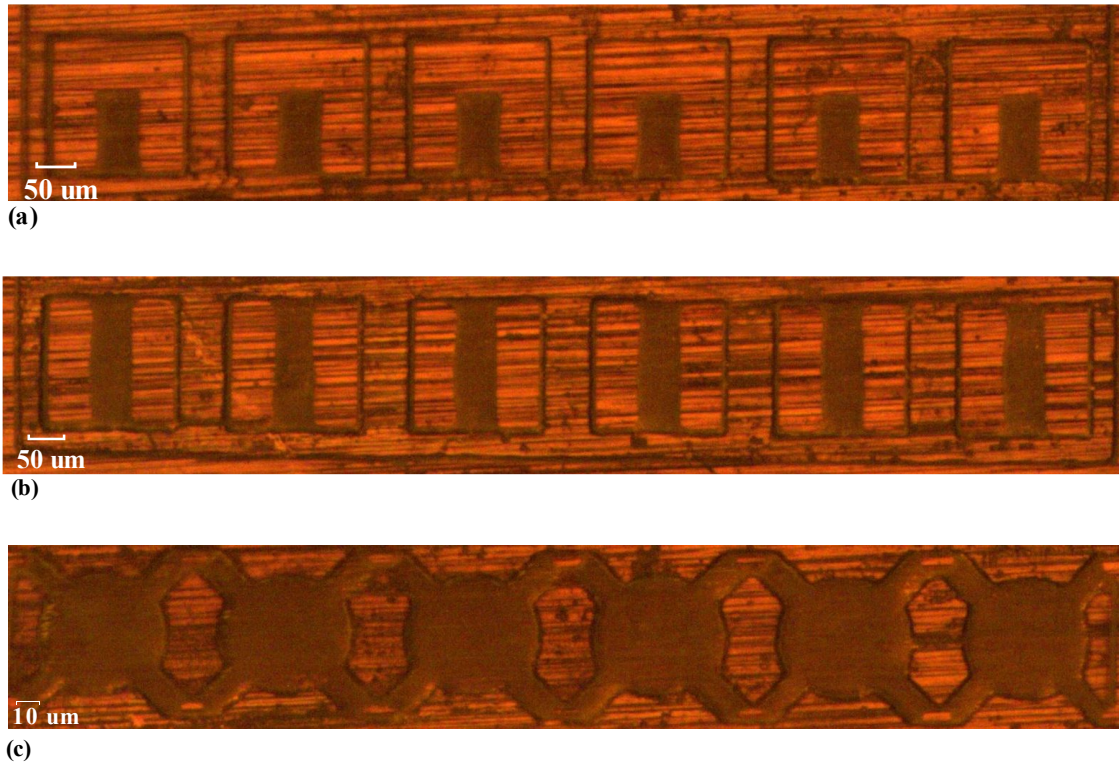


Figure 5.9 Yellow light microscopic inspection for the fabricated SU-8 transducers. (a) Cantilevers. (b) Doubly-clamped beams. (c) Circular membranes.

Figure 5.9 shows that the structures corresponding to grayscale masks are darker than the structures corresponding to the white patterns. The study in Section 5.1.2 has concluded that such optical brightness signifies successful release and suspending. The optical inspection demonstrates the feasibility of using grayscale lithography to make suspended SU-8 microstructures on the copper surface of Pyrulax™ composites. Thirty fabricated structures have been selected for each test structure type to measure the actual planar dimensions. The statistics of the measurement are summarized in Table 5.4.

Tese structure	Average measured planar geometry		Standard deviation		Relative error to design	
	Width (μm)	Length (μm)	Width (μm)	Length (μm)	Width	Length
Cantilever	47.77	96.58	2.1 (4.4%)	2.64 (2.8%)	4.4%	3.4%
Beam	49.22	147.77	2.14 (4.3%)	2.36 (1.6%)	1.7%	1.4%
Circular plate Diameter	89.06		2.07 (2.3%)		1.0%	

Table 5.4 Measurement of transducer planar dimensions and comparison with design

In Table 5.4, the standard deviation in planar dimensions was lower than 3%, and the relative error to the design was lower than 4.5%. Though the lithography result's uncertainty is higher than the one on a silicon wafer, it is still within the acceptable range defined in Chapter 1.

Figure 5.10 supplements some optical inspection of the test structures after the metallization for electrodes.

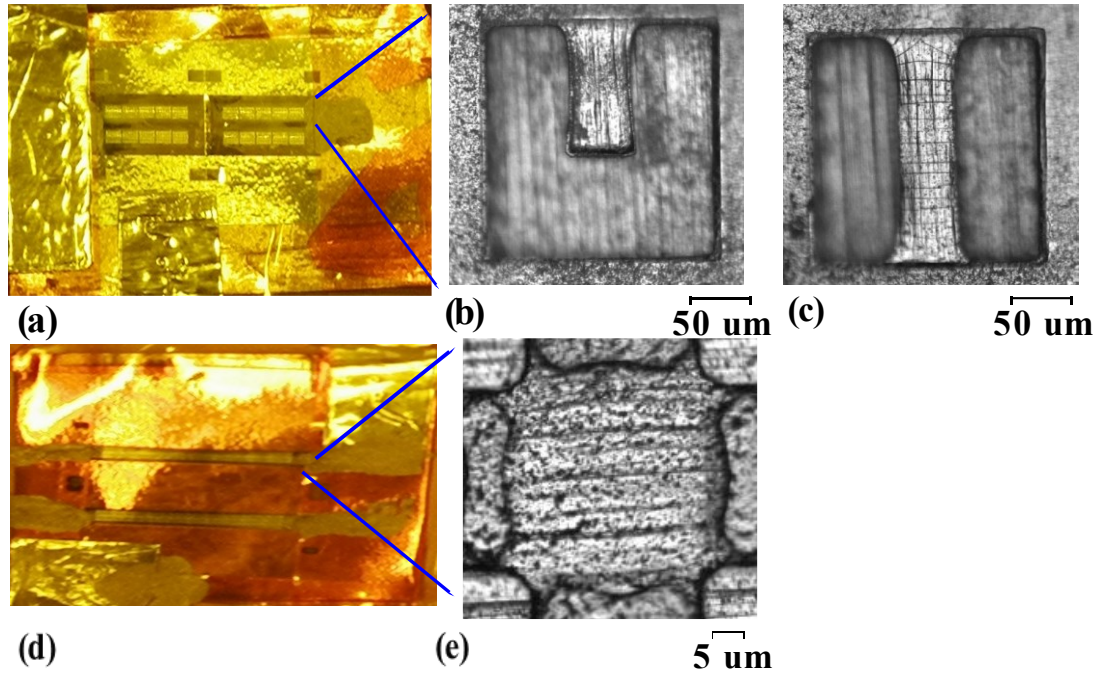


Figure 5.10 Proof-of-concept out-of-plane MEMS structures after metallization. (a) The arrays of cantilevers and doubly-clamped beams after the metallization and packaging. (b) The zoom-in view of a cantilever after the metallization process. (c) The zoom-in view of a doubly-clamped beam after the metallization process. (d) The arrays of circular membranes after the metallization and packaging. (e) A single circular membrane after the metallization process.

The packaging process in Figure 5.10 has been done using silver paint. Some dark particles and cracks are observable. They randomly distribute on the surface of the metal film. Uncleaned composites can be one of the potential contamination sources responsible for the reduced quality of deposition.

5.3.2 Mechanical resonance during the electrostatic actuation

Twenty individual devices have been selected to measure mechanical resonance under electrical actuation for each type of proof-of-concept structure. The statistics of the measurement result are summarized in Table 5.5.

Structure types	Resonant frequency before bending is applied		Resonant frequency after bending is withdrawn		The relative difference before and after bending
	Mean (MHz)		Mean (MHz)		
Single-clamped cantilevers	Mean (MHz)	0.375	Mean (MHz)	0.374	0.26%
	Standard deviation	3.77%	Standard deviation	3.78%	~0
Double-clamped beams	Mean (MHz)	0.790	Mean (MHz)	0.791	0.13%
	Standard deviation	4.61%	Standard deviation	4.66%	1.1%
Circular membranes	Mean (MHz)	1.996	Mean (MHz)	1.990	0.3%
	Standard deviation	3.60%	Standard deviation	3.63%	0.84%

Table 5.5 Statistical information on mechanical resonance for selected devices to test

As shown in Table 5.5, the average resonant frequency and the standard deviation for all three types of proof-of-concept structures have been almost identical before and after the temporary bending. This consistency in performance reflects a minor impact of the temporary bending, as predicted by the simulation.

The standard deviations of resonant frequency for each structure design have been between 3.5% and 4.7%. They are more significant than the standard deviations of samples on a polished silicon surface but still within the acceptable range defined in Chapter 1.

In Table 5.5, the averaged resonant frequencies presented are closer to the resonant frequency simulated for 2x exposure dose increment (Figure 5.5a to 5.5c). The relative errors to these simulation results, before and after the temporary bendings, are summarized in Table 5.6.

Structure types	The relative error between averaged measurement and simulation for 2x exposure dose increment	
	Before 100 times of bending	After 100 times of bending
Circular membranes	-1.2%	-1.4%
Cantilevers	-2.3%	-2.6%
Doubly-clamped beams	0.4%	0.5%

Table 5.6 Relative error between the measured resonant frequency and the FEA simulations

The result in Table 5.6 demonstrated that the substrate surface condition of the selected copper-polyimide composite has resulted in a 2x relative increment in the exposure dose.

The difference in resonant characteristics before and after the temporary bending is visualized in Figures 5.11, 5.12, 5.13, and 5.14. The first three figures compare the measurement distribution before and after the temporary bending. The last one shows the similarity in the averaged measurement result before and after the temporary bending.

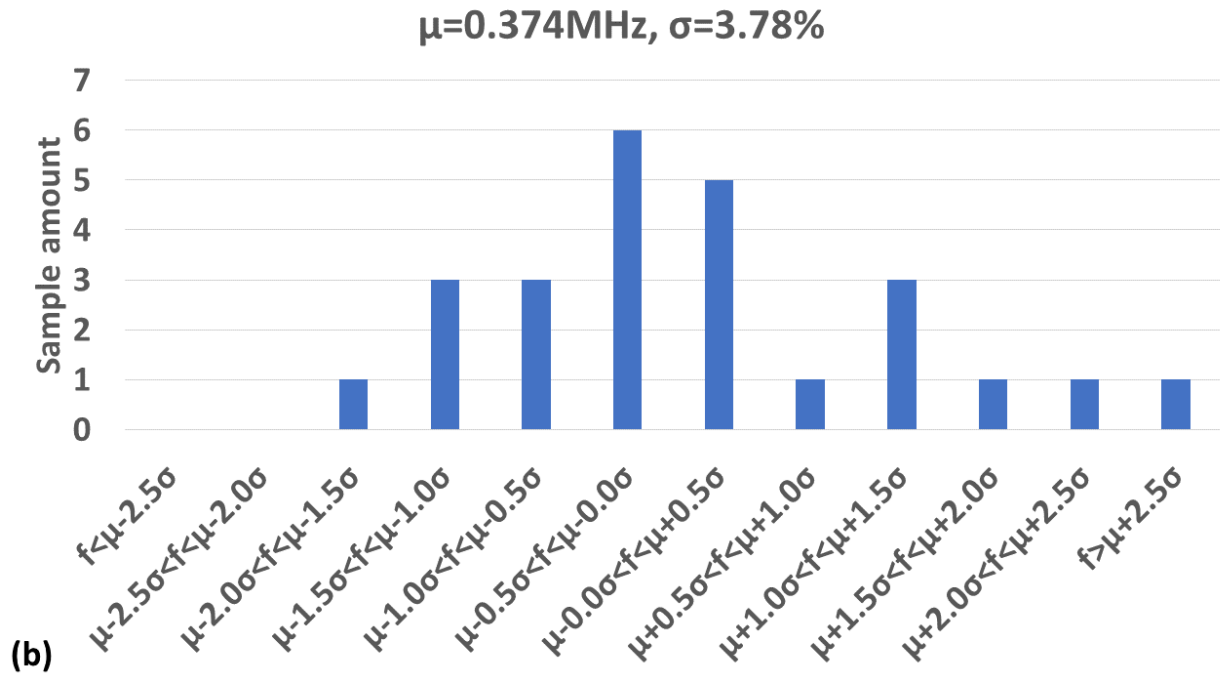
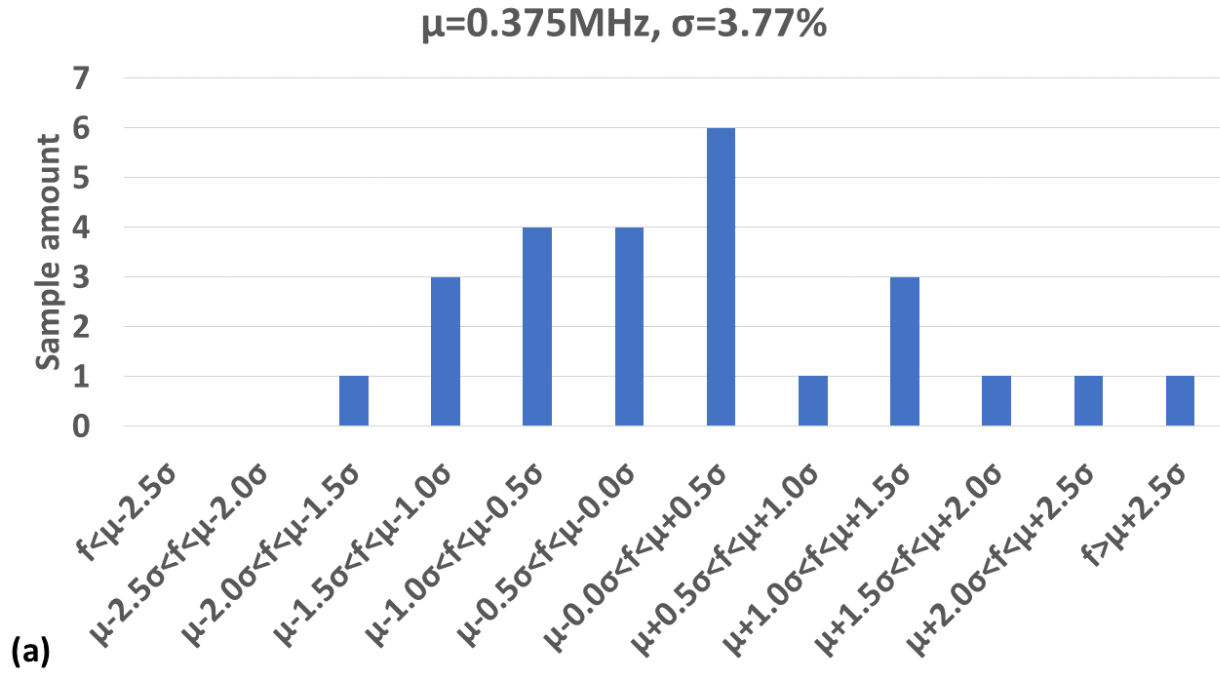


Figure 5.11 The distribution of natural frequency measurement for cantilevers. (a) Before the temporary bending; (b) After the temporary bending.

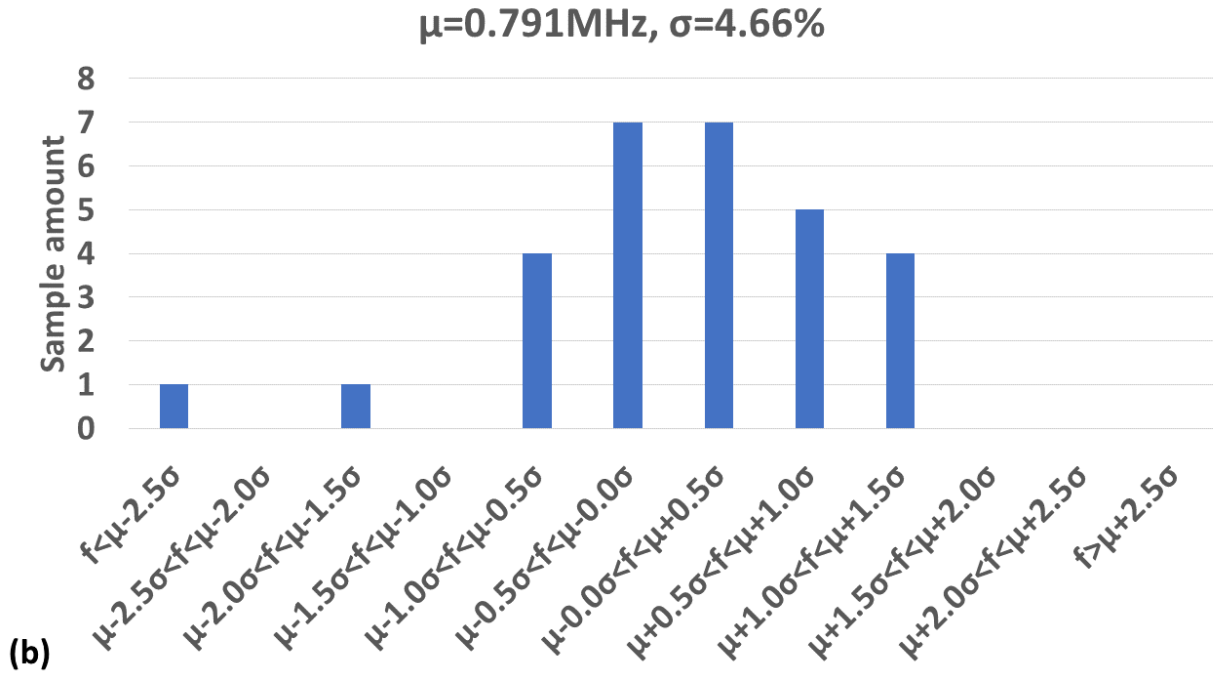
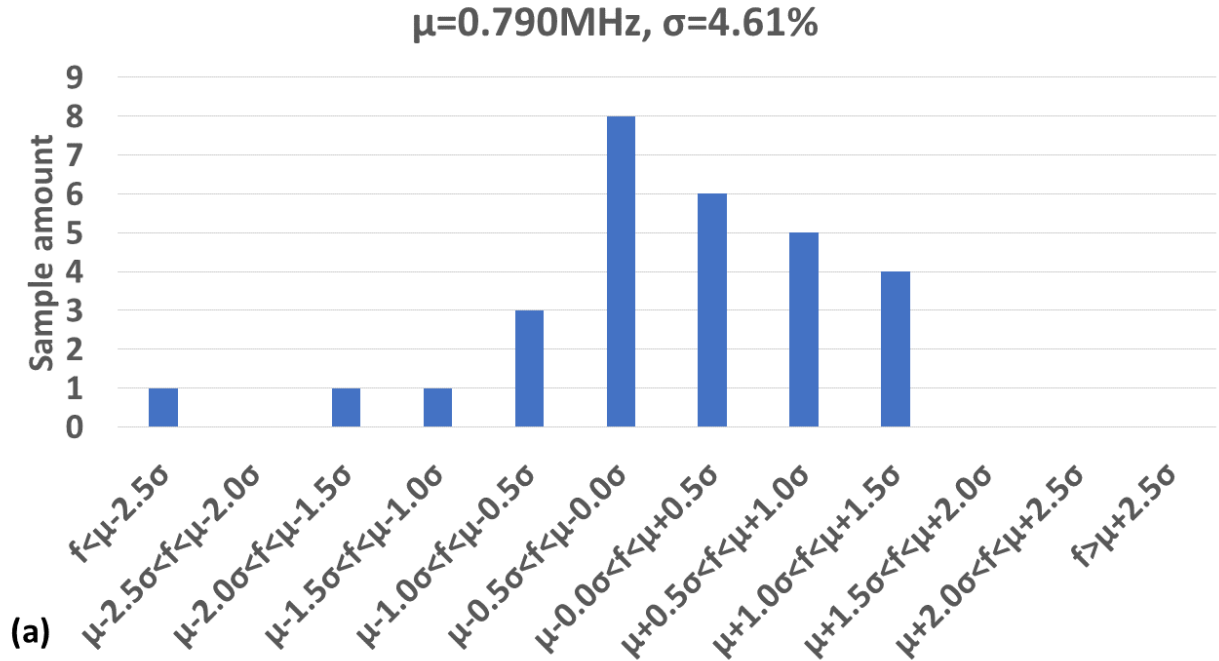


Figure 5.12 The distribution of natural frequency measurement for double-clamped beams. (a) Before the temporary bending; (b) After the temporary bending.

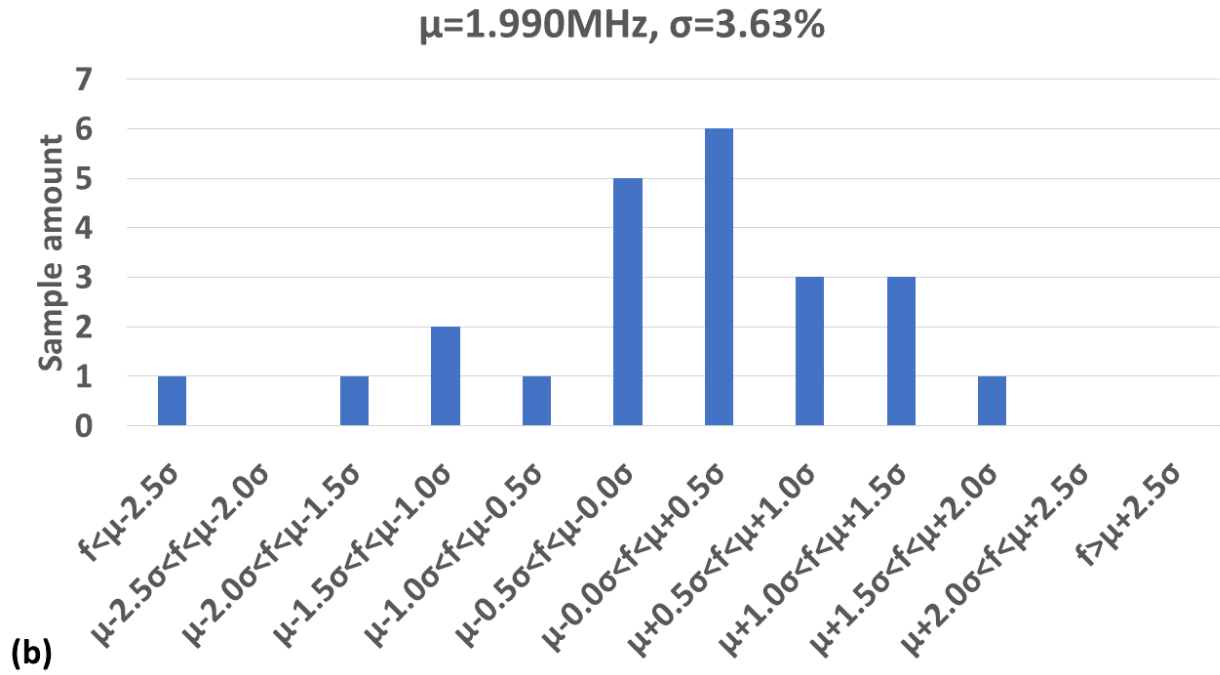
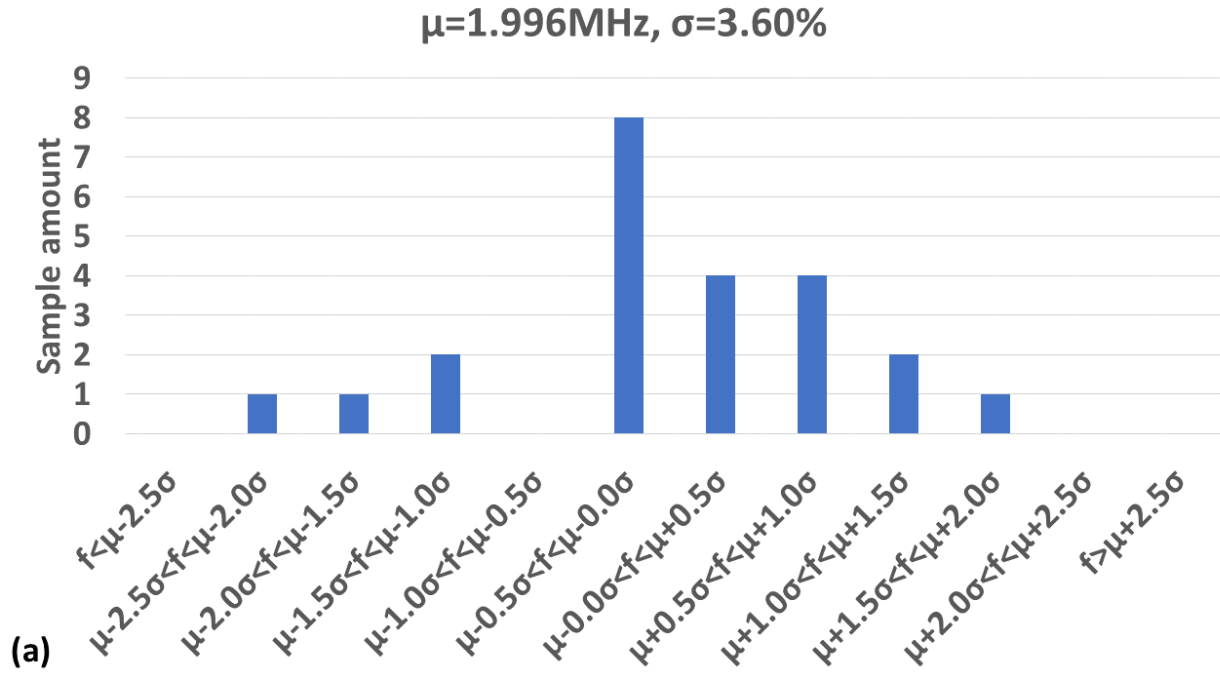


Figure 5.13 The distribution of natural frequency for circular membranes. (a) Before the temporary bending; (b) After the temporary bending.

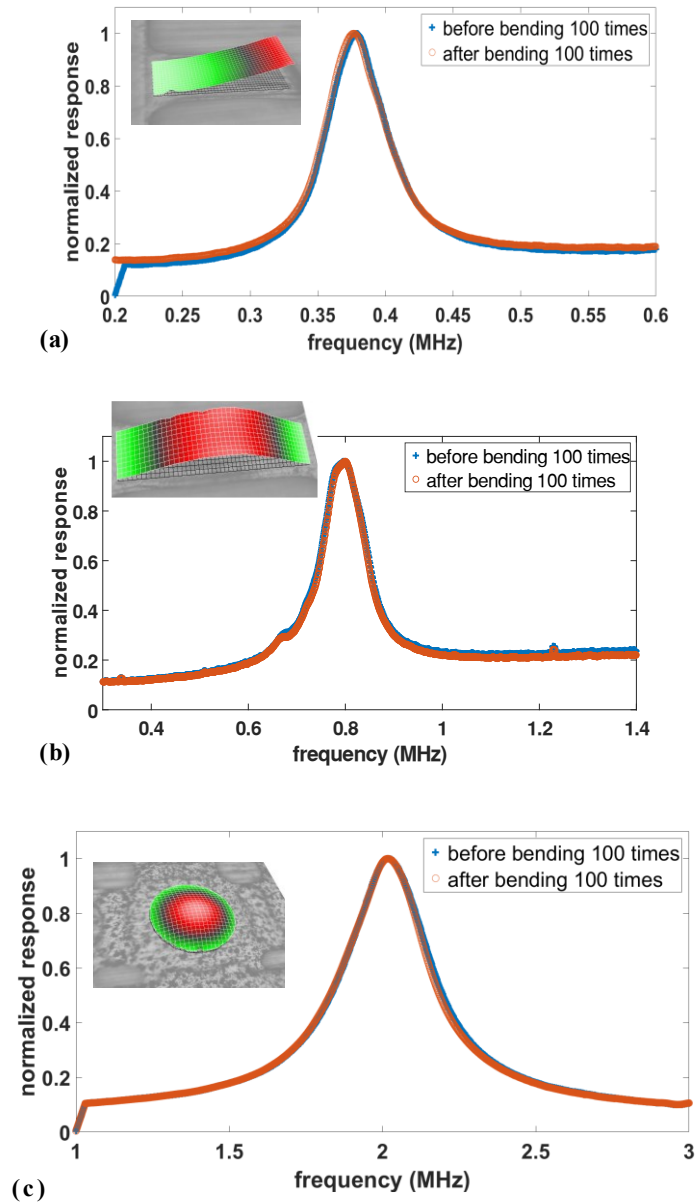


Figure 5.14 Visualization of electrostatically actuated mechanical vibrations of the fabricated structures before and after the temporary bending. (a) The normalized frequency response curve of 20 measured cantilevers, (b) Normalized frequency response curve of 20 measured double clamped beams, (c) Normalized frequency response curve of 20 measured circular plates.

As shown in Figures 5.11, 5.12 and 5.13, no significant variation in natural frequency measurement distribution can be found after the temporary bending. The resonant modes for

measurement after the temporary bendings have been extracted and presented on the upper left corner in Figure 5.14. The measured modal shapes share high similarity with the simulated shapes for the fundamental resonant mode. This similarity indicates that no significant structural damage has been induced by the temporary bendings. The averaged resonant curves before and after the temporary bending are also highly overlapped, which is another evidence for the minor influence of the temporary bendings on device performance. The magnitude of variation in the resonant frequency at the level of the individual device is shown in Figure 5.15.

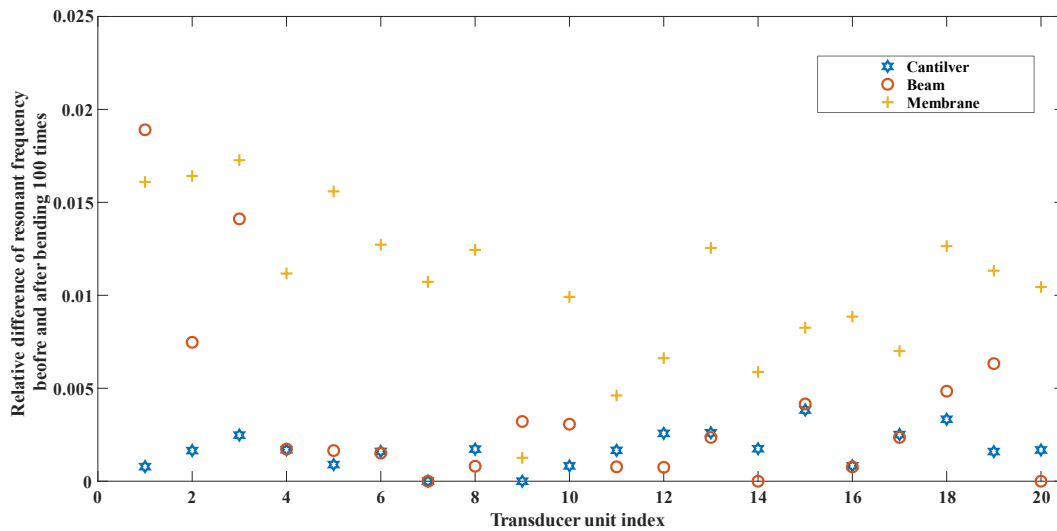


Figure 5.15 Comparison of resonant frequency shift before and after the temporary bending at the individual transducer level

As shown in Figure 5.15, none of the resonant frequency variations before and after the temporary bendings has exceeded 2%. The result supplements evidence of the process robustness against temporary bendings when the sacrificial-layer-free fabrication technology is used on flexible substrates.

5.3.3 Measurement of the electrical impedance magnitude

The measured electrical impedance curves of the circular membrane arrays, before and after the temporary bendings, are shown in Figure 5.16.

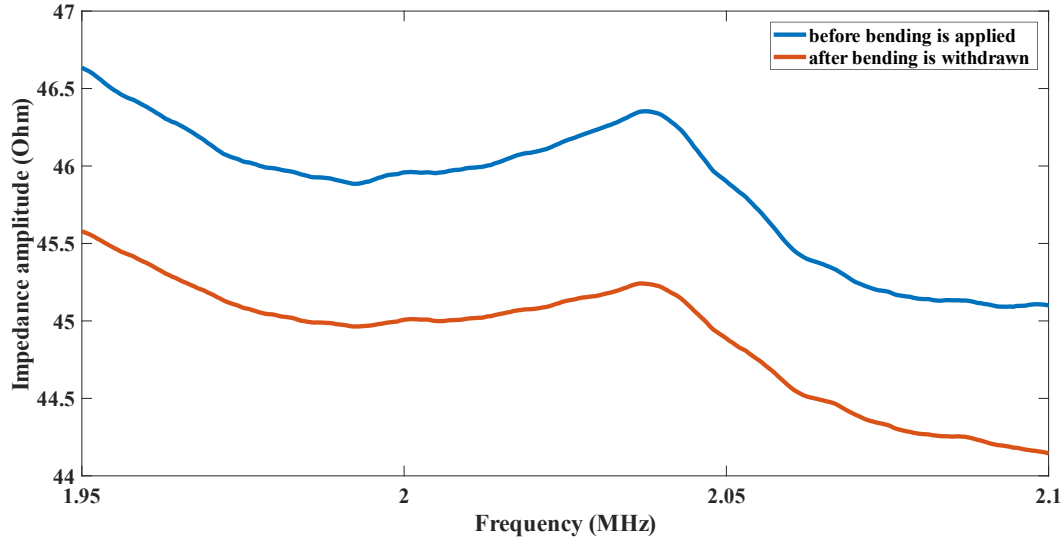


Figure 5.16 Electrical impedance measurement of the SU-8 circular membranes before and after the temporary bending.

Figure 5.16 shows that the reflect-back of mechanical resonance onto the impedance magnitude curves can be observed both before and after the temporary bendings, indicating that the bi-directional electromechanical interface exists in the circular membranes.

The difference between the two curves is mainly the electrical impedance magnitude's vertical shift. The shift can be expected because the sample was disconnected from the impedance analyzer before the temporary bending and re-connected afterward—the contact resistance experience minor changes during such a process. No significant frequency shift for the peak of the mechanical resonance reflect-back is observable. The frequency value corresponding to the peak is around 2.04 MHz, 0.99% deviated from the simulated natural frequency. Since all 1500 circular membranes are connected in parallel for the impedance measurement, such a minor variation

between the measurement and the simulation demonstrates that the overall process predictability and reproducibility are acceptable.

5.4 Summary

Chapter 5 applies the fabrication method developed in Chapter 4 for SU-8 out-of-plane capacitive MEMS structures on Dupont® Pyrulax™ copper-polyimide composites.

Experimental case studies have confirmed that the newly-developed fabrication technology retains acceptable process controllability on these metal-polymer composites. It is also possible to use the newly-developed technology to manufacture SU-8 out-of-plane MEMS structures with bi-directional coupling interfaces.

The variation in the manufactured test structures' electromechanical behaviors before and after the temporary bendings has been minor. The performance consistency validates the robustness of the fabrication technology from another perspective.

These experimental results mean that on flexible substrates, the sacrificial-layer-free fabrication method of SU-8 out-of-plane MEMS devices has a performance similar to the traditional SU-8 surface micromachining, providing additional evidence for the application potential of the novel technology path.

This chapter's research work also systematically validates the suitability of using Pyrulax™ composites as reliable, low-cost substrates for polymeric capacitive MEMS structures. These composites can be processed in more flexible manners, bringing a solution to address a critical issue in polymeric in-plane capacitive MEMS structure manufacturing. The detail of the corresponding work will be presented in Chapter 6.

Chapter 6: A new fabrication technology for SU-8 in-plane MEMS structures

Chapter 6 is dedicated to the development of a new fabrication technology for SU-8 in-plane MEMS structures. Such research helps create a comprehensive technology framework that can manufacture the two primary types of MEMS devices using SU-8 photoresist. Figure 6.1 illustrates the research carried out in this chapter.

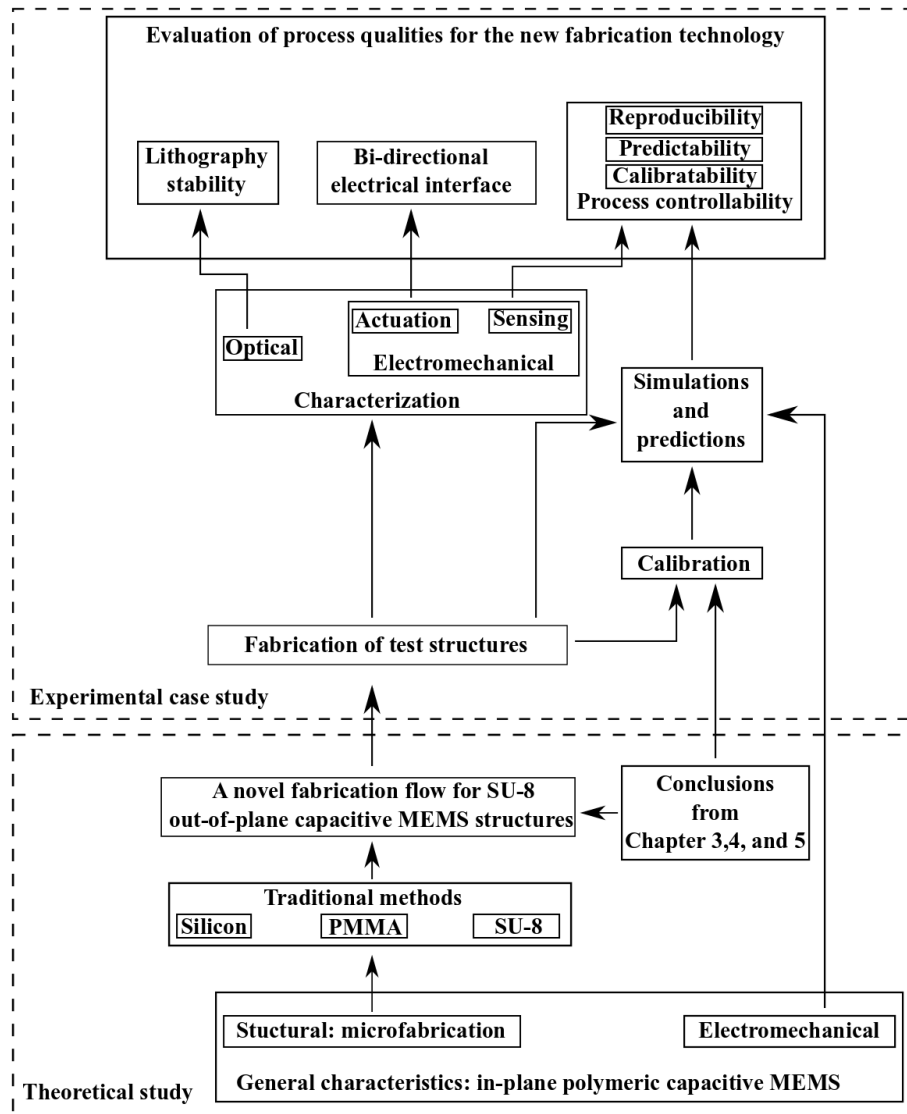


Figure 6.1 Depiction of the detailed research work carried out in Chapter 6

Chapter 6 is organized in the following way to implement the research shown in Figure 6.1. Section 6.1 presents the generic structural characteristics of in-plane MEMS structures. Existing fabrication flows for SU-8 in-plane MEMS structures, and their issues are introduced in Section 6.2. In the same section, a four-step fabrication flow based on a new micromachining strategy is introduced. The preparation work in the experimental case study is presented in Section 6.3. Section 6.4 presents the characterization result and the corresponding discussions on the process qualities of the newly-developed fabrication flow. Section 6.5 summarizes the whole chapter.

6.1 General characteristics of in-plane SU-8 MEMS structures

6.1.1 Structural characteristics

The generic schematic of in-plane MEMS structures is illustrated in Figure 6.2.

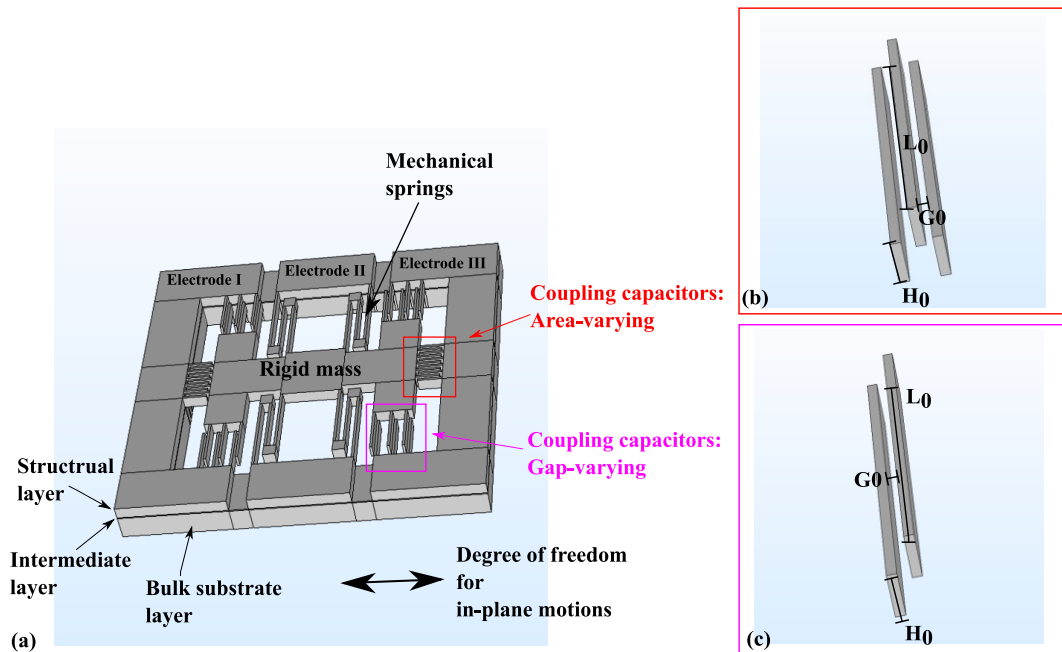


Figure 6.2 The generic characteristics of in-plane MEMS structures. (a) 3D model of the whole in-plane MEMS structures. (b) Capacitors for electromechanical coupling, area-varying principle; (c) Capacitors for electromechanical coupling, gap-varying principle.

As shown in Figure 6.2a, an in-plane MEMS structure consists of three functional layers. The bulk substrate layer supports the whole device. The intermediate layer is responsible for electrical insulations. The MEMS devices are implemented in the structure layer. Their movable components are released by etching the intermediate layer. Sometimes, the bulk substrate layer is also etched to release the structures[9, 58, 59]. The components in structural layers generally have their aspect ratios significantly higher than 1 to promote the in-plane motions and inhibit the out-of-plane motions.

The components of an in-plane MEMS device can be categorized into mechanical springs and rigid resonant mass. The mechanical springs are the primary objects to elastic deformation. Their mass is negligible compared with the rigid mass. It is common to implement the springs as folded beams. This configuration can grant low mechanical spring constant and structural stability. Springs will not deform due to being excessively narrow. The rigid mass moves as a whole and barely deforms. It makes up most of the effective resonant mass. Parts of the rigid mass are made into the parallel-plate capacitors responsible for the electromechanical couplings.

There are two ways to configure the coupling capacitors. When the plates' orientation is parallel with the degree-of-freedom for in-plane motions, as shown in Figure 6.2b, the in-plane device uses area-varying capacitors for electromechanical coupling. When the plates' orientation is vertical to the direction of the motion, as shown in Figure 6.2c, the coupling is done through gap-varying capacitors.

6.1.2 Electromechanical behaviors

The electromechanical coupling behaviors of SU-8 in-plane capacitive MEMS structures are still described by lumped micromodel with reduced order, obeying the conservation laws:

$$\left\{ \begin{array}{l} \frac{d}{dt}(E_{\text{capacitor}}) = u(t)i(t) + f_{\text{total}}(t) \frac{dx(t)}{dt} \\ i(t) = C(t) \frac{du(t)}{dt} + \frac{dC(x)}{dx} u(t) \frac{dx(t)}{dt} \\ f_{\text{electrical}}(t) = -\frac{1}{2} \frac{dC(x)}{dx} u(t)^2 \\ m_{\text{effective}} \frac{d^2x}{dt^2} + b \frac{dx}{dt} + k_M x = f(t) \end{array} \right. \quad (6.1)$$

The variables in Eq(6.1) have been defined in Chapter 4. Gap-varying SU-8 in-plane MEMS structures have the same non-linear coupling principle as out-of-plane MEMS devices. The corresponding electrostatic force, pull-in voltage, and displacement can be expressed by:

$$\left\{ \begin{array}{l} C_0 = \frac{\varepsilon A}{g_0} \left(1 + \frac{x}{g_0}\right)^{-1} \\ F = -\frac{1}{2} \frac{C_0}{g_0} \left(1 + \frac{x}{g_0}\right)^{-2} u^2(t) \\ u_{\text{pull-in}} = \sqrt{\frac{8g_0 k^2}{27C_0}} \\ x_{\text{max}} = \frac{1}{3} g_0 \end{array} \right. \quad (6.2)$$

The electromechanical coupling for area-varying SU-8 in-plane capacitive MEMS structures can be described by:

$$\left\{ \begin{array}{l} C = \frac{\varepsilon L_0 H_0}{G_0} \left(1 + \frac{x(t)}{L_0}\right) \\ f(t) = \frac{1}{2} \frac{dC}{dx} u(t)^2 = \frac{1}{2} \frac{\varepsilon H_0}{G_0} u(t)^2 \\ i(t) = C \frac{du(t)}{dt} + \frac{\varepsilon H_0}{G_0} u(t)v(t) \end{array} \right. \quad (6.3)$$

In Eq(6.3), C is the area-varying capacitor; ε is the dielectric constant; L_0 , H_0 , and G_0 are the initial overlapped length, the thickness of the parallel plate, and the gap in-between; $x(t)$ is the mechanical

displacement; $f(t)$ is the electrostatic force; $u(t)$ is the electrical voltage; $i(t)$ is the electrical current; $v(t)$ is the mechanical velocity. As shown in Eq(6.3), area-varying electromechanical coupling gets a constant electrostatic force, making the devices free from the non-linear pull-in effect. However, area-varying ones do not possess the flexibility in tuning the sensitivity through electrical ways. It is common for in-plane capacitive MEMS structures to use area-varying for actuation purposes and gap-varying for sensing.

6.2 A novel fabrication methodology for SU-8 in-plane capacitive MEMS structures

6.2.1 Fabrication flows: from silicon to SU-8 photoresist

Figures 6.3, 6.4, and 6.5 depict three fabrication flows of in-plane MEMS structures. Figure 6.3 presents an industrial-level fabrication flow of silicon in-plane MEMS structures, SOIMUMPs[9]. This thesis considers SOIMUMPs as the benchmark for manufacturing technologies of in-plane MEMS devices. Figure 6.4 shows the method to make polymeric in-plane MEMS through micro-molding. Figure 6.5 presents the surface micromachining of SU-8 photoresist to make polymeric in-plane MEMS structures [8, 58, 59].

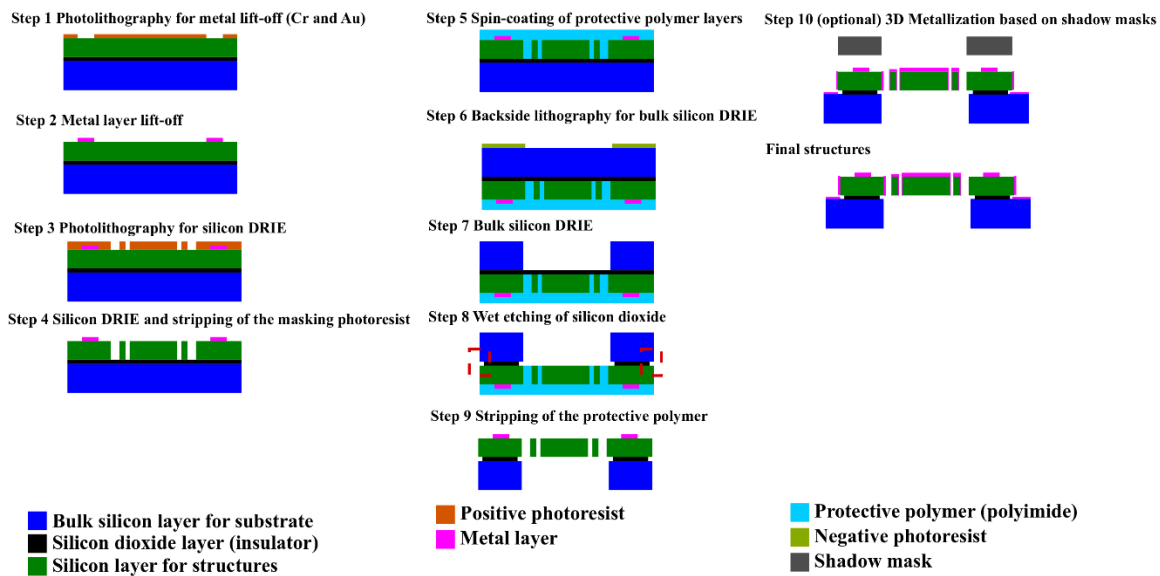


Figure 6.3 SOIMUMPs, the fabrication technology for silicon-based in-plane MEMS structures.

In Figure 6.3, SOIMUMPs uses silicon-on-insulator (SOI) as the raw material for processing [9]. The silicon structure layer generally has a thickness of 25 μm , while the bulk substrate layer is several hundred micrometers thick. The silicon dioxide layer in-between has a sub-micro level thickness. The whole fabrication flow can be subdivided into three phases.

First, the in-plane MEMS structures are fabricated by the classic silicon surface micromachining executing the deposition-masking-etching cycles on the structure layer. Second, the in-plane MEMS structures are released through a two-step processing sequence. Silicon bulk micromachining is conducted to create an open window on the bulk substrate silicon layer. Then a vapor wet etching of the exposed SiO_2 is done using hydro fluoride. The metallization process is used by SOIMUMPs to help the post-fabrication wire-bonding, packaging, and protect the structures from oxidation [9].

In-plane MEMS structures fabricated by SOIMUMPs are suspended within an open window on the substrate layer. The substrate and the intermediate layer underneath the movable components are removed. Such a process reduces the risk of process-related failures. The device area of in-plane MEMS transducers manufactured by SOIMUMPs is also free from process-level constraints [9]. Hence, this thesis considers such a method to release in-plane MEMS devices as an optimum microfabrication process. It should also be implemented for the fabrication of SU-8 in-plane MEMS devices.

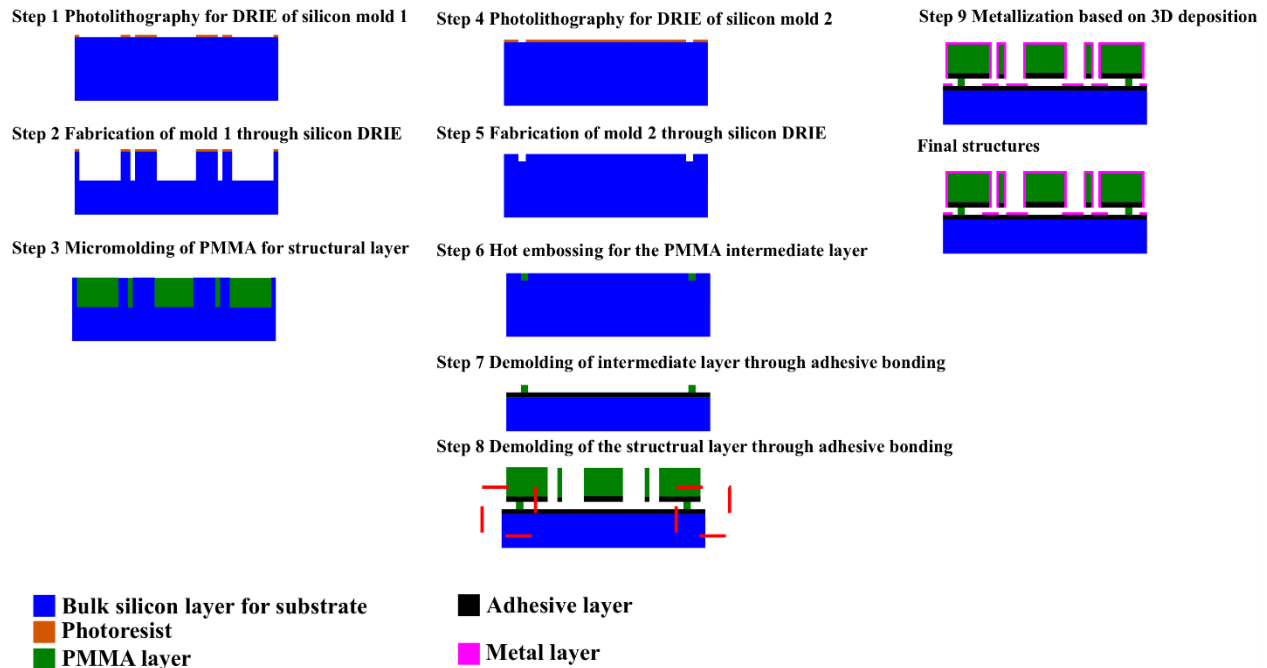


Figure 6.4 Polymeric micro-molding for in-plane MEMS devices

The hot-embossing process (a micro-molding method) in Figure 6.4 can be considered as a universal method to fabricate polymeric in-plane MEMS structures. It can be used for both non-photosensitive polymers and photoresists. As far as to the author's knowledge, this method was first reported and validated using PMMA in the research work of Zhao *et al.*[8]. It has used silicon DRIE to create molds for in-plane MEMS structures and spacers. The two components were assembled on another substrate using wafer bonders [8]. Since the spacers have been smaller than the anchors of the movable components, overhangs were formed after the assembly. These overhangs guarantee electrical insulation during metallization. Polymer in-plane MEMS devices need conductive layers on the vertical walls. 3D metallization methods, such as magnetron sputtering, are used to do so. These methods have good step coverage. If overhangs are not created, different electrodes are short-circuited through the common substrate. Though Zhao *et al.* are the pioneers in manufacturing polymeric in-plane MEMS devices. The Processing techniques used in

their work, such as silicon DRIE for the molds, offset most of the advantages in using polymers to make MEMS devices.

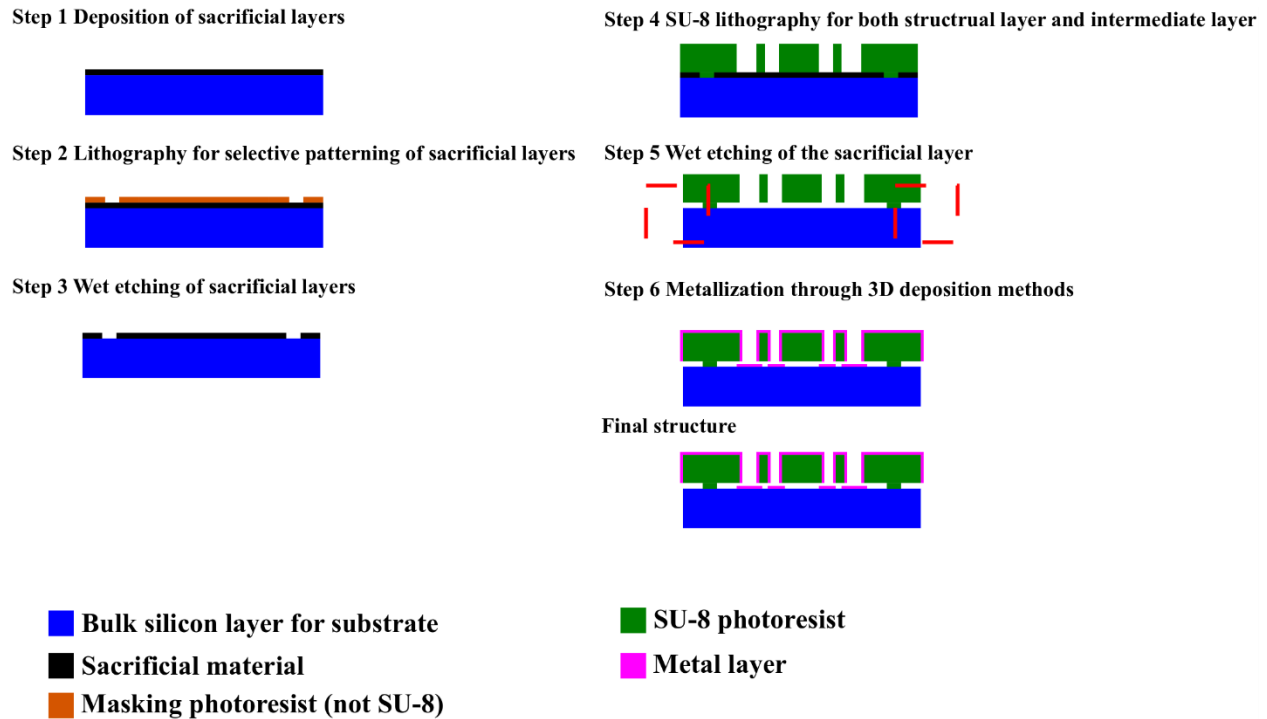


Figure 6.5 SU-8 surface micromachining for in-plane MEMS devices.

The fabrication method in Figure 6.5 is much simpler than the method in Figure 6.4, mainly because SU-8 lithography has been used to directly create microstructures in a single lithography process. The method in Figure 6.5 was first reported by Dai *et al.* in 2007. They supplemented some improvement in their manufacturing method in 2008 [58, 59]. They used copper as sacrificial layers. The selective patterning of the copper layers has been done in two ways: wet etching masked by a photoresist layer or electroplating masked by a positive photoresist layer. Small open windows are created through copper etching on the sacrificial layers. These small open windows help the formation of overhangs. The depth of the overhangs is controlled by the size of the open windows and the anchor of movable components. Dai *et al.* have used tilted e-beam evaporation

for the metallization to guarantee the full coverage of metal on the SU-8 vertical walls [59]. The tilting angle can be estimated by:

$$\theta = \arctan\left(\frac{g}{H}\right) \quad (6.4)$$

In Eq(6.4), g is the actual gap obtained during the SU-8 lithography, while H is the thickness of the vertical walls.

6.2.2 Issues for SU-8 in-plane MEMS fabrication

The main issue of the SU-8 surface micromachining in Figure 6.5 is that the methodology to release the in-plane movable microstructures is not optimum compared to SOIMUMPs.

Technically, this issue can be addressed by using silicon bulk micromachining, the same as SOIMUMPs. However, most of the advantages of making polymeric in-plane MEMS devices will be lost by doing so. Novel micromachining strategies need to be developed to implement the optimum processing method for SU-8 in-plane MEMS devices.

6.2.3 A four-step fabrication flow of in-plane SU-8 MEMS structures

This thesis provides one novel strategy to remove the supportive layers underneath in-plane microstructures for release. This new strategy is named ‘Border-bulk.’ A new fabrication method of in-plane SU-8 MEMS structures has been implemented based on this new strategy. This new method consists of only four steps, making it simpler than the method in Figure 6.5. The schematics of the new fabrication flow are illustrated in Figure 6.6 to Figure 6.9.

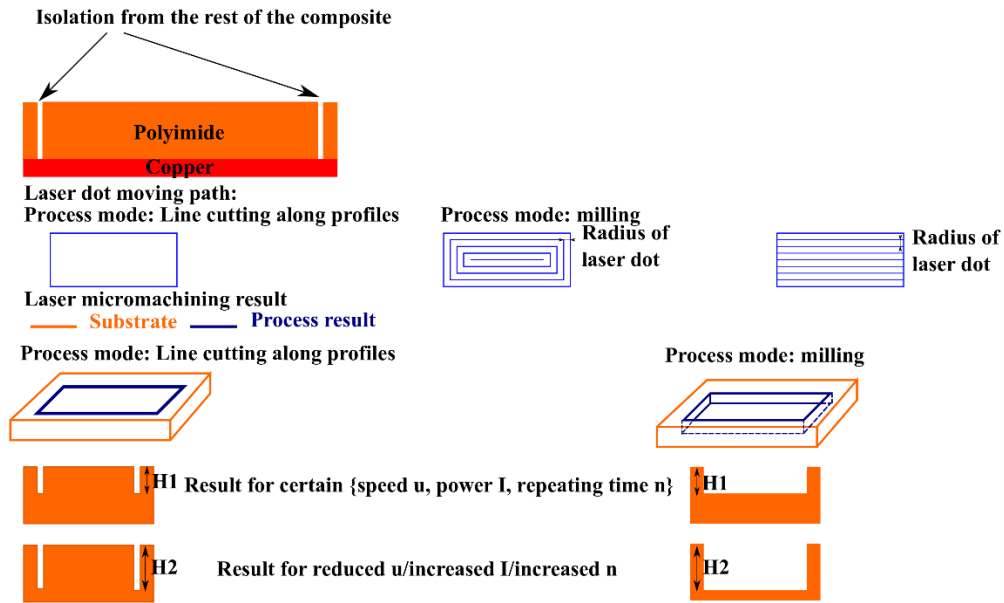


Figure 6.6 Step 1, copper-polyimide processing based on a new strategy

As shown in Figure 6.6, the new fabrication method's first step reflects well the core idea of the 'Border-bulk' approach. This new strategy process only the profile of the area to be removed. Sacrificial layers will be exposed after the profile's processing is completed, isolating the area-to-be-removed from the rest of the substrate. Once the sacrificial layer on the top of the isolated area is removed, the isolated area will detach. In comparison with traditional bulk micromachining, methods based on 'Border-bulk' reduce the consumption of resources. Meanwhile, it becomes possible to use novel methods for simpler processing when the micromachining flow is based on the 'Border-bulk' method. This advantage is reflected in Figure 6.6 by the processing method of the substrate material.

In this thesis, the new fabrication flow based on the 'Border-bulk' methodology uses the Dupont[®] Pyrulax[™] copper-polyimide composite as substrates. As shown in Figure 6.6, the implementation of the 'Border-bulk' method on these composites has used the laser micromachining process. Laser micromachining can make the whole process simpler and safer.

This direct micromachining method removes the polyimide on the laser dot path. There is no need to use protective layers or conduct the corresponding deposition-masking-etching cycles to process them, increasing the process simplicity. Conventional wet etchant of polyimide contains potassium hydroxide (a strong, corrosive alkali). The etching process requires heating the solution to 85°C [134]. Laser micromachining of polyimide does not need such highly hazardous chemicals and the high temperature, increasing process safety.

Though laser micromachining is a serial process [134, 135, 146], the processing speed is not an issue. As shown in Figure 6.6, laser micromachining can implement two types of processing with the same mask design. It can either inscribe the profile of a 2D geometry or create a concave pattern of the design on the surface of a material. The laser cutting constrains the moving path along the border of the geometry, while the laser milling fills the area enclosed by the geometry with the moving path in the format of either contour or zig-zag routes. In both cases, the depth of the created patterns is determined by the setup of output power, laser moving speed, and repeated times. Higher output power, lower moving speed, and more repeated time create deeper patterns. Since laser cutting only etches the material along with the profile of geometry, it is a rapid process, particularly on materials like polyimide. Such material has a relatively low degradation temperature (300°C to 450°C) [134, 135, 146, 147], so it is possible to cut through the material using a moderate power, fast laser moving speed, and only a few repeated cycles. The only extra work is to obtain a proper set of processing parameters (the output power, moving speed, and repeating time) through experimental calibration. When laser micromachining is used to implement the process in Figure 6.6, it needs to avoid the excessive removal of the copper layer.

SU-8 lithography for in-plane MEMS structures

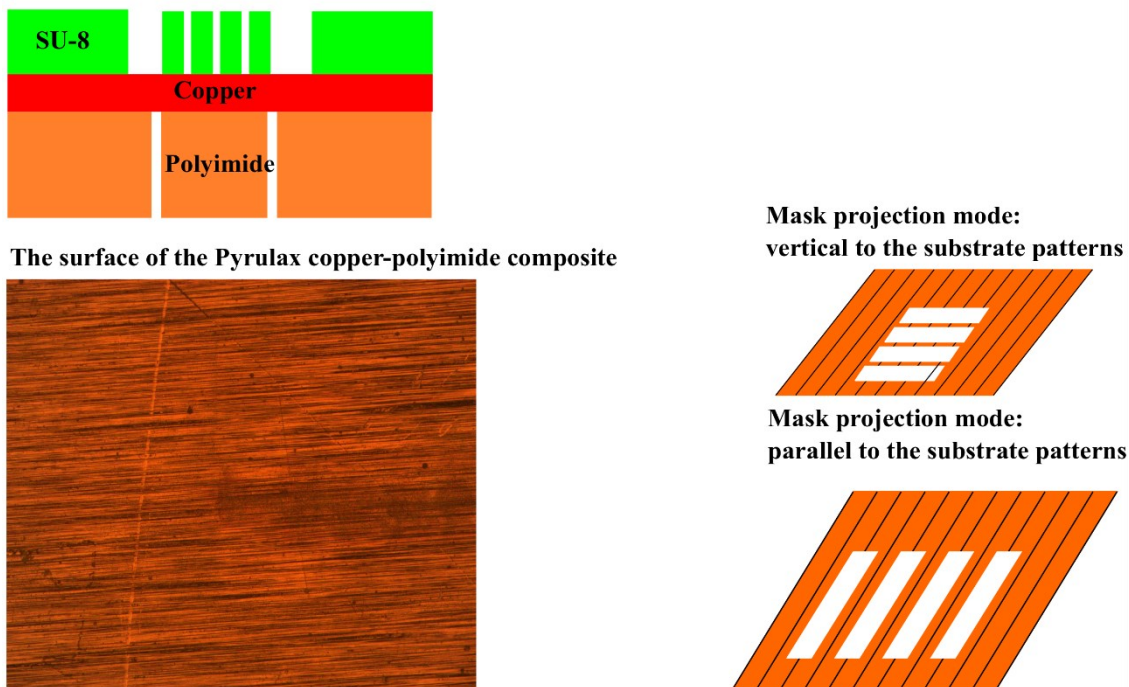


Figure 6.7 Step 2: SU-8 lithography on the copper surface.

As shown in Figure 6.7, the SU-8 lithography process is directly conducted on the copper surface. The conclusion from Chapter 5 supports the suitability of such a practice with respect to process controllability. Binary lithography is used here instead of grayscale lithography. Experimental calibrations are necessary for two reasons. As shown in Figure 6.7, when the mask is projected onto the substrate, the mask design can be parallel or vertical to the thread-like topological patterns. Whether the ‘threads’ on the copper surface affect the lithography result needs to be experimentally checked. The lithography resolution constraints also need experimental determination. They determine the actually-achievable gap width and the corresponding design. In-plane MEMS devices need parallel plates closely spaced to form the coupling capacitors, so the lithography resolution constraints are very important.

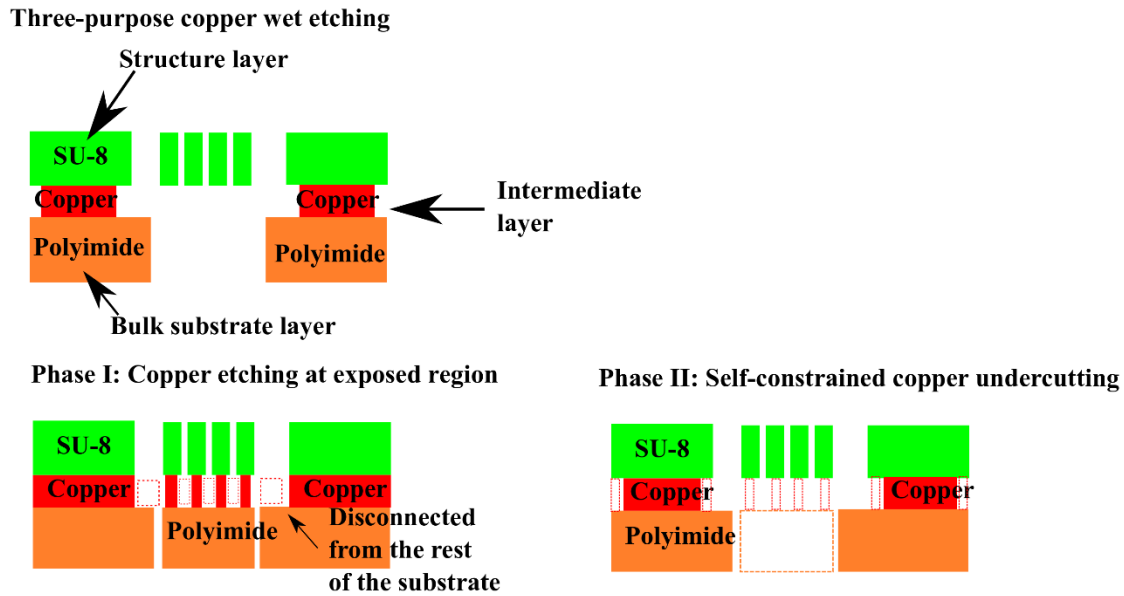


Figure 6.8 Step 3: multi-purpose copper etching

The wet etching of copper layers in Figure 6.8 uses a Ferric Chloride water solution. The release of SU-8 movable components, removing the polyimide substrate, and the formation of overhangs within the copper layer are implemented simultaneously in a single copper etching process.

The dissolution of copper can be divided into two phases. After the sample is immersed into the solution, the copper layer within the regions not covered by SU-8 structure layers is etched vertically down to the polyimide layer. This is the first phase in Figure 6.6. The copper etching propagates horizontally within the gap between SU-8 structural layers and the polyimide substrates, similar to moving in a microfluidic channel[148]. Both SU-8 and polyimide are hydrophobic[118, 149]. The contact angle of water with a SU-8 surface is 90° , while the angle with a polyimide surface is over 80° . Such large contact angles limit the depth that the etchant solution can propagate. When the copper etching stops, a significant amount of copper should

remain, forming the spacers within the intermediate layer. After the dehydration, the microfluidic channels left behind become overhangs.

Releasing holes on the body of rigid mass may be necessary to guarantee the thorough removal of the copper underneath. When the copper underneath the movable components is removed, the polyimide layer is disconnected from the rest of the substrate layer, peeling them off and suspending the movable SU-8 components within an open window on the substrate layer.

Tilted magnetron sputtering

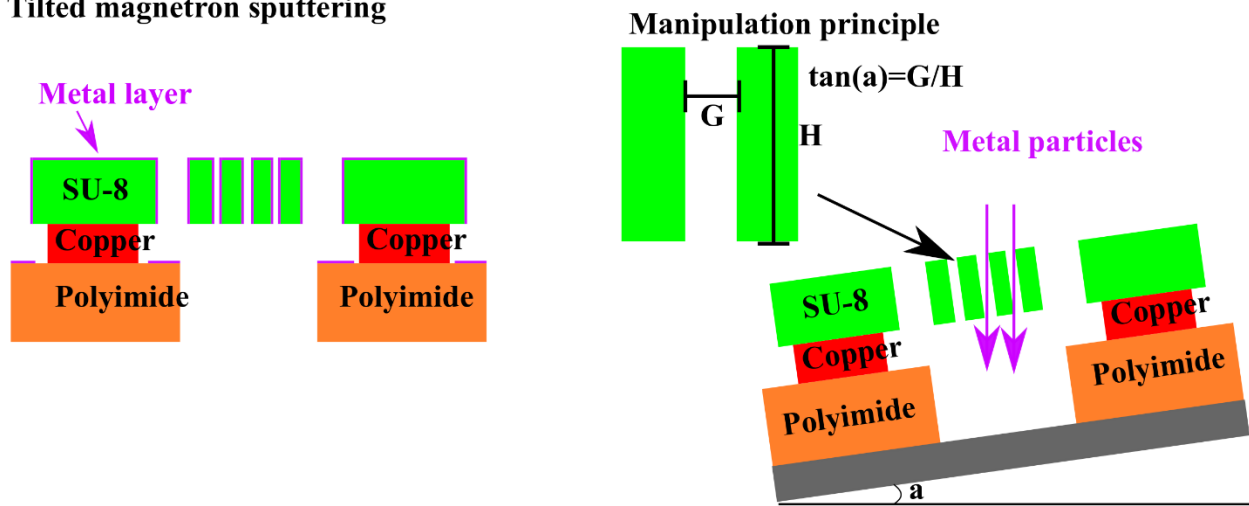


Figure 6.9 The metallization process of the in-plane structures

As shown in Figure 6.9, the newly-designed method uses tilted magnetron sputtering to get conductive layers on the vertical polymeric walls. The tilting angle is computed by the thickness of the coated layer and the gap between the two parallel plates, based on Eq(6.4).

6.3 Experimental case study of the newly-developed fabrication flow

The Pyrulax™ composites used in this chapter have a 45μm thick polyimide layer and a 35μm thick copper layer. 75μm thick SU-8 2050 layers were deposited onto the copper surface to fabricate in-plane capacitive MEMS test structures.

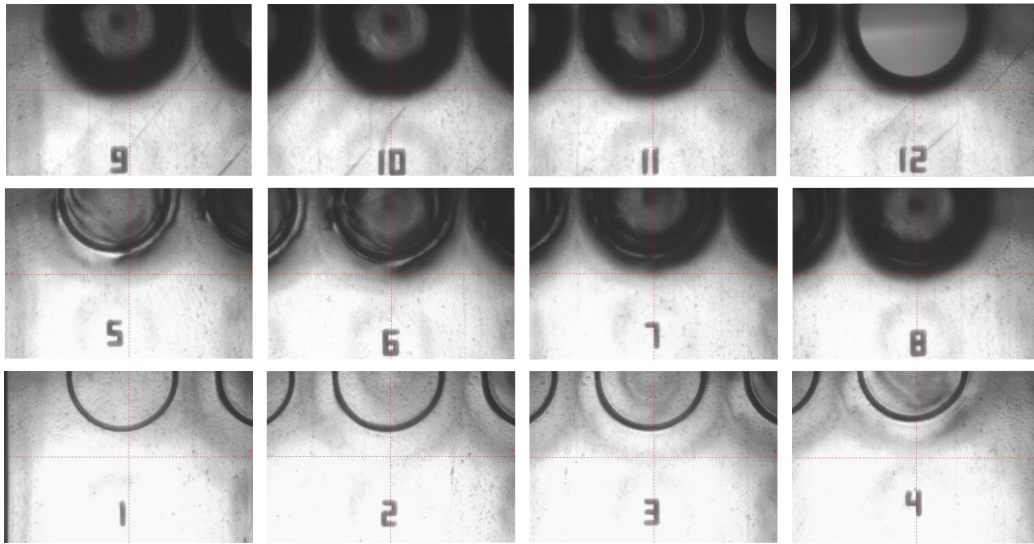
6.3.1 Calibration for laser micromachining on the copper-polyimide composite

The laser micromachining process used an Oxford[®] laser micromachining system (laser wavelength: 355 nm). This equipment provides three tunable parameters: the relative output power (in percentage), the moving speed of the laser dot, and the repeated cycles. The goal of the experimental calibrations is to find out the proper repeated times for fixed output power and moving speed. These repeated times allow the laser micromachining to penetrate only the 45 μm polyimide layer but not the 35 μm copper layer. The setup of the experimental calibration is summarized in Table 6.1.

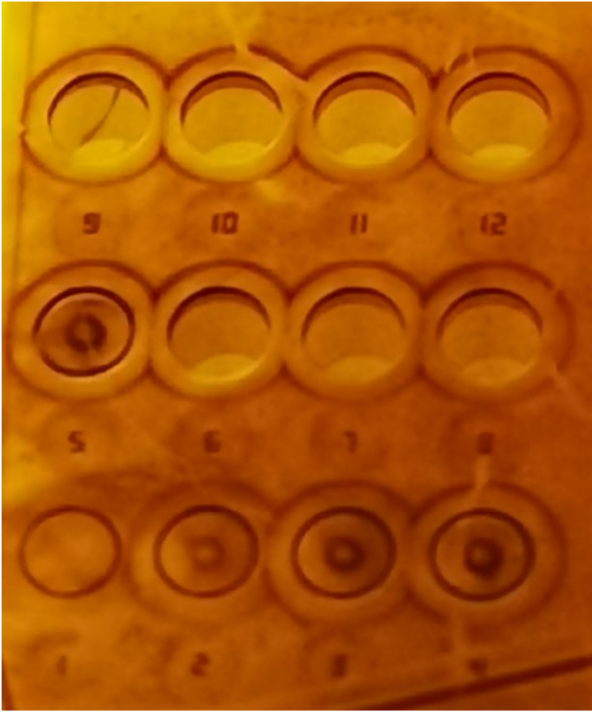
Fixed laser process parameters		Repeating cycles			Calibration geometry design	
I%	u (mm/s)	Initial	step	Final	Structure:	Circular plate
85	1	1	1	12	Radius (mm)	0.5

Table 6.1 Setup of the laser micromachining to determine the proper repeated times

In Table 6.1, the output intensity is fixed at 85%, and the moving speed is fixed at 1mm/s. Circles are used as calibration designs. Their radius is 0.5mm. The laser-cut is repeated from 1 to 12 times. Then, laser-micromachined samples are immersed in the FeCl_3 water solution for copper etching. If the repeating cycles have resulted in the complete removal of the polyimide layer, the corresponding circular plates will detach from the substrate. The calibration result is shown in Figure 6.10.



(a) $\bar{\text{—}}$ 300 μm



(b) — 1mm

Figure 6.10 Experimental calibration result for laser cutting on polyimide layers. (a) Samples under the inspection camera of the Oxford[®] laser system. (b) Samples after the copper wet etching

In Figure 6.10, the values of repeated cycles have also been engraved on the polyimide surface below the corresponding circles. When the laser cut was repeated more than six times, the

peripheral of the resulted circles become blackened in Figure 6.10a. When the cut was repeated 12 times, the circular plate has detached from the substrate, indicating that both polyimide and copper layers were penetrated. As shown in Figure 6.8b, circular plates made from laser cuttings repeated by six times or more have detached from the substrates after the copper etching. This result indicates that the lower limit for repeating times is 6. The experimental result in Figure 6.8b also indicates that the blackened profile in Figure 6.8a can be used as a convenient criterion to judge if the penetration has been achieved.

6.3.2 SU-8 lithography calibration

An SF-100™ maskless lithography system is used to carry out the UV lithography. The influence of the surface topological characteristics (thread-like patterns on the substrate) on the lithography quality is experimentally studied using the process recipe in Table 6.2.

Soft baking		UV exposure	Post-exposure baking		Developing
65°C	95°C	10 mW/cm ²	65°C	95°C	6 min (immersion)
3 min	5 min	5s ~ 10s, 0.1s increment	3min	5min	

Table 6.2 Process parameters for SU-8 lithography calibration

In Table 6.2, the soft baking duration at 95°C has been shortened to enhance the crosslinking density and strength. Figure 6.11 shows the mask design used to evaluate the influence of surface topological characteristics and the representative lithography result.

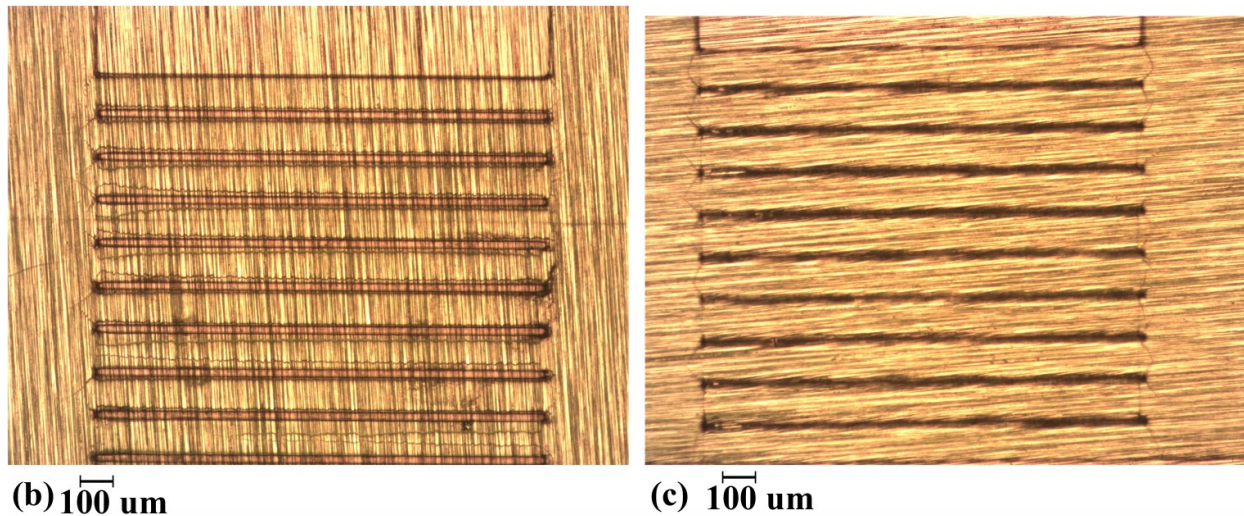


Figure 6.11 Experimental study for the influence of the surface thread-like pattern on the lithography qualities. **(a)** Mask designs; **(b)** Representative result when the orientation of the substrate thread-like pattern is aligned with the Y-axis of the mask; **(c)** Representative result when the orientation of the substrate thread-like pattern is aligned with the X-axis of the mask.

In Figure 6.11a, the stripes are $1000\mu\text{m}$ in length and $100\mu\text{m}$ in width. The gap between each stripe is $25\mu\text{m}$. The influence of the substrate topological characteristic is evaluated by the achieved gap width after lithography. The separation of stripes can only be implemented if the

stripes are oriented vertically to the thread-like patterns, as shown in Figure 6.11b. Stripes can not be separated if the stripes are in parallel with the threads, like in Figure 6.11c.

The calibration for lithography resolution constraints for 75 μm SU-8 2050 layers has been conducted with the mask design in Figure 6.12.

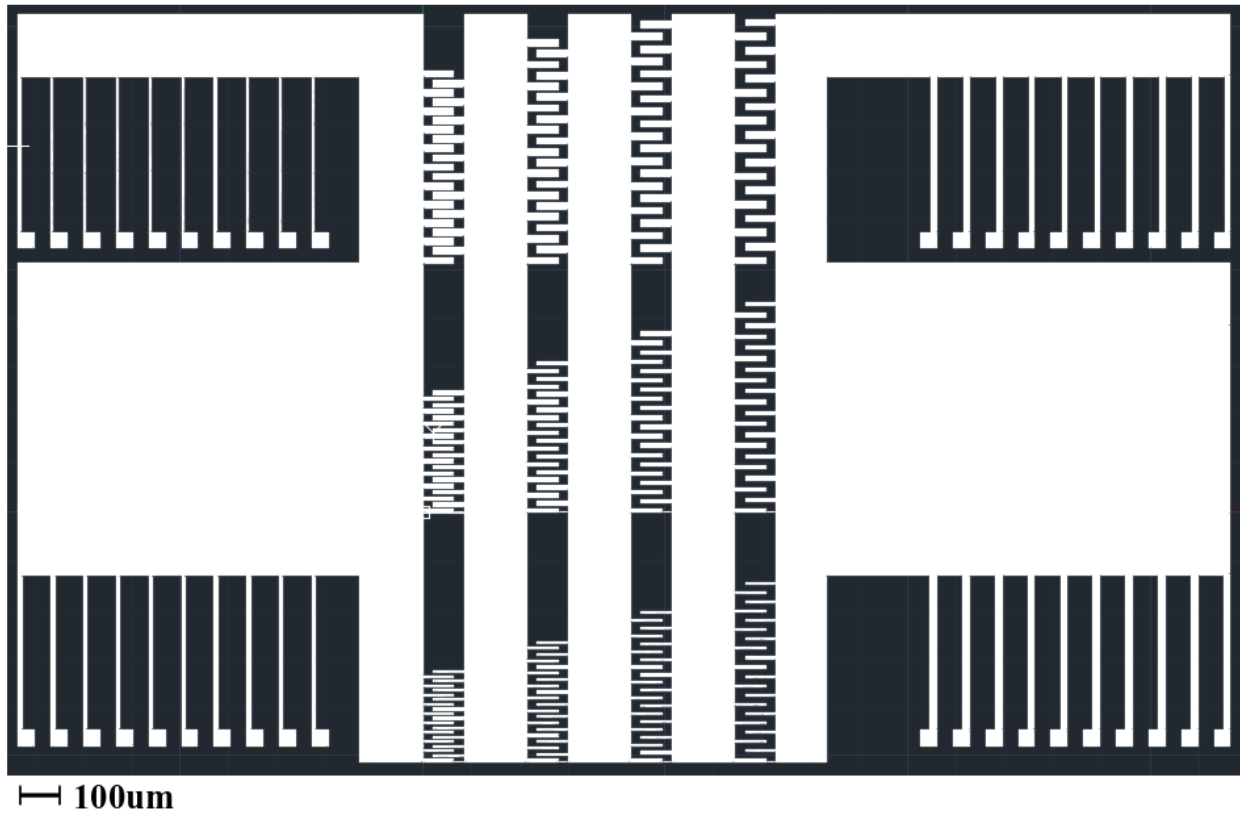


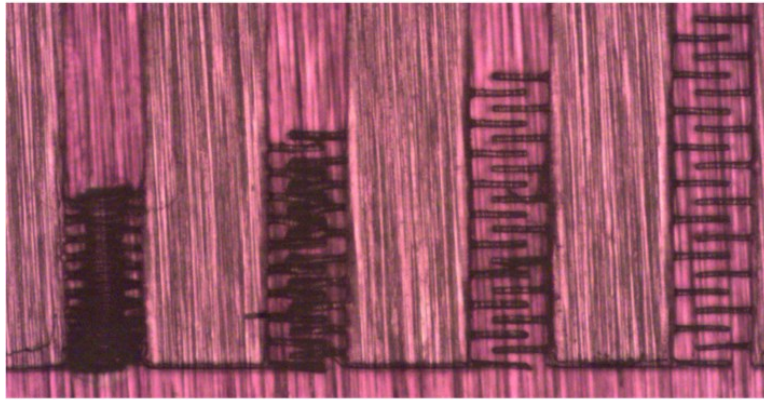
Figure 6.12 Mask design to calibrate SU-8 lithography for optimum exposure duration and structure design.

Figure 6.12 determines the limitations on the width of elastic spring beams, as well as the width and spacing of the parallel plates. Table 6.3 summarizes the dimension designs of the mask.

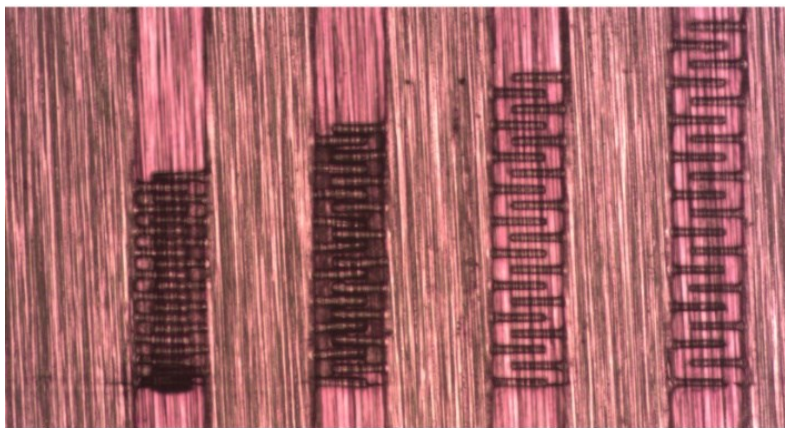
Elastic spring beams			
Length:	500 μm	Width:	5 μm , 10 μm , 15 μm , 20 μm
Interdigitated plates			
Length:	Width:		Spacing:
125 μm	5 μm , 10 μm , 20 μm		10 μm , 15 μm , 20 μm , 25 μm

Table 6.3 Dimensions of the mask design for SU-8 lithography calibration

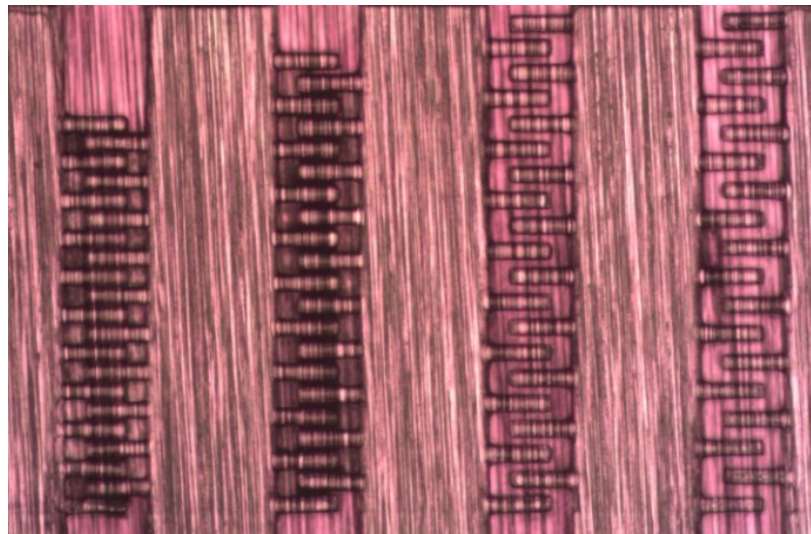
It has been experimentally discovered that exposure durations between 7s and 8s provide the optimum balance between crosslinking strength and lithography resolution. Shorter exposure durations have resulted in a significant increment in structural deformations (an indication of weak crosslinking strength), while elongated durations diminished the gaps. The lithography result corresponding to these optimum exposure durations is shown in Figures 6.13 and 6.14.



(a) |—| 100 μm



(b) |—| 100 μm



(c) |—| 100 μm

Figure 6.13 Calibration result for interdigitated fingers in Table 6.3. (a) Width: 5 μ m; (b) Width: 10 μ m; (c) Width: 20 μ m

As shown in Figure 6.13, the 10 μm spacing design is not achievable. The plates have been widened during the lithography process, eliminating the gap in-between. The 15 μm spacing design can be implemented in an unstable way. Mergings and deformations related to the crosslinking beyond exposed regions are still observable. The first duplicatable spacing design is 20 μm . Since the 10- μm spacing design is not achievable, the numerical value for the widening effect is estimated to be 5 μm . A design of 20 μm provides an actual gap that is 10 μm wide. This processing capability is at the same level as the existing fabrication technologies for polymeric MEMS structures[8, 58, 59].

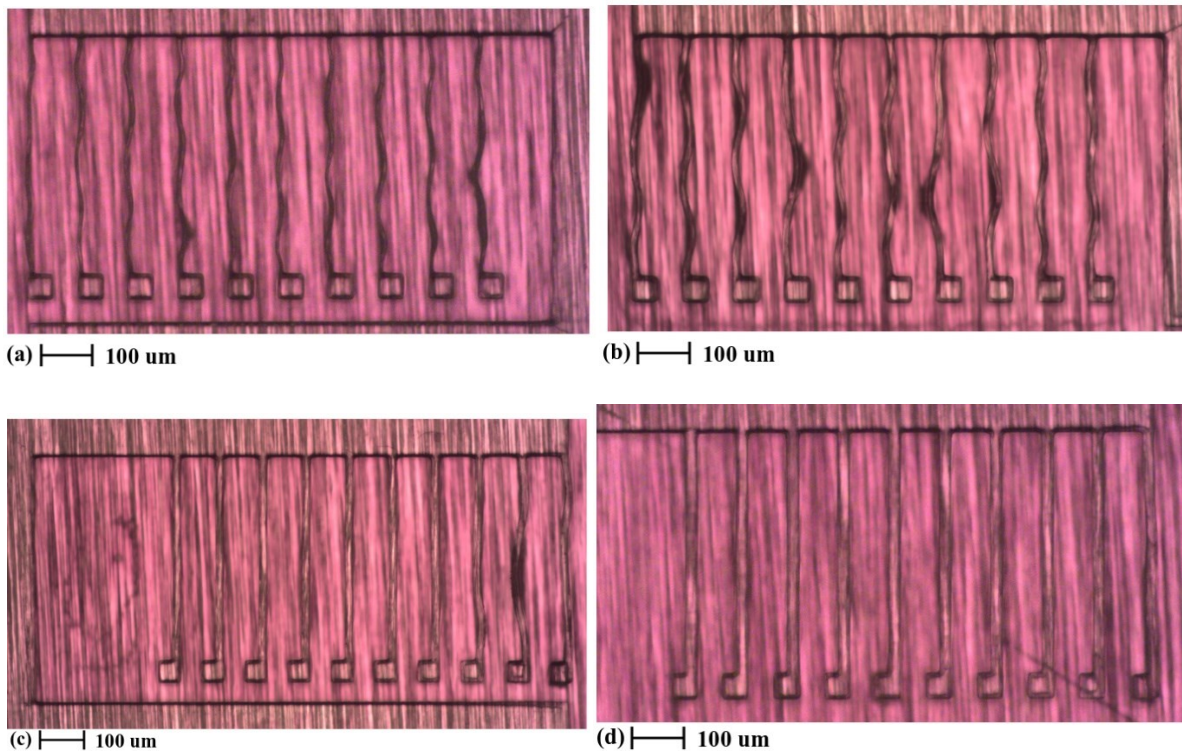


Figure 6.14 Calibration result for the elastic beams in Table 6.3.

As shown in Figure 6.14, the elastic spring beams that are 500 μm long need a width of over 15 μm to make them free from deformations.

6.3.3 Design and simulation of in-plane MEMS test structures

Table 6.4 summarizes the design of in-plane MEMS test structures. Table 6.5 presents the SU-8 material properties used in computations and simulations.

Actuation/Sensing principle:			Area variation			
Dimensional parameters						
Interdigitated plates	Length (<i>um</i>)	Overlapping length (<i>um</i>)	Width (<i>um</i>)	Thickness (<i>um</i>)	Gap (<i>um</i>)	Amount
	50	25	10	75	25	100
Movable plate ridge	Length (<i>um</i>)		Width (<i>um</i>)	Thickness (<i>um</i>)		Amount
	350		50	75		12
Bulk mass	Length (<i>um</i>)		Width (<i>um</i>)	Thickness (<i>um</i>)	Release hole radius (<i>um</i>)	Releasing hole amount
	1300		100	75	30	13
Elastic beam	Length (<i>um</i>)		Width (<i>um</i>)	Thickness (<i>um</i>)		Amount
	375		20	75		4
The estimated capacitance of a single test structure (fF)			110.63			

Table 6.4 Design of the in-plane MEMS test structures

Material properties of SU-8 2050 used for simulation		
Young's Modulus (GPa)	Poisson's ratio	Density (kg/m ³)
4.95 [30]	0.33[31]	1200 [150]

Table 6.5 SU-8 material properties used for simulation and computation

In Table 6.4, the test structures use area-varying for the electromechanical coupling so that the non-linear disturbance on the electromechanical coupling is minimized. The mask designs for the laser micromachining of the polyimide substrate layer and the UV lithography of the SU-8 structure layer are presented in Figure 6.15.

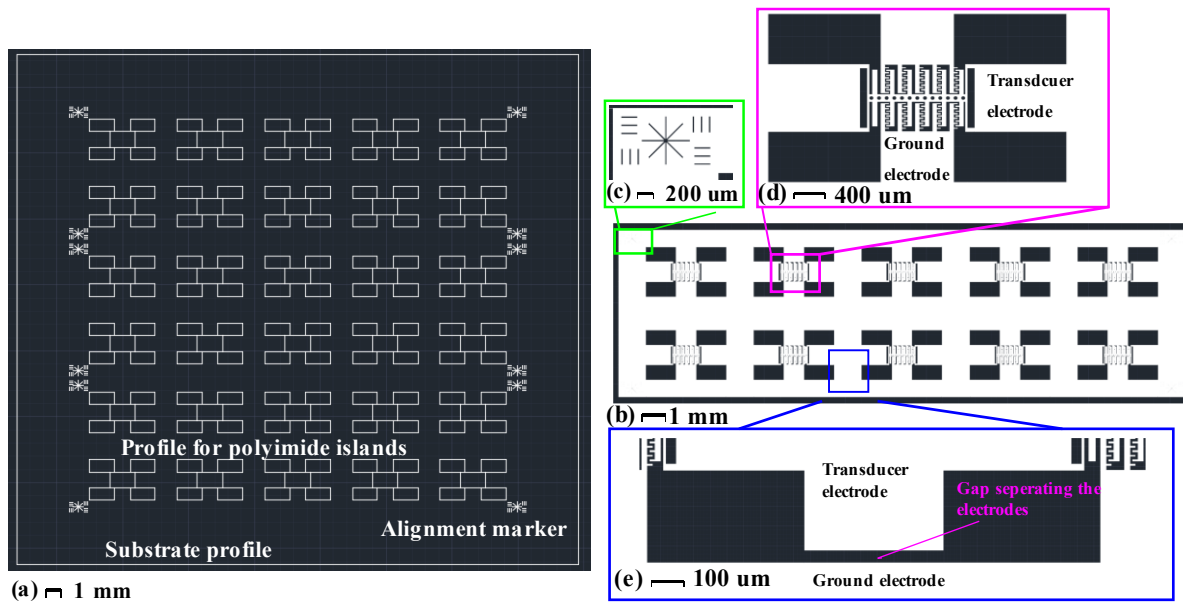


Figure 6.15 Mask files used to fabricate the proof-of-concept SU-8 in-plane MEMS comb drives. (a) Mask for laser micromachining of the polyimide layers. (b) Lithography mask for the proof-of-concept structures. (c) Zoom-in view of the alignment markers. (d) Zoom-in view of MEMS structures. (e) Zoom-in view of the gap separating the transducer electrodes from the ground electrodes.

In Figure 6.15a, the size of the PyraluxTM substrate is 30 mm by 33.4 mm. Two separate laser cuttings are done to create 30 ‘islands’ corresponding to 30 in-plane SU-8 MEMS structures

and 12 alignment markers. The laser cutting for the ‘islands’ needs only to penetrate the polyimide layer. The cut for the markers must penetrate both the polyimide and copper layer to make them visible on the copper surface. Figure 6.15c shows the detail of the alignment marker. Figure 6.15d shows the implementation of the area-varying in-plane test structures. Release holes are spaced by 100 μm from each other on the movable parts. In Figure 6.13e, a 50 μm gap is designed between the transducer electrodes and the ground electrodes to avoid electrical short-circuits.

6.3.4 Simulation and prediction for electromechanical behaviors

Simulations for the first two mechanical resonant modes of the test structures are carried out in COMSOL[®] Multiphysics[™] 5.3, using the material properties shown in Table 6.5. The results are shown in Figure 6.16.

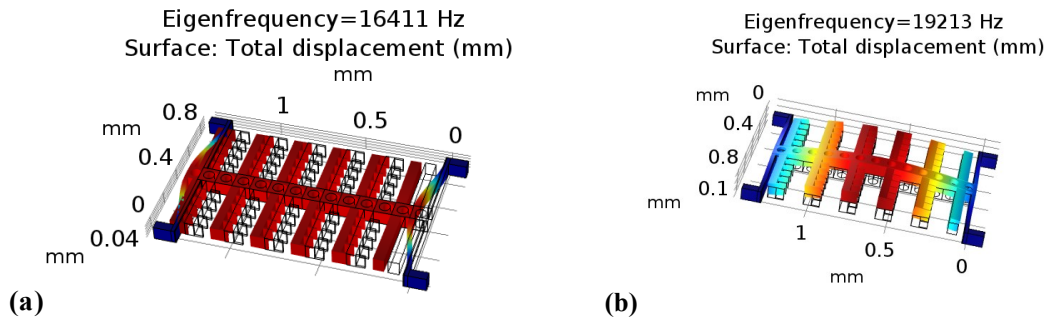


Figure 6.16 Finite element analysis simulation result for the resonant mode of the in-plane MEMS test structures. (a) Fundamental mode, in-plane motion, resonant frequency: 16.41 kHz; (b) Second mode, out-of-plane motion, resonant frequency: 19.21 kHz.

According to Eq(6.3), the electrical impedance of the test structures can be expressed as:

$$Z(\omega j) = R_{parasitic} + \frac{1}{(C_0 + 2 \frac{\epsilon h}{g} X(\omega j)) \omega j} \quad (6.5)$$

According to Eq(6.5), when the measuring frequency band is centered at the resonant frequency, bumps superimposed onto the capacitive impedance curve should be observable for both

impedance magnitude and phase. The frequency corresponding to the bumps should be close to the mechanical resonant frequency. The bumps indicate the existence of the bi-directional electrical-to-mechanical coupling interface. When the measuring frequency band is far away from the mechanical resonant frequency, the mechanical forced-vibration becomes negligible. Eq(6.5) becomes very similar to the general expression for capacitive impedance:

$$\begin{cases} |Z(\omega j)| = \frac{1}{C_0 \omega} \\ \log_{10}(|Z(\omega j)|) = -\log_{10}(C_0) - \log_{10}(\omega) \end{cases} \quad (6.6)$$

In such cases, the logarithm curve of the impedance magnitude becomes linear to the logarithm value of the frequency. The vertical shift between curves indicates the degree of difference in C_0 . If the metallization process of the new fabrication flow covers most of the vertical walls of the test structures, the shift between simulation by Eq(6.6) and the actual measurement should be minor.

6.3.5 Fabrication of the in-plane MEMS test structures

Two batches of samples for a total of 60 test structures were fabricated using the mask designs in Figure 6.15.

The relative output power and the laser moving speed were set to 85% and 1mm/s for the polyimide cutting. The cutting has been repeated seven times to create the isolated ‘islands,’ while the cut for the alignment markers was repeated fourteen times.

The SU-8 lithography for structural layers has used the processing parameters in Table 6.2. The exposure duration has been set to 7.5 seconds.

The releasing of the structures was done by immersing the samples in the copper etchant for 5 hours. The etchant was purchased from MG Chemicals (labeled etch rate: 4.4 to 5 $\mu\text{m}/\text{min}$).

200 nm Aluminum has been deposited afterward onto the structures by tilted magnetron sputtering using an AJA® thin film deposition system. The tilting angle for the 25- μm gap design is computed to be 11.3°. A 5- μm resolution degeneration is considered for the gap width. The height of the vertical wall is set to 75 μm .

6.3.6 Characterization methods

The first characterization is optical microscopic inspections. The purpose is to confirm the release of the movable SU-8 components and the formation of overhangs. The result of optical inspections evaluates the *lithography stability* of the newly-designed fabrication flow.

Then, the electromechanical coupling behaviors of the fabricated simple in-plane structures are characterized, with two types of measurement. First, the mechanical resonance of individual test structures under electrostatic actuation was measured. Fifteen out of the 30 test structures were randomly selected for each batch to measure the mechanical resonance, using the planar motion analyzer module of a Polytec® MSA-500 system. The actuation signal consists of 5V DC bias with an additional 3V peak-to-peak AC chirp wave. The signal is amplified by 20 times using an A Tegam® 2350 amplifier before it is used as the electrical actuation voltage for the comb drives. The electrical actuation validates the existence of metal coating on the vertical wall. The standard deviation of the measured frequency is used to evaluate the *reproducibility* of the developed fabrication process, while the average resonant frequency reflected the process *predictability*.

The electrical impedance of all 60 fabricated test structures during the electrostatic actuation is measured. The impedance measurement has two purposes. It validates the existence of the bi-directional electromechanical coupling and evaluates the coverage of the thin metal film on the vertical walls. The measurement for the bi-directional interface selects a frequency band centered at the simulated mechanical resonant frequency. The measurement to evaluate the metal

coverage uses a frequency band away from the mechanical resonant frequency. An Agilent® A4294A impedance analyzer was used for the impedance measurement. The input excitation signal consists of a 40V DC bias and a 2V peak-to-peak AC chirp wave.

6.4 Characterization result and discussion

6.4.1 Optical inspection

The microscopic images of the in-plane MEMS test structures for the fabrication technology are shown in Figure 6.17.

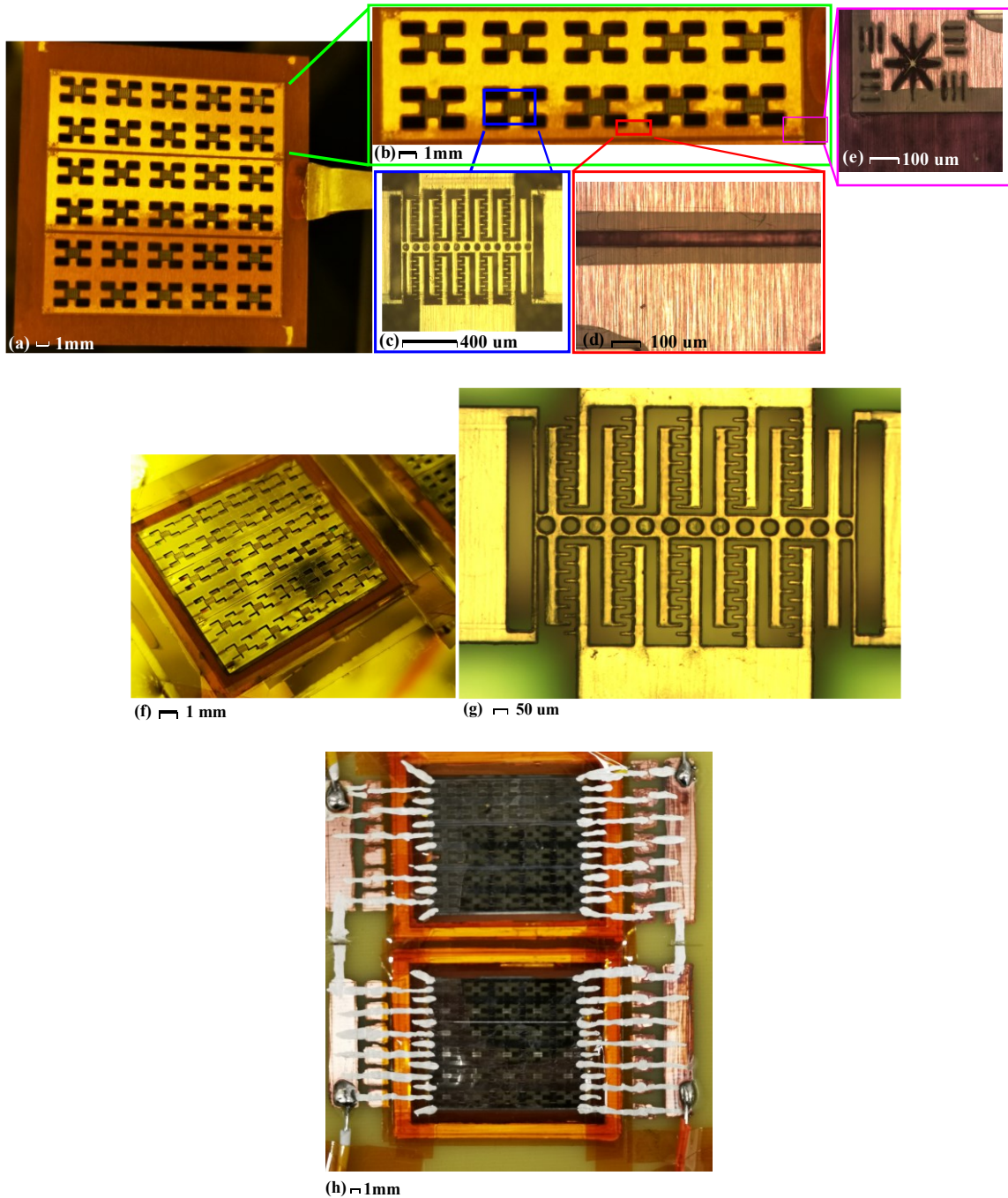


Figure 6.17 Optical inspections of the in-plane MEMS test structures at different phases of the new fabrication flow. (a) After the multi-purpose copper wet etching. (b) Zoom-in view of 10 test structures after the copper wet etching. (c) Zoom-in view of a single released test structure. (d) and (e) Overhangs formed at different locations of the design. (f) A single batch of test structures after the metallization. (g) Zoom-in view of a single test structure after metallization. (h) The two batches of in-plane MEMS test structures after the packaging.

As shown in Figures 6.17, no polyimide layers have remained connected with the movable components of the test structures after the copper wet etching. This result indicates that the newly-designed fabrication flow is controllable and stable. In Figure 6.17c, no significant deformation can be spotted, which is a good sign of high crosslinking strength and structural robustness. In Figures 6.17 d and e, overhangs have been formed uniformly at the edges of the fixed electrodes. The depth of the overhang was around 150 μ m. If the undercut depth had been computed with the labeled reaction rate of the ferric chloride etchant, this value should have been 1.3mm to 1.5mm. The much shallower depth confirms that the copper etching in the new fabrication method is self-constrained.

In Figure 6.17f, the surface of the test structures after the metallization has been reflective, demonstrating a metal deposition with acceptable qualities. Figure 6.17g has further validated this conclusion. Figure 6.17h shows the packaging of the test structures after the whole fabrication flow. Conductive silver paint has been used to draw the interconnects.

6.4.2 Measurement of mechanical resonance under electrical actuation

The statistics of the measured mechanical resonance for the 30 selected structures are summarized in Table 6.6.

Average frequency measured (kHz)	Standard deviation	Relative error to simulation	Average quality factor
16.2590	3.2%	-0.92%	60.82

Table 6.6 Statistics of the mechanical resonance for selected in-plane MEMS test structures

The average frequency of the 30 selected test structures (15 from each batch) is 16.259 kHz. It is only slightly smaller (-0.92% in Table 6.5) than the simulation result. The match between the measurement result and the simulation supports good process *predictability*. The standard

deviation among the 30 measured structures has been 3.2%, indicating acceptable process *reproducibility*. The measured characteristics of mechanical resonant frequency are shown in Figure 6.18.

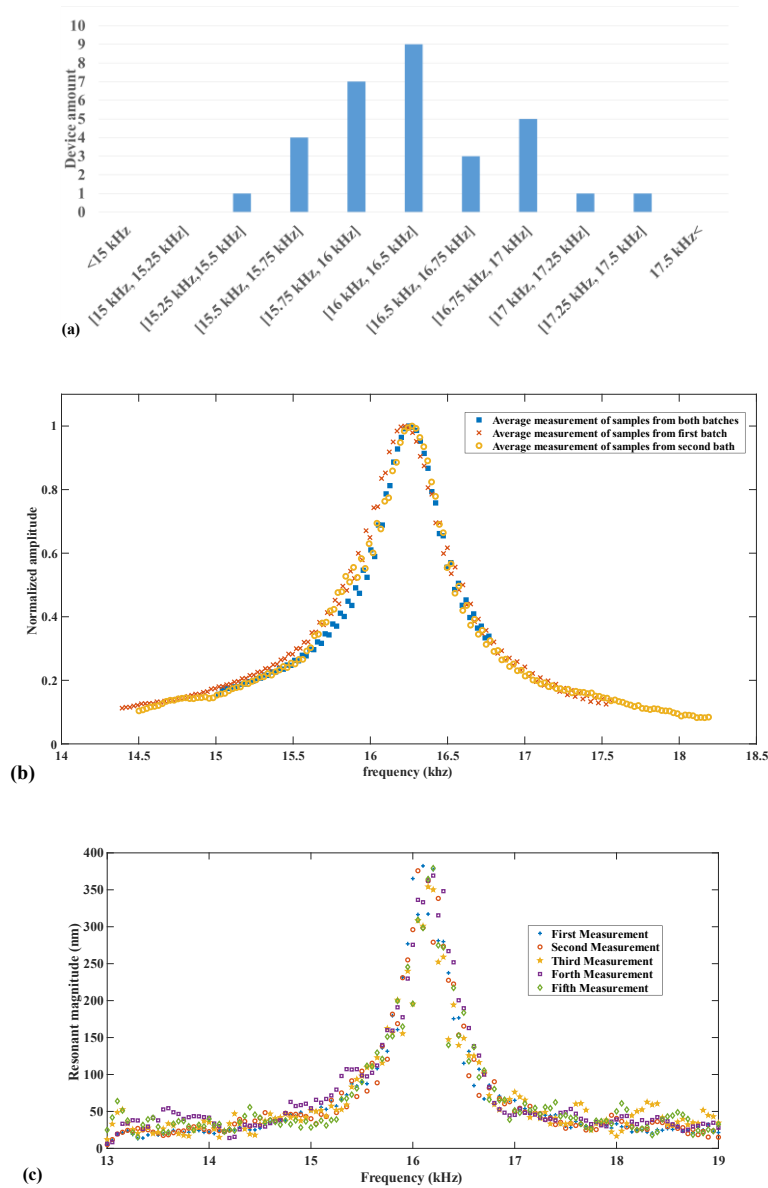


Figure 6.18 Visualization of the mechanical resonance measurement of the fabricated in-plane MEMS test structures. (a) The distribution of individual measurement results; (b) The average resonant frequency of each batch, in comparison with the overall average result; (c) The comparison of five measurement results for a single test structure.

In Figure 6.18a, over 90 % of the manufactured test structures have their resonant frequency values deviated from the average frequency by less than $\pm 4\%$. In Figure 6.16b, the average measurement results for the two batches share a high similarity in profiles. The deviation of these profiles from the one for the average measured frequency has been minor, which provides evidence for *reproducibility* at the batch-level. In Figure 6.16c, the consistency among the five separate measurements of a single device indicates that the performance of the test structures is repeatable.

6.4.3 Electrical impedance measurement

The electrical impedance measurement result of all of the 60 in-plane MEMS test structures connected in parallel is shown in Figure 6.19.

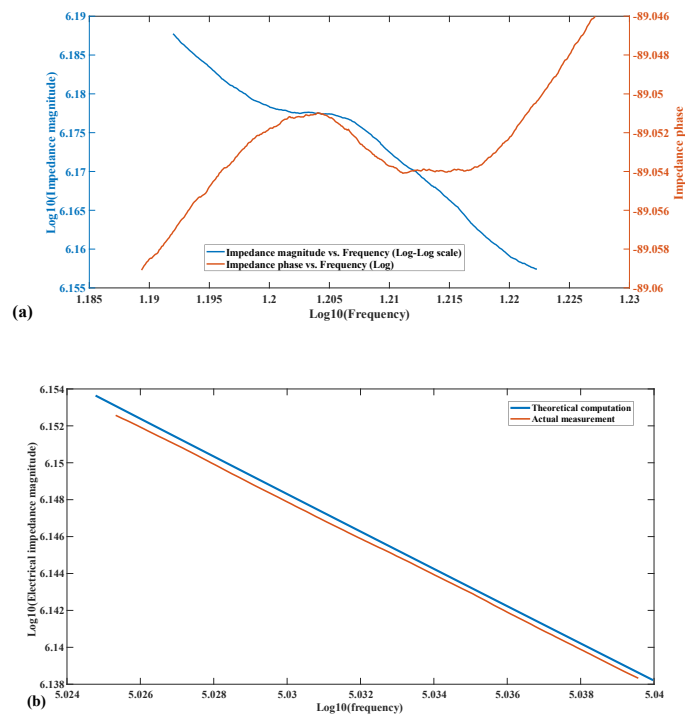


Figure 6.19 Measurement of the electrical impedance of the in-plane MEMS test structures. (a) Electrical impedance magnitude (log scale) vs. frequency (log scale) and phase vs. frequency (log scale), for a frequency band centered at the mechanical resonant frequency; (b) Electrical impedance magnitude (log scale) vs. frequency (log scale) for a frequency away from the mechanical resonant frequency.

In Figure 6.19a, a back-reflection of the mechanical resonance onto the dominant capacitive behavior can be observed. The back-reflection demonstrates the existence of the mechanical-to-electrical coupling interface. The minor deviation from the measured average frequency could be related to the parasitic effect in the electrical circuit.

In Figure 6.19b, the measurement of impedance magnitude (log scale) is compared with the curve estimated with the capacitance in Table 6.4. According to Figure 6.17b, the measurement result has only deviated from the theoretical computation by less than 1%, indicating excellent metallic coverage during the experimental case study.

6.5 Discussion about the practicability of the new strategy and technology

The main concern related to the ‘Border-bulk’ strategy is that the strategy might be bound to the laser micromachining process. If this were true, fabrication technologies based on this new strategy would only be suitable for R&D and prototyping, limiting the application potential of the ‘Border-bulk’ approach.

The author does not think the process scalability would be an issue. The ‘Border-bulk’ strategy can be implemented in a more parallel way, dedicated to large-scale production of SU-8 in-plane MEMS devices.

Researchers have demonstrated the possibility of etching polyimide layers through dry etching methods [151-153]. Buder *et al.* have experimentally validated the possibility of using reactive ion etching (RIE) to etch over 40 μ m polyimide in less than an hour[151]. An aluminum layer was used as the hard masks of the RIE in their research. The research achievements of Buder *et al.* shine light on one technological path to address the scalability issue for ‘Border-bulk’ fabrication methods. The fabrication technology developed in this chapter can be modified to use

polyimide RIE, instead of laser micromachining, for large-scale fabrication of in-plane MEMS devices. The corresponding fabrication flow is illustrated in Figure 6.20.

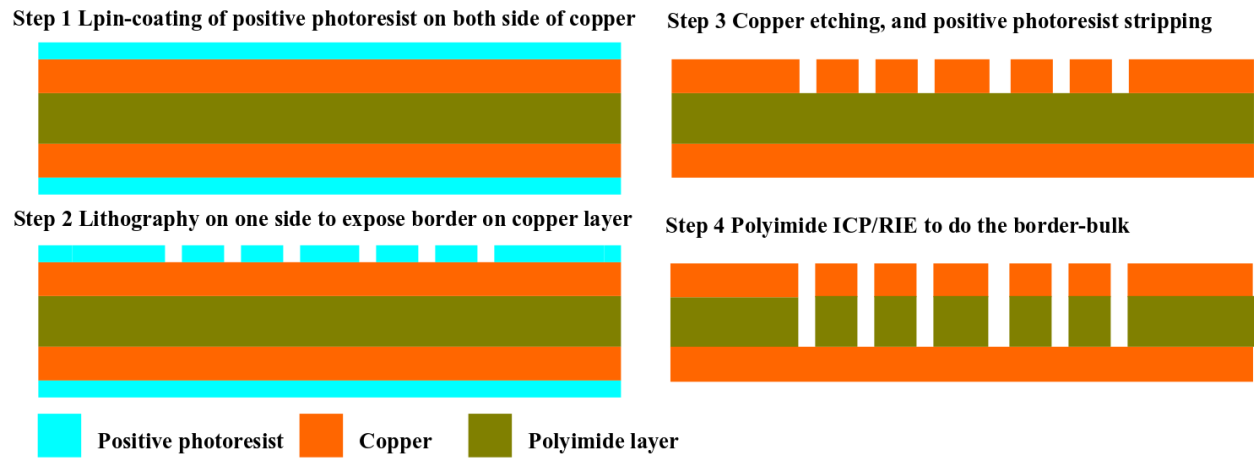


Figure 6.20 Illustration of the implementation of the ‘Border-bulk’ strategy based on polyimide RIE

In Figure 6.20, the modified method uses Pyrulax[®] AP composites with two copper layers. One copper layer is selected as the hard mask layer for polyimide RIE. The photoresist deposited on this layer will undergo lithography to expose the copper layer for wet etching. The copper etching exposes polyimide underneath, which will be etched by the subsequent RIE process. The copper layer of Pyrulax[®] has a maximum thickness of 35 μm . The laser dot diameter for laser micromachining is 25 μm . In the modified fabrication flow, the width of the profile trench will not be significantly enlarged.

6.6 Summary

Chapter 6 introduces a new micromachining strategy, ‘Border-bulk,’ for SU-8 in-plane capacitive MEMS structures. This new micromachining strategy implements a better method to release SU-8 in-plane MEMS devices. The layers of supportive material underneath the movable components are removed in a way simpler than silicon bulk micromachining. As far as to the

author's acknowledgment, this is the first time that this process advantage is implemented for SU-8 in-plane MEMS.

As the incipient research of this new technology path, a new fabrication flow has been developed to test the feasibility of the 'Border-bulk' strategy. The new fabrication technology consists of four steps, removing two steps from the existing layer-by-layer SU-8 surface micromachining for similar structures.

Experimental case studies have been carried out to evaluate the process controllability. Area-varying comb drives were designed, fabricated, and characterized as test structures. The characterization result has demonstrated that the new fabrication flow has acceptable controllability and general robustness. The technologies' capability to implement a bi-directional electrical-mechanical coupling interface has also been verified.

The practicability of the new strategy has also been discussed. Theoretically, the 'Border-bulk' strategy can also be used for fabrication technologies that possess higher scalability and processing speed, suitable for massive manufacturing.

The research work in this chapter demonstrates that the new micromachining strategy, 'Border-bulk,' has great potential in improving the manufacturing of SU-8 in-plane MEMS devices and promoting their applications.

Chapter 7: Thesis summary

7.1 Summary of accomplished research work

A new fabrication technology framework for SU-8 MEMS devices has been developed in this thesis. Novel methodologies have been used in this technology framework to manufacture SU-8 MEMS devices.

Sacrificial-layer-free fabrication of SU-8 out-of-plane MEMS devices has been implemented based on pixel-level dose-modulation during UV exposure. This novel methodology has been used to develop a 3-step fabrication technology for SU-8 out-of-plane MEMS devices. The new fabrication technology removes three to four steps from the existing SU-8 surface micromachining process. This achievement demonstrates that the fabrication process of SU-8 out-of-plane MEMS devices can be further simplified.

Removal of supportive layers underneath SU-8 in-plane MEMS devices has been implemented based on a novel micromachining strategy, 'Border-bulk.' This novel strategy has been used to develop a 4-step fabrication technology for SU-8 in-plane MEMS devices. The new fabrication technology is 2-step simpler than existing SU-8 surface micromachining. More importantly, the new strategy and the corresponding fabrication flow demonstrate that the fabrication process of SU-8 in-plane MEMS devices could realize the optimum release of movable structures, similar to SOIMUMPs for silicic in-plane MEMS devices, but with reduced cost on resources.

Experimental case studies have evaluated the two methodologies and the corresponding fabrication flows. Table 7.1 summarizes the corresponding result.

Criteria		For out-of-plane SU-8 MEMS structures	For in-plane SU-8 MEMS structures
		A 3-step method using maskless grayscale lithography	A 4-step method using a novel micromachining strategy, ‘Border-bulk’
Process controllability	Being calibratable (calibratability)	Reliable calibration possible	Reliable calibration possible
	Being predictable (predictability)	Relative error < 3%	Relative error < 2%
	Being consistent (reproducibility)	Standard deviation < 4%	Standard deviation < 3.5%
	Robustness	acceptable	acceptable
Process usability		Possible to create the bi-directional electro-mechanical interface	Possible to create the bi-directional electro-mechanical interface

Table 7.1 Summary of the fabrication technology developed in this thesis: process controllability

As shown in Table 7.1, the new fabrication technologies proposed in this thesis, as the incipient step on two novel methodologies for SU-8 MEMS fabrication, have exhibited satisfying performance when compared with the goals set in Chapter 1. The result of their experimental case studies demonstrated the feasibility and the application potential of the two new technological paths for SU-8 MEMS fabrication.

As far as to the author’s acknowledgment, this thesis is among the very first that uses SU-8 grayscale lithography/pixel-level dose modulation to make SU-8 out-of-plane MEMS structures, validated by measurement of electromechanical coupling.

As far as to the author's acknowledgment, this thesis is among the very first that releases the movable components of SU-8 in-plane MEMS devices by removing the supporting material underneath, validated by measurement of electromechanical coupling. Before this thesis, such final status is only achievable for silicon in-plane MEMS made by SOIMUMPs.

This thesis provides the two new methodologies for polymeric MEMS fabrication, with their basic feasibility validated. From a more general scope, the two new methodologies have great potential in further enhancing the coupling between the MEMS design and the fabrication and shortening the R&D cycles of polymeric MEMS devices. The conducted research work helps polymer-based microfabrication technologies to enter the MEMS field as disruptive innovations. They can fulfill MEMS designers' demand for customizable, fast, low-cost, and robust MEMS microfabrication to accelerate the corresponding research progress.

7.2 Scope of future work

The author provides three possible future research directions based on the accomplishments in this thesis.

7.2.1 Implementation of SU-8 MEMS devices for specific applications

Future work in this direction is directly based on the two fabrication technologies developed in this thesis.

This thesis used a bottom-to-top method for research activities. Developed fabrication technologies do not target any specific application topics. However, experimental case studies have demonstrated the capability of the newly-developed fabrication technologies in creating the bi-directional electromechanical coupling interface. Meanwhile, as discussed in Chapter 4 and Chapter 6, the usage of maskless grayscale lithography (for sacrificial-layer-free fabrication based on dose-modulation) and laser micromachining (for the 'Border-bulk' strategy) have the advantage

in process flexibility, making them more suitable for the R&D of SU-8 MEMS devices. In such an application scenario, adjustments on MEMS design are frequent. The two fabrication technologies introduced in this Ph.D. thesis can implement rapid fabrication to accelerate the validation at the design phase. In this context, one future research topic is to use the developed fabrication technologies to manufacture SU-8 MEMS devices for specific applications.

7.2.2 Research and development towards massive production

Future work in this direction is related to the two principles/methodologies validated in this thesis for SU-8 MEMS fabrication.

The practicability of the two novel methodologies and the corresponding fabrication flows have been discussed in Chapter 4 and Chapter 6. There are no theoretical obstacles blocking the two methodologies from being used for the massive production of SU-8 MEMS devices. However, there are some constraints on the process scalability of the fabrication technologies developed to validate the feasibility of these principles in this thesis. Maskless grayscale lithography (for sacrificial-layer-free fabrication based on dose-modulation) and laser micromachining (for the ‘Border-bulk’) are semi-serial or full-serial processes. New fabrication flows based on hard-mask alternation or polyimide DRIE should be developed if the two novel methodologies are to be used for massive manufacturing. As the next step after the incipient step in this thesis, the characterization and validation of these fabrication flows will also be more extensive.

7.2.3 Functionalized SU-8 for controllable MEMS fabrication

Future work in this direction is related to the material platform of polymeric MEMS device fabrication.

The research in this thesis has demonstrated that the aggregation of insoluble conductive fillers is inevitable when they are mixed with SU-8. These insoluble fillers are also unable to

crosslink with SU-8 monomers, so structural damages can be frequently spotted on the MEMS structures manufactured using conductive SU-8. The aggregation and structural damages compromise the process reproducibility.

If a conductive additive that shares common solvents with the monomer of SU-8 can be found or synthesized, the development of an ‘intrinsically’ conductive photoresist would become possible. When these soluble conductive fillers are added into SU-8 photoresist, they are broken down to the molecular level. Optimum dispersion, minimum aggregation, and minimum percolation threshold become possible. Their negative impact on SU-8 lithography and process qualities would be kept at a minimal level. Since polymeric MEMS fabrication using conductive photoresist does not need a separate metallization process, conductive SU-8 made by soluble fillers will further improve the process simplicity. Some conductive organic materials from the thiophane family can dissolve in chemicals like acetone. They are very promising candidates for research in this direction.

Bibliography

- [1] M. Gad-el-Hak, *MEMS: applications*: CRC press, 2005.
- [2] C. Liu, "Recent developments in polymer MEMS," *Advanced Materials*, vol. 19, pp. 3783-3790, Nov 2007.
- [3] T. Winterstein, M. Staab, C. Nakic, H. J. Feige, J. Vogel, and H. F. Schlaak, "SU-8 Electrothermal Actuators: Optimization of Fabrication and Excitation for Long-Term Use," *Micromachines*, vol. 5, pp. 1310-1322, Dec 2014.
- [4] H. Lorenz, M. Despont, N. Fahrni, N. LaBianca, P. Renaud, and P. Vettiger, "SU-8: a low-cost negative resist for MEMS," *Journal of Micromechanics and Microengineering*, vol. 7, p. 121, 1997.
- [5] A. Bertsch and P. Renaud, "Special issue: 15 years of SU8 as MEMS material," ed: Multidisciplinary Digital Publishing Institute, 2015.
- [6] J. M. Bustillo, R. T. Howe, and R. S. Muller, "Surface micromachining for microelectromechanical systems," *Proceedings of the Ieee*, vol. 86, pp. 1552-1574, Aug 1998.
- [7] G. T. A. Kovacs, N. I. Maluf, and K. E. Petersen, "Bulk micromachining of silicon," *Proceedings of the Ieee*, vol. 86, pp. 1536-1551, Aug 1998.
- [8] Y. J. Zhao and T. H. Cui, "Fabrication of high-aspect-ratio polymer-based electrostatic comb drives using the hot embossing technique," *Journal of Micromechanics and Microengineering*, vol. 13, pp. 430-435, May 2003.
- [9] M. A. Huff, S. F. Bart, and P. Lin, "MEMS Process Integration," in *MEMS Materials and Processes Handbook*, R. Ghodssi and P. Lin, Eds., ed Boston, MA: Springer US, 2011, pp. 1045-1181.
- [10] S. C. Wang, Y. P. Hao, and S. J. Liu, "The design and analysis of a MEMS electrothermal actuator," *Journal of Semiconductors*, vol. 36, p. 5, Apr 2015.
- [11] P. Abgrall, V. Conedera, H. Camon, A. M. Gue, and N. T. Nguyen, "SU-8 as a structural material for labs-on-chips and microelectromechanical systems," *Electrophoresis*, vol. 28, pp. 4539-4551, Dec 2007.
- [12] A. del Campo and C. Greiner, "SU-8: a photoresist for high-aspect-ratio and 3D submicron lithography," *Journal of Micromechanics and Microengineering*, vol. 17, pp. R81-R95, Jun 2007.
- [13] J. N. Lee, C. Park, and G. M. Whitesides, "Solvent Compatibility of Poly(dimethylsiloxane)-Based Microfluidic Devices," *Analytical Chemistry*, vol. 75, pp. 6544-6554, 2003/12/01 2003.
- [14] C. Zhang, C. Yang, and D. Ding, "Deep reactive ion etching of PMMA," *Applied Surface Science*, vol. 227, pp. 139-143, 2004/04/15/ 2004.
- [15] L. Weber, W. Ehrfeld, H. Freimuth, M. Lacher, H. Lehr, and B. Pech, "Micromolding: a powerful tool for large-scale production of precise microstructures," in *Micromachining and Microfabrication Process Technology II*, 1996, pp. 156-167.
- [16] H. Becker and U. Heim, "Silicon as tool material for polymer hot embossing," in *Technical Digest. IEEE International MEMS 99 Conference. Twelfth IEEE International Conference on Micro Electro Mechanical Systems (Cat. No. 99CH36291)*, 1999, pp. 228-231.
- [17] J. Elders, H. V. Jansen, M. Elwenspoek, and W. Ehrfeld, "DEEMO: a new technology for the fabrication of microstructures," in *Proc. IEEE MEMS*, 1995, pp. 238-243.
- [18] L. Lin, C.-J. Chiu, W. Bache, and M. Hecke, "Microfabrication using silicon mold inserts and hot embossing," in *MHS'96 Proceedings of the Seventh International Symposium on Micro Machine and Human Science*, 1996, pp. 67-71.
- [19] J. Akedo, M. Ichiki, K. Kikuchi, and R. Maeda, "Fabrication of three dimensional micro structure composed of different materials using excimer laser ablation and jet molding," in *Proceedings IEEE The Tenth Annual International Workshop on Micro Electro Mechanical Systems. An Investigation of Micro Structures, Sensors, Actuators, Machines and Robots*, 1997, pp. 135-140.
- [20] T. Hanemann, R. Ruprecht, and J. H. Haußelt, "Micromolding and photopolymerization," *Advanced Materials*, vol. 9, pp. 927-929, 1997.
- [21] X. M. Zhao, Y. Xia, and G. M. Whitesides, "Fabrication of three-dimensional micro-structures: Microtransfer molding," *Advanced Materials*, vol. 8, pp. 837-840, 1996.
- [22] E. Kim, Y. Xia, and G. M. Whitesides, "Polymer microstructures formed by moulding in capillaries," *Nature*, vol. 376, p. 581, 1995.
- [23] I. Christiaens, G. Roelkens, K. De Mesel, D. Van Thourhout, and R. Baets, "Thin-film devices fabricated with benzocyclobutene adhesive wafer bonding," *Journal of Lightwave Technology*, vol. 23, p. 517, 2005.

- [24] V. Dragoi, T. Glinsner, G. Mittendorfer, B. Wieder, and P. Lindner, "Adhesive wafer bonding for MEMS applications," in *Smart Sensors, Actuators, and MEMS*, 2003, pp. 160-167.
- [25] J. N. Lee, C. Park, and G. M. Whitesides, "Solvent compatibility of poly (dimethylsiloxane)-based microfluidic devices," *Analytical chemistry*, vol. 75, pp. 6544-6554, 2003.
- [26] M. Zhang, J. Wu, L. Wang, K. Xiao, and W. Wen, "A simple method for fabricating multi-layer PDMS structures for 3D microfluidic chips," *Lab on a Chip*, vol. 10, pp. 1199-1203, 2010.
- [27] M. Abadie, N. Chia, and F. Boey, "Cure kinetics for the ultraviolet cationic polymerization of cycloliphatic and diglycidyl ether of bisphenol-A (DGEBA) epoxy systems with sulfonium salt using an auto catalytic model," *Journal of applied polymer science*, vol. 86, pp. 1587-1591, 2002.
- [28] K. Nakamura, *Photopolymers: photoresist materials, processes, and applications*: CRC Press, 2018.
- [29] L. Dellmann, S. Roth, C. Beuret, G. A. Racine, H. Lorenz, M. Despont, *et al.*, *Fabrication process of high aspect ratio elastic structures for piezoelectric motor applications*. New York: I E E E, 1997.
- [30] L. Dellmann, S. Roth, C. Beuret, G. A. Racine, H. Lorenz, M. Despont, *et al.*, "Fabrication process of high aspect ratio elastic and SU-8 structures for piezoelectric motor applications," *Sensors and Actuators a-Physical*, vol. 70, pp. 42-47, Oct 1998.
- [31] R. Feng and R. J. Farris, "The characterization of thermal and elastic constants for an epoxy photoresist SU8 coating," *Journal of Materials Science*, vol. 37, pp. 4793-4799, Nov 2002.
- [32] N. Labianca and J. D. Gelorme, *High aspect ratio resist for thick film applications* vol. 2438. Bellingham: Spie - Int Soc Optical Engineering, 1995.
- [33] J. Melai, C. Salm, S. Smits, J. Visschers, and J. Schmitz, "The electrical conduction and dielectric strength of SU-8," *Journal of Micromechanics and Microengineering*, vol. 19, p. 7, Jun 2009.
- [34] J. R. Thorpe, D. P. Steenson, and R. E. Miles, "High frequency transmission line using micromachined polymer dielectric," *Electronics Letters*, vol. 34, pp. 1237-1238, Jun 1998.
- [35] S. Lucyszyn, "Terahertz time-domain spectroscopy of films fabricated from SU-8," *Electronics Letters*, vol. 37, pp. 1267-1267, Sep 2001.
- [36] D. Armani, C. Liu, and N. Aluru, "Re-configurable fluid circuits by PDMS elastomer micromachining," in *Technical Digest. IEEE International MEMS 99 Conference. Twelfth IEEE International Conference on Micro Electro Mechanical Systems (Cat. No. 99CH36291)*, 1999, pp. 222-227.
- [37] R. C. Voicu, M. Al Zandi, R. Muller, C. H. Wang, and Iop, "Nonlinear numerical analysis and experimental testing for an electrothermal SU-8 microgripper with reduced out-of-plane displacement," in *28th Micromechanics and Microsystems Europe Workshop*. vol. 922, ed Bristol: Iop Publishing Ltd, 2017.
- [38] R. C. Voicu, C. Tibeica, R. Muller, A. Dinescu, M. Pustan, and C. Birleanu, "SU-8 Microgrippers based on V-shaped Electrothermal Actuators with Implanted Heaters," *Romanian Journal of Information Science and Technology*, vol. 19, pp. 269-281, 2016.
- [39] X. H. Wang, D. B. Xiao, Z. H. Chen, and X. Z. Wu, "Arrayed SU-8 polymer thermal actuators with inherent real-time feedback for actively modifying MEMS' substrate warpage," *Journal of Micromechanics and Microengineering*, vol. 26, p. 10, Sep 2016.
- [40] W. Y. Zhang, M. Gnerlich, J. J. Paly, Y. H. Sun, G. S. Jing, A. Voloshin, *et al.*, "A polymer V-shaped electrothermal actuator array for biological applications," *Journal of Micromechanics and Microengineering*, vol. 18, p. 8, Jul 2008.
- [41] G. K. Lau, J. P. Yang, B. Thubthimthong, N. B. Chong, C. P. Tan, and Z. M. He, "Fast electrothermally activated micro-positioner using a high-aspect-ratio micro-machined polymeric composite," *Applied Physics Letters*, vol. 101, p. 4, Jul 2012.
- [42] R. Voicu, R. Muller, L. Effime, and Ieee, *A NEW DESIGN BASED ON ELECTRO-THERMALLY ACTUATION FOR AN SU-8 MICROGRIPPER*. New York: Ieee, 2008.
- [43] G. K. Lau, T. C. Duc, J. F. L. Goosen, P. M. Sarro, and F. van Keulen, "An in-plane thermal unimorph using confined polymers," *Journal of Micromechanics and Microengineering*, vol. 17, pp. S174-S183, Jul 2007.
- [44] J. W. Kim, K. Yoshida, K. Kouda, and S. Yokota, "A flexible electro-rheological microvalve (FERV) based on SU-8 cantilever structures and its application to microactuators," *Sensors and Actuators a-Physical*, vol. 156, pp. 366-372, Dec 2009.
- [45] C. Prokop, N. Irmeler, B. Laegel, S. Wolff, A. Mitchell, and C. Karnutsch, "Optofluidic refractive index sensor based on air-suspended SU-8 grating couplers," *Sensors and Actuators a-Physical*, vol. 263, pp. 439-444, Aug 2017.
- [46] M. M.-W. Chang, M. T. Deng, J. T. Gwo, J. D. Mai, and E. Hsu, "Polymer-based capacitive micromachined

- ultrasonic transducers (cmut) for micro surgical imaging applications," in *Nano/Micro Engineered and Molecular Systems, 2006. NEMS'06. 1st IEEE International Conference on*, 2006, pp. 61-65.
- [47] M. W. Chang, H. C. Deng, D. C. Pang, and M. Y. Chen, "6F-6 A Novel Method for Fabricating Sonic Paper," in *2007 IEEE Ultrasonics Symposium Proceedings*, 2007, pp. 527-530.
- [48] V. Oliveira, R. Ibrahim, E. Barros, L. Mendonça, B. Lima, H. Piazzeta, *et al.*, "MEMS-Based Ultrasound Transducer: CMUT Modeling and Fabrication Process," *ECS Transactions*, vol. 49, pp. 431-438, 2012.
- [49] M. A. Tadayon and S. Ashkenazi, "Optical micromachined ultrasound transducers (OMUT)-a new approach for high-frequency transducers," *IEEE Transactions on Ultrasonics, Ferroelectrics, and Frequency Control*, vol. 60, pp. 2021-2030, 2013.
- [50] J. Joseph, S. G. Singh, S. R. K. Vanjari, and Ieee, "A Low Pull-in SU-8 based Capacitive Micromachined Ultrasonic Transducer for Medical Imaging Applications," in *2014 36th Annual International Conference of the Ieee Engineering in Medicine and Biology Society*, ed New York: Ieee, 2014, pp. 1398-1401.
- [51] P.-F. Chong, X. Shi, and C.-H. Cheng, "Capacitive micromachined ultrasonic transducer (CMUT) with graphene membrane," in *Ultrasonics Symposium (IUS), 2016 IEEE International*, 2016, pp. 1-4.
- [52] D.-C. Pang and C.-M. Chang, "Development of a Novel Transparent Flexible Capacitive Micromachined Ultrasonic Transducer," *Sensors*, vol. 17, p. 1443, 2017.
- [53] D.-C. Pang and Y.-H. Chiang, "A transparent capacitive micromachined ultrasonic transducer (CMUT) array for finger hover-sensing dial pads," in *Solid-State Sensors, Actuators and Microsystems (TRANSDUCERS), 2017 19th International Conference on*, 2017, pp. 2171-2174.
- [54] X. Zhang, O. Adelegan, F. Y. Yamaner, and Ö. Oralkan, "An optically transparent capacitive micromachined ultrasonic transducer (CMUT) fabricated using SU-8 or BCB adhesive wafer bonding," in *Ultrasonics Symposium (IUS), 2017 IEEE International*, 2017, pp. 1-4.
- [55] T. Fujita, K. Maenaka, and Y. Takayama, "Dual-axis MEMS mirror for large deflection-angle using SU-8 soft torsion beam," *Sensors and Actuators A: Physical*, vol. 121, pp. 16-21, 2005.
- [56] M.-H. Jun, S. Yun, M. G. Kim, S.-K. Lee, and J.-H. Lee, "A micromirror scanner with vertical combs tilted by assembly process," in *2008 IEEE/LEOS International Conference on Optical MEMs and Nanophotonics*, 2008, pp. 146-147.
- [57] T. Liu, A. J. Svidunovich, B. C. Wollant, and D. L. Dickensheets, "MEMS 3-D scan mirror with SU-8 membrane and flexures for high NA microscopy," *Journal of Microelectromechanical Systems*, vol. 27, pp. 719-729, 2018.
- [58] W. Dai and W. J. Wang, "Fabrication of comb-drive micro-actuators based on UV lithography of SU-8 and electroless plating technique," *Microsystem Technologies-Micro-and Nanosystems-Information Storage and Processing Systems*, vol. 14, pp. 1745-1750, Oct 2008.
- [59] W. Dai, K. Lian, and W. Wang, "Design and fabrication of a SU-8 based electrostatic microactuator," *Microsystem Technologies*, vol. 13, pp. 271-277, February 01 2007.
- [60] P. Abgrall, V. Conedera, H. Camon, A.-M. Gue, and N.-T. Nguyen, "SU-8 as a structural material for labs-on-chips and microelectromechanical systems," *Electrophoresis*, vol. 28, pp. 4539-4551, Dec 2007.
- [61] M. S. Chiriaco, M. Bianco, F. Amato, E. Primiceri, F. Ferrara, V. Arima, *et al.*, "Fabrication of interconnected multilevel channels in a monolithic SU-8 structure using a LOR sacrificial layer," *Microelectronic Engineering*, vol. 164, pp. 30-35, Oct 2016.
- [62] C. Berger, R. Phillips, A. Centeno, A. Zurutuza, and A. Vijayaraghavan, "Capacitive pressure sensing with suspended graphene-polymer heterostructure membranes," *Nanoscale*, vol. 9, pp. 17439-17449, 2017.
- [63] C.-H. Cheng, C. Chao, X. Shi, and W. W. Leung, "A flexible capacitive micromachined ultrasonic transducer (CMUT) array with increased effective capacitance from concave bottom electrodes for ultrasonic imaging applications," in *Ultrasonics Symposium (IUS), 2009 IEEE International*, 2009, pp. 996-999.
- [64] J. Joseph, S. G. Singh, S. R. K. Vanjari, and Ieee, "Fabrication of SU-8 Based Capacitive Micromachined Ultrasonic Transducer for Low Frequency Therapeutic Applications," in *2015 37th Annual International Conference of the Ieee Engineering in Medicine and Biology Society*, ed, 2015, pp. 1365-1368.
- [65] F. Zamkotsian, V. Conedera, H. Granier, A. Liotard, P. Lanzoni, L. Salvagnac, *et al.*, "Electrostatic polymer-based micro-deformable mirror for adaptive optics - art. no. 64670P," in *MEMS Adaptive Optics*. vol. 6467, S. S. Olivier, T. G. Bifano, and J. A. Kubby, Eds., ed Bellingham: Spie-Int Soc Optical Engineering, 2007, pp. P4670-P4670.
- [66] M. Vinchurkar, A. Joshi, S. Pandey, and V. R. Rao, "Polymeric Piezoresistive Microcantilevers With Reduced Electrical Variability," *Journal of Microelectromechanical Systems*, vol. 24, pp. 1111-1116, Aug 2015.

- [67] S. Juodkazis, V. Mizeikis, and H. Misawa, "Three-Dimensional Structuring of Resists and Resins by Direct Laser Writing and Holographic Recording," in *Photoresponsive Polymers I*. vol. 213, S. R. Marder and K. S. Lee, Eds., ed, 2008, pp. 157-206.
- [68] F. Larramendy, L. Mazonq, P. Temple-Boyer, and L. Nicu, "Three-dimensional closed microfluidic channel fabrication by stepper projection single step lithography: the diabolito effect," *Lab on a Chip*, vol. 12, pp. 387-390, 2012.
- [69] C. Accoto, A. Quattieri, F. Pisanello, C. Ricciardi, C. F. Pirri, M. De Vittorio, *et al.*, "Two-Photon Polymerization Lithography and Laser Doppler Vibrometry of a SU-8-Based Suspended Microchannel Resonator," *Journal of Microelectromechanical Systems*, vol. 24, pp. 1038-1042, Aug 2015.
- [70] A. Bertsch, H. Lorenz, and P. Renaud, "3D microfabrication by combining microstereolithography and thick resist UV lithography," *Sensors and Actuators A: Physical*, vol. 73, pp. 14-23, 1999.
- [71] M. Gaudet, J.-C. Camart, L. Buchaillet, and S. Arscott, "Variation of absorption coefficient and determination of critical dose of SU-8 at 365 nm," *Applied Physics Letters*, vol. 88, p. 024107, 2006.
- [72] R. S. Nesbitt, S. L. Smith, R. A. Molnar, and S. A. Benton, "Holographic recording using a digital micromirror device," in *Proceedings of SPIE- The International Society for Optical Engineering*, 1999, pp. 12-20.
- [73] A. Rammohan, P. K. Dwivedi, R. Martinez-Duarte, H. Katepalli, M. J. Madou, and A. Sharma, "One-step maskless grayscale lithography for the fabrication of 3-dimensional structures in SU-8," *Sensors and Actuators B: Chemical*, vol. 153, pp. 125-134, 2011.
- [74] A. K. Dubey and V. Yadava, "Laser beam machining—a review," *International Journal of Machine Tools and Manufacture*, vol. 48, pp. 609-628, 2008.
- [75] F. H. Dausinger, V. I. Konov, V. Y. Baranov, and V. Y. Panchenko, "Laser Processing of Advanced Materials and Laser Microtechnologies," 2002.
- [76] J. Cheng, C.-s. Liu, S. Shang, D. Liu, W. Perrie, G. Dearden, *et al.*, "A review of ultrafast laser materials micromachining," *Optics & Laser Technology*, vol. 46, pp. 88-102, 2013.
- [77] P. Coelho and A. R. Morales, "Percolation electrical models applied to conductive polymers composites," *Polimeros-Ciencia E Tecnologia*, vol. 27, pp. 1-13, 2017.
- [78] X. Quan, "INVESTIGATION OF THE SHORT-RANGE COHERENCE LENGTH IN POLYMER COMPOSITES BELOW THE CONDUCTIVE PERCOLATION-THRESHOLD," *Journal of Polymer Science Part B-Polymer Physics*, vol. 25, pp. 1551-1560, Jul 1987.
- [79] M. Majidian, C. Grimaldi, A. Pisoni, L. Forro, and A. Magrez, "Electrical conduction of photo-patternable SU8-graphene composites," *Carbon*, vol. 80, pp. 364-372, Dec 2014.
- [80] B. Xue, Y. Q. Zou, and Y. C. Yang, "A photochemical approach for preparing graphene and fabrication of SU-8/graphene composite conductive micropatterns," *Materials & Design*, vol. 132, pp. 505-511, Oct 2017.
- [81] M. Mionic, K. Pataky, R. Gaal, A. Magrez, J. Brugger, and L. Forro, "Carbon nanotubes-SU8 composite for flexible conductive inkjet printable applications," *Journal of Materials Chemistry*, vol. 22, pp. 14030-14034, 2012.
- [82] C. Grimaldi, M. Mionic, R. Gaal, L. Forro, and A. Magrez, "Electrical conductivity of multi-walled carbon nanotubes-SU8 epoxy composites," *Applied Physics Letters*, vol. 102, Jun 3 2013.
- [83] M. M. Said, J. Yunas, R. Ekapawinto, B. Y. Majlis, B. Bais, and Ieee, "Synthesization of Nickel Nanoparticles Embedded in SU8 Polymer for Electromagnetic Actuator Membrane," *2014 Ieee International Conference on Semiconductor Electronics (Icse)*, pp. 213-216, 2014.
- [84] S. Jiguet, A. Bertsch, H. Hofmann, and P. Renaud, "Conductive SU8 photoresist for microfabrication," *Advanced Functional Materials*, vol. 15, pp. 1511-1516, Sep 2005.
- [85] S. Jiguet, A. Bertsch, H. Hofmann, P. Renaud, and Ieee, "Conductive SU8-silver composite photopolymer," in *Mems 2004: 17th Ieee International Conference on Micro Electro Mechanical Systems, Technical Digest*, ed, 2004, pp. 125-128.
- [86] C. V. Patel, A. Khosla, and S. Kassegne, "Micropatternable, Electrically Conducting Polyaniline Photoresist Blends For MEMS Applications," in *Chemical Sensors 10 -and- Mems/Nems 10*. vol. 50, A. Simonian, M. Carter, N. Miura, Y. Shimizu, P. Srinivasan, P. Vanysek, *et al.*, Eds., ed, 2012, pp. 525-535.
- [87] M. K. Gunde, N. Hauptman, and M. Macek, "Electrical properties of thin epoxy-based polymer layers filled with n-carbon black particles - art. no. 68820M," in *Micromachining and Microfabrication Process Technology Xiii*. vol. 6882, M. A. Maher, J. C. Chiao, and P. J. Resnick, Eds., ed, 2008, pp. M8820-M8820.
- [88] R. J. Hurditch, D. J. Nawrocki, and D. W. Johnson, "Fast drying thick film negative photoresist," ed: Google Patents, 2002.

- [89] J. A. Lawton, W. J. Nebe, G. A. Thommes, and J. V. Caspar, "Photohardenable epoxy composition," ed: Google Patents, 2006.
- [90] J. Zhang, K. Tan, G. Hong, L. Yang, and H. Gong, "Polymerization optimization of SU-8 photoresist and its applications in microfluidic systems and MEMS," *Journal of Micromechanics and Microengineering*, vol. 11, p. 20, 2001.
- [91] T. A. Anhoj, A. M. Jorgensen, D. A. Zauner, and J. Hübner, "The effect of soft bake temperature on the polymerization of SU-8 photoresist," *Journal of Micromechanics and Microengineering*, vol. 16, pp. 1819-1824, 2006/07/28 2006.
- [92] K. Wouters and R. Puers, "Diffusing and swelling in SU-8: insight in material properties and processing," *Journal of Micromechanics and Microengineering*, vol. 20, p. 095013, 2010/08/10 2010.
- [93] J. L. Dektar and N. P. Hacker, "Photochemistry of triarylsulfonium salts," *Journal of the American Chemical Society*, vol. 112, pp. 6004-6015, 1990.
- [94] C. A. Mack, "Absorption and reflectivity: designing the right photoresist," *Microlithography World*, pp. 20-21, 1999.
- [95] Z. G. Ling, K. Lian, and L. Jian, *Improved patterning quality of SU-8 microstructures by optimizing the exposure parameters* vol. 3999: SPIE, 2000.
- [96] J. Zhang, M. B. Chan-Park, and S. R. Conner, "Effect of exposure dose on the replication fidelity and profile of very high aspect ratio microchannels in SU-8," *Lab on a Chip*, vol. 4, pp. 646-653, 2004.
- [97] J. Kim, C. Kim, M. G. Allen, and Y. Yoon, "Fabrication of 3D nanostructures by multidirectional UV lithography and predictive structural modeling," *Journal of Micromechanics and Microengineering*, vol. 25, p. 10, Feb 2015.
- [98] S. Keller, G. Blagoi, M. Lillemose, D. Haefliger, and A. Boisen, "Processing of thin SU-8 films," *Journal of micromechanics and microengineering*, vol. 18, p. 125020, 2008.
- [99] R. Feng and R. J. Farris, "Influence of processing conditions on the thermal and mechanical properties of SU8 negative photoresist coatings," *Journal of Micromechanics and Microengineering*, vol. 13, pp. 80-88, Jan 2003.
- [100] E. Dermitzaki, B. Wunderle, J. Bauer, H. Walter, and B. Michel, "Structure property correlation of epoxy resins under the influence of moisture; and comparison of diffusion coefficient with MD-simulations," in *EuroSimE 2008 - International Conference on Thermal, Mechanical and Multi-Physics Simulation and Experiments in Microelectronics and Micro-Systems*, 2008, pp. 1-8.
- [101] Q. Xue and J. Sun, "Electrical Conductivity and Percolation Behavior of Polymer Nanocomposites," in *Polymer Nanocomposites: Electrical and Thermal Properties*, X. Huang and C. Zhi, Eds., ed Cham: Springer International Publishing, 2016, pp. 51-82.
- [102] R. Mezzenga, J. Ruokolainen, G. H. Fredrickson, E. J. Kramer, D. Moses, A. J. Heeger, *et al.*, "Templating Organic Semiconductors via Self-Assembly of Polymer Colloids," *Science*, vol. 299, pp. 1872-1874, 2003.
- [103] Y. Shen, Z. Yue, M. Li, and C.-W. Nan, "Enhanced Initial Permeability and Dielectric Constant in a Double-Percolating Ni_{0.3}Zn_{0.7}Fe_{1.95}O₄-Ni- Polymer Composite," *Advanced Functional Materials*, vol. 15, pp. 1100-1103, 2005.
- [104] A. L. R. Bug, S. A. Safran, and I. Webman, "Continuum Percolation of Rods," *Physical Review Letters*, vol. 54, pp. 1412-1415, 04/01/ 1985.
- [105] A. L. R. Bug, S. A. Safran, and I. Webman, "Continuum percolation of permeable objects," *Physical Review B*, vol. 33, pp. 4716-4724, 04/01/ 1986.
- [106] I. Balberg, "Tunneling and nonuniversal conductivity in composite materials," *Physical Review Letters*, vol. 59, pp. 1305-1308, 09/21/ 1987.
- [107] C.-W. Nan, "Physics of inhomogeneous inorganic materials," *Progress in Materials Science*, vol. 37, pp. 1-116, 1993/01/01/ 1993.
- [108] L. Berhan and A. M. Sastry, "Modeling percolation in high-aspect-ratio fiber systems. I. Soft-core versus hard-core models," *Physical Review E*, vol. 75, p. 041120, 04/30/ 2007.
- [109] R. M. Mutiso and K. I. Winey, "Electrical properties of polymer nanocomposites containing rod-like nanofillers," *Progress in Polymer Science*, vol. 40, pp. 63-84, 2015/01/01/ 2015.
- [110] W. Zheng and S.-C. Wong, "Electrical conductivity and dielectric properties of PMMA/expanded graphite composites," *Composites Science and Technology*, vol. 63, pp. 225-235, 2003/02/01/ 2003.
- [111] K. Zhang, Y. Huang, J. Yan, and L. Sun, "Dynamic infrared scene simulation using grayscale modulation of digital micro-mirror device," *Chinese Journal of Aeronautics*, vol. 26, pp. 394-400, 2013/04/01/ 2013.

- [112] C. D. Gerardo, E. Cretu, and R. Rohling, "Fabrication of circuits on flexible substrates using conductive SU-8 for sensing applications," *Sensors*, vol. 17, p. 1420, 2017.
- [113] O. P. Parida and N. Bhat, "Characterization of optical properties of SU-8 and fabrication of optical components," in *Int. Conf. on Opt. and Photon.(CSIO)*, 2009, pp. 4-7.
- [114] D. E. Aspnes and A. A. Studna, "Dielectric functions and optical parameters of Si, Ge, GaP, GaAs, GaSb, InP, InAs, and InSb from 1.5 to 6.0 eV," *Physical Review B*, vol. 27, pp. 985-1009, 01/15/ 1983.
- [115] S. Chen and M. Wambsganss, "Design guide for calculating natural frequencies of straight and curved beams on multiple supports," Argonne National Lab., Argonne, IL (USA)1974.
- [116] C. Mastrangelo and C. Hsu, "Mechanical stability and adhesion of microstructures under capillary forces. II. Experiments," *Journal of Microelectromechanical systems*, vol. 2, pp. 44-55, 1993.
- [117] Z. Yapu, "Stiction and anti-stiction in MEMS and NEMS," *Acta Mechanica Sinica*, vol. 19, pp. 1-10, 2003.
- [118] F. Walther, P. Davydovskaya, S. Zürcher, M. Kaiser, H. Herberg, A. M. Gigler, *et al.*, "Stability of the hydrophilic behavior of oxygen plasma activated SU-8," *Journal of Micromechanics and Microengineering*, vol. 17, p. 524, 2007.
- [119] L. Amato, S. S. Keller, A. Heiskanen, M. Dimaki, J. Emnéus, A. Boisen, *et al.*, "Fabrication of high-aspect ratio SU-8 micropillar arrays," *Microelectronic Engineering*, vol. 98, pp. 483-487, 2012.
- [120] N. Suma, N. Veda Sandeep, S. L. Pinjare, K. N. Neethu, and K. M. Sudharshan, "Design and characterization of MEMS thermal actuator," in *2012 International Conference on Devices, Circuits and Systems (ICDCS)*, 2012, pp. 638-642.
- [121] J.-L. Lai, C.-J. Liao, and G.-D. Su, "Using an SU-8 photoresist structure and cytochrome c thin film sensing material for a microbolometer," *Sensors*, vol. 12, pp. 16390-16403, 2012.
- [122] L. Guerin, M. Bossel, M. Demierre, S. Calmes, and P. Renaud, "Simple and low cost fabrication of embedded micro-channels by using a new thick-film photoplastic," in *Proceedings of International Solid State Sensors and Actuators Conference (Transducers' 97)*, 1997, pp. 1419-1422.
- [123] I. O. Wygant, M. Kupnik, G. Yaralioglu, B. T. Khuri-Yakub, J. C. Windsor, W. M. Wright, *et al.*, "6F-4 50-kHz Capacitive Micromachined Ultrasonic Transducers for Generating Highly Directional Sound with Parametric Arrays," in *2007 IEEE Ultrasonics Symposium Proceedings*, 2007, pp. 519-522.
- [124] G. C. Hill, R. Melamud, F. E. Declercq, A. A. Davenport, I. H. Chan, P. G. Hartwell, *et al.*, "SU-8 MEMS Fabry-Perot pressure sensor," *Sensors and Actuators A: Physical*, vol. 138, pp. 52-62, 2007/07/20/ 2007.
- [125] C. Pang, Z. Zhao, L. Du, and Z. Fang, "Adhesive bonding with SU-8 in a vacuum for capacitive pressure sensors," *Sensors and Actuators A: Physical*, vol. 147, pp. 672-676, 2008/10/03/ 2008.
- [126] N. Xue, S. P. Chang, and J. Lee, "A SU-8-based compact implantable wireless pressure sensor for intraocular pressure sensing application," in *2011 Annual International Conference of the IEEE Engineering in Medicine and Biology Society*, 2011, pp. 2854-2857.
- [127] E. Cretu, *Inertial MEMS Devices: Modeling, Design and Applications*: Acco, 2003.
- [128] H. A. Tilmans, "Equivalent circuit representation of electromechanical transducers: I. Lumped-parameter systems," *Journal of Micromechanics and Microengineering*, vol. 6, p. 157, 1996.
- [129] W.-M. Zhang, H. Yan, Z.-K. Peng, and G. Meng, "Electrostatic pull-in instability in MEMS/NEMS: A review," *Sensors and Actuators A: Physical*, vol. 214, pp. 187-218, 2014.
- [130] S. Chowdhury, M. Ahmadi, and W. C. Miller, "Pull-in voltage study of electrostatically actuated fixed-fixed beams using a VLSI on-chip interconnect capacitance model," *Journal of Microelectromechanical systems*, vol. 15, pp. 639-651, 2006.
- [131] I. Ladabaum, X. Jin, H. T. Soh, A. Atalar, and B. Khuri-Yakub, "Surface micromachined capacitive ultrasonic transducers," *IEEE transactions on ultrasonics, ferroelectrics, and frequency control*, vol. 45, pp. 678-690, 1998.
- [132] L. Zhang, Y. Jiang, B. H. Liu, M. L. Zhang, W. Pang, and Ieee, "HIGHLY FLEXIBLE PIEZOELECTRIC MEMS RESONATORS ENCAPSULATED IN POLYMER THIN FILMS," in *2018 Ieee Micro Electro Mechanical Systems*, ed, 2018, pp. 170-173.
- [133] M. Vomero, P. Van Niekerk, V. Nguyen, N. Gong, M. Hirabayashi, A. Cinopri, *et al.*, "A novel pattern transfer technique for mounting glassy carbon microelectrodes on polymeric flexible substrates," *Journal of Micromechanics and Microengineering*, vol. 26, Feb 2016.
- [134] J. A. Kreuz and C. M. Hawkins, "High speed etching of polyimide film," ed: Google Patents, 1984.
- [135] R. Schaeffer, *Fundamentals of laser micromachining*: CRC press, 2016.
- [136] W. M. Van Spengen, R. Puers, and I. De Wolf, "A physical model to predict stiction in MEMS," *Journal of*

- micromechanics and microengineering*, vol. 12, p. 702, 2002.
- [137] G. G. Yaralioglu, A. S. Ergun, B. Bayram, E. Haeggstrom, and B. T. Khuri-Yakub, "Calculation and measurement of electromechanical coupling coefficient of capacitive micromachined ultrasonic transducers," *IEEE transactions on ultrasonics, ferroelectrics, and frequency control*, vol. 50, pp. 449-456, 2003.
- [138] W. Zhang, H. Zhang, F. Du, J. Shi, S. Jin, and Z. Zeng, "Pull-in analysis of the flat circular CMUT cell featuring sealed cavity," *Mathematical Problems in Engineering*, vol. 2015, 2015.
- [139] A. Neild, D. Hutchins, and D. Billson, "Imaging using air-coupled polymer-membrane capacitive ultrasonic arrays," *Ultrasonics*, vol. 42, pp. 859-864, 2004.
- [140] H. Al-Chami, "Inkjet printing of transducers," University of British Columbia, 2010.
- [141] V. I. de Oliveira, R. C. Ibrahim, D. Torikai, B. L. S. de Lima, L. G. D. Mendonça, M. H. de Oliveira Piazzeta, *et al.*, "MODELING, SIMULATION AND FABRICATION OF A MEMS-BASED ELECTROSTATIC CAPACITIVE EFFECT-CMUT: FOR GENERATION AND RECEPTION OF ACOUSTIC WAVES," 2011.
- [142] D. A. Hutchins, D. Billson, R. Bradley, and K. Ho, "Structural health monitoring using polymer-based capacitive micromachined ultrasonic transducers (CMUTs)," *Ultrasonics*, vol. 51, pp. 870-877, 2011.
- [143] S. Cho, S. Kim, J. Lee, and N.-E. Lee, "Micro-scale metallization of high aspect-ratio Cu and Au lines on flexible polyimide substrate by electroplating using SU-8 photoresist mask," *Microelectronic engineering*, vol. 77, pp. 116-124, 2005.
- [144] S. Cho, S. Kim, N.-E. Lee, H. Kim, and Y. Nam, "Micro-scale metallization on flexible polyimide substrate by Cu electroplating using SU-8 photoresist mask," *Thin Solid Films*, vol. 475, pp. 68-71, 2005.
- [145] P. B. Johnson and R. W. Christy, "Optical Constants of the Noble Metals," *Physical Review B*, vol. 6, pp. 4370-4379, 12/15/ 1972.
- [146] M. Knowles, G. Rutterford, D. Karnakis, and A. Ferguson, "Micro-machining of metals, ceramics and polymers using nanosecond lasers," *The International Journal of Advanced Manufacturing Technology*, vol. 33, pp. 95-102, 2007.
- [147] J. A. Cella, "Degradation and stability of polyimides," *Polymer Degradation and Stability*, vol. 36, pp. 99-110, 1992/01/01/ 1992.
- [148] A.-J. Mäki, S. Hemmilä, J. Hirvonen, N. N. Girish, J. Kreutzer, J. Hyttinen, *et al.*, "Modeling and Experimental Characterization of Pressure Drop in Gravity-Driven Microfluidic Systems," *Journal of Fluids Engineering*, vol. 137, 2014.
- [149] B. Medgyes, B. Illés, and L. Gál, "Measurements of water contact angle on FR4 and polyimide substrates relating electrochemical migration," in *Proceedings of the 36th International Spring Seminar on Electronics Technology*, 2013, pp. 157-160.
- [150] I. Roch, P. Bidaud, D. Collard, and L. Buchaillot, "Fabrication and characterization of an SU-8 gripper actuated by a shape memory alloy thin film," *Journal of Micromechanics and Microengineering*, vol. 13, pp. 330-336, 2003/02/13 2003.
- [151] U. Buder, J.-P. Von Klitzing, and E. Obermeier, "Reactive ion etching for bulk structuring of polyimide," *Sensors and Actuators A: Physical*, vol. 132, pp. 393-399, 2006.
- [152] G. J. Dishon, S. M. Bobbio, T. G. Tessier, Y.-S. Ho, and R. F. Jewett, "High rate magnetron RIE of thick polyimide films for advanced computer packaging applications," *Journal of Electronic Materials*, vol. 18, pp. 293-299, 1989.
- [153] A. Furuya, F. Shimokawa, T. Matsuura, and R. Sawada, "Micro-grid fabrication of fluorinated polyimide by using magnetically controlled reactive ion etching (MC-RIE)," in *[1993] Proceedings IEEE Micro Electro Mechanical Systems*, 1993, pp. 59-64.